UNIVERSITÀ DEGLI STUDI DI GENOVA - ITALY

PH.D. IN MATHEMATICS AND APPLICATIONS

XXIV CYCLE

Giovanni Giorgi

Mathematical tools for microwave mammography and prostate cryosurgery

Advisors

Prof. Michele Piana
Dipartimento di Matematica
Università di Genova, Italia

Prof. Houssem Haddar
Centre de Mathmatique Appliques
Ecole Polytechnique, Francia

To my uncle Sandro,
mathematician of plants and gardens

Contents

Preface

This Ph.D. Thesis is focused on two main arguments which find a common denominator in the respective applications to biomedical problems. The most part of the Thesis is dedicated to *inverse scattering*, the problem of retrieving some physical information of an object (called scatterer) from the knowledge of scattered field data. The resolution of the inverse scattering problem is, for example, behind the operation of a microwave tomography device and, more in general, the range of applicability of inverse scattering techniques is wide but always related to imaging: non destructive testing, seismic imaging and biomedical imaging are only some of the possible examples. The rest of the Thesis is dedicated to the description of the problem of *cryosurgery planning* and to its resolution through the use of a particular method based on stochastic optimization. Cryosurgery is a technique utilized to fight different types of cancer through the insertion of freezing probes inside the tumoral tissue: when freezed, the tissue is heavily damaged and the cryosurgery planning is the problem of setting the free parameters of the operation in order to limit the action of cold just to the tumoral tissue, without involving healthy regions.

The aim of the Thesis is to analyze some crucial mathematical aspects of these two different fields but maintaining a special attention to their applications to realistic and relevant biomedical situations: in particular, the problem of early detecting breast tumors and the problem of defeating prostate tumors with minimal invasivity are the two contexts in which the inverse scattering and the cryosurgery planning techniques presented in this Thesis are respectively tested.

From a more strictly mathematical viewpoint, the part of the Thesis dedicated to inverse scattering mainly deals with the *linear sampling method*, a technique born almost twenty years ago which allows the reconstruction of shape and position of an object from the knowledge of electromagnetic or acoustic scattering data. The original subjects presented in the Thesis are collected in Chapters three and four which basically develop the arguments of [7, 55, 56, 57] and cover:

- An analysis of the theory concerning the linear sampling method based on its physical interpretation, with the aim of trying to cover some lacks in the theoretical justification of the operation of the method. The linear sampling method is a technique which does

not rise from physical laws and the central argument of the proposed interpretation is to consider the far field equation (i.e. the equation whose resolution is at the basis of the method) as a constraint on the power fluxes of the scattered wave. Following this approach, the operation of the method is justified after some assumptions on the flow lines of the scattered field (Chapter three and [7]).

- The definition of a hybrid technique where the use of the linear sampling method together with an inhomogeneous-background formulation of the scattering problem allows the reduction of the complexity of the scattering scenario and facilitate the proper convergence of quantitative techniques. This approach can be relevant in the case of small inclusions embedded in an inhomogeneous background of large dimension (Chapter four and [55]).

- The definition of a technique able to obtain, from the knowledge of the smallest *transmission eigenvalue*, a constant approximation of the refractive index of the scatterer. Given a scatterer, a transmission eigenvalue is a wave number for which no wave is scattered. This technique is useful to complement qualitative methods such as the linear sampling method since, by nature, they are not able to provide any quantitative information on the scatterer and since the operation of the here proposed technique requires the use of a qualitative method in several important steps (Chapter four and [56, 57]).

The literature regarding cryosurgery planning techniques is very short. As an original contribution, the Thesis presents a planning technique based on the *ant colony optimization method*, a stochastic optimization method of wide range of applicability. The definition of this (inverse) planning technique requires the construction and the implementation of a direct method able to compute, given some freezing sources, the temperature distribution inside a biological tissue by solving the associated problem for heat propagation in biological tissues. The formulations and the numerical validations of the direct and the inverse techniques are presented in Chapters two and five. Many of the arguments relate to [54].

Introduction

After the two decades of '80s and '90s, when *AIDS* was considered the new plague, *cancer* has become the modern illness. Although it was probably already known more than four thousands years ago (the most ancient document concerning cancer is dated back to Egyptians), the incidence of cancer has incredibly grown up in the last century and this unstoppable growth has seemed not to be weakened by all the efforts that medicine and science in general are, at present, employing. Although it is difficult to identify precise causes, the dangerousness that cancer has assumed in the last two decades for humanity seems to be in a great part related to the modern human life-style: for this reason, someone speaks about cancer as the illness of modernity. Pollution, sedentariness, unhealthy diets and the increase of the average life duration are considered as relevant elements that can favor the occurrence of cancer and that have importantly contributed to the growth of cancer incidence.

At the origin of cancer there is the mutation of particular genes that allows the uncontrolled growth of tumoral cells. When these cells are malign, they can detach and invade other areas and give life to new tumors. Cancer can affect different kinds of organs, in different forms and with different intensities: for these reasons, many are the procedures able to detect and treat cancer and the choice of the most appropriate modality may change depending on type of cancer, on type of organ affected and on environmental considerations. In last years, the support that science has given to medicine for cancer fighting has been huge: the war that humans are moving to tumor is not anymore performed only through surgery removal, chemotherapy or radiotherapy but new families of more and more sophisticated diagnosis and therapy techniques based on surprising and unthinkable physical, chemical and biological phenomena are rising. However, the most sophisticated are the techniques employed and the widest is the range of scientific phenomena that one technique exploits, the strongest is the necessity of mathematical systems that rule or monitor the progress of such techniques. More in general, a common point between many of the most used techniques in cancer detection and therapy is the utilization of sophisticated mathematical deployments. Sometimes they are just auxiliary tools making the medical doctor's activity easier and less risky for the patient but more often advanced mathematical instruments are entirely required for the whole operation of diagnosis or therapy.

This Thesis proposes a description and an analysis of some mathematical techniques that

have a direct application to cancer detection and treatment. In particular, although the range of applicability of the presented methods is wider and not only related to medicine, the Thesis is focused on providing mathematical tools for the treatment of two particular kinds of tumors: breast cancer and prostate cancer. More specifically, the main part of the Thesis is dedicated to investigate, from many different points of views, the so-called *scattering problem* that is the problem that rules the behavior of acoustic and electromagnetic waves when they are sent against an object, and whose resolution allows the operation of a microwave tomography device. Although presented basing on a purely mathematic point of view, each technique will be tested against realistic mammographic situations in order to assess the efficacy of the presented methods when applied in the framework of mammographic screenings. A second and smaller part of the Thesis is dedicated to *cryosurgery planning*: cryosurgery is a therapy technique by which a tumor is fought by making its cells freezing through an opportune insertion of freezing probes. Mathematics gives an important contribution in the planning of a cryosurgery operation: in fact, before each operation, many free parameters, such as positions and insertion depths of the probes, have to be fixed depending on the shape of the portion of tissue that has to be freezed and on the temperature that probes are able to reach.

The development of *microwave mammography* and *prostate cryosurgery* can represent an important step forward in the war that humans are fighting against cancer. The set up of a device able to detect breast tumors at early stages is a target that, if achieved avoiding the employment of X-rays or other invasive techniques, can bring to a drastic reduction of the mortality due to breast cancer. In fact, it is a common opinion that, particularly for what concerns breast cancer, an early-stage detection of the tumor is the most important element to be reached for having chances to survive. A reasonable reliability of an early-stage diagnosis can be achieved only by subjecting the patient to very frequent controls, i.e. to a screening procedure. At present, X-ray mammography is the most effective technique for detecting breast tumors but its invasiveness limits its applicability to large scale screening; the introduction of microwave mammography screenings can avoid this drawback and allow as many control as one wants, since microwaves are non-invasive.

If microwave mammography is a detection technique (i.e. it is utilized in order to find the presence of a tumor), cryosurgery is a therapy instrument, able to defeat the tumor when it has been identified by medical imaging modalities. Cryosurgery is a recently developed technique which is starting to be used for the treatments of prostate and liver tumors after it has been introduced for the medication of skin tumors and of other skin diseased. If assisted by an efficient planning tool, cryosurgery is able to minimize the side effects that cancer therapies generally cause and to guaranty good possibilities to completely defeat the tumor.

The operation of a microwave tomography device is based on the resolution of a problem called *inverse scattering problem* which, in principle, allows the reconstruction of the physical parameters of an object from the knowledge (on some points) of the value of the field that

has been scattered. More precisely, when one sends a wave against a penetrable object, such a wave is everywhere scattered by the object (called scatterer) depending on the point by point value of its *refractive index*. The way in which the total electromagnetic or acoustic field is scattered depending on the value of the refractive index of the scatterer and on the incident field is generally ruled by a differential problem called *direct scattering problem*. Hence, the resolution of a direct scattering problem provides the value of the field in the whole space. The value of the field on some points (i.e. where receiving antennas are placed) provides the data of the inverse scattering problem, whose resolution aims to provide information on the refractive index of the scatterer.

Although both problems take place in the same physical domain, from a mathematical point of view the direct and the inverse are two extremely different problems. One (the direct problem) is well-posed in the sense of Hadamard while the other (the inverse problem) is ill-posed. In other words, the direct scattering problem admits always one solution and this solution depends continuously on the data; on the other hand, it is not always clear if the inverse scattering problem has one single solution and, moreover, this solution is always non-continuously dependent from the data. The ill-posedness of the inverse scattering problem prevents its trivial resolution and oblige to make use of regularization techniques that the direct scattering problem does not need at all. Due to the greater simplicity of the problem, almost everything has been said about the direct scattering problem and, at present, research mostly concerns on how to speed up numerical methods providing field values. On the contrary, in the framework of the inverse scattering problem, many are the targets that still have to be achieved: the rush to develop methods able to improve the quality of the reconstructions is very challenging and, also from a purely theoretical point of view, the number of open problems is still big.

The part of the Thesis dedicated to inverse scattering basically deals with the *linear sampling method*, a qualitative technique which allows the detection of position and shape of the scatterer from field data but does not provide any kind of quantitative information on its refractive index. The idea inside the Thesis is to first investigate the theoretical foundation (Chapter 3, Section 2) and the quality of the operation (Chapter 3, Section 1) of the method when applied to microwave mammography and then to use it as a tool placed side by side to other techniques in order to achieve better or new results. More precisely, it will be shown that the linear sampling method can be used as a zooming instrument able to narrow the domain under investigation guarantying improvements in the reconstructions of other quantitative techniques (Chapter 4, Section 1); moreover, it will be shown that, exploiting the proved ability of the method of detecting also those wave number for which the scatterer is invisible (i.e. the so-called *transmission eigenvalues*), an innovative technique providing constant estimates on the refractive index could be formulated (Chapter 4, Section 2).

The cryosurgery planning problem is the problem of setting those free parameters that has

to be fixed before a cryosurgery operation; in general, this problem refers directly to those parameters that are patient-dependent and more related to the physics of heat propagation than to physiological considerations. The input of a cryosurgery planning problem is the shape and the location of the portion of tissue that has to be freezed; the output is a configuration of parameters such that the corresponding freezing front fits as much as possible the boundary of the tumoral region without invading the healthy areas. In other words, since the goal of the operation is to freeze the tumoral up to its boundary, the cryosurgery planning problem can be seen as that inverse problem where, from the knowledge of the temperature on the boundary of the target region, one wants to find the initial conditions that have brought to such a temperature distribution. In this perspective, it is again fair to speak about a direct problem and of an inverse problem, where the direct problem will be that problem where, given the initial conditions, one looks for the corresponding the temperature distribution.

Similarly to the case of the scattering problem, one can see that the direct cryosurgery problem is well posed in the sense of Hadamard, while the inverse problem is ill posed. The present Thesis is interested in investigating the inverse cryosurgery problem, nevertheless also the direct cryosurgery problem plays a relevant role and this is due to the fact that many inverse techniques operate iteratively and requiring, at each iteration, the numerical resolution of the direct problem. In particular, in this Thesis, after an introductive presentation of the existing techniques concerning the direct and the inverse problem, an enthalpy-based numerical approach to the direct problem will be presented (Chapter 2, Section 2) while, finally, an innovative inverse (i.e. planning) technique based on stochastic optimization will be proposed and tested against simple prostate phantoms (Chapter 5).

Summing up, the structure of the Thesis is the following. Chapter 1 presents some generalities about breast cancer, prostate cancer and cancer in general by shortly analyzing causes, incidences and therapies. Chapter 2 introduces microwave tomography and prostate cryosurgery by explaining the principles of their practical operation and the mathematics which rules the physical phenomena and the methodologies at their bases. Chapter 3 and 4 are entirely dedicated to inverse scattering: in Chapter 3, Section 1 the linear sampling method is introduced and its efficacy when applied to breast cancer detection is tested while Chapter 3, Section 2 tries to give the answer to some open problems concerning the theoretical foundation of the linear sampling method; Chapter 4, Section 1 proposes an hybrid technique based on the integration of the linear sampling method to quantitative techniques while in Chapter 4, Section 2 a new technique able to compute estimates on the value of the refractive index of a scatterer is formulated. Finally, in Chapter 5, the subject changes back to cryosurgery: in fact, an inversion method based on a stochastic optimization approach is presented and its practical efficacy assessed through realistic numerical simulations.

CHAPTER 1

Breast and prostate cancer

Breast and prostate cancer are two of the most common and diffused forms of cancer. Both can take place with the age and in correspondence of unhealthy habits and life styles. Breast cancer is often lethal if not early-detected, while prostate cancer is less dangerous than other types of cancer if properly cured. Cancer takes place as a degenerated growth of cells that, when the tumor is or become malign, can be able to detach and invade other healthy tissues. Hence, even in the case in which only a non-vital organ has developed a tumor, cancer has to be cured, otherwise new organs will be contaminated bringing to the death of the person.

The aim of this chapter is to provide a short introduction to the medical and statistical aspects of cancer. Due to the interest that these two particular types of cancer will assume in the following of this Thesis, we will focus on breast cancer and prostate cancer. More specifically, in the first section, some general information about cancer will be provided, while second and third sections will be dedicated to breast and prostate cancer.

1.1. Some generalities on cancer

It is not possible to refer to cancer as to a general disease which could affect the human body: cancer affects different kind of organs in different manners and the way in which a specific type of cancer manifests itself can depend on a large number of factors such as the part of body affected by tumor, the type of cancer and its properties. Nevertheless, all the different types of cancer have something in common: each kind of cancer is originated by an out of control growth of cells.

Normally, cells have some genetic control tools on the multiplication and on the proliferation of the cell itself, where the specific task of these tools is to prevent "wrong" cells to survive. When this control over the cells lacks, cells starts to reproduce in an unchecked way. In this manner, cancer process starts and a large number of new cells are generated: in particular, what happen is that abnormal cells survive giving rice to a new group of abnormal cells and so on. At this point, the body has no control on the growing of these cells and the disease called cancer starts.

In general, all the different kinds of cancer can be grouped into two families: benign cancers and malign cancers. The main difference between these two families consists in the property, which can belong (malign cancers) or not belong (benign cancers) to the cancerous cell, of leaving the tissue where cancer started and colonizing other healthy tissues. Often a benign cancer becomes malign after some time; in other cases, cancers do not transform from benign into malign for years or they jump the step of benign cancer and manifests itself as malign from the beginning.

The wrong behaviors of cells which give rice to cancer have a common origin: in fact, all of them, are originated by a sum of different DNA mutations. These mutations can happen during intervals of time of different lengths and many can be their causes. In rare cases, these causes can already been found in the genes of a person, hence inherited from family members; in other cases, they can be related to habits, life style or to the place where one spends most of his time. For example, when associated to a weak genetic resistance to cancer-causing agents, bad habits like smoking cigarettes or drinking big amounts of alcohol, as well as sedentary life style or unbalanced diets, can contribute to the cancer arise. Environmental causes can also be at the basis of a cancer affection: for example, large time expositions to ultraviolet sun light or to certain chemical substances as well as to smog, petrol, carbon or asbestos can cause those genetic mutations inside the cells that give rice to cancer.

In Italy, the 4% of the population is affected by cancer and, for the 55% of them, cancer has been diagnosed more than five years ago. In 2010, the number of the living persons affected by cancer has been doubled with respect to 1992: the reasons can be addressed to the increasing of the number of new cases (due to the increase of the average duration of life and to the

increase of the incidence of some kinds of tumor) but also to the improvement achieved in fighting tumors and in keeping alive cancer-affected persons. In Europe, in 2006, 3.2 millions of new cases have been diagnosed (53% of males and 47% of females) and 1.7 millions of deaths (56% of males and 44% of females) due to cancers has been registered.

In Italy, the most diagnosed cancer for women is breast cancer (in 2010 the number of women living together with this disease has reached the 42% of all the living cancer affected women): in general, it has been valued that breast cancer affects one Italian woman over 10 and it represents the 25% of the tumors affecting women. Instead, the main tumor affecting males is represented by prostate cancer: the 22% of cancer-affected men has this disease and it has been valued that each man over 16 will be affected by prostate cancer. The incidence of this kind of disease is continuously increasing and, again, it has been doubled in the last ten years.[1][2][3]

1.2. Breast cancer

Female breast is made of a series of 15 or 20 glands connected by ducts and surrounded first by fat tissue and than by a skin layer. Breast cancer starts with the uncontrolled proliferation of glandular or duct cells that are transformed into malign cells. A woman over 10 is affected by breast cancer which represents the 25% of all the tumors affecting women. It is one of the first causes of women death and it constitutes the 17% of cancer deaths.

Some personal situations or behaviors can increase the probability of being affected by breast cancer. First of all, the age: the 80% of woman affected by breast cancer are over 50 years old; then, the presence of particular genes called BRCA1 and BRCA2 can bring to the formation of breast cancer and, overall in the case of cancer affecting young women, having relatives who had this disease increase the probability of a person to be affected by cancer. Often, breast cancer is associated to a an exceeding presence of oestrogenic hormones: for this reason, a good diet where foods which have a good interaction with hormones metabolism are privileged, is generally suggested. More generally, a diet made of good quantities of vegetables or fruits and frequent sport activities can help to prevent the occurrence of cancer; obesity and smoke has to be avoided.

Breast cancer generally does not present any symptom. Eventually, in rare occasions, the occurrence of nodules can be felt by palpation or even been visible. The most part of breast cancers are diagnosed through the use of X-ray mammography (or through ultrasound scan when the woman is young). Although, in general, it is a grave disease, in the case of early

[1] Data provided by AIRTUM (Associazion Italiana dei Registri Tumori)
[2] Data provided by AIRC (Associazione Italiana Ricerca sul Cancro)
[3] Data provided by IARC (International Agency of Research on Cancer)

detections, breast cancer can be cured and the probability to survive can be very high. For these reasons, the most important tool that humans have to fight this disease is to set up an efficient system able to detect the presence of a tumor when it is still at an early stage. In Italy, women are advised to subject to a X-ray mammographic session every two years when they are older than fifty but the cadence can vary depending on the risk factors previously mentioned. Younger women can resort to ultrasound scan when they belong to high risk cases or when there is the evidence of a presence of nodules. Anyway, in general, all the women are suggested to visit a specialist at least once a year.

Breast cancer is generally cured through the removal of the area affected by cancer and of the lymph node which is closer to the tumoral area. When the tumor is at a serious stage, the breast is entirely removed. In order to erase also the microscopical cells that can be detached from the removed tumoral area, the patient has to subject to several cycles of anticancer medicines. A part from chemotherapy, also radiotherapy techniques are, at present, applied in order to reduce presence and power of tumoral cells. Finally, once the tumor has been removed, some high risk patients can be subjected to hormonal cures in order to reduce the possibility of relapses.

It is clear that, at present, the most promising way in order to fight breast cancer is the large scale screening where one has at disposal tools and devices for subjecting all the women to frequent controls. Although X-ray mammography is actually effectively used in this sense and its good operation has been proved by many years of use, there are still some open problems which has to be faced and some drawbacks which has to be overcome. Sometimes, X-ray mammography does not provide a clear evidence of the possible presence of a tumor due to the denseness of the tissue: in this cases, the only way to diagnose for the medical doctor is to compare the actual X-ray slice with several previous ones. Moreover, it is well known that X-rays are invasive and that there is a bound over which a person can not be anymore exposed to the effect of X-rays. For these reasons, researchers are working to find different techniques able to increase the resolution of the images that a medical doctor has to examine and, at the same time, reduce the invasiveness of the technique in order to enable women to subject to more frequent controls.

The possibility to apply microwave tomography to the detection of breast cancer is an issue which many researchers and many institutions are currently investigating and which could represent a step forward in the war against breast cancer. Once its effectiveness is proved, such a device can be extremely useful for what concerns large scale screening since the invasiveness of microwaves is well accepted to be nonexistent and costs could be very held down. Unfortunately, at present, the quality of the resolution provided by this application is not as good as medicine expects and a lot of work has still to be done in order to make microwave able to compete with X-rays for detecting cancer.[4]

[4]Data provided by AIRC (Associazione Italiana Ricerca sul Cancro)

1.3. Prostate cancer

Prostate is a gland belonging only to men and producing a part of the seminal fluid released during ejaculation. It is situated in front of rectum with a dimension comparable to the dimension of a nut which can grow up to create problems to the urinary system because of age or of some pathologies. Prostate cancer starts with an abnormal grow of cells generally belonging to the internal part of the gland.

In recent years, it has been proved that a man each 16 will be affected by prostate cancer during his life. The incidence of prostate cancer, that is the number of new cases in a given time, is continuously increasing due to the increase of the average duration of life and to the invention of a new type of exam called PSA able to monitoring the status of the gland by checking, inside the blood, the level of presence of a molecule that only prostate produces. Fortunately, prostate cancer is not one of the most dangerous type of cancer since, if the tumor is detected at an early stage, the probability to survive can be very high. For example, at present, the average of the patients alive after more than five years from the diagnosis is of 70% which can be considered a very good result if one take also into account the average high age of the patients.

Similarly to breast cancer, age, familiarity and hormones are the most influent factors in causing the occurrence of prostate cancer. The possibilities of being affected by this disease are very small for under forty years old persons but they increase tremendously after fifty years. Two prostate tumors every three are diagnosed to over 65 years old persons and researchers estimate that between 70 and 90 % of over-80 years old men is affected by prostate cancer although in some cases the tumor does not manifest itself. The probability of being affected by cancer doubles if one has at least one relative which had this disease. Moreover, high levels of hormones like testosterone or IGF1, as well as the presence of mutations in BRCA1, BRCA2 and HPC1 genes, can have an influence in the occurrence of this disease. Finally, the probability of being taken ill with prostate cancer can be linked to non-correct life styles: for example, obesity, lack of physical activity, sedentariness can help the take place of cancer process.

In its first stage, prostate cancer does not present any symptom. Only later, when the gland increases its dimension, a person can understand the presence of some problems, most of the time by remarking difficulties or pain in urinating or abnormal need of urinating or presence of blood traces in urine and sperm. Nevertheless, it has to be taken into account that, often, similar symptoms can be related to benign diseases and hence, when such kinds of problems occur, a urological medical examination is recommended before taking any conclusions. Frequent urological medical examinations after a certain age as well as a healthy life style is the prescription that every medical doctor would suggest in order to reduce the probability of

incurring in malign prostate cancers. When, after PSA tests and medical doctor visits, the suspect of a prostate tumor remains, a biopsy on some samples of prostate cells will confirm the eventual presence of cancer. Then, the status and the gravity of the tumor will be assessed through medical imaging modalities as TC (computerized tomography) and MRI (Magnetic Resonance Imaging).

At present, the range of possible therapies that can be utilized in order to cure prostate cancer is wide. In general, medical doctors focus on a specific therapy depending on the personal features of the patient, that are age, illness gravity, presence of other diseases and even patient preferences. In some cases, the preferred strategy could even be not to cure the patient and wait for further evolutions of the disease by continuous monitoring the cancer status: this is the case of old patients and patients with other more serious diseases and where prostate cancer is at a beginning stage. More often, prostate tumor is cured by a surgery removal of the entire gland and of the closer lymph nodes. When the tumor is at an advanced stage, radiotherapy and hormonotherapy are used to kill cells that have not been removed and that can move and affect other organs. A whole removal of the gland is not the only solution for fighting prostate cancer: for example, IORT (Intra Operative Radiation Therapy) and brachytherapy are two techniques that are of common use for treating early stage prostate cancers.

Again as examples of prostate cancer therapies, several techniques are still under investigation: cryosurgery is a technique which aims to the destruction of the tumoral cells by making them reaching extremely low temperatures through the insertion - inside the tumoral region - of freezing probes. Then HIFU-technique obstruct the growth of tumoral cells by bombing them through ultrasound waves. Finally, researchers are experimenting some vaccines able to push the immune defence system to react against the tumor as well as anti-angiogenic medicines which are thought to stop the formation of blood-vessels in the tumoral area, preventing the tumor to receive the feeding needed to grow and survive.[5]

[5]Data provided by AIRC (Associazione Italiana Ricerca sul Cancro)

CHAPTER 2

The mathematics of microwave tomography and cryosurgery

In this chapter, we will give an introduction about the mathematical background behind microwave tomography and cryosurgery operation.

The mathematical problem associated to microwave tomography is generally called *scattering problem* preceded by the words *direct* or *inverse* when one refers to the problem of computing the value of the field given a scatterer (direct problem) or to the problem of retrieving information on the scatterer given field measurements (inverse problem). The direct problem is generally solved to simulate the data of a tomographic experiment while the inverse scattering problem formalizes, in a mathematical framework, what is requested during a microwave tomography session.

If tomography is a diagnosis tool, cryosurgery is a therapy instrument in the sense that, through cryosurgery, tumors are fought by decreasing the temperature of their cells. In fact, the achievement of extremely low temperatures inside a tissue allows the growth of crystals, whose formation affects the health of the cell. In other words, the aim of a cryosurgery operation is to kill tumoral cells through the power of cold and, hence, the mathematical problem behind this operation is concerned with the equations ruling heat propagation in biological tissues. We will speak about direct problem when, given the location of the freezing sources (i.e. boundary conditions) one wants to seek the temperature distribution after a give time. Otherwise, if one is interested in finding location or, more generally, information on the sources from the knowledge of the temperature in some points, we will speak about inverse problem.

Section 2.1 is concerned with with microwave tomography and will first provide a brief description of the origin and of the operation of a tomography device. Then, in subsections 2.1.1 and 2.1.2, the direct scattering problem ruling the behavior of the field given a scatterer will be faced from theoretical and computational point of views. Finally, Section 2.1.3 offers an overview on the methods for solving the inverse scattering problem of reconstructing

information on the scatterer given field data.

The second part of this chapter (i.e. Section 2.2) regards cryosurgery: Section 2.2.1 presents the cryosurgery operation by introducing the physical principles at its basis and by shortly describing the practice of the operation. Section 2.2.2 resumes the dynamic of heat propagation by starting from pure substances to biological tissues. Then an enthalpy-based approach to the modelization of heat propagation with phase change in biological tissues is described in Section 2.2.3 and, in Subsection 2.2.4 the problem of the planning of a cryosurgery operation is finally introduced.

2.1. Microwave tomography

The word "tomography" is generally referred to that medical imaging modality where a three dimensional representation of the structure of an object is provided by a series of two dimensional images. The principle of a tomograph is to send a wave against an object and to measure the scattered field on some antennas placed on the same plane of the emitter. A tomograph can operate based on different physical phenomena: for example, the most common X-ray tomography (CT) is utilized for practical applications since many years, as well as the gamma ray (or photon-emission) tomography (SPECT) and the positron emission tomography (PET).

X-ray tomography is, at present, the most utilized modality for what concerns human body imaging. It guaranties good results at reasonable costs but has the drawback, as well as many other imaging modalities, to be invasive, due to the fact that X-rays are very energetic. For this reason, there is a threshold on the number of X-ray tomographies which a person can be subjected to and, this fact, limits its application to screening modality.

During the last decades, many efforts have been done in order to extend this medical imaging modality to microwaves [110]. The reason is due to the fact that, through the use of microwaves, the invasiveness of tomography is completely erased: hence, a microwave tomography could be, for example, utilized as a screening tool for fighting those tumors whose incidence is very high and whose causes are too less understood (e.g. breast cancer) or in general be very useful for every kind of medical protocol requiring frequent patient controls.

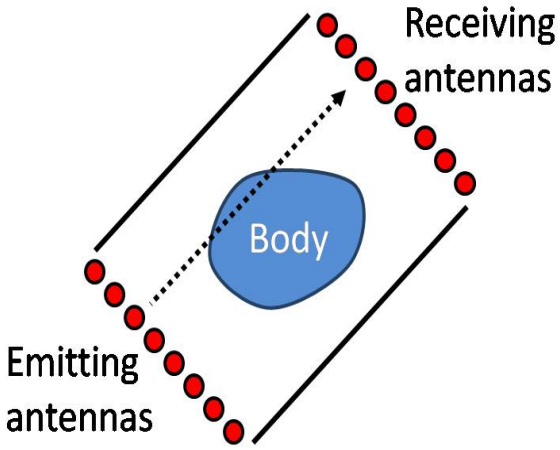

Figure 2.1: A very simple scheme of the structure of a X-ray tomography device. X-rays move on straight lines from emitting to receiving antennas and the whole device structure turns around the investigation area in order to provide a full view of the body.

Although inspired by the same principle, all the tomography modality have differences and these differences are also expressed in the corresponding devices. If we consider, for example,

the most simple scheme of a CT scanner, it will be made of two lines of antennas (one emitting and one receiving) of the same length (see Figure 2.1), with the rectangle formed by the two segments and by the conjunction of their vertices embedding the object (i.e. body) and rotating around an axis. X-rays move on straight lines and the presence on their ways of the object decreases the ray intensity of a factor proportional to density of the body on that line but does not modify its direction: for this reason, a line of emitters and a line of measurements are enough to have a complete description of the object when they can rotate around it.

A microwave is, by its nature, oscillating and hence it does not move by straight lines. And when a microwave crashes a penetrable object, it penetrates the object being refracted in all the directions, and scattered in the whole space. For this reason, a scanner whose antennas are lay in parallel lines provide a too small amount of data for the resolution of the problem and a placement of the measuring antennas on a curve around the object and on the same plane of the direction of the incident wave results more appropriate and more utilized.

Nevertheless, the fact that a microwave is scattered towards all the direction when it crashes an object, brought to the birth of a three dimensional tomography where field data are collected all around the three dimensional object and not only on a single plane. In this case, a fully $3D$ reconstruction of the object is sought from the data.

2.1.1. The direct scattering problem

The direct scattering problem is the problem of describing how a wave is scattered by a medium, when an incident wave is sent from far away against it. The associated differential problem assumes different formulations depending on the physical situation involved: for example, the formulation of the problem is different depending on the type of wave utilized (e.g. acoustic or electromagnetic), on the polarization of the wave (in the case of electromagnetic scattering), on the physical properties of the scatterer (e.g. penetrable medium, conductor, etc.), on the dimension of the problem that one is considering or on other factors. In this section we will propose a survey on the definition of the scattering problem in the case of penetrable media, in acoustic and electromagnetic regime: the propagation of an acoustic wave will be ruled by the equations of continuum mechanics for an inviscid fluid whereas, in the electromagnetic case, the propagation of the wave will be ruled by Maxwell equations. All the formulations will refer to the scattering phenomenon by time-harmonic waves.

In the case of the propagation of an acoustic wave of small amplitude, the velocity vector

field $v(x,t)$ - with $x \in \mathbb{R}^3$ (space) and $t \in [0, +\infty[$ (time) - is solution of the following system

$$\frac{\partial v}{\partial t} + (v \cdot \nabla)v + \frac{1}{\rho}\nabla p = 0 \tag{2.1}$$

$$\frac{\partial \rho}{\partial t} + \nabla \cdot (\rho v) = 0 \tag{2.2}$$

$$p = f(\rho, S) \tag{2.3}$$

$$\frac{\partial S}{\partial t} + v \cdot \nabla S = 0 \tag{2.4}$$

where $p(x,t)$ is the pressure field, $\rho(x,t)$ the density, $S(x,t)$ the specific entropy and f a fluid-dependent function.

Linearizing v, p, ρ and S around the static case corresponding to $v = 0$, $p = p_0 = const$, $\rho = \rho_0$, $S = S_0$, $p_0 = f(\rho_0, S_0)$ (see [41]), we obtain that

$$\frac{\partial^2 p}{\partial t^2} = c^2(x)\rho_0(x)\nabla \cdot (\frac{1}{\rho_0(x)}\nabla p) \tag{2.5}$$

$$c^2(x) = \frac{\partial}{\partial \rho} f(\rho_0(x), S_0(x)). \tag{2.6}$$

If we assume that p is time-harmonic of angular frequency ω

$$p(x,t) = Re\{u(x)\exp^{-i\omega t}\} \tag{2.7}$$

and that terms involving $\nabla\rho_0$ are negligible, we obtain that the pressure field satisfies

$$\Delta u + \frac{\omega^2}{c^2}u = 0 \tag{2.8}$$

where $c(x)$ is the sound speed. Defined the wave number k and the refractive index n

$$k := \frac{\omega}{c_0} \tag{2.9}$$

$$n(x) := \frac{c_0^2}{c^2(x)}, \tag{2.10}$$

the direct acoustic scattering problem by penetrable object is

$$\Delta u + nu = 0 \quad \mathbb{R}^3 \text{ or } \mathbb{R}^2 \tag{2.11}$$

$$u = u^i + u^s \quad \mathbb{R}^3 \text{ or } \mathbb{R}^2 \tag{2.12}$$

$$\lim_{r\to\infty}(\frac{\partial u^s}{\partial r} - iku^s) = 0 \tag{2.13}$$

where u^i and u^s are the incident and the scattered field and $r = |x|$. Equation (2.13) is called Sommerfeld radiation condition and states the decay of the scattered field far from the scatterer. Although presented for $x \in \mathbb{R}^3$, the same arguments are valid for $x \in \mathbb{R}^2$.

Since, for what concerns tomographic applications, waves are sent from antennas posed outside the region under investigation D, we will assume that the index of refraction is homogeneous, well-known and equal to 1 outside a ball B containing D; hence, that the function $m = 1 - n$ has compact support. The value of the index of refraction inside B will identify the presence of the scatterer: $n(x)$ will be a complex number (a complex n corresponds to an absorbing medium), positive in real and imaginary part, and - for what concerns this Thesis, such that $Re(n(x)) > 1$ for each x.

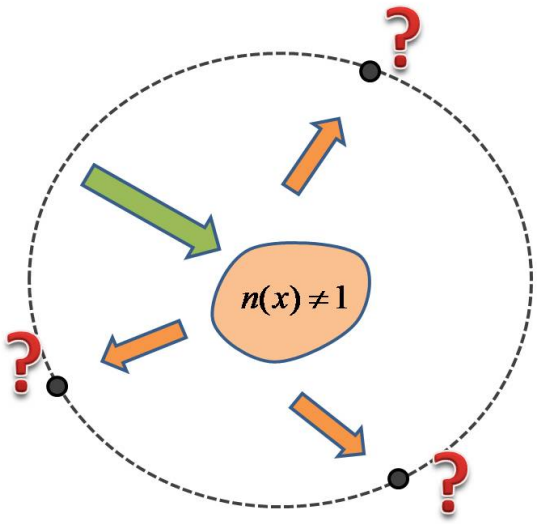

Figure 2.2: The direct scattering problem.

The scattering of an incident electromagnetic field by a scatterer D is ruled by Maxwell equations

$$\nabla \times \tilde{E} + \mu_0 \frac{\partial \tilde{H}}{\partial t} = 0 \tag{2.14}$$

$$\nabla \times \tilde{H} + \varepsilon \frac{\partial \tilde{E}}{\partial t} = J \tag{2.15}$$

$$J = \sigma \tilde{E} \tag{2.16}$$

$$\nabla E = \frac{\eta}{\varepsilon_0} \tag{2.17}$$

where $\tilde{E}(x,t)$ and $\tilde{H}(x,t)$ are respectively the electric and the magnetic field, $J(x,t)$ is the current density, $\varepsilon(x)$ is the electric permittivity, μ_0 the magnetic permeability of the vacuum (we do not consider ferromagnetic scatterers), η is the total charge density and $\sigma(x)$ is the electric conductivity. Defined ε_0 as the electric permittivity of the vacuum, if we assume that

electric and magnetic field are time harmonic, i.e.

$$\tilde{E}(x,t) = \tfrac{1}{\sqrt{\varepsilon_0}} E(x) \exp^{-i\omega t} \tag{2.18}$$

$$\tilde{H}(x,t) = \tfrac{1}{\sqrt{\mu_0}} H(x) \exp^{-i\omega t} \tag{2.19}$$

we have that E and H satisfy

$$\nabla \times E - ikH = 0 \tag{2.20}$$

$$\nabla \times H + ik\tfrac{1}{\varepsilon_0}(\varepsilon + i\tfrac{\sigma}{\omega})E = 0 \tag{2.21}$$

with $k = \omega\sqrt{\varepsilon_0\mu_0}$.

Substituting $H = \frac{1}{ik}\nabla \times E$ in (2.21) and using $\nabla E = 0$, (η=0 can be assumed when the incident field is emitted sufficiently far from the scatterer), one obtains

$$\nabla^2 E + k^2 N E = 0 \tag{2.22}$$

where $N(x) = \frac{1}{\varepsilon_0}(\varepsilon(x) + i\frac{\sigma(x)}{\omega})$.

On the contrary, if one substitutes $E = \frac{-ik}{N}\nabla \times H$ in equation (2.20), it will follows that

$$\nabla \times [\frac{1}{N}(\nabla \times H)] + k^2 H = 0. \tag{2.23}$$

If we assume that the scatterer is an infinitely long cylinder of cross section D and that it is orthotropic, (i.e. $N(x)$ does not depend on the coordinate whose axis is parallel to the cylinder axis), equations (2.22) and (2.23) can be simplified by taking proper polarizations of the electromagnetic field. If the incident field is polarized perpendicular to the axis of the cylinder then the electric field will be constant in the direction of the cylinder; this polarization is known in literature as *transverse magnetic* polarization (TM). On the other hand, if the incident field is polarized parallel to the axis of the cylinder, the magnetic field will have only one component in the direction of the cylinder; this polarization is known as *transverse electric* polarization (TE). When the incident field is respectively TM and TE polarized, it is possible to prove that equations (2.22) and (2.23) become

$$\Delta u_H + k^2 n u_H = 0 \tag{2.24}$$

$$\nabla \cdot (\tfrac{1}{n}\nabla u_E) + k^2 u_E = 0 \tag{2.25}$$

where u_H and u_E are the vector fields respectively associated to H and E and n is the two-entries index of refraction. In other words, if we assume that the cylinder axis is parallel to x_3, third coordinate axis, it will be true that $H = (0, 0, u_H(x_1, x_2))$ and $E = (0, 0, u_E(x_1, x_2))$ where u_H and u_E satisfy (2.24) and (2.25).

Summing up, the direct scattering problem for electromagnetic waves, when the scatterer is assumed to be an infinite cylinder of cross section D, is defined as

$$\Delta u + k^2 n u = 0 \quad \mathbb{R}^2 \tag{2.26}$$

$$u = u^i + u^s \quad \mathbb{R}^2 \tag{2.27}$$

$$\lim_{r\to\infty}(\frac{\partial u^s}{\partial r} - iku^s) = 0 \tag{2.28}$$

for TM-polarization and as

$$\nabla \cdot (\frac{1}{n}\nabla u_E) + k^2 u_E = 0 \quad \mathbb{R}^2 \tag{2.29}$$

$$u = u^i + u^s \quad \mathbb{R}^2 \tag{2.30}$$

$$\lim_{r\to\infty}(\frac{\partial u^s}{\partial r} - iku^s) = 0 \tag{2.31}$$

in the case of TE-polarization.

In [41], [37] and [45] it is established that, given a scatterer of index of refraction n (subjected to some regularity conditions) and an incident field u^i, problems (2.11)-(2.13), (2.26)-(2.28) and (2.29)-(2.31) have a unique solution continuously dependent on the initial data n and u^i (or, in other words, that the those problems are *well posed* in sense of Hadamard [50]).

Problems (2.11)-(2.13) and (2.26)-(2.28) can be equivalently rewritten in integral formulation as

$$u(x) = u^i(x) - \int_D \Phi(x,y)(1-n(y))u(y)dy \tag{2.32}$$

where Φ is the Green's function of the background (for example, $\Phi(x,y) = \frac{i}{4}H_0^1(k|x-y|)$ if the background is the vacuum, with $H_0^{(1)}$ is the zero-order Hankel function of the first kind). (2.32) is called *Lippmann-Schwinger equation* and in [41] it is proved to be equivalent to (2.11)-(2.13) and (2.26)-(2.28) respectively for $x \in \mathbb{R}^3$ or $x \in \mathbb{R}^2$ and for $n \in C^1$. Analogously, (2.29)-(2.31) admits an equivalent integral formulation which can be found for example in [45].

A deeper analysis of the origin and the role of the Lippmann-Schwinger formulation for inverse scattering problems can be found in Section 4 of this Thesis.

2.1.2. Numerical techniques for the direct scattering problem

The computation of an electromagnetic or an acoustic field can be performed through a wide range of typologies of numerical methods. When one deals with scatterers of particular shape (that are, for example, cylinders or sphere) the easiest way to compute the field is using its analytic expansion. Otherwise, if the shape of the scatterer is general, the solution to the differential problem describing the behavior of the field with respect to incident field and to the index of refraction can be obtained by the use of different methods, such as, for example, finite-difference methods, integral equation methods or finite-element methods.

In this section we will show the principles of some numerical methods utilized for providing the data used to test the inversion procedure presented in this Thesis. In particular we will investigate the $2D$ TM electromagnetic cases of a spherical penetrable scatterer (from two different view points) and of a generic penetrable scatterer and the case of the acoustic scattering of a $3D$ sound-soft impenetrable sphere. Further, a brief discussion of the other possible methodologies of resolution for the direct scattering problem will be provided.

Let first consider the case of a TM electromagnetic scattering (see (2.26)-(2.28)) by a circular penetrable object of radial dependent refractive index n. In the case of incident plane waves, the total field u solution of (2.26)-(2.28) is of the form

$$u(x) = \sum_{m=-\infty}^{+\infty} [\alpha_m^\ell H_m^{(1)}(kr_x\sqrt{n(x)}) + \beta_m^\ell J_m(kr_x\sqrt{n(x)})] \exp^{im\theta_x} \tag{2.33}$$

in the region ℓ where $n(x)$ is constant, where (r_x, θ_x) are the polar coordinates of x and where H_m and J_m are respectively Hankel and Bessel functions. The coefficients α_m^ℓ and β_m^ℓ only depend on the incident field and on the geometry. If $\ell = 0$ denotes the outer domain (the vacuum or a general homogeneous background) and $\ell = L$ denotes the inner homogeneous domain then $\alpha_m^L = 0$ and $\beta_m^0 = 0$ correspond to the expansion of the incident field in the neighborhood of the outer boundary. More precisely, using the Jacobi-Anger expansion [41], the incident field is expanded as

$$u^i(x) = \sum_{m=-\infty}^{+\infty} \beta_m^0 J_m(kr_x) \exp^{im\theta_x} . \tag{2.34}$$

The remaining coefficients in expansion (2.33) are determined by imposing the continuity of the total field and of its normal derivative on the interfaces. One obtains for each harmonic m a system of $2L$ equations for $2L$ unknowns. Truncating the infinite series to a value $m = M$, the resolution of the $2M$ systems provide the coefficients and hence the value of the total field u [57, 53].

If the shape of the scatterer is general, it is not anymore possible to use the asymptotic expansion in order to achieve an approximation of the value of the total field u. The so called *method of moments* [88] provides an approximation of u by discretizing the Lippmann-Schwinger equation (2.32).

If $\Phi(x, y) = \frac{i}{4} H_0^1(k|x - y|)$ then the total field u is solution of

$$u(x) = u^i(x) - k^2 \int_{\mathbb{R}^2} (1 - n)(y)u(y)\Phi(x, y)dy. \tag{2.35}$$

Since $1 - n$ vanishes outside the scatterer, we assume to divide its cross section into L cells, small enough to be able to consider n and u constants inside each cell. Then, equation (2.35)

can be rewritten as

$$u(x_m) = u^i(x_m) - k^2 \sum_{j=1}^{L} (1 - n(x_j)) u(x_j) \int_{cell-j} \Phi(x_m, y) dy \tag{2.36}$$

where $j = 1, \ldots, m$ and x_m identifies the center of each cell.

The approximation of

$$\int_{j-cell} \frac{i}{4} H_0^1(k|x_m - y|) dy \simeq \begin{cases} \frac{i\pi ka}{2} J_1(ka) H_0^1(k|x_m - x_j|) & m \neq j \\ \frac{i}{2}[\pi ka H_1^1(ka) + 2i] & m = j \end{cases} \tag{2.37}$$

where $a = \sqrt{\Delta/\pi}$ and Δ the area of the cell transforms (2.35) into a linear system.

Once one has computed the value of u on each pixel of belonging to the support of $1 - n$ by solving a system of the type $(A - I)\vec{u} = \vec{u^i}$, the value of u outside the region where the scatterer lyes is computable through (2.35). We remark that the operation of the method can be accelerated through the use of fast Fourier transform as explained in [15, 109].

Let consider the scattering by a $3D$ sound soft impenetrable scatterer of spherical shape. The value of the total field u can be computed analogously to the $2D$ electromagnetic case (2.33). If we move to spherical coordinates

$$x = r\sin(\theta)\cos(\varphi) \quad y = r\sin(\theta)\sin(\varphi) \quad x = r\cos(\theta), \tag{2.38}$$

and we suppose to send an incident wave $u^i = \exp^{ikz} = \exp^{ikrcos(\theta)}$ parallel to the z axis, then incident field and scattered field assumes [63] the form of

$$u^i(x) = \sum_{m=0}^{\infty} (2m+1)(-i)^m j_m^{(1)}(kr) P_m(\cos(\theta)) \tag{2.39}$$

$$u^s(x) = \sum_{m=0}^{\infty} c_m h_m^{(1)}(kr) P_m(\cos(\theta)) \tag{2.40}$$

where j_m and h_m are the spherical Bessel and Hankel functions and P_m is the Legendre Polynomial of order m [41]. Again, truncating the series at $m = M$ and imposing the boundary condition $u^s = -u^i$ on the surface of the sphere it is possible to compute c_m and hence the value of u^s.

The three methods described above have been used for computing the data of the numerical simulations presented in the following of the Thesis. In general, the literature is full of different types of methods able to compute the value of the field: for example, in [76] are discussed all the issues concerning the application of a finite element method to electromagnetism as well as in [39, 41] theoretical and computational aspects of integral equation methods in scattering are presented. In [59], an overview on the methods of moments for inverse scattering is provided.

2.1.3. The inverse scattering problem

The inverse scattering problem is generally intended as the problem of retrieving the whole information on the scatterer from the only knowledge of the scattered field measured far from it. With respect to the direct problem, the inverse scattering problem presents many more difficulties in its resolution since, as it will be clarified in the following, it is *ill-posed* in the sense of Hadamard (uniqueness of the solution is not always guarantied and there is no continuous dependence of the solution from the data) and non-linear. For these reasons we will see that the definition of "inverse scattering problem" could be weakened up to the problem of "retrieving information" on the scatterer. A weakening in the inversion purposes shall allow the overcoming of some of the pathologies which affects the whole inverse scattering problem: this is the case of qualitative methods where the only problem of reconstructing the shape (and not the whole value of the index of refraction!) will be faced, leading to a reformulation of the problem where the uniqueness of the solution is guarantied and non-linearity is avoided.

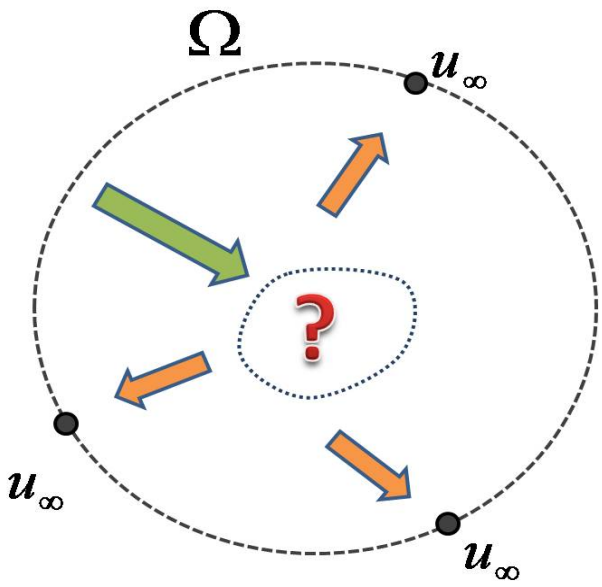

Figure 2.3: The inverse scattering problem.

Although it has been proved in [41] that in the case of time-harmonic acoustic scattering in three dimensions (i.e. problem (2.11)-(2.13)) different scatterers provide different far field patterns, it is still unclear if the same is valid for the two dimensional time-harmonic electromagnetic problems (2.26)-(2.28) and (2.29)-(2.31). Moreover numerical evidences (see [81] or [23]) suggest that, in these cases, to a single far field pattern could correspond more than one refractive index. For these reasons, the existence of a unique solution to the inverse scattering problem of reconstructing the point wise value of the index of refraction by the knowledge of

the far field at a single frequency on a circle (in 2 dimensions) or on a sphere (in 3 dimensions) Ω, has been well established just for the three dimensional case. Nevertheless, the uniqueness result can be achieved also in the two dimensional electromagnetic case when we suppose to have at disposal data on a circle and for an interval of frequencies (see [41]). In [41] it is proved that far field measurements at fixed frequency uniquely identify the shape of a scatterer or, more generally, its discontinuities with respect to a known background.

If we call $\mathfrak{F}$ the operator mapping the index of refraction n in the far field pattern u_∞, it is possible to show, (for example in [15] for $\mathfrak{F} : C^0(\bar{D}) \cup C^1(D) \to C^0(\Omega)$ in the $2D$ electromagnetic case), that $\mathfrak{F}$ is compact and then that the inverse scattering problem is ill-posed. In particular, the compactness of $\mathfrak{F}$ encodes the lack of continuous dependence of the solution from the initial data of the inverse scattering problem.

The set of the existing inversion technique for the resolution of an inverse scattering problem can be divided in four big families which differentiate based either on the purposes of the methods (i.e. if the target is or is not the reconstruction of the whole information on n), on the approximation utilized or on the type of technique employed: the families of *quantitative methods*, of *Born-approximation methods*, of *qualitative methods* and the family of *spectral-quantitative methods*.

The aim of quantitative methods and of Born-approximation methods is a full reconstruction of the value of the index of refraction. The inversion is performed by applying iterative techniques to functionals opportunely defined in order to both keep connected the measured field to the reconstructed refractive index and to avoid the occurrence of situations in which the procedure sticks into local minima. Quantitative methods face the inverse scattering problem in its full non-linearity, whereas in Born-approximation methods the operator $\mathfrak{F}$ is linearized. Both the techniques present advantages and disadvantages: Born methods are lighter than quantitative methods in terms of computational weight but can be applied only to situation of weak scattering [41]; on the other hand quantitative methods are, at least in theory, applicable to every kind of scattering situations but practical evidence suggests that these methods often converge to local minima when they are not initialized with a proper a priori information. Examples of quantitative methods for inverse scattering can be found in [104], [12], [41] and [50] while Born-approximation techniques have been proposed for example in [41] and [48].[95] and [52] present some applications of Born-approximation and quantitative techniques to breast cancer detection by microwaves.

Qualitative methods are a recent range of methods where, instead of retrieving a point wise information on the value of the index of refraction, one attempts to reconstruct just location and shape of the scatterer. From a mathematical point of view, this change of perspective for what concerns the concept of "inverse scattering problem" leads to a reformulation of the problem where the operator $\mathfrak{F}$ is not anymore central in the inversion procedure since it is

substituted by the so called *far field operator* $F : L^2(\Omega) \to L^2(\Omega)$,

$$[Fg](\hat{x}) = \int_{\Omega} u_\infty(\hat{x}, d)g(d)ds(d) \tag{2.41}$$

where $\hat{x} \in \Omega$ and u_∞ is the measured scattered field. Qualitative methods are based on the solution of a one-parameter family of linear equations and provide just a visual and not step-like reconstruction of the scatterer since such a reconstruction is obtained exploiting the behavior of the norm of its solutions which explodes next to the boundary of the scatterer and remains large outside. The advantages of qualitative methods are that they are faster than traditional methods and that they do not require at all any kind of a priori information on the inclusion; unfortunately, when one deals with media embedded in non-empty background, a rather precise knowledge of the index of refraction of the background is necessary. The most famous and utilized qualitative methods are the *linear sampling method* [38, 46, 45, 37] and the *factorization method* [66, 68]: although most of the theoretical background is in common, they distinguish since the factorization method is more theoretically justified than the linear sampling method whereas the linear sampling method is much more generally applicable. Other qualitative methods can be found in [6, 36, 83]; [47, 16] are examples of applications of qualitative techniques to microwave mammography.

In the last years a new generation of techniques is growing up: these methods base their operation on the knowledge of a discrete set of wave numbers - spectrum - of the scatterer, that is the set of wave numbers for which the inclusion remains "invisible" to the incident field. The existence, for each (non-absorbing) scatterer, of a set of such wave numbers - called *transmission eigenvalues* [41, 78] - was a well known fact to the scientific community since many years [40] but transmission eigenvalues were considered just as values for which qualitative methods could not operate. A notable increase of the interest into the field of transmission eigenvalues has been registered when it has been proved that transmission eigenvalues are detectable from far field data [26] and that they encode information on the index of refraction of the scatterer [29, 25]: these two facts gave rise to a new family of inversion methods, the here-called spectral-quantitative methods. The literature concerning spectral-quantitative methods is still short and, at this moment, the state of the art for these methods is able just to associate a constant estimate of the index of refraction to the knowledge of the first real transmission eigenvalue (see [97],[56] and [57]). Nevertheless, theoretical results indicate that the spectrum carries much more information on the scatterer than a simple estimate (see [31], [43] and [24]); for example, it has been proved [24] that the knowledge of the whole spectrum is sufficient to uniquely determine a radially symmetric index of refraction. These basis, together with the fact that the detectability of transmission eigenvalues has been extended to many different scattering situations, suggest the grow of spectral-quantitative methods during the next years.

2.2. Cryosurgery

Cryosurgery is a minimally invasive technique aiming at the destruction of cancerous tissues by application of extremely cold temperatures. It may be used in the treatment of localized prostate and liver carcinomas, in alternative to resection, radiation and chemotherapy [34, 102, 107, 33, 94].

The cooling and the subsequent destruction of living tissues is performed by insertion of multiple cryoprobes in the shape of long hypodermic needles connected to an external generator of supercooled fluid [91]. Subtraction of heat from the biological system leads to a phase change from the liquid to the solid state, starting around the tip of the cryprobes. The process is carried on until the entire cancerous tissue is frozen with temperature range of the solid phase below the lethal limit. To obtain an effective destruction of cancerous tissues several freezing-thawing cycles at appropriate temperature variation rates may be required [33]. To minimize cryoinjury to the surrounding healthy cells and blood vessels, cryoheaters have also been developed, to be inserted into the tissues [86, 91].

The aim of this section is to give an introduction about all the aspects playing a role in cryosurgical operation. We will describe the practical aspects concerning how the operation is carried out and the physical aspects of heat propagation in a tissue. Then, the problem of the planning of a cryosurgery operation will be presented providing an overview about the state of the art in cryosurgery planning.

2.2.1. The cryosurgery operation

A cryosurgery operation consists in the insertion of a number of cryoprobec into the portion of biological tissue that needs to be treated and to its freezing up to a lethal temperature. The target tissue could consist in a whole organ, as in the case of a prostate affected by carcinoma where the destruction of the whole organ's tissue is considered less risky than ad hoc treatments, or in little parts of organs, as in the case of the liver, whose operation is necessary to the body and where any kind of treatment can not compromise the whole status of the organ [93]. Cryosurgery is also used to treat superficial masses as skin tumors [77].

During a cryosurgery operation the tissue is carried to extremely low temperatures through the action of the cryoprobes which - connected to a supercooled fluid generator - reach freezing temperatures on their boundaries and subtract heat from the tissue by contact. In order to achieve such a temperature, the cryoprobes are connected by thermic insulated tubes to a generator where a fluid is cooled and then pushed into the tubes up to the cryoprobes. When the fluid has reached the cryoprobe the heat exchange begins and the fluid starts loosing its cooling power. Hence the fluid is moved back to the generator and replaced by new cooler fluid

and so on.

The action of cold on the tissues is in general destructive and it becomes lethal when the tissue is kept for an amount of time under the temperature of -45^oC [51]. Moreover the employment of freezing and thawing cycles have been showed to improve the efficacy of cryosurgical treatments [51].

But, since a freezing temperature is destructive for a general biological tissue and not just for the cancerous one, the successive issue in a cryosurgical operation is to find a way to preserve healthy tissues from the action of the cryoprobes. For this reason, in parallel with the born of cryosurgery devices, several planning techniques have been developed. The aim of these techniques is to set those experimental parameters which can be case-dependent and related to the physics of heat propagation: for examples the main aim of a planning technique for cryosurgery is to set the optimal position of the cryoprobes with respect with the portion of tissue to treat; other examples can be the definition of the optimal insertion depth, of the optimal shape of the probes or of the optimal duration of the operation.

Finally it has to be mentioned that, in order to answer to the necessity of keep enough hot the healthy organs, the insertion into the healthy tissue of heating probes called cryoheaters [86] has recently been considered.

2.2.2. Heat propagation with phase change: from pure substances to biological tissues

The temperature distribution θ in an open set S (contained in $\mathbb{R}$,$\mathbb{R}^2$ or $\mathbb{R}^3$) of pure substance is modeled by the following differential problem

$$\rho c \frac{\partial}{\partial t}\theta(x,t) = k\Delta\theta(x,t) \quad S \tag{2.42}$$

$$\theta(x,t) = f(x) \quad \partial S \tag{2.43}$$

$$\theta(x,0) = g(x) \quad S \tag{2.44}$$

where t represents the time, x is the spacial coordinate, f and g are the assigned boundary and initial condition, ρ, c and k are respectively mass density, specific heat and thermal conductivity. The well posedness of (2.42)-(2.44) has been already deeply analyzed and stated for example in [106].

When initial conditions and boundary conditions are one above the phase change temperature of the substance and one under that temperature, a phase change in the substance occurs. The consequences of a phase change is that parts of S would see a modification in the corresponding thermal parameters and that some energy is dissipated for the phase change as latent heat.

If one does not consider the contribute of the latent heat, the thermal distribution in case of phase change is the solution of the so called *Stefan Problem*

$$\rho_1 c_1 \tfrac{\partial}{\partial t}\theta(x,t) = \nabla(k_1 \nabla\theta(x,t)) \quad S_1 \tag{2.45}$$

$$\rho_2 c_2 \tfrac{\partial}{\partial t}\theta(x,t) = \nabla(k_2 \nabla\theta(x,t)) \quad S_2 \tag{2.46}$$

$$\theta(x,t) = f(x) \quad \partial S \tag{2.47}$$

$$\theta(x,0) = g(x) \quad S \tag{2.48}$$

where $S = S_1 \cup S_2$ and subscripts identify the two different substances (i.e. solid and liquid) and the common boundary $\partial S_{1,2}$ corresponds to the subspace where $\theta(x,t)$ is equal to the phase change temperature. The existence of a unique solution to the Stefan Problem is established for example in [92].

When the substance is non-pure, one has to face the problem of dealing with thermal parameters which vary with the temperature. This problem is accentuated when the temperature is around the phase change threshold: in fact, although when the phase of the substance is well defined one can often approximate to constants all the thermal parameters, when a non-pure substance is close to change phase, the dependence of the thermal parameters on the value of the temperature is higher, due to the different phase change temperatures of the different components belonging to the substance. In these cases it is common to consider a range of temperature in which the phase change occurs. Sometimes, in the case of more accurate models, the phase change is modeled through several different steps where each one describes a precise physical passage of the substance.

The freezing of a biological tissue can not be treated in the way of (2.45)-(2.48) since a biological tissue is not a pure substance. Moreover, heat propagation in a tissue has to take into account several other heat contributes: in fact, the traditional heat equation is substituted by the Pennes bio-heat equation [80]

$$\rho\, c\, \frac{\partial \theta}{\partial t} = \nabla \cdot (k\, \nabla\theta) + \omega_b\, \rho_b\, c_b\, (\theta_b - \theta) + q_m \tag{2.49}$$

where the subscript $_b$ stands for blood and q_m is the metabolic heat generation rate. Hence, the temperature distribution, solution of equation (2.49), is influenced not only by the heat exchange due to contact but also from the blood perfusion and from the metabolism that locally warm S. Phase change is generally identified in a single range of temperatures [107, 108, 33] but it is generally difficult to properly model the freezing of a tissue particularly when big gradient of temperatures occur in a small region. For this reason, more sophisticated models as [89, 101] are in general preferred when one does not have to mind computational costs and cpu-time limitations.

2.2.3. An enthalpy-based approach to the Stefan problem in biological (cancerous) tissues

The setup of a cryosurgical operation begins by decreasing the temperature of the cryoprobes according to a prescribed law down to a minimum value. The cryoprobes act as heat sinks removing sensible and latent heat from the tumor. The related direct Stefan problem for biological tissues is solved under the following assumptions.

(a) During freezing, heat is moved from the cancerous tissue towards the cryoprobes by conduction. Inside the volume where phase-change occurs, we take into account the transformation between sensible heat and latent heat. Local heat supply by blood perfusion and metabolism is also considered until the tissue is frozen. There is no heat supply by radiation.

(b) The biological tissue is not regarded as a pure substance. Thus phase change takes place over a temperature range, where the upper limit θ_M and the lower limit θ_m are differently chosen in the literature, (for example, $\theta_m = -10$, $\theta_M = 0$ in [107] and $\theta_m = -8$, $\theta_M = -1$ in [85]). This means that the formation of ice crystals during freezing begins at θ_M and ends at θ_m; within this temperature interval, both latent heat and sensible heat are removed from the tissue. The temperature interval (θ_m, θ_M) identifies the intermediate region V_2 of the phase change, which is placed between solid and liquid phases. The temperature interval $\theta > \theta_M$ determines the region V_3, filled by tissue-liquid phase, while the condition $\theta < \theta_m$ determines the region V_1, filled by the frozen-solid tissue (see Figure 2.4).

(c) The material parameters in V_1 and V_3, such as mass density, specific heat capacity, and thermal conductivity are taken as constant. However they are supposed to assume different values inside the frozen and the unfrozen region. Volume changes and the related stress depending on temperature changes are neglected.

(d) The latent heat in the intermediate region V_2 is constant. The latent heat effect is modeled by assuming a suitable heat capacity over the corresponding temperature range [14]. The thermal conductivity of the intermediate region is regarded as a function of temperature.

(e) The initial temperature value in the Stefan problem is 37 ^{o}C for the whole tissue. The (boundary) value of the temperature varies according to a prescribed law at the boundary of the cryoprobes while it is fixed at 37 ^{o}C in the surrounding healthy tissue and at the boundary of the cryoheaters.

The heat transfer process is described in terms of the corresponding temperature field $\theta(\mathbf{x}, t)$, where $\mathbf{x}$ is the position vector and t the time. The partial differential equations for the temperature field in the regions V_1, V_2 and V_3 follow from the previous assumptions, as well as the related boundary and initial conditions.

In the unfrozen region, V_3, the temperature θ satisfies the classical heat balance equation

for biological tissues [80],

$$\rho_3\, c_3\, \frac{\partial \theta}{\partial t} = \nabla \cdot (k_3\, \nabla \theta) + \omega_b\, \rho_b\, c_b\, (\theta_b - \theta) + q_m. \tag{2.50}$$

In the frozen region, V_1, equation (2.50) simplifies to

$$\rho_1\, c_1\, \frac{\partial \theta}{\partial t} = \nabla \cdot (k_1\, \nabla \theta). \tag{2.51}$$

Subscripts $1, 2, 3$ refer to the corresponding region or phase; b refers to the arterial blood; ρ is the mass density, kg/m^3; c is the specific heat, J /(kg ^{o}C); t is the time, s; k is the thermal conductivity, W/(m ^{o}C); w_b is the capillary blood perfusion rate, 1/s; θ_b is the blood temperature, ^{o}C; q_m is the metabolic heat generation rate, W/m^3.

Eq. (2.50) expresses conservation of (thermal) energy in mechanical equilibrium. The three terms at the right hand side of (2.50) are related to *a*) heat transfer by conduction; *b*) heat supply to the tissue by blood flow, under the assumption that blood enters the capillaries at temperature θ_b; *c*) heat supply as a consequence of chemical reactions inside the cells. Eq. (2.51) is the classical heat equation in the simplest form, showing that heat transfer inside the frozen region is only due to conduction.

The heat transfer process in the intermediate region V_2 is modeled by approximating latent heat exchange in the interval (θ_m, θ_M) with a predefined heat capacity [14]. This is essentially correspondent to an enthalpy formulation, although enthalpy is not explicitly introduced [14], [108]. The thermal conductivity k is represented by a linear function of θ which is continuous at the boundary of the intermediate region and leads to convenient boundary conditions. Specifically, we let

$$\rho_2\, c_2 := \frac{L}{\theta_M - \theta_m} + \frac{\rho_1\, c_1 + \rho_3\, c_3}{2}, \tag{2.52}$$

$$k_2(\theta) := k_1 + \frac{k_3 - k_1}{\theta_M - \theta_m}\, (\theta - \theta_m), \tag{2.53}$$

where L denotes the latent heat per unit volume. In particular we have $k_2(\theta_m) = k_1$ and $k_2(\theta_M) = k_3$. The resulting equation for θ in V_2 takes the form

$$\rho_2\, c_2\, \frac{\partial \theta}{\partial t} = \nabla \cdot (k_2(\theta)\, \nabla \theta) + \omega_b\, \rho_b\, c_b\, (\theta_b - \theta) + q_m. \tag{2.54}$$

As usual, it is required that the temperature and the normal component of the heat flux vector are continuous at the common boundaries of the three regions. Finally, the temperature is given at the boundary of the cryoprobes and at the external boundary of V_3, where $\theta = 37$ ^{o}C. The initial datum is $\theta = 37$ ^{o}C everywhere.

Our numerical approach to the direct Stefan problem is based on the following compact formulation. We define

$$a(\theta) := \begin{cases} \rho_1\, c_1 & \text{in } V_1 \\ \rho_2\, c_2 & \text{in } V_2 \\ \rho_3\, c_3 & \text{in } V_3 \end{cases} \tag{2.55}$$

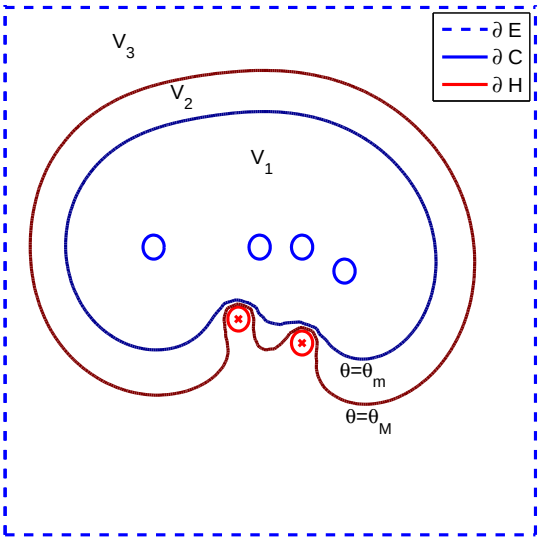

Figure 2.4: Scheme of a generic cryosurgery experiment: four cryoprobes (circles) and two cryoheaters (circles with crosses).

$$k(\theta) := \begin{cases} k_1 & \text{in } V_1 \\ k_2 & \text{in } V_2 \\ k_3 & \text{in } V_3 \end{cases} \tag{2.56}$$

$$b(\theta) := \begin{cases} 0 & \text{in } V_1 \\ \omega_b\, \rho_b\, c_b\, (\theta_b - \theta) + q_m & \text{in } V_2 \\ \omega_b\, \rho_b\, c_b\, (\theta_b - \theta) + q_m & \text{in } V_3. \end{cases} \tag{2.57}$$

Therefore equations (2.50), (2.51) and (2.54) may be reformulated in the equivalent compact form

$$a(\theta)\, \frac{\partial \theta}{\partial t} = \nabla \cdot (k(\theta)\, \nabla \theta) + \, b(\theta) \tag{2.58}$$

in the fixed open volume $V = V_1 \cup V_2 \cup V_3$.

Denote by ∂C, ∂H and ∂E the union of the boundaries of all cryoprobes, all cryoheaters, and the external boundary between V and healthy tissues (see Figure 2.4), respectively. Boundary and initial conditions of (2.58) are set as

$$\begin{cases} \theta(\mathbf{x}, t) = \alpha(t) & \mathbf{x} \in \partial C,\ t > 0 \\ \theta(\mathbf{x}, t) = 37^o\text{C} & \mathbf{x} \in \partial H \cup \partial E,\ t > 0 \\ \theta(\mathbf{x}, 0) = 37^o\,\text{C} & \mathbf{x} \in V. \end{cases} \tag{2.59}$$

Here α is a given function of time expressing the decay law of the temperature of the cryoprobes: to simplify we have considered the same decay law for all cryoprobes, although the algorithm works as well if the decay law changes with the cryoprobe.

2.2.4. The planning of a cryosurgery operation

Before a cryosurgery operation, some parameters have to be set in order to maximize the effectiveness of the operation and to minimize its invasivity. Most of the times, the optimal configuration of those parameter is case dependent and related more to the physics of heat propagation in a biological tissue than to physiological reasons. Hence, the definition of these parameters, can not be completely left to the decision of a medical doctor but planning tools have to assist him during a cryosurgery session. It is clear that any cryosurgery planning device has to include a computational method providing the temperature distribution given some initial experimental parameters, a criterium able to order the possible configurations of the free parameters in terms of their functionality and an optimization algorithm identifying an optimal final configuration for the operation.

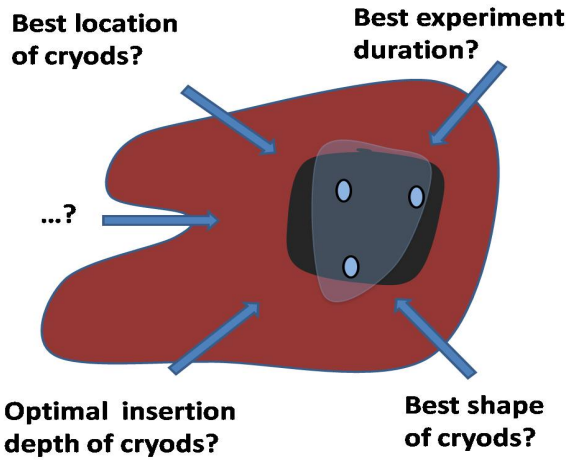

Figure 2.5: The cryosurgery planning problem.

The literature concerning the design of a cryosurgery operation is not wide and it is at most concentrated around the optimal disposition of the cryoprobes with respect to the area which has to be freezed. One of the first example of application of optimization methods to cryosurgery planning is [64] where the simplex method [60] was applied to the problem of optimizing the fitting of the freezing front with the shape of the prostate when the position of the cryoprobes were initially established through geometric considerations. Although the simplex method resulted suitable for the examples considered in [64], the intrinsic non-linearity of the problem invalidates the effectiveness of the simplex method when one faces directly the problem of finding the best position of the probes.

If, on the one hand, the approach of [64] utilizes a too simplistic optimization approach with respect to the complexity of the whole problem, on the other hand neither too mathematically sophisticated approaches are suitable for the problem. In fact, if, for example, one wants to

apply traditional optimization techniques, the first big difficulty will be to build a suitable cost function to minimize. In fact, in general, we do not have at disposal an explicit formula for the distribution of the temperature field given boundary and initial conditions and moreover these conditions change case by case (e.g. depending on where one places the cryoprobes). This is the case of the approaches [14] and [11] where gradient descent technique are applied to minimize objective functionals whose definition is inspired by the behavior of the temperature field around the cryoprobes.

A good compromise between the previous two techniques is represented by the force field analogy method [73]. This method works, in some sense, independently from the cost function that one utilizes and requires just that, at each iteration, after the computation of the distribution of the temperature in the tissue, a visualization of the defective areas is provided. In fact, for each one of the pixels which did not reach a proper temperature (i.e. defective pixel), the method computes a displacement vector for the cryoprobe and the resultant will determine the displacement of that particular cryoprobe at the given iteration. Differently from gradient descent techniques and simplex techniques, force field analogy has been tested in many realistic simulations showing its real applicability to cryosurgery planning [84, 100], although the computational time required to converge to a solution is, at present, far from real-time applications.

A way to increase the speed of optimization method in cryosurgery could be to try to avoid the computation of the temperature distribution at each iteration. For example, in the case of a planning of the location of the cryoprobes, one can concentrate on geometrical considerations and define methods able to converge to a configuration where cryoprobes are homogeneously distributed inside the shape of the tissue, that is far enough from each other and from the boundary of the tumor. The bubble-packing method [99] is born in this perspective, first as an initialization tool to the force field analogy method [100] and then as planning algorithm itself [90] able to optimize even the insertion depth [91].

Recently, in [54], the applicability of a particular genetic algorithm (called *ant colony optimization* [96]) to cryosurgery planning has been investigated. Such an approach has the advantage to be completely general and of allowing the setting of different types of experimental parameters without changing optimization technique. Unfortunately, similarly to the force field analogy method, it has the drawback of not being able to provide real-time results although it can be notably speeded up by integrating it with geometrically-based optimization tools. A complete investigation of ant colony optimization method (ACO) applied to cryosurgery will be provided in Chapter 5 of this thesis.

CHAPTER 3

The linear sampling method as a qualitative approach in microwave tomography

The following chapter is dedicated to the linear sampling method (LSM) [28], probably the most important qualitative method in inverse scattering. The aim of the chapter is to analyze the operation of the method from two different points of views: first, with an introductive part dedicated to the definition of the method and to the analysis of its applicability to breast cancer detection; then, with a second more theoretical section, where some open issues related to the LSM will be investigated.

Section 3.1 is dedicated to the description of the method in the framework of a scattering situation of a penetrable object embedded in an homogeneous or inhomogeneous background; then the method - in one of its variation aimed to maximize the speed of the reconstruction - is tested in the setting of mammographic microwave tomography where highly realistic simulations are performed through the use of breast phantoms derived from magnetic resonance images.

Section 3.2 describes a physical interpretation of the method by presenting the results published in [7]. The aim of the section is to cover some issues which are still open although not concerning any practical aspects of the operation of the LSM. In fact, although the linear sampling method has been showed to be effective in many different physical situations, its theoretical background is still not fully developed and the operation of the method is not wholly explained. The section will first present the issue and the state of the art in the field and then our physical approach will be introduced.

3.1. The linear sampling method and microwave mammography

This section is concerned with an application of the linear sampling method to microwave mammography. The setting is the two dimensional scattering by a TM-electromagnetic field: this means that we suppose to image the breast by slices. In the Section 3.1.1 the direct scattering problem is recalled and the linear sampling method (LSM) introduced by first describing its theoretical basis, then focusing on its implementation in the case of homogeneous and inhomogeneous background (Sections 3.1.1, 3.1.2, ,3.1.3). Finally, in Section 3.1.4, a faster version of the LSM will be introduced and and its efficacy will be assessed through realistic mammographic simulations (Section 3.1.5).

3.1.1. Principles of the linear sampling method

Let consider the (well-posed [41]) differential problem

$$\Delta u + k^2 n u = 0 \quad \mathbb{R}^2 \tag{3.1}$$

$$u = u^i + u^s \quad \mathbb{R}^2 \tag{3.2}$$

$$\lim_{r\to\infty}(\frac{\partial u^s}{\partial r} - iku^s) = 0 \tag{3.3}$$

describing the behavior of the total electromagnetic field u when $u^i = \exp^{ikx\cdot d}$, incident plane wave of direction d, is sent against a two dimensional scatterer D of index of refraction n embedded in an homogeneous background (i.e. $n = n_b$ with n_b constant). If u^s is the scattered field, then it admits the following asymptotic representation holding uniformly on $\hat{x} := \frac{x}{|x|} \in \Omega := \{x \in \mathbb{R}^2 : |x| = 1\}$

$$u^s(x) = \frac{\exp^{ikr}}{r} u_\infty(\hat{x}) + O(r^{-2}) \qquad r \to \infty \tag{3.4}$$

with $r = |x|$ and where u_∞ is the *far field pattern* of the scattered field u^s.

Given $\Phi_\infty(\hat{x}, z) = \frac{\exp^{i\pi/4}}{\sqrt{8\pi k}} \exp^{-ik\hat{x}\cdot z}$ far field pattern of the fundamental solution to the Helmholtz equation $\Phi(x, z) = \frac{i}{4} H_0^{(1)}(k|x - z|)$, where $H_0^{(1)}$ is the Hankel function of the first kind, let define the far field operator $F : L^2(\Omega) \to L^2(\Omega)$

$$[Fg](\cdot) = \int_\Omega u_\infty(\cdot, d) g(d) ds(d) \tag{3.5}$$

and the far field equation

$$\int_\Omega u_\infty(\hat{x}, d) g_z(d) ds(d) = \Phi_\infty(\hat{x}, z) \qquad \hat{x} \in \Omega. \tag{3.6}$$

Fg is the far field associated to a particular incident field

$$v_g(x) := \int_\Omega \exp^{ikx\cdot d}\, g(d)ds(d) \tag{3.7}$$

called Herglotz wave function of density g.

We further define as *transmission eigenvalues* those wave numbers k for which the following *homogeneous interior transmission problem* has a non-trivial solution

$$\Delta w + k^2 n w = 0 \quad D \tag{3.8}$$

$$\Delta v_g + k^2 v = 0 \quad D \tag{3.9}$$

$$w = v \qquad \partial D \tag{3.10}$$

$$\tfrac{\partial w}{\partial \nu} = \tfrac{\partial v}{\partial \nu} \qquad \partial D. \tag{3.11}$$

When v is the incident field, the scattered field has to be zero on ∂D and then in $\mathbb{R}^2 \setminus D$. In other words, transmission eigenvalues identify waves which can not be scattered by the scatterer since, if $w = v$ on ∂D, then w can be uniquely (well-posedness of the direct problem) extended outside D as the solution to the Helmholtz equation. The set of real transmission eigenvalues has been proved to be infinite and discrete [31] when $Imn = 0$; if $Imn \neq 0$ real transmission eigenvalues do not occur.

Except for the values of k which coincide with transmission eigenvalues, it holds [28]

Theorem 3.1.1. *If $z \in D$, for every $\varepsilon > 0$ there exists an approximate solution $g_z^\varepsilon \in L^2(\Omega)$ to the far field equation (i.e. g_z^ε satisfies $\|Fg_z^\varepsilon - \Phi_\infty(\cdot, z)\| \leq \varepsilon$) such that*

- $\lim_{\varepsilon\to 0} \|v_{g_z^\varepsilon}\|_{L^2(D)} < \infty$ *and*
- $\lim_{z\to\partial D} \|g_z^\varepsilon\|_{L^2(\Omega)} = \infty$, $\lim_{z\to\partial D} \|v_{g_z^\varepsilon}\|_{L^2(D)} = \infty$.

If $z \notin D$, for every $\varepsilon > 0$ and $g_z^\varepsilon \in L^2(\Omega)$ satisfying $\|Fg_z^\varepsilon - \Phi_\infty(\cdot, z)\| \leq \varepsilon$ we have that

- $\lim_{\varepsilon\to 0} \|g_z^\varepsilon\|_{L^2(\Omega)} = \infty$ *and* $\lim_{\varepsilon\to 0} \|v_{g_z^\varepsilon}\|_{L^2(D)} = \infty$

Theorem 3.1.1 inspires the following algorithm: taken a grid of points $\mathfrak{Z}$ enough big to contain the scatterer, solve the far field equation (3.6) for each $z \in \mathfrak{Z}$; then plot $\|g_z\|_{L^2(\Omega)}$ (or its composition with a monotone function). This algorithm provides a visualization of the support of the scatterer, whose boundary will approximatively correspond with those points where $\|g_z\|_{L^2(\Omega)}$ explodes.

3.1.2. The method and its implementation

A central role in the linear sampling method is played by the far field equation (3.6). In fact, its resolution for z belonging to a grid containing the inclusion, provides a z-dependent

family of functions whose L^2-norm opportunely plotted allows the visualization of the scatterer. Unfortunately, the resolution of equation (3.6) is not straightforward because very rarely the right hand side of (3.6) belongs to the range of the far field operator F [22, 23, 3] and F is compact [23], hence (3.6) is ill-posed. Moreover one has to think that in real applications the data on the far field are perturbed by a noise whose magnitude depends on the precision of the devices utilized. In addition, this noise does not affect the right hand side of (3.6) as it happens for more traditional inverse problems, but directly the definition of the operator F.

For these reasons, the resolution of (3.6) requires regularization [23]. Although, at least in theory, there are no restrictions on the type of regularization scheme that can be applied to (3.6), (in [98] different regularization schemes are compared), the linear sampling method is now commonly identified as utilizing the Tikhonov regularization scheme [103] provided with the generalized discrepancy principle [103] as a criteria to choose the optimal regularization parameter.

If F_h is the noisy far field operator where h is an estimate on the magnitude of the noise (e.g. $h = \|F_h - F\|$), Tikhonov regularization applied to equation (3.6) corresponds to solve the problem of finding the minimum $g_z^{\alpha_z}$ to the functional

$$\|F_h g_z^{\alpha_z} - \Phi_{\infty,z}\|_{L^2(\Omega)} + \alpha_z \|g_z^{\alpha_z}\|_{L^2(\Omega)} \tag{3.12}$$

where α_z is the regularization parameter. Minimizing functional (3.12) is equivalent to solve the associated Euler's equation

$$(F_h^* F_h + \alpha I) g_z^{\alpha_z} = F_h^* \Phi_{\infty,z} \tag{3.13}$$

where I is the identic function.

When to the noisy far field operator F_h is associated a singular value decomposition $\{\sigma_h^k, u_h^k, v_h^k\}_{k=1}^{\infty}$ [50], the expression of the Tikhonov regularized solution to the far field equation becomes

$$g_z^{\alpha_z} = \sum_{k=1}^{\infty} \frac{\sigma_h^k}{\alpha_z + (\sigma_h^k)^2} (\Phi_\infty(\cdot, z), v_h^k)_{L^2(\Omega)} u_h^k \tag{3.14}$$

whose series is cut off to a finite value when we deal with the discretized version of F_h and where $(\cdot,\cdot)_{L^2(\Omega)}$ denotes the scalar product in $L^2(\Omega)$.

A proper choice of the regularization parameter α_z is provided by the generalized discrepancy principle [103] which identifies the optimal choice of α_z in the zero of the functional

$$\rho_h(\alpha) = \|F_h g_z^{\alpha} - \Phi_{\infty,z}\|^2_{L^2(\Omega)} - h^2 \|g_z^{\alpha}\|^2_{L^2(\Omega)} \tag{3.15}$$

which, through (3.14), becomes

$$\rho_h(\alpha) = \sum_{k=1}^{\infty} \frac{\alpha^2 - h^2 (\sigma_h^k)^2}{(\alpha + (\sigma_h^k)^2)^2} |(\Phi_\infty(\cdot, z), v_h^k)_{L^2(\Omega)}|^2. \tag{3.16}$$

Summarizing, the linear sampling method can be schematized as follows:

- Let $\mathfrak{Z}$ be a grid containing the inclusion, then for each $z \in \mathfrak{Z}$ do
  - compute α_z by (3.16);
  - compute $g_z^{\alpha_z}$ by (3.14);
  - store the value of $\|g_z^{\alpha_z}\|_{L^2(\Omega)}$.
- The plot of $g_z^{\alpha_z}$ for each $z \in \mathfrak{Z}$ provides a reconstruction of the shape of the object.

We conclude the section with a remark: if one compares the method with its inspiring theorem (Th. 3.1.1) he will notice that the method is not completely justified by the theorem. In fact, nothing ensures that the (Tikhonov) regularized solution to the far field equation coincides with that particular solution whose behavior is described by the theorem. Nevertheless a twenty-years validation of the linear sampling method shows the effectiveness of the method, even for different types of regularization techniques, and suggests that results of Theorem 3.1.1 can be improved. Section 3.2 analyzes this issue by first presenting an overview on the state of the art and then proposing a physical interpretation of the method able to extend (under some assumptions) the result of Theorem 3.1.1 to all the approximate solutions to the far field equation.

3.1.3. The LSM in inhomogeneous backgrounds

In Sections 3.1.1 and 3.1.2 we have described the principles and the implementation of the linear sampling method when dealing with a scatterer surrounded by an homogeneous background and with far field measurements. This section is dedicated to its extension to the case of the detection of an inclusion embedded in an inhomogeneous background and to the case of near field measurements.

When one has to take into account an inhomogeneous background, the algorithm can be stated as well, providing, as output, the reconstruction of the curve of discontinuity of the scatterer with respect to the background. In other words it provides the shape of the inclusion. Moreover, when one is interested in reconstructing the shape of a buried object, often the measurements curve is placed close to the region under investigation and not in the far field region. The reason can be related to the practice of the applications or to the possible presence of a dissipative component in the refractive index of the background. In fact, in this last case, the farer are placed the antennas, the less energetic will be the measured wave and the more powerful will be the noise. The linear sampling method is not influenced by the occurrence of near field measurements (or emissions) and its structure and operation remains the same of the far field case [35, 20].

Results stated in Theorem 3.1.1 are achieved in [42, 35] for the case of a penetrable object embedded in an inhomogeneous background provided that some of the mathematical tools

introduced in Section 3.1.1 are modified as follows.

If u_b^s is the field scattered by the inhomogeneous background of (non-constant) index n_b, i.e. u_b^s is the scattered field for which the corresponding total field u satisfies

$$\Delta u + n_b(x)u = 0 \quad \text{in } \mathbb{R}^2 \tag{3.17}$$

$$u = u^i + u^s \quad \text{in } \mathbb{R}^2 \tag{3.18}$$

$$\lim_{r\to\infty}(\frac{\partial u^s}{\partial r} - iku^s) = 0 \tag{3.19}$$

and $u_{\infty,b}$ is its far field pattern, then the far field operator $\tilde{F}$ is now defined as

$$[\tilde{F}g](\cdot) = \int_\Omega [u_\infty(\cdot,d) - u_{\infty,b}(\cdot,d)]g(d)ds(d). \tag{3.20}$$

The far field equation takes now the form of

$$[\tilde{F}g_z](\cdot) = G_\infty(\cdot,z) \tag{3.21}$$

where G_∞ is the Green's function of the background which could not be anymore considered analytically known but will have to be numerically computed.

Theorem 3.1.1 can be proved to remain valid when F and Φ are substituted by $\tilde{F}$ and G (see [42, 35, 37]) and the structure of the algorithm described in Section 3.1.2 is left unaltered.

A last remark concerning the choice of the optimal regularization parameter α is however required. As previously seen, in order to approximate the shape of the inclusion by the LSM, one is supposed to know the index of refraction n_b of the background; if, for example, one thinks to practical applications, it is not possible to assume that, in general, such an a priori information is at disposal without taking into account any kind of mistake in this knowledge. Due to this possible lack of precision in the knowledge of the background, an other type of noise has to be considered when one has to solve the far field equation. If we call δ the estimate on the magnitude of the error present in the right hand side of (3.21), (e.g $\delta = \|G_\infty^\delta(\cdot,z) - G_\infty(\cdot,z)\|_{L^2(\Omega)}$), equation (3.21) is more realistically rewritten as

$$[\tilde{F}^h g_z](\cdot) = G_\infty^\delta(\cdot,z). \tag{3.22}$$

Following the generalized discrepancy principle, an optimal value of the Tikhonov regularization parameter for the regularization of (3.22) can be chosen as that particular α_z for which

$$\|\tilde{F}_h g_z^\alpha - G_\infty^\delta\|_{L^2(\Omega)} = h\|g_z^\alpha\|_{L^2(\Omega)} + \delta. \tag{3.23}$$

Such a criterium is equivalent of choosing the α_z such that $\rho_{h,\delta}(\alpha_z) = 0$ with

$$\rho_{h,\delta}(\alpha) = \|\tilde{F}_h g_z^\alpha - G_\infty^\delta\|_{L^2(\Omega)}^2 - (h\|g_z^\alpha\|_{L^2(\Omega)} - \delta)^2. \tag{3.24}$$

3.1.4. The no-sampling formulation of the LSM

In order to visualize the presence and the shape of an inclusion, the linear sampling method requires the resolution of the regularized far field equation for each z in a grid containing the scatterer. This means that the step of choosing the optimal regularization parameter as well as the step of solving the far field equation occur a number of times equal to the number of points of the grid $\mathfrak{Z}$. In particular when we deal with a three dimensional scattering problem, such a procedure, although much lighter than quantitative techniques, can require time, due to this series of operations. [6] and [18] present an algorithm based on the LSM where only one regularization (and inversion) process is required. In the following we will briefly introduce the *no-sampling linear sampling method* (nSLSM) referring to [6, 17] for a more technical discussion. Then, next section will show some numerical simulations based on the application of the no-sampling linear sampling to breast cancer detection by microwaves.

Let consider the discretized far field operator F consisting in an N by M matrix, where N and M are respectively the number of emissions and measurements and let introduce a new far field operator $\hat{F} : L^2(\mathfrak{Z})^N \to L^2(\mathfrak{Z})^M$ such that

$$\hat{g} := \{\hat{g}_j(\cdot)\}_{j=1}^N \mapsto \{\sum_{j=1}^N F_{ij}\hat{g}_j(\cdot)\}_{i=1}^M. \tag{3.25}$$

Hence, $\hat{g}$ is, now, an element of $L^2(\mathfrak{Z})^N := L^2(\mathfrak{Z}) \bigoplus ... \bigoplus L^2(\mathfrak{Z})$, Hilbert space of scalar product

$$(f,g)_{2,M} := \sum_{i=0}^{M-1} (f,g)_2 \tag{3.26}$$

and induced norm

$$\|f\|_{2,M} = \sqrt{\int_{\mathfrak{Z}} \|f(z)\|^2_{\mathbb{C}^M} dz} \tag{3.27}$$

where $\|\cdot\|_{\mathbb{C}^M}$ is the norm in $\mathbb{C}^M$

The z-dependent family of far field equations is replaced by the single functional equation

$$[\hat{F}\hat{g}(\cdot)](\cdot) = \frac{N}{2\pi}\hat{G}_\infty(\cdot) \tag{3.28}$$

where $\hat{G}_\infty \in L^2(\mathfrak{Z})^M$ is trivially obtained by considering G_∞ - far field pattern of the Green's function of the background - as a function of z.

As a consequence, the reconstruction of the inclusion is provided by the inversion of the single equation (3.28). Then, the regularization parameter is chosen only once in the whole process and in particular its optimal value will be the zero of

$$\hat{\rho}_{h,\delta}(\alpha) = \|\hat{F}_h\hat{g}^\alpha - \hat{G}^\delta_\infty\|^2_{2,M} - (h\|\hat{g}^\alpha_z\|_{2,N} - \delta)^2 \tag{3.29}$$

where h and δ are the magnitudes of the noise affecting respectively $\hat{F}$ and $\hat{G}_\infty$ and where they refer to the noisy version of $\hat{F}$ or $\hat{G}_\infty$ when they appear as subscripts. When such an optimal value α^* has been chosen, the regularized solution to (3.28) takes the form of

$$\hat{g}_z^{\alpha^*} = \frac{N}{2\pi} \sum_{k=1}^{r_h} \frac{\hat{\sigma}_h^k}{\alpha^* + (\hat{\sigma}_h^k)^2} (\hat{G}_\infty(\cdot), \hat{v}_h^k)_{\mathbb{C}^N} \hat{u}_h^k \tag{3.30}$$

and the scatterer is visualized by plotting a monotone function of $\|\hat{g}^{\alpha^*}(z)\|^2_{\mathbb{C}^N}$.

3.1.5. Application to breast cancer detection by microwave

In this section we will test the no-sampling linear sampling method in the setting of the detection of breast tumors using microwaves. The numerical simulations we are going to show are based on highly realistic numerical breast phantoms (free to download[1]) derived by the segmentation of MRI (Magnetic Resonance Imaging) images of female breasts.

The fulcrum of the nSLSM is the resolution of equation (3.28) where, for these simulations, the field data required by the definition of $\hat{F}$ and $\hat{G}$ are computed through the refractive index map of scatterer and background provided by the MRI images. In particular, the refractive index of the breast affected by tumor will provide the value of u_∞, while $u_{\infty,b}$ and $G_{\infty,b}$ will be computed through the use of the map of the healthy breast.

If we think to the practical application of this technique, we will have that, although at the moment of a real mammography the value of u_∞ is measured, the values of $u_{\infty,b}$ and of $G_{\infty,b}$ have to be computed utilizing a map provided by some other imaging modality. Hence, what we show here is an example of application which could be set in the pattern of a screening involving highly risk women whose clinical situation is frequently monitored through a microwave mammography (non invasive and low cost) and where background information are provided by the *una tantum* employment of other medical imaging techniques.

The system configuration is schematized as in Figure 3.1 (a) and (b) where the blue stars represent the positions of the antennas. The color scale utilized in (a) and (b) visualizes how heterogeneous is the structure of the index of refraction of the breast (i.e. it changes point by point). Figures (c) and (d) provide a quantitative visualization of the value of n in its real and imaginary component.

In the following numerical examples we assume to dispone of data for 20 incidences and 20 measurements and to pose the antennas on a circle of ray 6 cm surrounding the breast. All the data are perturbed by a 3% of Gaussian noise. In the first numerical example (Figure 3.2) a tumor (in black) of diameter 0.5 cm is artificially added to the healthy slice (the value of the refractive index of the tumoral tissue is computed following [72]). Figure 3.2 (a) and (b) respectively show the vertical and the horizontal breast slice where the tumor is inserted while

[1] at http://uwcem.ece.wisc.edu/home.htm

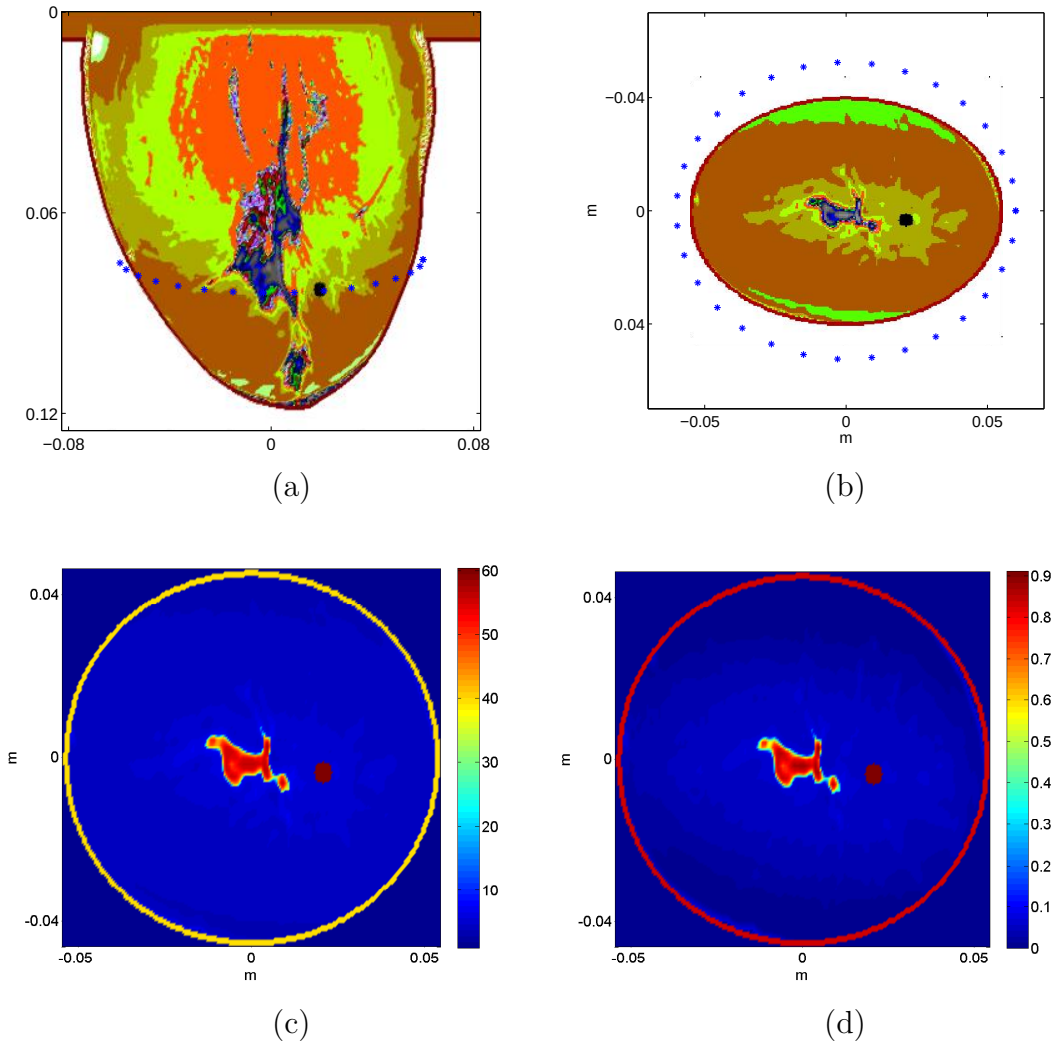

Figure 3.1: Set up of the microwave mammography: (a) represents a vertical breast slice where the black tumor is artificially added and the color scale is defined in a way such that the pixel wise variation of the index of refraction is emphasized; in black the artificially added tumor of diameter 0.5 cm. (b) is the horizontal slice of the breast. In (a) and (b) stars represent the presence of the antennas. In (c) and (d), the value of the real and the imaginary part of the index of refraction (at 2 GHz) is respectively shown.

(c) is the horizontal healthy breast slice. In other words, the data u_∞ of the tomography is simulated through the index of refraction shown in (b) and quantities $u_{\infty,b}$ and G_b are computed through (c) which constitutes the background information. (d) represents the behavior of $\|\hat{g}^{\alpha^*}(z)\|^2_{\mathbb{C}^N}$ for $z \in \mathfrak{Z}$.

In summary, these examples show the applicability of the method to breast cancer detection when a proper knowledge of the background is at disposal.

With Figure 3.3 we want to test the robustness of the method with respect to a non-complete knowledge of the background. The index of refraction of the ill breast is perturbed by a 5% of Gaussian noise point by point (see (a) and (b)) and the a priori knowledge of the background is left unaltered (see (c)). Figure 3.3 (d) shows the correspondent reconstruction.

The structure Figure 3.4 is the same of Figure 3.3. The difference is that a smaller tumor (diameter 0.3 cm) is artificially added. The nSLSM reconstruction (d) shows some artifacts, nevertheless the presence of the tumor can be easily detected.

3.1.6. Conclusions

The simulations showed in the previous section numerically assess the effective applicability of the linear sampling method to the problem of detecting breast tumors by microwaves.

The LSM has been proved to be able to detect inclusions of very small size which is the principal requirement in order to apply this technique in the setting of a large scale screening. Unfortunately, to operate, the LSM requires a large amount of a priori information which has to constitute the background of our scattering experiment. Hence, for what concerns the application of this technique to real mammographic situations, the LSM has to be supported by the use of other medical imaging modality as the MRI.

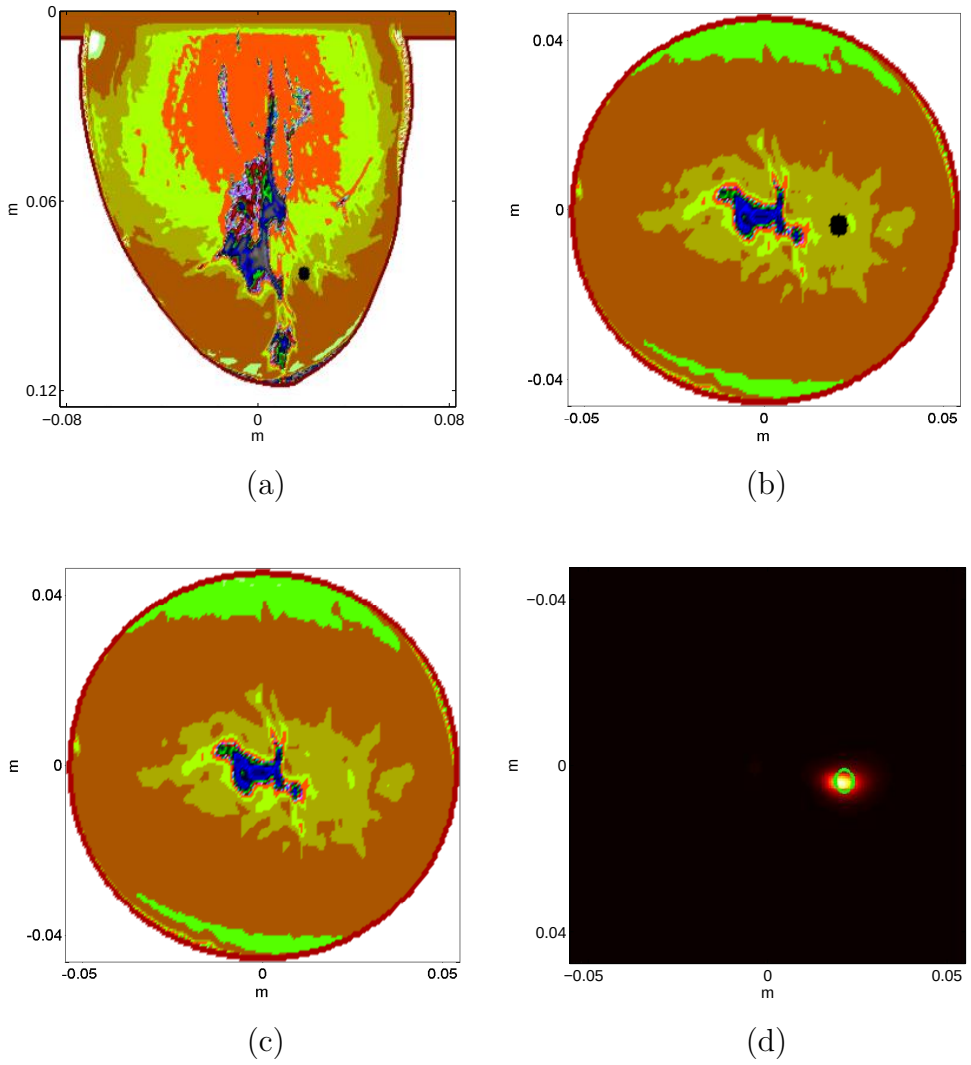

Figure 3.2: First numerical simulation: 2GHz of frequency, 20 emitting and measuring antennas, 3% of noise on the measured field. (a) represents a vertical breast slice where the black tumor is artificially added and the color scale is defined in a way such that pixelwise variation of the index of refraction is emphasized (the real values of the refractive index can be found in Figure 3.1 (c) and (d)); in black the artificially added tumor of diameter 0.5 cm. (b) is the horizontal slice of the breast. (c) shows the considered background (i.e. healthy breast). (d) is the reconstruction provided by the $nSLSM$.

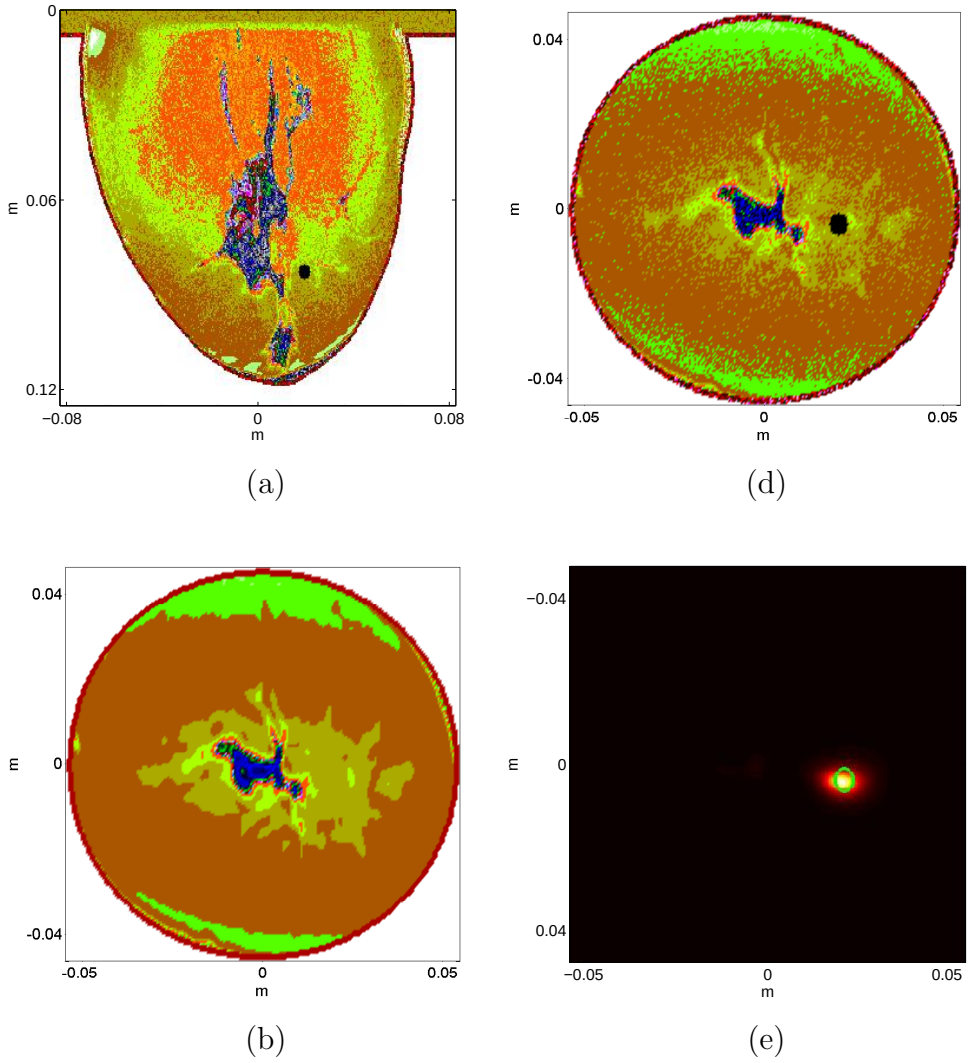

Figure 3.3: Second numerical simulation: 2GHz of frequency, 20 emitting and measuring antennas, 3% of noise on the measured field, 5% of pixel wise noise on the value of the refractive index of the background. (a) represents a vertical breast slice where the black tumor is artificially added and the color scale is defined in a way such that pixelwise variation of the index of refraction is emphasized (the real values of the refractive index can be found in Figure 3.1 (c) and (d)); in black the artificially added tumor of diameter 0.5 cm. (b) is the horizontal slice of the breast. (c) shows the considered background (i.e. healthy breast). (d) is the reconstruction provided by the $nSLSM$.

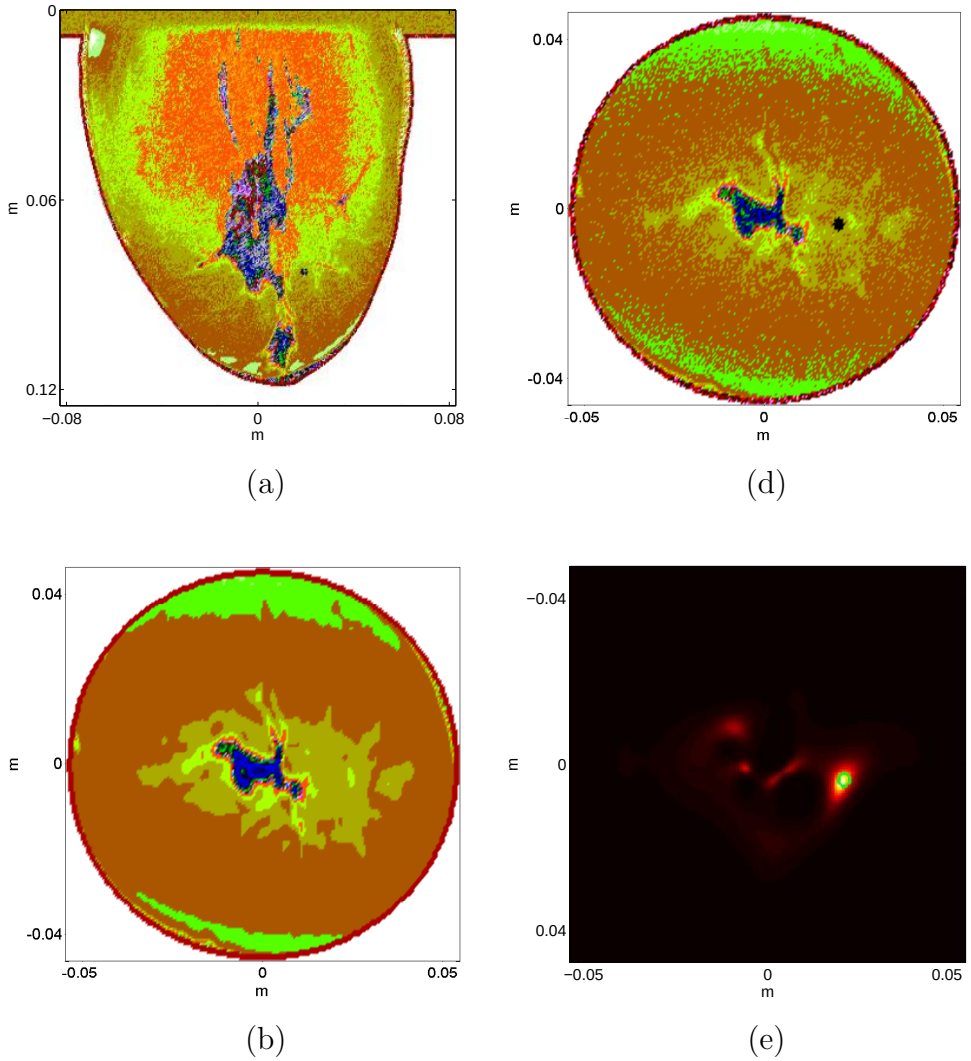

Figure 3.4: Third numerical simulation: 3GHz of frequency, 20 emitting and measuring antennas, 3% of noise on the measured field, 5% of pixel wise noise on the value of the refractive index of the background. (a) represents a vertical breast slice where the black tumor is artificially added and the color scale is defined in a way such that pixelwise variation of the index of refraction is emphasized (the real values of the refractive index can be found in Figure 3.1 (c) and (d)); in black the artificially added tumor of diameter 0.3 cm. (b) is the horizontal slice of the breast. (c) shows the considered background (i.e. healthy breast). (d) is the reconstruction provided by the $nSLSM$.

3.2. On the theoretical basis of the linear sampling method: a physical interpretation

Among qualitative methods in inverse scattering [23], the linear sampling method (LSM) [21, 37, 38, 46] is the earliest and probably the most popular. However, its theoretical foundation is not so sound as one might desire, since there is no clear link between its actual implementation and the general theorem inspiring the algorithm [22, 23]: in other terms, the theory available suggests, but does not justify the LSM. This gap is explained in Section 3.2.1, soon after a short review of the LSM.

In order to address this issue, some efforts have been made by the scientific community since the appearance of the first papers concerning the LSM. In this context, a prominent role is certainly played by the factorization method (FM) [66, 68]: it can be considered, in some sense, a modified version of the LSM, whereby the foundational problems affecting the latter are completely removed. Moreover, as a notable by-product, the FM can also inspire a revisitation and a consequent mathematical justification of the LSM [9, 10, 58]. However, the price to be paid for applying the FM is a non-negligible restriction of the class of scattering conditions and of the measurement set-up: hence, so far, the FM is somewhat less general [22, 23] than the LSM, and the same limitations clearly affect the FM-based justifications of the LSM. These points are briefly recalled and discussed in Section 3.2.2 of our paper.

To overcome this drawback, a physics-based approach has been recently proposed in [8] and [4], whereby the far-field equation at the basis of the LSM (which does not follow from physical laws) is regarded as a constraint on the power fluxes carried by the scattered field considered in the implementation of the LSM. According to this approach, the LSM is explained from a physical viewpoint by numerically observing the behavior of the flow lines of the scattered field and then by proving that such behavior forces the LSM to work as expected. In principle, this physical interpretation is feasible without restrictions on the scattering conditions: however, in [8] and [4], it is discussed in detail only for a two-dimensional, penetrable and electromagnetic scattering set-up. Then, we want to address here also the three-dimensional, impenetrable and acoustic case, in order to show the flexibility of this approach: the generalization is not trivial, as shown e.g. by the technical result in Section 3.2.9. Moreover, differently from [8], also the FM is taken into account and briefly discussed within this framework. Finally, in the present paper we numerically investigate also the case where the emitting and receiving antennas are placed according to an aspect-limited configuration.

To work out our physical interpretation of the LSM, in Section 3.2.3 we analyze the mechanism of power flux transport throughout the background medium for acoustic waves, both from a global and local viewpoint: in the latter case, the importance of the flow tubes of the scattered field is highlighted. Then, the far-field equation is regarded as a constraint on the

power fluxes in the far-field region, whereby the flux at infinity of the scattered field can be made arbitrarily close to the flux of the field radiated by a point source placed in the background. In Section 3.2.4, a technical result concerning the power fluxes across the boundary of the scatterer is proved, by taking inspiration from an analogous property of the FM: this result ensures the expected performance of the LSM close to the edge of the obstacle and involves neither the far-field equation nor the flow lines of the scattered field. In Section 3.2.5 the behavior of the flow lines is numerically investigated, while in Section 3.2.6 we prove that such behavior, together with the constraint expressed by the far-field equation, suffices to satisfy the hypotheses implying the technical result presented in Section 3.2.4, thus explaining how the LSM can correctly visualize the boundary of the scatterer. Section 3.2.7 extends the previous investigation, both from a numerical and theoretical viewpoint, to the visualization provided by the LSM outside the scatterer. Our conclusions and hints for future work are presented in Section 3.2.8, while in Section 3.2.9 we prove a minimum property for cones inscribed in a half-sphere: this result is an important tool for investigating the power fluxes across the boundary of the scatterer[2].

3.2.1. The scattering problem and the LSM

In this section we recall some basic notations and properties of direct and qualitative inverse scattering problems in the time-harmonic regime, by focusing, in particular, on the 3D acoustic case for an impenetrable, sound-soft obstacle put inside a homogeneous and non-absorbing host-medium; we refer to [23, 41] for details. If ω denotes the angular frequency of the wave and c_0 the speed of sound in the background, the corresponding wavenumber is $k = \omega/c_0 > 0$. The obstacle takes up a bounded and open C^2-domain $D \subset \mathbb{R}^3$, such that $\mathbb{R}^3 \setminus \bar{D}$ is connected (but D does not need to be connected). Factoring out the time dependence $e^{-\mathrm{i}\omega t}$, we denote by $u^i = u^i(x)$ the incident wave (assumed to be an entire solution of the Helmholtz equation with wavenumber k), by u^s the corresponding scattered field, and by $u = u^i + u^s$ the resulting total field. Then, the direct scattering problem can be formulated as the following exterior Dirichlet problem.

Problem 3.2.1. *Given u^i as above, find $u^s \in C^2(\mathbb{R}^3 \setminus \bar{D}) \cap C^{1,\alpha}(\mathbb{R}^3 \setminus D)$ such that*

$$\begin{cases} \Delta u^s(x) + k^2\, u^s(x) = 0 & \text{for } \; x \in \mathbb{R}^3 \setminus \bar{D}, \qquad \text{(a)} \\ u^s(x) = -u^i(x) & \text{for } \; x \in \partial D, \qquad \text{(b)} \\ \lim\limits_{r\to\infty} \left[r \left(\dfrac{\partial u^s}{\partial r} - \mathrm{i}k u^s \right) \right] = 0, & \qquad \text{(c)} \end{cases} \tag{3.31}$$

where $r = |x|$ and the limit (3.31)(c), which represents the Sommerfeld radiation condition, holds uniformly in all directions $\hat{x} = \frac{x}{|x|} \in \Omega := \{x \in \mathbb{R}^3 : |x| = 1\}$.

[2]The results showed in Section 3.2 are contained in [7]

Problem 3.2.1 is well-posed: in particular, the operator mapping the boundary data $-u^i$ into the solution u^s is continuous from $C^{1,\alpha}(\partial D)$ into $C^{1,\alpha}(\mathbb{R}^3 \setminus D)$. Moreover, the scattered field u^s admits the following asymptotic representation, uniformly in $\hat{x}$:

$$u^s(x) = \frac{e^{\mathrm{i}kr}}{r} u_\infty(\hat{x}) + O\left(r^{-2}\right) \qquad \text{as } r \to \infty, \tag{3.32}$$

where the function $u_\infty \in L^2(\Omega)$ is called the *far-field pattern* of the scattered field u^s.

A particular case of importance in our framework occurs when the incident field is a plane wave propagating along the direction identified by the unit vector $\hat{d} \in \Omega$, i.e., $u^i(x, \hat{d}) = e^{\mathrm{i}kx\cdot\hat{d}}$; the far-field pattern of the corresponding scattered field $u^s(x, \hat{d})$ will be denoted with $u_\infty(\hat{x}, \hat{d})$. Then, the inverse problem we are interested in can be formulated as follows.

Problem 3.2.2. *Given the far-field pattern $u_\infty(\hat{x}, \hat{d})$ for all incidence and observation directions $\hat{d}, \hat{x} \in \Omega$, determine the boundary ∂D of the obstacle.*

A qualitative approach to solving Problem 3.2.2 is provided by the LSM. The formulation of this method relies on the following mathematical tools:

a) the *far-field operator* $F : L^2(\Omega) \to L^2(\Omega)$, with $Fg(\hat{x}) := \int_\Omega u_\infty(\hat{x}, \hat{d}) g(\hat{d}) d\sigma(\hat{d})$. In particular, one can easily realize that $Fg(\hat{x})$ is the far-field pattern of the field

$$u_g^s(x) := \int_\Omega u^s(x, \hat{d}) g(\hat{d}) d\sigma(\hat{d}) \qquad \text{for } x \in \mathbb{R}^3 \setminus D, \tag{3.33}$$

which is scattered by the obstacle when the incident wave u^i is the *Herglotz wave function* v_g of kernel g, i.e., $u^i(x) = v_g(x) := \int_\Omega e^{\mathrm{i}kx\cdot\hat{d}} g(\hat{d}) d\sigma(\hat{d})$ for $x \in \mathbb{R}^3$;

b) the far-field pattern $\Phi_\infty(\hat{x}, z) = \frac{1}{4\pi} e^{-\mathrm{i}k\hat{x}\cdot z}$ of the fundamental solution $\Phi(x, z) = \frac{1}{4\pi} \frac{e^{\mathrm{i}k|x-z|}}{|x-z|}$ of the Helmholtz equation;

c) the *far-field equation*, written (for each sampling point $z \in \mathbb{R}^3$) in the unknown $g_z \in L^2(\Omega)$ as

$$Fg_z(\hat{x}) = \Phi_\infty(\hat{x}, z), \quad \hat{x} \in \Omega. \tag{3.34}$$

It is worth noting that, in general, this equation is not solvable for almost all (f.a.a.) sampling point $z \in \mathbb{R}^3$, i.e., $\Phi_\infty(\cdot, z)$ does not belong to the range of F f.a.a. $z \in \mathbb{R}^3$. However, this range is dense in $L^2(\Omega)$, as explained in the following point d);

d) the *general theorem*, as we call it, which can be stated as follows.

Theorem 3.2.1. (General theorem) *Let $D \subset \mathbb{R}^3$ be a nonempty, open, bounded and C^2-domain, such that $\mathbb{R}^3 \setminus \bar{D}$ is connected; let us assume that k^2 is not a Dirichlet eigenvalue for the negative Laplacian in D. Then:*

(i) if $z \in D$, for every $\varepsilon > 0$ there exists a solution $g_z^\varepsilon \in L^2(\Omega)$ of the inequality $\|Fg_z^\varepsilon - \Phi_\infty(\cdot, z)\|_{L^2(\Omega)} \leq \varepsilon$ such that, for every $z^* \in \partial D$,

$$\lim_{z \to z^*} \|g_z^\varepsilon\|_{L^2(\Omega)} = \infty \quad \text{(a)} \quad \textit{and} \quad \lim_{z \to z^*} \left\|v_{g_z^\varepsilon}\right\|_{H^1(D)} = \infty, \quad \text{(b)} \tag{3.35}$$

where $v_{g_z^\varepsilon}$ is the Herglotz wave function with kernel g_z^ε;

(ii) if $z \notin D$, for every $\varepsilon > 0$ and $\delta > 0$ there exists a solution $g_z^{\varepsilon,\delta} \in L^2(\Omega)$ of the inequality $\left\| F g_z^{\varepsilon,\delta} - \Phi_\infty(\cdot, z) \right\|_{L^2(\Omega)} \leq \varepsilon + \delta$ such that

$$\lim_{\delta \to 0} \left\| g_z^{\varepsilon,\delta} \right\|_{L^2(\Omega)} = \infty \quad \text{(a)} \quad \textit{and} \quad \lim_{\delta \to 0} \left\| v_{g_z^{\varepsilon,\delta}} \right\|_{H^1(D)} = \infty, \quad \text{(b)} \tag{3.36}$$

where $v_{g_z^{\varepsilon,\delta}}$ is the Herglotz wave function with kernel $g_z^{\varepsilon,\delta}$.

Theorem 3.2.1 establishes, in particular, the denseness of the range of F, as well as the existence of ε-approximate solutions of the far-field equation such that their L^2-norm can be used as an *indicator function* for the support of the scatterer, i.e., a function that is bounded inside the obstacle, blows up on its boundary and remains arbitrarily large outside, as indicated by limits (3.35)(a) and (3.36)(a).

Then, inspired by Theorem 3.2.1, the algorithm of the LSM can be summarized by the following steps: 1) choose a grid of sampling points z in a bounded region Z containing $\bar{D}$; 2) for each $z \in Z$, compute the Tikhonov regularized solution [50, 103] g_z^α of the far-field equation (3.34), written in an angle-discretized and noisy version; 3) fix the value $\alpha^*(z)$ of the regularization parameter α by means of the generalized discrepancy principle [103]; 4) visualize the boundary ∂D of the scatterer as the set of grid points where the (discretized) L^2-norm of $g_{\alpha^*(z)} := g_z^{\alpha^*(z)}$ grows up.

Evidently, there is a gap between Theorem 3.2.1 and the previous algorithm, which is not only due to the discretization and the noise affecting the far-field pattern, but is much deeper: indeed, a priori there is no reason why the L^2-norm of the Tikhonov regularized solution of the far-field equation for each z should behave (when regarded as a function of z) as an indicator function, i.e., in agreement with limits (3.35)(a) and (3.36)(a). In particular, no useful convergence result can be obtained as $\alpha \to 0^+$: indeed, since the range $\mathcal{R}(F)$ of the far-field operator F is dense in $L^2(\Omega)$ and $\Phi_\infty(\cdot, z)$ does not belong, in general, to $\mathcal{R}(F)$, we have that $\lim_{\alpha \to 0^+} \|g_z^\alpha\|_{L^2(\Omega)} = \infty$ f.a.a. $z \in \mathbb{R}^3$ [50, 103].

This is also the reason why an alternative version of part (b) of Theorem 3.2.1, as proposed e.g. at p. 166 of [68], does not fill in this gap: indeed, according to [68], for $z \notin D$ one can in particular identify the regularization parameter α with the tolerance ε and then find

$$\lim_{\alpha \to 0^+} \|F g_z^\alpha - \Phi_\infty(\cdot, z)\|_{L^2(\Omega)} = 0, \quad \lim_{\alpha \to 0^+} \|g_z^\alpha\|_{L^2(\Omega)} = \infty. \tag{3.37}$$

Nevertheless, these two limits hold f.a.a. $z \in \mathbb{R}^3$ and not only for $z \notin D$, since they follow from the denseness of $\mathcal{R}(F)$ and from the fact that $\Phi_\infty(\cdot, z) \notin \mathcal{R}(F)$ f.a.a. $z \in \mathbb{R}^3$ (cf. [50], p. 54 and [103], p. 19). Hence, the typical behavior of $z \mapsto \|g_{\alpha^*(z)}\|_{L^2(\Omega)}$ as an indicator function cannot be explained by simply considering that $\alpha^*(z) \to 0^+$: at least, one should prove a complementary property, whereby a vanishing regularization parameter is only enforced when

$z \in D$ approaches the boundary ∂D, or when $z \notin D$. (In fact, our approach will provide such enforcement, as we shall explain in Remarks 3.2.2 and 3.2.4.)

For future purpose, we briefly recall that analogous results and problems hold for an aspect-limited configuration of antennas [23, 68]. Let Ω^i and Ω^o be the two (measurable) subsets of Ω identifying the incidence and observation angles, respectively. Then, we can define the modified far-field operator $F_{al} : L^2(\Omega^i) \to L^2(\Omega^o)$ and introduce the modified far-field equation $F_{al}\, g_z(\hat{x}) = \Phi_\infty(\hat{x}, z)$ in the unknown $g_z \in L^2(\Omega^i)$, for $\hat{x} \in \Omega^o$. By definition, an ε-approximate solution g_z^ε of this equation verifies the inequality $\|F_{al}\, g_z^\varepsilon - \Phi_\infty(\cdot, z)\|_{L^2(\Omega^o)} \leq \varepsilon$. We shall come back to the aspect-limited case later on.

Among the efforts to overcome this theoretical drawback, the FM certainly plays a major role: then, the next section is devoted to briefly describing this qualitative method and the insight it can give into the LSM.

Throughout the paper, we shall adopt the following notations for spheres and balls: if $x_0 \in \mathbb{R}^3$ and $R > 0$, then

$$B(x_0, R) := \left\{x \in \mathbb{R}^3 : |x - x_0| < R\right\}, \quad B_R := \left\{x \in \mathbb{R}^3 : |x| < R\right\}, \quad B := B_1; \tag{3.38}$$

$$\Omega(x_0, R) := \left\{x \in \mathbb{R}^3 : |x - x_0| = R\right\}, \quad \Omega_R := \left\{x \in \mathbb{R}^3 : |x| = R\right\}, \quad \Omega := \Omega_1. \tag{3.39}$$

However, the symbols denoting centers and radii may vary, depending on the context.

3.2.2. The LSM justified by the FM

The classical Problem 3.2.1 can be regarded as a particular case of the following weak boundary-value problem, which involves the space

$$H^1_{loc}(\mathbb{R}^3 \setminus \bar{D}) := \left\{u : u \in H^1\left((\mathbb{R}^3 \setminus \bar{D}) \cap B_R\right) \forall R > 0 : (\mathbb{R}^3 \setminus \bar{D}) \cap B_R \neq \emptyset\right\}.$$

Problem 3.2.3. *Given $\varphi \in H^{1/2}(\partial D)$, determine $u^s \in H^1_{loc}(\mathbb{R}^3 \setminus \bar{D})$ such that*

$$\begin{cases} \Delta u^s + k^2\, u^s = 0 & \text{in } \mathbb{R}^3 \setminus \bar{D}, \quad \text{(a)} \\ u^s = \varphi & \text{on } \partial D, \quad \text{(b)} \\ \lim\limits_{r \to \infty} \left[r \left(\dfrac{\partial u^s}{\partial r} - \mathrm{i}k u^s \right) \right] = 0. & \quad \text{(c)} \end{cases} \tag{3.40}$$

Problem 3.2.3 is well-posed [23]: as a trivial consequence, the next problem is too.

Problem 3.2.4. *Given $\varphi \in H^{1/2}(\partial D)$, determine the far-field pattern $u_\infty \in L^2(\Omega)$ of the field $u^s \in H^1_{loc}(\mathbb{R}^3 \setminus \bar{D})$ solving Problem 3.2.3.*

As proved in [66], the far-field operator F having as integral kernel the far-field pattern determined by Problem 3.2.4 is *normal* (but only for a full-view configuration of antennas

[23, 68]); moreover, if k^2 is not a Dirichlet eigenvalue of $-\Delta$ in D (as we shall always assume throughout the paper), F is injective with dense range. The solution operator of Problem 3.2.4 is denoted by $G : H^{1/2}(\partial D) \to L^2(\Omega)$, with $G(\varphi) := u_\infty$. In particular, remembering that Fg is the far-field pattern of the field $u_g^s(x)$ given by (3.33), we have $G(-v_g|_{\partial D}) = Fg$. This amounts to establishing the factorization $F = -GH$, where $H : L^2(\Omega) \to H^{1/2}(\partial D)$ is the *Herglotz operator* defined as $Hg(x) := \int_\Omega e^{\mathrm{i}kx\cdot\hat{d}} g(\hat{d}) d\sigma(\hat{d})$, for $x \in \partial D$. Moreover, two important properties can be established:

1. G provides an exact characterization of D, i.e., $\Phi_\infty(\cdot, z) \in \mathcal{R}(G) \Longleftrightarrow z \in D$;
2. $\mathcal{R}(G) = \mathcal{R}\left(F^*F\right)^{1/4}$, where F^* denotes the adjoint of F.

The two previous points suggest to replace the far-field equation (3.34), involved in the LSM, with the following one:

$$\left(F^*F\right)^{1/4} \tilde{g}_z(\hat{x}) = \Phi_\infty(\hat{x}, z), \tag{3.41}$$

which forms the core of the FM and provides an exact characterization of the domain D, since it is (uniquely) solvable in $L^2(\Omega)$ if and only if $z \in D$. Moreover, since $\mathcal{R}\left(F^*F\right)^{1/4}$ is dense in $L^2(\Omega)$, using Tikhonov regularization to approximately solve (3.41) is justified by two convergence/divergence results: a) for $z \in D$, $\lim_{\alpha\to 0^+} \|\tilde{g}_z^\alpha\|_{L^2(\Omega)} = \|\tilde{g}_z\|_{L^2(\Omega)} \in \mathbb{R}^+$, where $\tilde{g}_z$ is the unique solution of equation (3.41); b) for $z \notin D$, $\lim_{\alpha\to 0^+} \|\tilde{g}_z^\alpha\|_{L^2(\Omega)} = \infty$.

For future purpose, we also observe that, even in absence of noise, the FM (as well as the LSM) has only a limited resolution power, i.e., the indicator function $\|\tilde{g}_z\|_{L^2(\Omega)}$ cannot exhibit a step-like behavior in the transition from the interior to the exterior of the scatterer, but rather becomes larger and larger as the sampling point z approaches ∂D from inside (and remains arbitrarily large outside). This property, which is analogous to the limit (3.35)(a) for the LSM, is formalized by the following theorem (for a proof, see e.g. [10]).

Theorem 3.2.2. *For each $z \in D$, let $\tilde{g}_z \in L^2(\Omega)$ be the unique solution of equation (3.41). Then, for any $z^* \in \partial D$, the limit $\lim_{z\to z^*} \|\tilde{g}_z\|_{L^2(\Omega)} = \infty$ holds.*

The FM can also be extended to some situations where the far-field operator is not normal, but it remains, so far, considerably less general than the LSM [23]. However, the theoretical foundation of the latter is notably improved by the FM, when applicable. Then, let us briefly recall how this improvement can be achieved.

The first step, made in [9], is to identify an appropriate family of regularization methods $\tilde{R}_\alpha$ for the far-field operator F, i.e., $\tilde{R}_\alpha h := \sum_{n=1}^\infty \frac{q(\alpha,\mu_n)}{\mu_n}(h, h_n) g_n$, where $\{\mu_n, g_n, h_n\}_{n=1}^\infty$ is a singular system of F such that $h_n = s_n g_n$ with $s_n \in \mathbb{C}$, $|s_n| = 1$, and $q : (0, +\infty) \times (0, \|F\|] \to \mathbb{R}$ verifies three conditions detailed in [9]. For our purposes, it suffices to observe that Tikhonov regularization is obtained from the particular choice $q(\alpha, \mu) = \frac{\mu^2}{\alpha+\mu^2}$. Then, the following theorem can be proved [9].

Theorem 3.2.3. *If $\tilde{R}_\alpha : L^2(\Omega) \to L^2(\Omega)$ is a regularization method for F as above, then $R_\alpha := -H\tilde{R}_\alpha : L^2(\Omega) \to H^{1/2}(\partial D)$ is a regularization method for G.*

In our framework, this theorem is important and can be paraphrased as follows. It is well known [41] that having a control over the norm of far-field patterns does not allow, in general, a control over the corresponding fields outside the scatterer. In other terms, small (in the $L^2(\Omega)$-norm) far-field patterns do not need to correspond to small (in any reasonable norm) fields in a finite region surrounding the obstacle. In particular, when the Tikhonov regularized solution g_z^α of the far-field equation (3.34) is considered (for $z \in D$), the fact that the far-field pattern $Fg_z^\alpha - \Phi_\infty(\cdot, z)$ can be made arbitrarily small in $L^2(\Omega)$ for $\alpha \to 0^+$ does not imply that the field characterized by this far-field pattern is small in $H^1(B_R \setminus \bar{D})$, with $B_R \supset \bar{D}$. However, Theorem 3.2.3, by exploiting the normality of F, states just this implication: indeed, by this theorem, we have that, for $z \in D$, $-Hg_z^\alpha \to \Phi(\cdot, z)$ in $H^{1/2}(\partial D)$ as $\alpha \to 0^+$ and then the well-posedness of Problem 3.2.3, together with definition (3.33), implies that $u^s_{g_z^\alpha} \to \Phi(\cdot, z)$ in $H^1(B_R \setminus \bar{D})$ as $\alpha \to 0^+$. In other terms, establishing that the regularization of F is inherited by G, in the sense of Theorem 3.2.3, amounts to stating that this regularization, together with the operator $-H$, is responsible for the stable back-propagation (up to the scatterer boundary) of the information expressed in the far-field region by the far-field equation. We shall revisit this point in the next section.

Another important consequence of Theorem 3.2.3, developed in [10, 68] (for Tikhonov regularization only), consists in the possibility of replacing the usual indicator function of the LSM, i.e., $z \mapsto \|g_z^\alpha\|_{L^2(\Omega)}$, with the absolute value of the Herglotz wave function with kernel g_z^α, i.e., with $z \mapsto \left|v_{g_z^\alpha}(z)\right|$: indeed, if the FM can be applied, it is possible to show that the new indicator function satisfies good convergence/divergence properties, i.e.,

$$\lim_{\alpha \to 0^+} \left|v_{g_z^\alpha}(z)\right| < \infty \ \text{ for } z \in D \ \text{ (a)} \quad \text{and} \quad \lim_{n \to \infty} \left|v_{g_z^{\alpha_n}}(z)\right| = \infty \ \text{ for } z \notin \bar{D} \ \text{ (b)} \tag{3.42}$$

for an appropriate vanishing sequence $\{\alpha_n\}_{n=0}^\infty$. The two limits in (3.42) give rise to a new and mathematically justified version of the LSM: it is understood that the gap with respect to the algorithm actually implemented in numerical applications can be filled by assuming that discretization effects are not important and that the presence of noise affecting the far-field operator entails, in any case, 'small' values of the regularization parameter α.

Summing up, the FM can give a satisfactory justification of the LSM, provided that 1) the class of scattering conditions is conveniently restricted; 2) the traditional indicator function $z \mapsto \|g_z^\alpha\|_{L^2(\Omega)}$ is replaced by $z \mapsto \left|v_{g_z^\alpha}(z)\right|$; 3) the regularization parameter is assumed to tend to zero.

In the following, we shall face the problem of understanding the LSM in a completely different perspective, by relying on a physical interpretation of the far-field equation in terms of power fluxes and by investigating how these fluxes are propagated throughout the background. In this framework, 1) the class of scattering conditions does not need to be restricted (anyway,

only the impenetrable case will be explicitly discussed here; for two-dimensional penetrable scatterers, see [8, 4]); 2) the usual indicator function $z \mapsto \|g_z^\alpha\|_{L^2(\Omega)}$ is maintained; 3) the regularization parameter is not assumed to tend to zero.

However, we point out that, unlike the previous *a priori*, FM-based justification, our approach is an *a posteriori* one, since we need to make some assumptions on the geometry of the power fluxes in the background: although not based on theoretical predictions, these assumptions are supported by numerical simulations (also when F is not normal) and generalize in a rather natural way the main features of the field radiated by a point-like source placed in the host medium. In spite of this theoretical limitation, we shall be able to provide sufficient conditions ensuring that the L^2-norm of any ε-approximate (and, in particular, Tikhonov regularized) solution of the far-field equation behaves as a good indicator function for the support of the scatterer as z varies in $\mathbb{R}^3$.

3.2.3. Flow tubes of the scattered field

Numerical simulations show that the LSM can work even when the FM is not applicable: this suggests that the back-propagation of the constraint expressed by the far-field equation from the far-field to the near-field region is not necessarily related to the normality of F and to the regularization of the far-field equation, as discussed in the previous section. Rather, it seems to be related to the physics of wave propagation or, more precisely, to how power is carried throughout the background.

To pursue this approach, we recall that time-harmonic sound waves of small intensity, propagating in a homogeneous, isotropic and inviscid fluid surrounding the obstacle D, can be described [41] by a velocity potential $U(x,t) = \mathrm{Re}\left\{u(x)e^{-\mathrm{i}\omega t}\right\}$ such that

$$v(x) = \frac{1}{\rho_0}\nabla u(x) \quad \text{and} \quad p(x) = \mathrm{i}\omega u(x) \quad \Rightarrow \quad v(x) = \frac{1}{\mathrm{i}\omega\rho_0}\nabla p(x), \tag{3.43}$$

where $p = p(x)$ and $v = v(x)$ are the (complex-valued) velocity and excess pressure of the fluid, respectively, while ρ_0 is its constant equilibrium density. In particular, the second equality in (3.43) shows that p and u differ by a multiplicative constant only; then, Problems 3.2.1 and 3.2.2, although written in terms of u, u^s, u^i, can also be regarded as a problem for p, p^s, p^i, as we shall do in the following. Of course, the *physical* pressure and velocity fields are given by:

$$v_{ph}(x,t) = \mathrm{Re}\left\{v(x)e^{-\mathrm{i}\omega t}\right\} \quad \text{and} \quad p_{ph}(x,t) = \mathrm{Re}\left\{p(x)e^{-\mathrm{i}\omega t}\right\}. \tag{3.44}$$

Let us now consider a surface $\Sigma \subset \mathbb{R}^3 \setminus \bar{D}$ admitting a piecewise smooth parametric representation $\tilde{\Sigma} : A \to \mathbb{R}^3$, with $A \subset \mathbb{R}^2$ and $\tilde{\Sigma}(A) = \Sigma$ (throughout the paper, the piecewise smoothness of the parametric representations of surfaces or curves will be always understood); moreover, let $\nu = \nu(x)$ be the unit normal to Σ at x, chosen as outward when Σ is closed.

The traction forces induced in the background fluid by the scattered pressure field p^s develop a power per unit surface $P(x,t) = p^s_{ph}(x,t)\, v^s_{ph}(x,t) \cdot \nu(x)$, outgoing from Σ; by using relations (3.43) and (3.44), this power can be computed as

$$P(x,t) = \frac{1}{2}\mathrm{Re}\left\{ \frac{e^{-2\mathrm{i}\omega t}}{\mathrm{i}\omega\rho_0} p^s(x)\nabla p^s(x) + \frac{1}{\mathrm{i}\omega\rho_0}\bar{p}^s(x)\nabla p^s(x) \right\} \cdot \nu(x), \tag{3.45}$$

where the dot and the bar denote the canonical scalar product in $\mathbb{C}^3$ and the complex conjugation respectively. Expression (3.45) suggests computing the average $P_{av}(x)$ of $P(x,t)$ over one period $T = 2\pi/\omega$, i.e.,

$$P_{av}(x) = \frac{1}{T}\int_0^T P(x,t)dt = \frac{1}{2}\mathrm{Re}\left\{ \frac{1}{\mathrm{i}\omega\rho_0}\bar{p}^s(x)\nabla p^s(x) \right\} \cdot \nu(x). \tag{3.46}$$

Then, the average power flux across the surface Σ is given by

$$\mathcal{F}_\Sigma(p^s) = \frac{1}{2}\int_\Sigma \mathrm{Re}\left\{ \frac{1}{\mathrm{i}\omega\rho_0}\bar{p}^s(x)\nabla p^s(x) \right\} \cdot \nu(x) d\sigma(x), \tag{3.47}$$

where $d\sigma(x)$ is the standard measure on Σ. The right-hand side of (3.47) is the flux across Σ of the vector field $\mathcal{S}$ associated with p^s via the following definition:

$$\mathcal{S}(x) := \frac{1}{2}\mathrm{Re}\left\{ \frac{1}{\mathrm{i}\omega\rho_0}\bar{p}^s(x)\nabla p^s(x) \right\} = \frac{1}{4\mathrm{i}\omega\rho_0}\left\{ \bar{p}^s(x)\nabla p^s(x) - p^s(x)\nabla\bar{p}^s(x) \right\}, \tag{3.48}$$

which is analogous to the Poynting vector in the electromagnetic case [8]. For brevity, we shall speak of the 'flux of the scattered field', or the 'flux of p^s'.

Since p^s satisfies the Helmholtz equation (3.31)(a) in the background fluid, it is easy to show that the vector field $\mathcal{S}(x)$ is divergence free in $\mathbb{R}^3 \setminus \bar{D}$. As a consequence, if $E \subset \mathbb{R}^3$ is a compact integration domain such that its boundary $\Sigma := \partial E$ is a simple and closed surface enclosing no subset of D, by Gauss' divergence theorem we have $\mathcal{F}_\Sigma(p^s) = 0$. For the same reason, if $E_1, E_2 \subset \mathbb{R}^3$ are two compact domains such that $E_1 \subset E_2$ and their boundaries Σ_1 and Σ_2 are non-intersecting, simple and closed surfaces surrounding the whole scatterer D, by applying Gauss' theorem in $E_2 \setminus E_1$ we have

$$\mathcal{F}_{\Sigma_1}(p^s) = \mathcal{F}_{\Sigma_2}(p^s). \tag{3.49}$$

This is consistent with the fact that the scatterer can be regarded [13] as an unknown equivalent source radiating the scattered field p^s in the background: if there are no sources inside Σ, the flux of p^s across Σ is zero; if Σ encloses the whole source, the flux across Σ is completely determined by the source itself. In the latter case, one can choose $\Sigma = \Omega_R$ in (3.47), with R large enough. Then, remembering (3.48), any of the fluxes in (3.49) can be computed as the

flux at infinity of p^s, i.e.,

$$\mathcal{F}_\infty(p^s) := \lim_{R\to\infty} \int_{\Omega_R} \mathcal{S}(x)\cdot\nu(x)d\sigma(x) = \\ = \frac{1}{4\mathrm{i}\omega\rho_0} \lim_{R\to\infty} \int_{\Omega} \left[\bar{p}^s \frac{\partial p^s}{\partial r} - p^s \frac{\partial \bar{p}^s}{\partial r}\right](R,\hat{x})\, R^2 d\sigma(\hat{x}), \tag{3.50}$$

where $(R,\hat{x})$ are modulus and direction of $x \in \Omega_R$, while $d\sigma(\hat{x}) = \sin\theta\, d\theta\, d\varphi$ is the surface element on the unit sphere Ω. In order to compute the limit (3.50), we observe that the Sommerfeld radiation condition (3.31)(c) and the asymptotic behavior (3.32) together imply

$$\frac{\partial p^s}{\partial r} = \mathrm{i}k\frac{e^{\mathrm{i}kr}}{r} p_\infty(\hat{x}) + o(r^{-1}) \quad \text{as } r\to\infty. \tag{3.51}$$

Hence, by using (3.32) and (3.51), we obtain

$$\bar{p}^s \frac{\partial p^s}{\partial r}(R,\hat{x}) = \frac{\mathrm{i}k}{R^2}\,|p_\infty(\hat{x})|^2 + o(R^{-2}) \quad \text{as } R\to\infty, \tag{3.52}$$

uniformly in $\hat{x}$. Then, by substituting (3.52) into (3.50), we find

$$\mathcal{F}_\infty(p^s) = \frac{k}{2\omega\rho_0}\,\|p_\infty\|^2_{L^2(\Omega)}\,. \tag{3.53}$$

We now point out that equality (3.49) is a way to express, at a global level, the conservation of energy inside a lossless background. However, for our purposes, it is also interesting to study how power is locally transported (and conserved) from the near-field to the far-field region. In this framework, a key-role is played by the flow lines of the vector field $\mathcal{S}(x)$ associated with p^s (also called, for brevity, 'flow lines of p^s'). For any point $x_0 \in \mathbb{R}^3 \setminus \bar{D}$, the flow line $\tilde{\zeta}_{x_0}(\tau)$ of $\mathcal{S}(x)$ starting from x_0 is the unique solution (considered only for $\tau \geq 0$) of the Cauchy problem

$$\frac{dx}{d\tau}(\tau) = \mathcal{S}(x(\tau)), \quad \text{with} \quad x(0) = x_0. \tag{3.54}$$

The local existence and uniqueness of the solution to problem (3.54) are ensured by the fact that $p^s \in C^2(\mathbb{R}^3\setminus\bar{D})$, as stated in Problem 3.2.1, and then $\mathcal{S} \in C^1(\mathbb{R}^3\setminus\bar{D})$ by definition (3.48). The case $x_0 \in \partial D$ is more delicate: while existence of solutions still holds [87], uniqueness does not, since $p^s \in C^{1,\alpha}(\mathbb{R}^3\setminus D)$, then $\mathcal{S} \in C^{0,\alpha}(\mathbb{R}^3\setminus D)$ and, in particular, $\mathcal{S}$ may not be Lipschitz on domains containing subsets of ∂D. Thus $x_0 \in \partial D$ may be a *ramification point* for the solutions of (3.54): we shall discuss this issue in Section 3.2.7. Finally, if x_0 is such that $\mathcal{S}(x_0) = 0$, the flow line starting from x_0 collapses into x_0 itself, which is then called a *critical point* of $\mathcal{S}$ [1]. In our framework, we shall focus on non-critical initial points x_0 and assume that the flow lines are defined for all $\tau \geq 0$.

We now focus on flow tubes as bundles of flow lines. Let $[a,b]$ be a non-empty and closed interval in $\mathbb{R}$ and $\tilde{\gamma} : [a,b] \to \mathbb{R}^3$ the parametric representation of a simple and closed curve,

i.e., $\tilde{\gamma}$ is an injective map on (a,b), but $\tilde{\gamma}(a)=\tilde{\gamma}(b)$. We assume that the image $\gamma:=\tilde{\gamma}([a,b])$ is *transverse* with respect to the flow lines, i.e., we require that, for any point $x_0\in\gamma$, the image $\zeta_{x_0}:=\tilde{\zeta}_{x_0}([0,+\infty))$ of the flow line $\tilde{\zeta}_{x_0}(\tau)$ starting from x_0 intersects γ only in x_0 itself. Then, for each $x_0\in\gamma$, consider $\tilde{\zeta}_{x_0}(\tau)$ and define the bundle of (images of) flow lines $T_\gamma:=\cup_{\{x_0\in\gamma\}}\zeta_{x_0}$: if T_γ is homotopic to a cylinder, it will be called a *flow tube of* p^s (starting from γ). Any curve like γ (i.e., simple, closed and transverse) will be named a *transverse section* of the flow tube T_γ. We observe that $T_\gamma\subset\mathbb{R}^3\setminus D$, since the field p^s is only defined on $\mathbb{R}^3\setminus D$.

Flow tubes are responsible for the transport of power (i.e., of information) in the background. In particular, they are the key-tool for understanding how the constraint expressed in the far-field region by the far-field equation can contain information on the shape and location of the scatterer, which is placed in the near-field region. To this end, we need to assume that flow tubes verify some regularity conditions. First, a flow tube starting from a curve γ should reach the far-field region: in particular, it should not refold on the scatterer. Second, in the far-field region this tube should identify a definite set of directions $W_\infty(\gamma)\subset\Omega$, so that a local counterpart of (3.53), with $L^2(\Omega)$ replaced by $L^2[W_\infty(\gamma)]$, could be considered (cf. (3.56) in the following).

The latter requirement is made rather natural by the fact that the vector field $\mathcal{S}$ tends to become radial in the far-field region. This can be shown by analyzing the behavior of the three spherical components of $\nabla p^s(r,\theta,\varphi)=\frac{\partial p^s}{\partial r}\hat{e}_r+\frac{1}{r}\frac{\partial p^s}{\partial\theta}\hat{e}_\theta+\frac{1}{r\sin\theta}\frac{\partial p^s}{\partial\varphi}\hat{e}_\varphi$, where $(\hat{e}_r,\hat{e}_\theta,\hat{e}_\varphi)$ are the intrinsic coordinate vectors associated to a point of spherical coordinates (r,θ,φ). From (3.51), we have that the radial component of ∇p^s decays as $1/r$ when $r\to\infty$; instead, the transverse components of ∇p^s are $O(r^{-2})$ as $r\to\infty$, as shown by using the series representation (see [39], pp. 72-75) $p^s(x)=\frac{e^{ikr}}{r}\sum_{n=0}^{\infty}\frac{F_n(\theta,\varphi)}{r^n}$, which holds for all $r>R$ such that $\Omega_R\subset\mathbb{R}^3\setminus\bar{D}$, and can be differentiated term by term with respect to r,θ,φ any number of times. Then, remembering relations (3.48) and (3.52), we can conclude that the radial component of $\mathcal{S}$ is increasingly dominant over the transverse ones in the far-field region.

Let us now formalize the previous discussion in the following definition.

Definition 3.2.1. *Given a flow tube $T_\gamma\subset\mathbb{R}^3\setminus D$ as above, it is called 'regular' if there exist $R_0>0$ and $a,b\in\mathbb{R}$, with $a<b$, such that the set $T_{R_0}:=T_\gamma\setminus B_{R_0}$ admits a parametrization defined on $A:=[R_0,+\infty)\times[a,b]\subset\mathbb{R}^2$, i.e.,*

$$\tilde{T}_{R_0}:A\to\mathbb{R}^3,\quad (R,s)\mapsto\tilde{T}_{R_0}(R,s),\tag{3.55}$$

with the following properties:

(i) $\forall R\geq R_0$, the map $\tilde{T}_{R_0}(R,\cdot):[a,b]\to\mathbb{R}^3$ is the parametric representation of a transverse section γ_R of T_γ, with $\gamma_R=T_\gamma\cap\Omega_R$;

(ii) $\forall s_0\in[a,b]$, the point $\tilde{T}_{R_0}(R,s_0)\in\mathbb{R}^3$ tends to a definite direction as $R\to\infty$, i.e., $\exists\lim_{R\to\infty}\frac{\tilde{T}_{R_0}(R,s_0)}{R}=:\tilde{\gamma}_\infty(s_0)\in\Omega$, where $\tilde{\gamma}_\infty(\cdot):[a,b]\to\Omega$ is the parametric representation of a simple and closed curve $\gamma_\infty\subset\Omega$.

Finally, the open and connected domain enclosed by γ_∞ on Ω is denoted with $W_\infty(\gamma)$, and its area $|W_\infty(\gamma)|$ is called the 'asymptotic angular width' of T_γ.

Apart from technicalities, Definition 3.2.1 simply describes a generalization of some relevant features of the field radiated by a point-like source in a homogeneous background, whereby the flow lines spread out from the source itself and can be continued up to infinity according to an asymptotically definite direction, with no narrowing of the corresponding flow tubes.

Under the previous regularity assumption, it is easy to describe how power is locally preserved and carried throughout the background. Given a regular flow tube T_γ, consider a finite portion T_γ^{12} of it, delimited by two non-intersecting transverse sections γ_1 and γ_2. Moreover, let Σ_1 and Σ_2 be two open and bounded surfaces with boundaries γ_1 and γ_2 respectively, such that $\Sigma := T_\gamma^{12} \cup \Sigma_1 \cup \Sigma_2$ is a simple and closed surface enclosing no subsets of D. Then, the power flux of p^s across Σ vanishes, as stated soon before equality (3.49). Since the lateral boundary T_γ^{12} of Σ is entirely formed by flow lines of p^s, i.e., lines that are tangent in each point to the vector field $\mathcal{S}$, the flux of p^s across T_γ^{12} is zero too, as shown by relations (3.47) and (3.48). Hence, by possibly interchanging the names of Σ_1 and Σ_2, we can choose the orientations of the normals to Σ_1 and Σ_2 in such a way that the flux of p^s through Σ_1 entering into the flow tube is equal to the flux through Σ_2 outgoing from it, and also equal to the flux at infinity outgoing from $W_\infty(\gamma)$, i.e.,

$$\mathcal{F}_{\Sigma_1}(p^s) = \mathcal{F}_{\Sigma_2}(p^s) = \mathcal{F}_{W_\infty(\gamma)}(p^s) = \frac{k}{2\omega\rho_0} \|p^s\|^2_{L^2[W_\infty(\gamma)]}\,, \tag{3.56}$$

where the last inequality holds as a local version of (3.53). Property (3.56) expresses the transmission (and conservation) of power inside each regular flow tube.

Also for future purpose, it is interesting to focus on the fundamental solution $\Phi(x,z) = \frac{1}{4\pi}\frac{e^{\mathrm{i}k|x-z|}}{|x-z|}$ of the Helmholtz equation. In absence of scatterers, $\Phi_z := \Phi(\cdot, z)$ is the radiating field generated in the background by an isotropic point source placed at z. It is easy to realize that the flow lines of Φ_z are half-lines outgoing from z (but not defined at the singularity point z). Since the far-field pattern of Φ_z is given by $\Phi_\infty(\hat{x}, z) = \frac{1}{4\pi}e^{-\mathrm{i}k\hat{x}\cdot z}$, we can use (3.53) to compute the flux at infinity of Φ_z as

$$\mathcal{F}_\infty(\Phi_z) = \frac{k}{8\pi\omega\,\rho_0}. \tag{3.57}$$

More generally, since $\left|\frac{1}{4\pi}e^{-\mathrm{i}k\hat{x}\cdot z}\right| = \frac{1}{4\pi}$, the flux of Φ_z conveyed by any one of its flow tubes (which are portions of cones with vertex at z) is expressed according to (3.56) as

$$\mathcal{F}_{\Sigma_1}(\Phi_z) = \mathcal{F}_{\Sigma_2}(\Phi_z) = \mathcal{F}_{W_\infty(\gamma)}(\Phi_z) = \frac{k}{2\omega\rho_0}\|\Phi_z\|^2_{L^2[W_\infty(\gamma)]} = \frac{k}{8\pi\omega\,\rho_0}\cdot\frac{\beta\,[W_\infty(\gamma)]}{4\pi}, \tag{3.58}$$

where $\beta\,[W_\infty(\gamma)]$ is the amplitude (in steradians) of the solid angle identified by $W_\infty(\gamma) \subset \Omega$ and by the origin O of Ω as its vertex.

The previous considerations naturally lead us to reformulate the constraint expressed by the far-field equation (3.34) as follows. Let $g_z^\varepsilon \in L^2(\Omega)$ be an ε-approximate solution of (3.34), i.e., such that $\|Fg_z^\varepsilon - \Phi_\infty(\cdot,z)\|_{L^2(\Omega)} \leq \varepsilon$. The last inequality immediately implies that $\|Fg_z^\varepsilon - \Phi_\infty(\cdot,z)\|^2_{L^2(\Omega^s)} \leq \varepsilon^2$ for any (measurable) subset $\Omega^s \subset \Omega$. Then, a simple computation shows that

$$\left| \|Fg_z^\varepsilon\|^2_{L^2(\Omega^s)} - \|\Phi_\infty(\cdot,z)\|^2_{L^2(\Omega^s)} \right| \leq \varepsilon'(\Omega^s), \tag{3.59}$$

having defined $\varepsilon'(\Omega^s) := \varepsilon\left(2\|\Phi_\infty(\cdot,z)\|_{L^2(\Omega^s)} + \varepsilon\right)$. Note that $\|\Phi_\infty(\cdot,z)\|_{L^2(\Omega^s)}$ and consequently $\varepsilon'(\Omega^s)$ are independent of z. Moreover, we recall that Fg_z^ε is the far-field pattern of the scattered field given by (3.33), i.e., with a slight change of notations,

$$p_z^{s,\varepsilon}(x) := \int_\Omega p^s(x,\hat{d}) g_z^\varepsilon(\hat{d}) d\sigma(\hat{d}) \quad \text{for } x \in \mathbb{R}^3 \setminus D, \tag{3.60}$$

and that the flux at infinity of any radiating field is proportional to the squared L^2-norm of its far-field pattern, as shown by (3.53) or by its local version (3.56). Then, relation (3.59) means that, for any observation solid angle Ω^s in the far-field region, the flux of the scattered field $p_z^{s,\varepsilon}$ and the flux of the elementary source $\Phi(\cdot,z)$ can be made arbitrarily close to each other, by choosing ε small enough.

Analogous considerations can be made for an aspect-limited configuration of antennas, as briefly described at the end of Section 3.2.1: in relation (3.59), it suffices to replace F with the modified far-field operator $F_{al} : L^2(\Omega^i) \to L^2(\Omega^o)$ and to require that Ω^s is any (measurable) subset of the region Ω^o where the receivers are placed; in definition (3.60), the integration domain Ω should be replaced by the set Ω^i of incidence directions, but the field $p_z^{s,\varepsilon}$ is anyway defined in all $\mathbb{R}^3 \setminus D$.

The next sections are devoted to understanding how the far-field constraint (3.59), back-propagated to the near-field region by regular flow tubes, can induce a behavior of the indicator function that is in agreement with limits (3.35)(a) and (3.36)(a).

3.2.4. Boundary power fluxes

In Section 3.2.2 we saw that the FM can provide a good indicator function $\|\tilde{g}_z\|_{L^2(\Omega)}$ for the support of the scatterer: in particular, let us now focus on the statement of Theorem 3.2.2. Apart from technicalities, this result can be explained as follows. Since $\mathcal{R}(G) = \mathcal{R}\left(F^*F\right)^{1/4}$, for each $\tilde{g} \in L^2(\Omega)$ the function $\left(F^*F\right)^{1/4}\tilde{g} \in L^2(\Omega)$ is the far-field pattern of a radiating solution $p^r[\tilde{g}]$ of the Helmholtz equation in $\mathbb{R}^3 \setminus \bar{D}$. (Note that $p^r[\tilde{g}]$ is different from $p^s_{\tilde{g}}$, as it would be given by (3.33), and that, in general, it is not even attainable as a scattered field.) In particular, consider the solution $\tilde{g}_z$ of equation (3.41) for $z \in D$: the equality of the two far-field patterns $\left(F^*F\right)^{1/4}\tilde{g}_z(\hat{x})$ and $\Phi_\infty(\hat{x},z)$ implies, by Rellich's lemma, that the corresponding

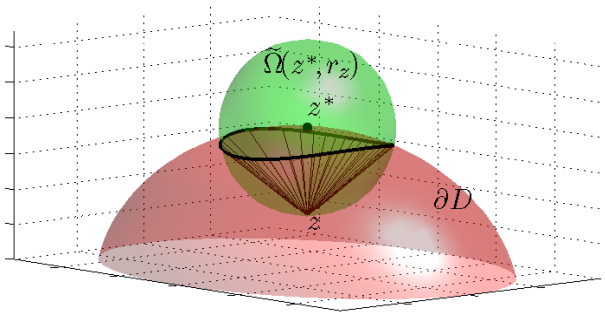

Figure 3.5: Geometric construction for $z^* \in \partial D$ and $z \in U_{z^*} \cap D$.

fields $p^r[\tilde{g}_z]$ and $\Phi(\cdot, z)$ are equal in $\mathbb{R}^3 \setminus \bar{D}$. But $\Phi(\cdot, z)$ is singular in z: then, as $z \to z^* \in \partial D$, the field $p^r[\tilde{g}_z]$ should become singular too, and this is possible only if $\tilde{g}_z$ fails to be in $L^2(\Omega)$.

Now, the fact that, for $z \in D$, $p^r[\tilde{g}_z]$ and $\Phi(\cdot, z)$ coincide in $\mathbb{R}^3 \setminus \bar{D}$ implies that the fluxes of $p^r[\tilde{g}_z]$ and $\Phi(\cdot, z)$ across any surface in the background are equal: this simple observation suggests an interesting result and generalization in the framework of the LSM, as we are going to show.

To this end, we first need to consider the following geometrical construction (see Figure 3.5). Given $z^* \in \partial D$, let $U_{z^*} \subset \mathbb{R}^3$ be a neighborhood of z^*; for each $z \in U_{z^*} \cap D$, define $r_z := |z - z^*|$, $\Omega(z^*, r_z) := \{x \in \mathbb{R}^3 : |x - z^*| = r_z\}$, and $\tilde{\Omega}(z^*, r_z) := \Omega(z^*, r_z) \cap (\mathbb{R}^3 \setminus D)$. Since D is a C^2-domain, for each $z^* \in \partial D$ the tangent plane $\tau(z^*)$ is well-defined: then, for r_z small enough (say $r_z < r_0$), $\tilde{\Omega}(z^*, r_z)$ is a connected and simply connected subset of $\Omega(z^*, r_z)$ that well approximates a half-sphere. Now, for $r_z < r_0$, consider the solid angle $\hat{z}(z^*, r_z)$ having its vertex in a point $z \in D \cap \Omega(z^*, r_z)$ and identifying the subset $\tilde{\Omega}(z^*, r_z)$ on $\Omega(z^*, r_z)$: as r_z decreases, $\hat{z}(z^*, r_z)$ better and better approximates the vertex angle of a cone inscribed in a half-sphere. Then, if we denote by $\beta_z := |\hat{z}(z^*, r_z)|$ the amplitude (in steradians) of $\hat{z}(z^*, r_z)$, it follows from Theorem 3.2.8 in the Section 3.2.9 that β_z is bounded from below, i.e., $\liminf_{z \to z^*} \beta_z = 2\pi \left(1 - \frac{\sqrt{2}}{2}\right) > 0$.

On the other hand, the flux across $\tilde{\Omega}(z^*, r_z)$ due to the elementary and isotropic source placed at z is directly proportional to β_z, as highlighted by (3.58). Then, remembering the previous limit, we find

$$\liminf_{z \to z^*} \mathcal{F}_{\tilde{\Omega}(z^*, r_z)}(\Phi_z) = \frac{k}{8\pi\omega\,\rho_0} \cdot \frac{2\pi \left(1 - \frac{\sqrt{2}}{2}\right)}{4\pi} = \frac{k\left(2 - \sqrt{2}\right)}{32\pi\omega\,\rho_0} > 0, \tag{3.61}$$

which states that, although the area of $\tilde{\Omega}(z^*, r_z)$ vanishes as $z \to z^*$, the flux of Φ_z across it has a positive lower bound. This is not surprising, since Φ_z is singular in z; however, it is

interesting to observe that the very same property, in the FM, holds for the radiating field $p^r[\tilde{g}_z]$, since $p^r[\tilde{g}_z] = \Phi_z$ in $\mathbb{R}^3 \setminus \bar{D}$ (for $z \in D$).

Notably, if we now assume an analogous property for the scattered field considered in the LSM (cf. (3.60)), we can prove that the indicator function blows up as $z \to z^*$, in analogy with Theorem 3.2.2. This is shown by the following theorem, which makes no use of the far-field equation.

Theorem 3.2.4. *Let z^*, U_{z^*}, $\Omega(z^*, r_z)$ and $\tilde{\Omega}(z^*, r_z)$ be as above. Suppose that a function $g_z \in L^2(\Omega)$ is associated to each $z \in U_{z^*} \cap D$. Consider the scattered field p_z^s defined in analogy with (3.60), and assume that the corresponding flux across $\tilde{\Omega}(z^*, r_z)$ is bounded from below as $z \to z^*$, i.e., there exists $c > 0$ such that*

$$\liminf_{z \to z^*} \mathcal{F}_{\tilde{\Omega}(z^*, r_z)}\left(p_z^s\right) = c. \tag{3.62}$$

Then, $\lim_{z \to z^*} \|g_z\|_{L^2(\Omega)} = \infty$.

Proof. Assume, by contradiction, that the limit does not hold. Then, there exist a sequence $\{z_n\}_{n=0}^{\infty} \subset U(z^*) \cap D$ and a positive constant $K > 0$ such that, for all $n \in \mathbb{N}$, we have $\|g_{z_n}\|_{L^2(\Omega)} \leq K$. Setting $r_n := r_{z_n}$, we are going to obtain a contradiction with hypothesis (3.62) by proving that $\mathcal{F}_{\tilde{\Omega}(z^*, r_n)}\left(p_{z_n}^s\right)$ vanishes as $n \to \infty$.

Let $\hat{d}(\theta, \varphi)$ be the unit vector of the direction identified by the spherical angles $(\theta, \varphi) \in [0, \pi] \times [0, 2\pi]$ (the ambiguities arising for $\theta = \pi$ or $\varphi = 2\pi$ are irrelevant in this context). Thus, if we regard the incident plane wave $p^i(x, \theta, \varphi) = e^{ikx \cdot \hat{d}(\theta, \varphi)}$ as a function of x, θ, φ, it is easy to realize that p^i, as well as its first and second partial derivatives with respect to the Cartesian coordinates x_j (for $j = 1, 2, 3$), are continuous functions on the compact set $A := \partial D \times [0, \pi] \times [0, 2\pi]$, and then uniformly continuous on A itself. The latter property implies that

$$\lim_{(\theta, \varphi) \to (\theta_0, \varphi_0)} \left\| p^i(\cdot, \theta, \varphi) - p^i(\cdot, \theta_0, \varphi_0) \right\|_{1, \alpha, \partial D} = 0 \quad \forall (\theta_0, \varphi_0) \in [0, \pi] \times [0, 2\pi], \tag{3.63}$$

where, following the notations of [41], $\|\cdot\|_{1,\alpha,\partial D}$ is the norm in the space $C^{1,\alpha}(\partial D)$. Then, by the well-posedness of Problem 3.2.1, we have

$$\lim_{(\theta, \varphi) \to (\theta_0, \varphi_0)} \|p^s(\cdot, \theta, \varphi) - p^s(\cdot, \theta_0, \varphi_0)\|_{1, \alpha, \mathbb{R}^3 \setminus D} = 0 \quad \forall (\theta_0, \varphi_0) \in [0, \pi] \times [0, 2\pi]. \tag{3.64}$$

In particular, the functions $p^s(x, \cdot, \cdot)$ and $\frac{\partial p^s}{\partial x_j}(x, \cdot, \cdot)$ are continuous in $[0, \pi] \times [0, 2\pi]$ uniformly with respect to $x \in \mathbb{R}^3 \setminus D$. On the other hand, the continuity in $\mathbb{R}^3 \setminus D$ of $p^s(\cdot, \theta, \varphi)$ and $\frac{\partial p^s}{\partial x_j}(\cdot, \theta, \varphi)$ for each $(\theta, \varphi) \in [0, \pi] \times [0, 2\pi]$ is a trivial consequence of the well-posedness of Problem 3.2.1. As a result, both p^s and $\frac{\partial p^s}{\partial x_j}$ are continuous in $(\mathbb{R}^3 \setminus D) \times [0, \pi] \times [0, 2\pi]$.

Consider now the open ball B_R, with $R > 0$ so large that $\bar{D} \subset B_R$, and define $G := B_R \setminus \bar{D}$. The continuity of p^s and $\frac{\partial p^s}{\partial x_j}$ on the compact set $A' := \bar{G} \times [0, \pi] \times [0, 2\pi]$ implies that there

exist constants $M_1, M_2 > 0$ such that

$$|p^s(x,\theta,\varphi)| \le M_1, \quad \left|\frac{\partial p^s}{\partial x_j}(x,\theta,\varphi)\right| \le M_2 \quad \forall (x,\theta,\varphi) \in A'. \tag{3.65}$$

Then, by using the Cauchy-Schwarz inequality, from relations (3.60), (3.65) and the assumption $\|g_{z_n}\|_{L^2(\Omega)} \le K$, we obtain

$$\begin{aligned} \left|p^s_{z_n}(x)\right| &\le \int_\Omega \left|p^s(x,\hat{d}) g_{z_n}(\hat{d})\right| d\sigma(\hat{d}) = \int_0^\pi \left[\int_0^{2\pi} |p^s(x,\theta,\varphi)| \cdot |g_{z_n}(\theta,\varphi)|\, d\varphi\right] \sin\theta\, d\theta \le \\ &\le M_1\sqrt{4\pi}\, \|g_{z_n}\|_{L^2(\Omega)} \le 2\sqrt{\pi} M_1 K =: Q_1 \qquad \forall x \in \bar{G},\ \forall n \in \mathbb{N}, \end{aligned} \tag{3.66}$$

and analogously, by Lebesgue's dominated convergence theorem,

$$\left|\frac{\partial p^s_{z_n}}{\partial x^i}(x)\right| \le M_2\sqrt{4\pi}\, \|g_{z_n}\|_{L^2(\Omega)} \le 2\sqrt{\pi} M_2 K =: Q_2 \qquad \forall x \in \bar{G},\ \forall n \in \mathbb{N}. \tag{3.67}$$

Let us now recall the expression of $\mathcal{F}_{\tilde{\Omega}(z^*,r_n)}\left(p^s_{z_n}\right)$ as given by (3.47) and (3.48), i.e.,

$$\mathcal{F}_{\tilde{\Omega}(z^*,r_n)}\left(p^s_{z_n}\right) = \frac{1}{4\mathrm{i}\omega\rho_0} \int_{\tilde{\Omega}(z^*,r_n)} \left[\bar{p}^s_{z_n} \frac{\partial p^s_{z_n}}{\partial \nu} - p^s_{z_n} \frac{\partial \bar{p}^s_{z_n}}{\partial \nu}\right](x)\, d\sigma(x). \tag{3.68}$$

It is clear that $\tilde{\Omega}(z^*, r_n) \subset \bar{G}$ for n large enough: then, we can use inequalities (3.66) and (3.67) to bound (3.68) as

$$\left|\mathcal{F}_{\tilde{\Omega}(z^*,r_n)}\left(p^s_{z_n}\right)\right| \le \frac{1}{2\omega\rho_0} \int_{\tilde{\Omega}(z^*,r_n)} \left|\bar{p}^s_{z_n}(x) \frac{\partial p^s_{z_n}}{\partial \nu}(x)\right| d\sigma(x) \le \frac{\sqrt{3}\left|\tilde{\Omega}(z^*,r_n)\right|}{2\omega\rho_0} Q_1\, Q_2, \tag{3.69}$$

where $\left|\tilde{\Omega}(z^*,r_n)\right|$ denotes the area of the surface $\tilde{\Omega}(z^*,r_n)$. As $n \to \infty$, this area vanishes: then, from the last inequality in (3.69), we have $\lim_{n\to\infty} \left|\mathcal{F}_{\tilde{\Omega}(z^*,r_n)}\left(p^s_{z_n}\right)\right| = 0$, in contradiction with (3.62). □

It is clear that Theorem 3.2.4 can be immediately adapted to the aspect-limited case: it suffices to properly restrict the set of incidence directions, i.e., to require that $\hat{d}(\theta,\varphi) \in \bar{\Omega}^i$.

The next step is now to formulate sufficient conditions for the fulfilment of the hypotheses of Theorem 3.2.4. According to the framework outlined in Section 3.2.3, these conditions should be related to the far-field equation and to the regular behavior of the flow tubes starting from the boundary of the scatterer and reaching the far-field region. Then, in the following section we numerically investigate this behavior, while in Section 3.2.6 the numerical results will be used to identify and formalize the sufficient conditions we are looking for.

3.2.5. Numerical simulations: the case of a sampling point inside the scatterer

We are going to consider two scattering experiments. For both of them, the scatterer is a sound-soft sphere placed in air and centred at the origin of an orthogonal Cartesian coordinate system (x_1, x_2, x_3); moreover, the wavelength of the incident pressure field is $\lambda = 1\,\mathrm{m}$ and the radius of the sphere is $a = 0.3\,\lambda$. In both cases, the LSM is implemented as described e.g. in [37, 46]. However, the former experiment deals with a full-view configuration of the emitting and receiving antennas, which entails the normality of the far-field operator F [9]; instead, the latter considers an aspect-limited configuration, whereby all antennas are placed in the far-field half-sphere $\Omega_{x_2\geq 0}$ contained in the half-space $x_2 \geq 0$. This means that the set of incidence directions is $\Omega^i = -\Omega_{x_2\geq 0} = \Omega_{x_2\leq 0}$, while the set of observation directions is $\Omega^o = \Omega_{x_2\geq 0}$: accordingly, the modified far-field operator $F_{al} : L^2(\Omega^i) \to L^2(\Omega^o)$ is not normal [23, 68].

For each experiment, we use 11×22 incident plane waves and 10×20 measurement points. Both the incidence and observation angles are chosen according to a uniform discretization step for the spherical angles: $\theta \in [0, \pi]$ and $\varphi \in [0, 2\pi]$ for the full-view case; $\theta \in [0, \pi]$ and $\varphi \in [0, \pi]$ for the aspect-limited case. For each incident wave, the far-field pattern of the corresponding scattered field is computed by exploiting the analytical results in [63] and then blurred by 3% Gaussian noise. The visualizations provided by the LSM for the two experiments are shown in Figure 3.6. In general, for each figure, the panels on the left and on the right will refer to the full-view and to the aspect-limited case, respectively. Then, in panels (a) and (c) of Figure 3.6 we show the reconstructed sphere together with a schematic representation of the positions of all antennas in the far-field region, while in panels (b) and (d) we plot a zoomed visualization of the scatterer. In particular, panel (d) highlights that, in the aspect-limited case, the quality of the reconstruction is lower, due to a lengthening along the x_2-axis.

We now investigate the behavior of the flow lines of the scattered field: more precisely, given a sampling point $z \in D = B_a$, we compute a discretized version of the field (3.60), where g_z^ε is given by the LSM. Then, for each point of a uniform and cubic grid with discretization step equal to $\lambda/10$ in a cubic domain with side at least 10λ long, we plot a discretized and normalized version of the vector $\mathcal{S}$ (see (3.48)) associated with the field (3.60). For the clarity of visualization, only zoomed plane sections, parallel to the coordinate axes, will be shown.

We first consider a sampling point placed at the center of the sphere: the resulting behavior of the vector field $\mathcal{S}$ is shown in Figure 3.7. The three panels (a), (b) and (c) on the left are obtained, for the full-view configuration, by orthogonally projecting onto the planes $x_1 = 0$, $x_2 = 0$, $x_3 = 0$ respectively the vectors $\mathcal{S}$ applied into the grid points of such planes. The same holds true for the panels (d), (e) and (f) on the right, except that they refer to the aspect-limited

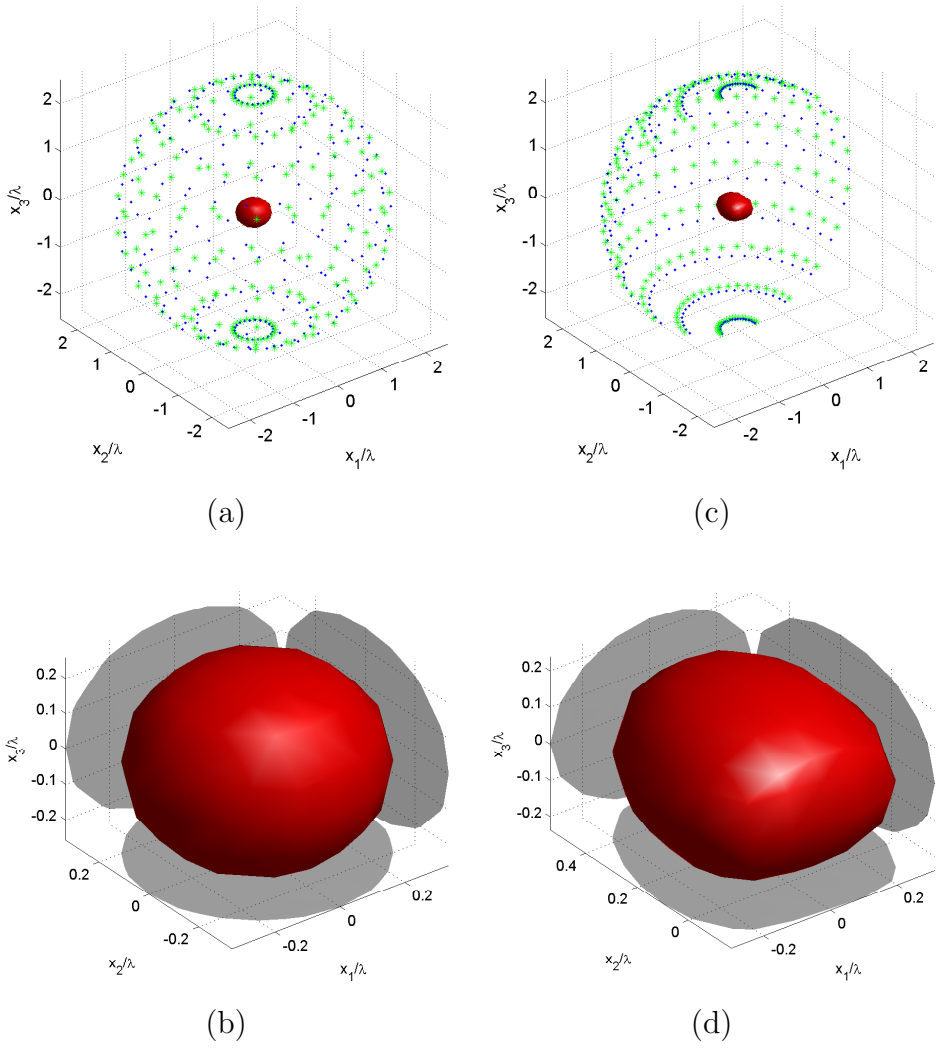

Figure 3.6: Visualization of the spherical and sound-soft scatterer provided by the LSM. Panels (a) and (b) correspond to the full-view configuration of antennas, panels (c) and (d) to the aspect-limited configuration. In panels (a) and (c), the points and the asterisks surrounding the reconstructed sphere represent the emitting and receiving antennas, respectively. In panels (b) and (d), a zoomed visualization of the scatterer is shown.

case: accordingly, we added a half-circle or a circle to indicate the position of the antennas in each plane section. In spite of normalization, the arrows representing $\mathcal{S}$ may be, in general, of different lengths: shorter arrows indicate that the corresponding $\mathcal{S}$ is not parallel to the plane section under exam. From Figure 3.7, the radial behavior of $\mathcal{S}$ with respect to z is evident in the full-view case (panels (a)-(c)), while it undergoes a slight deterioration for the aspect-limited case, as highlighted by panels (d) and (f); notably, such deterioration is negligible for the plane section $x_2 = 0$ (panel (e)), which corresponds to a planar full-view configuration. The observed behaviors turn out to be fully preserved also when larger investigation domains are visualized.

This (approximately) radial behavior of $\mathcal{S}$ with respect to the sampling point is not related to the symmetric position chosen for the previous sampling point: on the contrary, it is verified for any z inside the scatterer, or even on its boundary. For example, in the three pairs of panels (a)-(d), (b)-(e) and (c)-(f) of Figure 3.8 we can respectively see the three plane sections $x_1 = 0$, $x_2 = 0.2$ and $x_3 = 0$ for the sampling point $z = (0, 0.2, 0)$. Figure 3.9 is organized in an analogous way, but is concerned with the case of a sampling point on the boundary, i.e., $z = (0, 0.3, 0)$, and the corresponding plane sections $x_1 = 0$, $x_2 = 0.3$ and $x_3 = 0$. In any case, an approximate radiality of the flow lines of $\mathcal{S}$, and a consequent regularity of the flow tubes starting from the boundary of the scatterer, is suggested by these (and others, not shown here) numerical simulations.

3.2.6. Back-propagation of information from the far-field to the near-field region

We can now understand how the constraint expressed by the far-field equation is back-propagated to the near-field region. More precisely, taking inspiration from the numerical results of Section 3.2.5, we can identify sufficient conditions ensuring that the lower bound (3.62), concerning the flux outgoing from a small sphere centered at a point of ∂D, follows from the energy conservation inside a regular flow tube linking that portion of ∂D to the far-field region, where the far-field equation forces the tube itself to convey a positive flux. The next theorem formalizes these considerations (for the case of a full-view configuration of antennas).

Theorem 3.2.5. *Let z^*, U_{z^*}, $\Omega(z^*, r_z)$ and $\tilde{\Omega}(z^*, r_z)$ be as in Theorem 3.2.4. Given $\varepsilon > 0$, for each $z \in U_{z^*} \cap D$ consider an ε-approximate solution of the far-field equation, i.e., a function $g_z^\varepsilon \in L^2(\Omega)$ such that $\|Fg_z^\varepsilon - \Phi_\infty(\cdot, z)\|_{L^2(\Omega)} \leq \varepsilon$. Moreover, assume that, for each $z \in U_{z^*} \cap D$, the curve $\gamma_z := \partial\tilde{\Omega}(z^*, r_z) = \Omega(z^*, r_z) \cap \partial D$ is a transverse section of a regular flow tube T_{γ_z} of the scattered field $p_z^{s,\varepsilon}$, with asymptotic angular width $|W_\infty(\gamma_z)|$. Finally, assume that there exists an open and connected domain $W_\infty^* \subset \Omega$ such that its area $|W_\infty^*|$ is positive and $\lim_{z \to z^*} |W_\infty^* \Delta W_\infty(\gamma_z)| = 0$, where '$\Delta$' denotes the symmetric difference between two sets.*

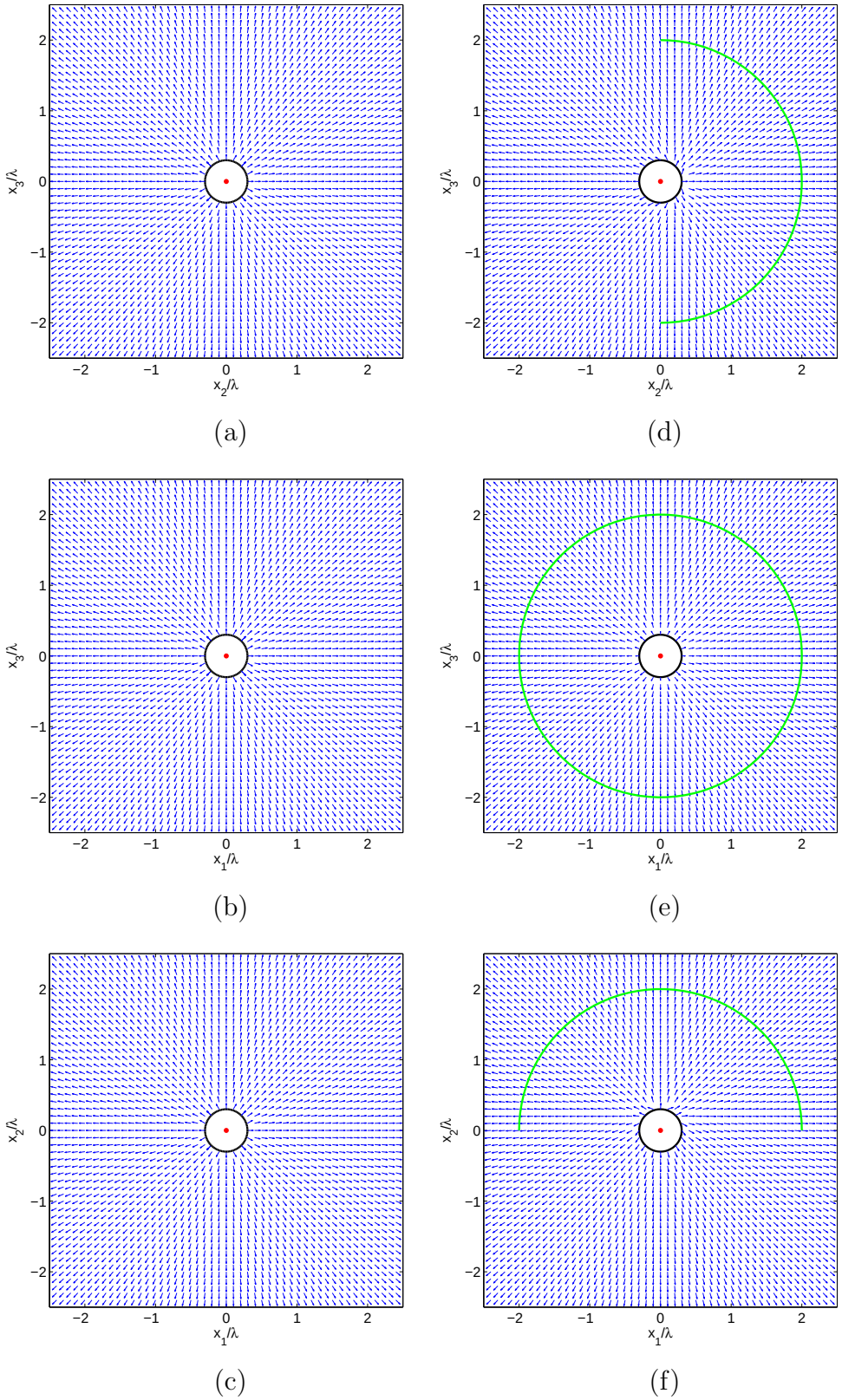

Figure 3.7: Qualitative behavior of the vector field $\mathcal{S}$ for a sampling point z (red bullet) at the center of the sphere (black contour). Full-view configuration of antennas: (a) plane section $x_1 = 0$; (b) plane section $x_2 = 0$; (c) plane section $x_3 = 0$. Aspect-limited configuration of antennas: (d) plane section $x_1 = 0$; (e) plane section $x_2 = 0$; (f) plane section $x_3 = 0$.

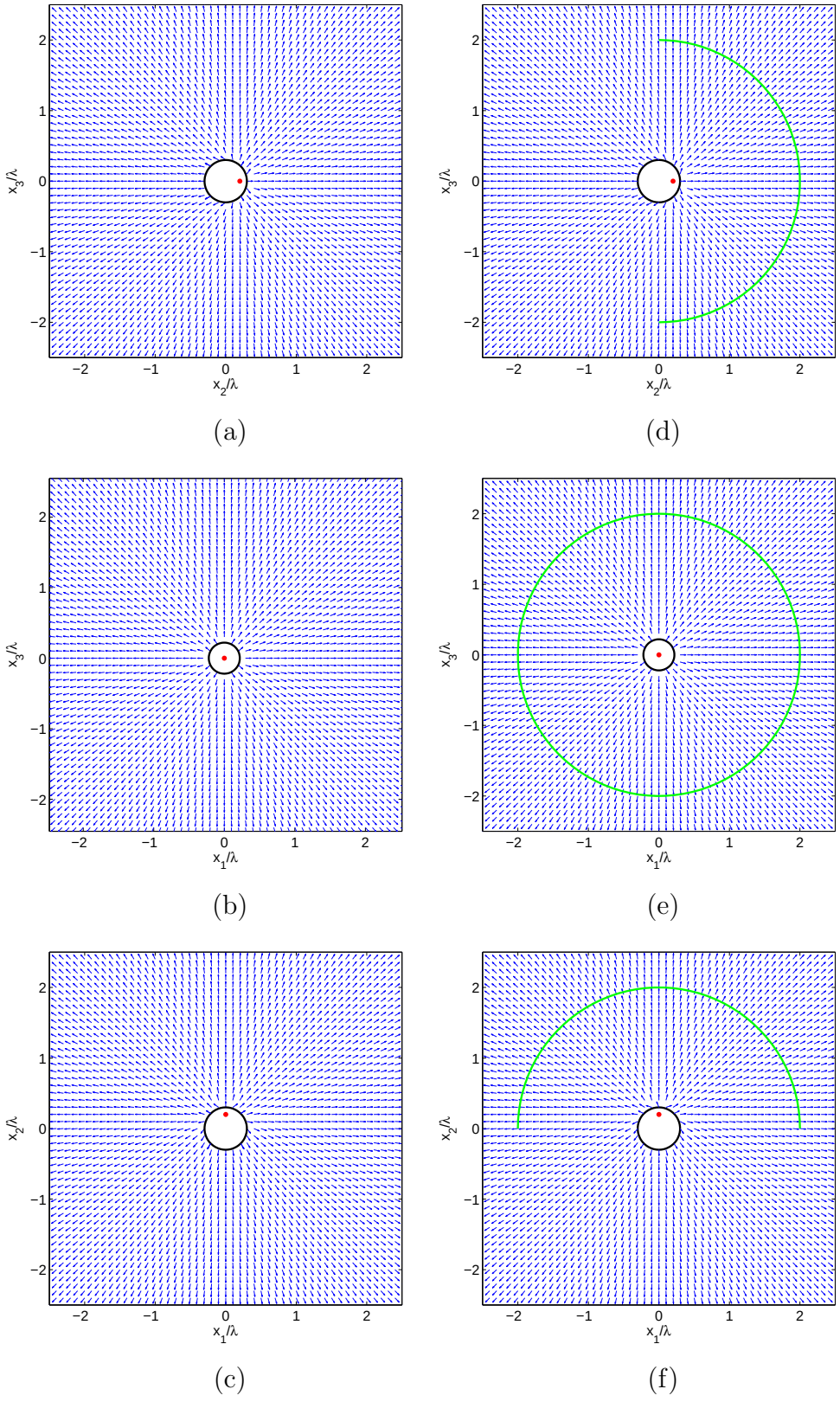

Figure 3.8: Qualitative behavior of the vector field $\mathcal{S}$ for a sampling point $z = (0, 0.2, 0)$ (red bullet) inside the sphere (black contour). Full-view configuration of antennas: (a) plane section $x_1 = 0$; (b) plane section $x_2 = 0.2$; (c) plane section $x_3 = 0$. Aspect-limited configuration of antennas: (d) plane section $x_1 = 0$; (e) plane section $x_2 = 0.2$; (f) plane section $x_3 = 0$.

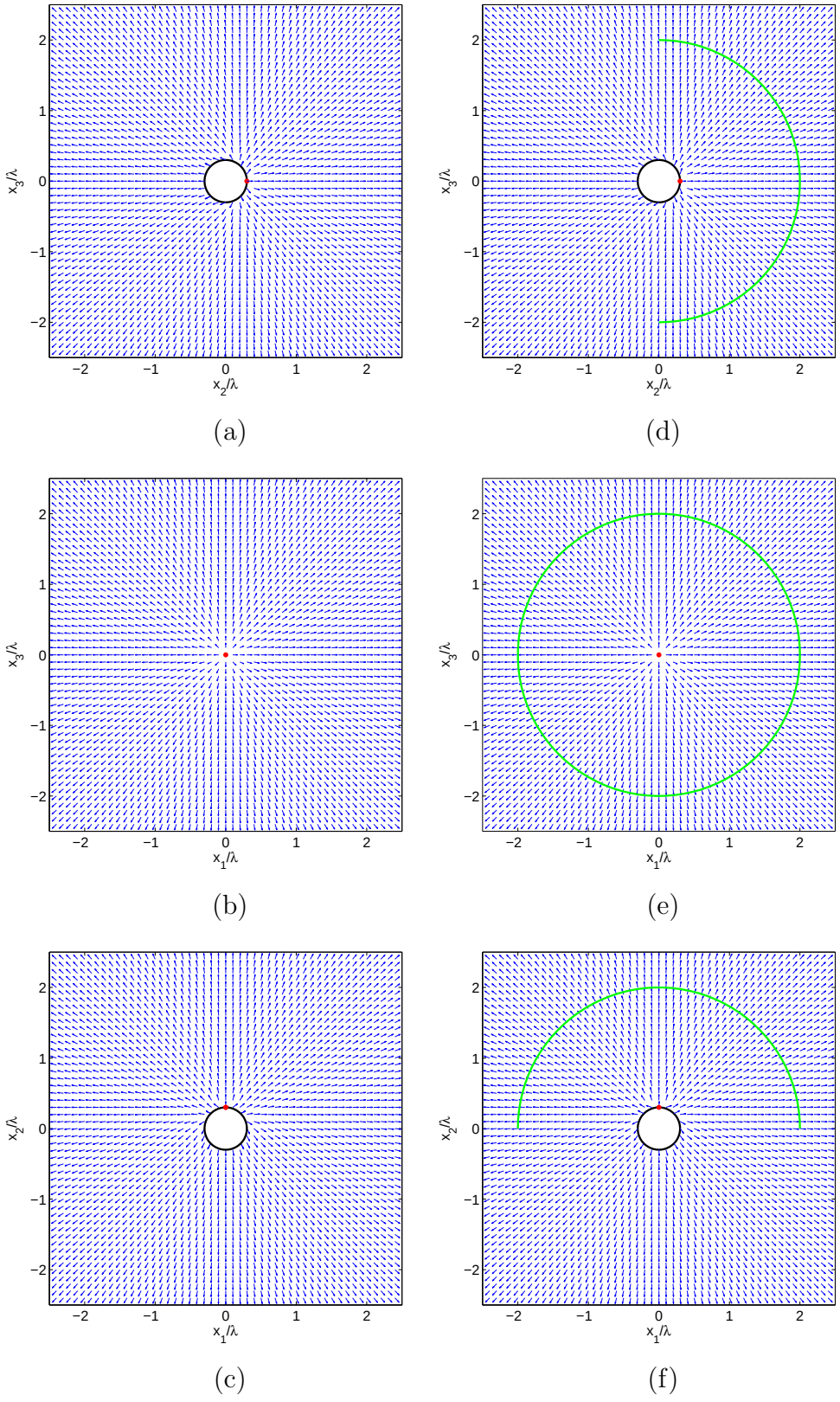

Figure 3.9: Qualitative behavior of the vector field $\mathcal{S}$ for a sampling point $z = (0, 0.3, 0)$ (red bullet) on the boundary of the sphere (black contour). Full-view configuration of antennas: (a) plane section $x_1 = 0$; (b) plane section $x_2 = 0.3$; (c) plane section $x_3 = 0$. Aspect-limited configuration of antennas: (d) plane section $x_1 = 0$; (e) plane section $x_2 = 0.3$; (f) plane section $x_3 = 0$.

Then, for any such $g_z^\varepsilon \in L^2(\Omega)$, the limit $\lim_{z\to z^*} \|g_z^\varepsilon\|_{L^2(\Omega)} = \infty$ holds, provided that ε is small enough.

Proof. The power flux of the scattered field $p_z^{s,\varepsilon}$ across $\tilde{\Omega}(z^*, r_z)$ is preserved, by energy conservation, along the regular flow tube T_{γ_z}, as highlighted in (3.56). In particular, with reference to property (i) of Definition 3.2.1, the flux outgoing from $\tilde{\Omega}(z^*, r_z)$ is equal to the flux across the domain $W_R(\gamma_z)$ enclosed on Ω_R by the section $(\gamma_z)_R = T_{\gamma_z} \cap \Omega_R$, for all $R \geq R_0$. Then, remembering also (3.59), we have for each $z \in U(z^*) \cap D$:

$$\begin{aligned}
\mathcal{F}_{\tilde{\Omega}(z^*,r_z)}\left(p_z^{s,\varepsilon}\right) &= \frac{1}{4\mathrm{i}\omega\,\rho_0} \int\limits_{\tilde{\Omega}(z^*,r_z)} \left[\bar{p}_z^{s,\varepsilon} \frac{\partial p_z^{s,\varepsilon}}{\partial \nu} - p_z^{s,\varepsilon} \frac{\partial \bar{p}_z^{s,\varepsilon}}{\partial \nu}\right](x)\, d\sigma(x) = \\
&= \frac{1}{4\mathrm{i}\omega\,\rho_0} \lim_{R\to\infty} \int\limits_{W_R(\gamma_z)} \left[\bar{p}_z^{s,\varepsilon} \frac{\partial p_z^{s,\varepsilon}}{\partial \nu} - p_z^{s,\varepsilon} \frac{\partial \bar{p}_z^{s,\varepsilon}}{\partial \nu}\right](R,\hat{x})\, R^2 d\sigma(\hat{x}) = \\
&= \frac{k}{2\omega\,\rho_0} \|F g_z^\varepsilon\|^2_{L^2[W_\infty(\gamma_z)]} \geq \\
&\geq \frac{k}{2\omega\,\rho_0} \left\{ \|\Phi_\infty(\cdot, z)\|^2_{L^2[W_\infty(\gamma_z)]} - \varepsilon'[W_\infty(\gamma_z)] \right\}. \qquad (3.70)
\end{aligned}$$

Now, the assumption $\lim_{z\to z^*} |W_\infty^* \Delta W_\infty(\gamma_z)| = 0$ clearly implies the two following limits: $\lim_{z\to z^*} \|\Phi_\infty(\cdot, z)\|^2_{L^2[W_\infty(\gamma_z)]} = \|\Phi_\infty(\cdot, z^*)\|^2_{L^2(W_\infty^*)}$ and $\lim_{z\to z^*} \varepsilon'[W_\infty(\gamma_z)] = \varepsilon'(W_\infty^*)$. Then, from the last inequality in (3.70), we obtain:

$$\liminf_{z\to z^*} \mathcal{F}_{\tilde{\Omega}(z^*,r_z)}\left(p_z^{s,\varepsilon}\right) \geq \frac{k}{2\omega\,\rho_0} \left[\|\Phi_\infty(\cdot, z^*)\|^2_{L^2(W_\infty^*)} - \varepsilon'(W_\infty^*) \right]. \qquad (3.71)$$

Now, by hypothesis, the area of W_∞^* is positive and then we have $\|\Phi_\infty(\cdot, z^*)\|^2_{L^2(W_\infty^*)} > 0$. Accordingly, we can take $\varepsilon > 0$ so small that the right-hand side of (3.71) is positive. More precisely, remembering the explicit expressions of $\Phi_\infty(\hat{x}, z^*) = \frac{1}{4\pi} e^{-\mathrm{i}k\hat{x}\cdot z^*}$ and of $\varepsilon'(W_\infty^*)$, as given soon below (3.59), it suffices to choose ε such that

$$0 < \varepsilon < (\sqrt{2} - 1) \|\Phi_\infty(\cdot, z^*)\|_{L^2(W_\infty^*)} = (\sqrt{2} - 1) \frac{\sqrt{|W_\infty^*|}}{4\pi}. \qquad (3.72)$$

With this choice of ε, the flux $\mathcal{F}_{\tilde{\Omega}(z^*,r_z)}\left(p_z^{s,\varepsilon}\right)$ is bounded from below as $z \to z^*$: then, we can apply Theorem 3.2.4 to conclude that $\lim_{z\to z^*} \|g_z^\varepsilon\|_{L^2(\Omega)} = \infty$, in agreement with limit (3.35)(a). □

Remark 3.2.1. By relying on the numerical experiments performed in Section 3.2.5, we can give a lower bound for the asymptotic angular width $|W_\infty^*|$ determining the upper bound (3.72). Indeed, for $z \in D$ (and even on ∂D) the flow lines of $p_z^{s,\varepsilon}$ resemble those of $\Phi(\cdot, z)$ in that they are essentially radial with respect to z. Hence, $|W_\infty^*|$ will not be less than the lower limit amplitude β_z of the angle $\hat{z}(z^*, r_z)$ as $z \to z^*$, i.e., as shown soon before (3.61), $2\pi\left(1 - \frac{\sqrt{2}}{2}\right)$.

Remark 3.2.2. Theorem 3.2.5 deals with generic ε-approximate solutions of the far-field equation. However, in the implementation of the LSM, Tikhonov regularized solutions g_z^α play a major role: then, it is interesting to specify the previous analysis to them. To this end, Theorem 3.2.5 can be paraphrased as follows. For each $z \in D$, consider the discrepancy $d_{\alpha^*(z)} := \left\| F g_{\alpha^*(z)} - \Phi_\infty(\cdot, z) \right\|_{L^2(\Omega)}$, where $\alpha^*(z)$ is chosen by means of some optimality criterion. Assume that the condition $d_{\alpha^*(z)} \leq \varepsilon$ holds, where $\varepsilon > 0$ fulfils bound (3.72): then, if the flow tubes of $p_z^{s,\varepsilon}$ satisfy the specified regularity requirements, we have $\lim_{z \to z^*} \left\| g_{\alpha^*(z)} \right\|_{L^2(\Omega)} = \infty$, which can only happen if $\lim_{z \to z^*} \alpha^*(z) = 0$. The latter limit shows that, although we do not assume $\alpha \to 0^+$ in our framework, we find such a result, but only for z approaching $z^* \in \partial D$: this is in qualitative agreement with numerical simulations, which highlight [46] a strong decrease of $\alpha^*(z)$ as $z \to z^*$.

Remark 3.2.3. The aspect-limited case can be dealt with in an analogous way, by restricting the set of incidence directions to Ω^i. However, an additional hypothesis is required in the statement of Theorem 3.2.5: the flow tubes under exam should reach the portion of the far-field region where the receiving antennas are placed, i.e., it should hold that $W_\infty^* \subset \Omega^o$. Indeed, outside Ω^o the modified far-field equation imposes no constraint whatsoever (cf. also the end of Section 6 in [8]).

We conclude this section by observing that, although redundant, a similar physical approach could be pursued also for the FM, with a notable simplification: since, for $z \in D$, the radiating field $p^r[\tilde{g}_z]$ is equal to Φ_z in $\mathbb{R}^3 \setminus \bar{D}$, the flow lines of interest are portions of half-lines outgoing from z, and the flow tubes are portions of cones with vertex at z. Notably, should a flow tube impinge on a portion of ∂D, this would not affect the value of the power flux carried by it beyond this obstruction, since the flux of $p^r[\tilde{g}_z]$ is always and exactly equal to that of Φ_z. Hence, in the FM, the requirements stated in Definition 3.2.1 would become partly useless, partly trivial, and no regularity issue would arise.

3.2.7. The case of a sampling point outside the scatterer

Soon after the formulation of the Cauchy problem (3.54), we noticed that an initial point $x_0 \in \partial D$ may be a ramification point, i.e., such that several flow lines may start from it. In particular, it is even possible that a flow tube originates from x_0: in other terms, x_0 might become a degenerate transverse section of a flow tube. Actually, the numerical simulations presented in Section 3.2.5 confirm this possibility. Indeed, the (approximately) radial behavior of the flow lines of the scattered field with respect to the sampling point is observed not only for $z \in D$, but also for $z \in \partial D$, as shown in Figure 3.9: then, in the latter case, z seems to be just a ramification point.

This introduces us to the analysis of what happens when the sampling point is chosen outside the scatterer. Interestingly, the numerical simulations performed in this case highlight that at least one ramification point shows up on ∂D. For example, with reference to the same two scattering experiments considered in Section 3.2.5, we now choose the exterior sampling point $z = (0, 1, 1)$. In the full-view case, a ramification point can be apparently detected at $z_0 = (-0.3, 0, 0)$, as shown by the three plane sections $x_1 = -0.3$, $x_2 = 0$ and $x_3 = 0$ represented in panels (a), (b) and (c) of Figure 3.10. In the aspect-limited case, a good candidate to be a ramification point is $z_0 = (0, 0.212, -0.212)$, as suggested by the three plane sections $x_1 = 0$, $x_2 = 0.212$ and $x_3 = -0.212$ plotted in panels (d), (e) and (f) of Figure 3.10. Note that, although the exterior sampling point is the same in the full-view and in the aspect-limited configurations, there is a priori no reason why the ramification point (or points) should be the same for both cases.

In our framework, the role played by ramification points can be formalized as follows.

Definition 3.2.2. *Let $u \in C^{1,\alpha}(\mathbb{R}^3 \setminus D)$ be a radiating solution of the Helmholtz equation in $\mathbb{R}^3 \setminus \bar{D}$, and $z_0 \in \partial D$ a ramification point for the flow lines of u. Let $I \subset \mathbb{R}$ be a set of indices, and denote a flow line of u starting from z_0 as $\tilde{\zeta}^i_{z_0}(\tau)$, for $i \in I$ (and $\tau \geq 0$). Consider the set (of images) of all flow lines $\left\{\zeta^i_{z_0}\right\}_{i\in I}$ and the ball $B(z_0, r) := \{x \in \mathbb{R}^3 : |x - z_0| < r\}$, with $r > 0$. Assume that there exists $I' \subset I$ such that $T_{z_0}(I') := \left\{\zeta^i_{z_0}\right\}_{i\in I'}$ is a regular flow tube with degeneracy in z_0, i.e., $T_{z_0}(I') \setminus [T_{z_0}(I') \cap B(z_0, r)]$ is regular (in the sense of Definition 3.2.1) for each $r < r_0$, being $r_0 > 0$ small enough. Then, the field u is called 'partially pseudo-radial' with respect to z_0. Moreover, let $|W_\infty(z_0, I')| > 0$ be the asymptotic angular width of each possible $T_{z_0}(I')$: then, the quantity $|W_\infty(z_0)| := \sup_{I'} |W_\infty(z_0, I')|$ is called the 'asymptotic angular width' of the beam of flow lines starting from z_0.*

We now have all the elements to pursue our physical approach to the LSM in the case of $z \notin D$. The first step consists in a preliminary result, analogous to Theorem 3.2.4, but much simpler to be proved.

Theorem 3.2.6. *Given $z^* \in \partial D$, define $\Omega(z^*, r) := \{x \in \mathbb{R}^3 : |x - z^*| = r\}$ and $\tilde{\Omega}(z^*, r) := \Omega(z^*, r) \cap (\mathbb{R}^3 \setminus D)$; moreover, let $\tilde{\Omega}'(z^*, r)$ be an open and connected subset of $\tilde{\Omega}(z^*, r)$. Then, there cannot exist $g \in L^2(\Omega)$ such that the flux across $\tilde{\Omega}'(z^*, r)$ of the corresponding scattered field p^s_g, defined analogously to (3.33), is bounded from below as $r \to 0$, i.e., such that $\liminf_{r\to 0} \mathcal{F}_{\tilde{\Omega}'(z^*,r)}\left(p^s_g\right) = c > 0$.*

Proof. Assume, by contradiction, that such a $g \in L^2(\Omega)$ exists. Similarly to the proof of Theorem 3.2.4 (cf. relation (3.69)) and by applying the mean-value theorem for integration, we can bound the flux under exam as follows:

$$\left|\mathcal{F}_{\tilde{\Omega}'(z^*,r)}(p^s_g)\right| \leq \frac{1}{2\omega\rho_0} \int\limits_{\tilde{\Omega}'(z^*,r)} \left|\bar{p}^s_g(x)\frac{\partial p^s_g}{\partial \nu}(x)\right| d\sigma(x) = \frac{\left|\tilde{\Omega}'(z^*, r)\right|}{2\omega\rho_0} |\bar{p}^s_g(\tilde{x}_r)| \cdot \left|\frac{\partial p^s_g}{\partial \nu}(\tilde{x}_r)\right|,$$

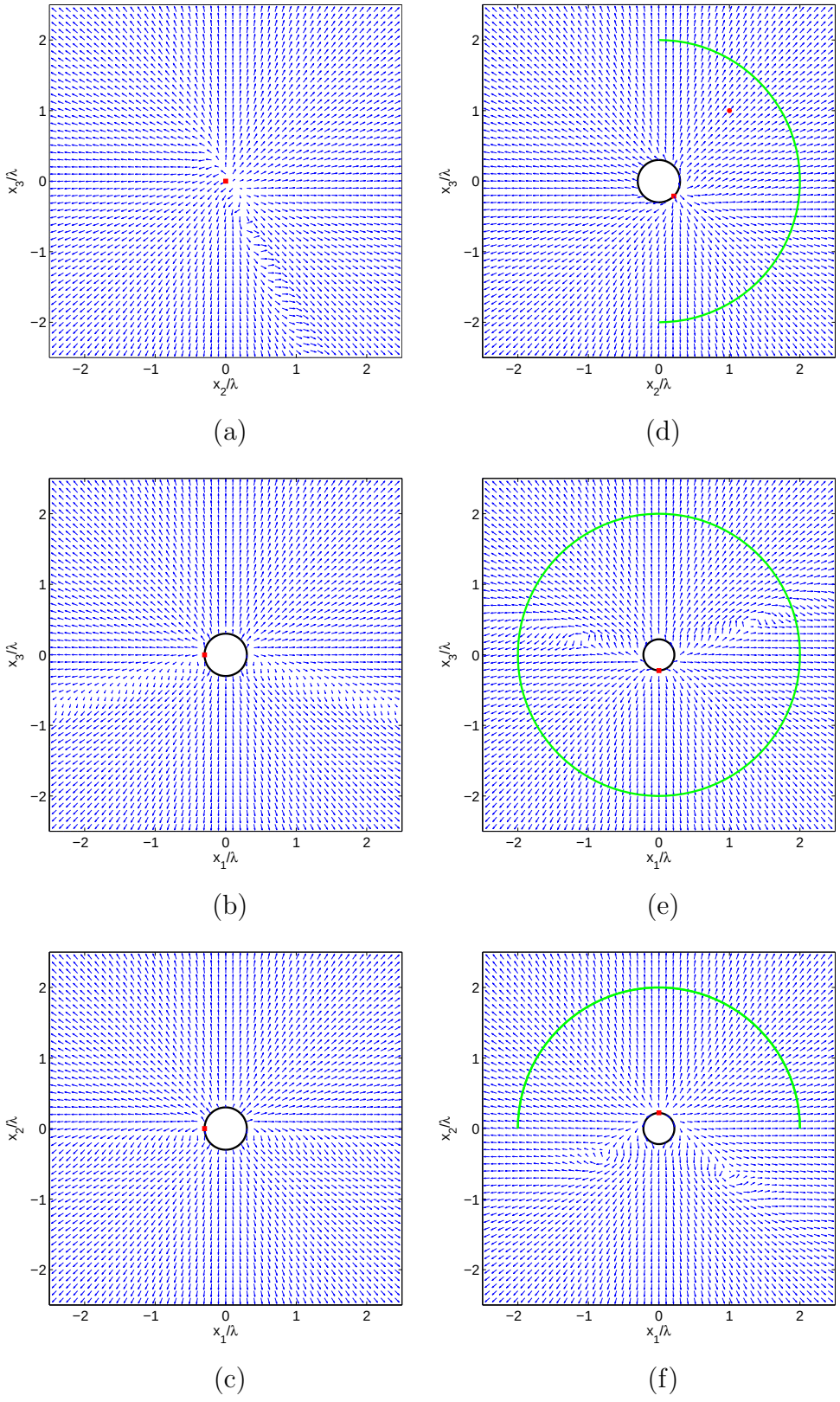

Figure 3.10: Qualitative behavior of the vector field $\mathcal{S}$ for a sampling point $z = (0, 1, 1)$ (red bullet) outside the sphere (black contour): a ramification point (red square box) is detectable on the boundary of the scatterer. Full-view configuration of antennas: (a) plane section $x_1 = -0.3$; (b) plane section $x_2 = 0$; (c) plane section $x_3 = 0$. Aspect-limited configuration of antennas: (d) plane section $x_1 = 0$; (e) plane section $x_2 = 0.212$; (f) plane section $x_3 = -0.212$.

where $\tilde{x}_r$ is an appropriate point of $\tilde{\Omega}'(z^*, r)$. It is clear that $\left|\tilde{\Omega}'(z^*, r)\right| \to 0$ and $|\tilde{x}_r - z^*| \to 0$ as $r \to 0$: then, the continuity of p_g^s and $\frac{\partial p_g^s}{\partial \nu}$ in $\mathbb{R}^3 \setminus D$ implies that the flux vanishes, i.e., $\lim_{r\to 0} \mathcal{F}_{\tilde{\Omega}'(z^*,r)}\left(p_g^s\right) = 0$, in contradiction with the positive lower boundedness condition for $\mathcal{F}_{\tilde{\Omega}'(z^*,r)}\left(p_g^s\right)$. □

Like Theorem 3.2.4, also Theorem 3.2.6 holds for the aspect-limited case, provided that a function $g \in L^2(\Omega^i)$ is considered and the integration domain Ω in (3.33) is replaced by Ω^i.

In analogy with Theorem 3.2.5, the second step consists in showing how the far-field equation and the pseudo-radiality of the scattered field allow applying Theorem 3.2.6.

Theorem 3.2.7. *Let $z \in \mathbb{R}^3 \setminus D$: if $\varepsilon > 0$ is small enough, there cannot exist $g_z^\varepsilon \in L^2(\Omega)$ such that $\|Fg_z^\varepsilon - \Phi_\infty(\cdot, z)\|_{L^2(\Omega)} \leq \varepsilon$ and the scattered field $p_z^{s,\varepsilon}$ is partially pseudo-radial with respect to some point $z_0 \in \partial D$.*

Proof. Assume, by contradiction, that such a $g_z^\varepsilon \in L^2(\Omega)$ exists, and define $\Omega(z_0, r) := \{x \in \mathbb{R}^3 : |x - z_0| = r\}$, $\tilde{\Omega}(z_0, r) := \Omega(z_0, r) \cap (\mathbb{R}^3 \setminus D)$ and $\tilde{\Omega}'(z_0, r) := \tilde{\Omega}(z_0, r) \cap T_{z_0}(I')$, where I' and $T_{z_0}(I')$ are as in Definition 3.2.2. By the same argument justifying relations (3.70), we have

$$\begin{aligned}\mathcal{F}_{\tilde{\Omega}'(z_0,r)}\left(p_z^{s,\varepsilon}\right) &= \frac{1}{4\mathrm{i}\omega\,\rho_0} \int\limits_{\tilde{\Omega}'(z_0,r)} \left[\bar{p}_z^{s,\varepsilon} \frac{\partial p_z^{s,\varepsilon}}{\partial \nu} - p_z^{s,\varepsilon} \frac{\partial \bar{p}_z^{s,\varepsilon}}{\partial \nu}\right](x)\, d\sigma(x) \geq \\ &\geq \frac{k}{2\omega\,\rho_0} \left\{\|\Phi_\infty(\cdot, z)\|^2_{L^2[W_\infty(z_0,I')]} - \varepsilon'[W_\infty(z_0, I')]\right\}, \end{aligned} \tag{3.73}$$

whence

$$\liminf_{r\to 0} \mathcal{F}_{\tilde{\Omega}'(z_0,r)}\left(p_z^{s,\varepsilon}\right) \geq \frac{k}{2\omega\,\rho_0} \left\{\|\Phi_\infty(\cdot, z)\|^2_{L^2[W_\infty(z_0,I')]} - \varepsilon'[W_\infty(z_0, I')]\right\}. \tag{3.74}$$

Since $|W_\infty(z_0, I')| > 0$, we can proceed as from (3.71) to (3.72), and make the right-hand side of (3.74) positive by choosing $\varepsilon > 0$ such that

$$0 < \varepsilon < (\sqrt{2} - 1)\, \|\Phi_\infty(\cdot, z^*)\|_{L^2[W_\infty(z_0,I')]} = (\sqrt{2} - 1) \frac{\sqrt{|W_\infty(z_0, I')|}}{4\pi}. \tag{3.75}$$

Incidentally, we note that, according to Definition 3.2.2, an upper bound for $|W_\infty(z_0, I')|$ is given by the asymptotic angular width $|W_\infty(z_0)|$. We can now apply Theorem 3.2.6 to conclude the proof with the desired contradiction. □

Remark 3.2.4. As in Remark 3.2.2, let us now focus on Tikhonov regularized solutions. In this case, Theorem 3.2.6 states that, for $z \notin D$, the pseudo-radiality of the scattered field is incompatible with a discrepancy $d_{\alpha^*(z)} \leq \varepsilon$, if ε verifies bound (3.75). This incompatibility means that $g_{\alpha^*(z)}$ cannot belong to $L^2(\Omega)$, i.e., $\left\|g_{\alpha^*(z)}\right\|_{L^2(\Omega)} \to \infty$, which can only happen if $\alpha^*(z) \to 0^+$, in agreement with limit (3.36)(a). Again, this is consistent with numerical simulations [46], which show that the values of $\alpha^*(z)$ are much smaller for $z \notin D$ than for $z \in D$.

Remark 3.2.5. As in Remark 3.2.3, we point out that Theorem 3.2.7 can be easily adapted to the aspect-limited case, by requiring, in particular, that $W_\infty(z_0, I') \subset \Omega^o$.

3.2.8. Conclusions and further developments

We have presented an approach to the LSM based on the conservation of energy inside the flow tubes of the scattered field. In this framework, a) the far-field equation expresses a constraint on the power flux of the scattered field in the far-field region; b) under appropriate assumptions (suggested by numerical simulations) on the flow tubes carrying this flux, the information contained in the far-field constraint is propagated throughout the background up to the boundary of the scatterer; c) the approximate fulfilment of this constraint forces the L^2-norm of any ε-approximate solution of the far-field equation to behave as a good indicator function for visualizing the shape and location of the scatterer.

Possible future developments of our approach are concerned with both theoretical and numerical issues. From the former viewpoint, we can mention the case of lossy and inhomogeneous backgrounds with near-field measurements, but the key-problem is clearly to predict the behavior of flow lines starting from the knowledge of the geometrical and material properties of the scatterer: achieving such a goal is the only way for making our physical approach a mathematical justification of the LSM, and seems to require tools and results in topological dynamics [1]. As far as numerics is concerned, it would be interesting to observe the behavior of flow lines for more complex scattering situations than those considered here: a starting point is, of course, a 3D direct code for penetrable and impenetrable scatterers.

3.2.9. Appendix: A minimum property for cones inscribed in a half-sphere

As usual, we denote by (x_1, x_2, x_3) and (r, θ, φ) the Cartesian and spherical coordinates in $\mathbb{R}^3$, respectively.

Theorem 3.2.8. *Let $\bar{B} := \{x \in \mathbb{R}^3 : |x| \leq 1\}$, $\tau := \{x \in \mathbb{R}^3 : x_3 = 0\}$ and $C := \bar{B} \cap \tau$. Let P be a point on $\Omega = \partial\bar{B}$ and let us consider the solid angle $\hat{P}$ identified by the cone of vertex P and basis C. Then, the amplitude $|\hat{P}|$ of the solid angle $\hat{P}$ is minimum when the cone is right, i.e., when $x_3(P) = 1$.*

Proof. In general, the amplitude $|\hat{P}_\Sigma|$ of the solid angle $\hat{P}_\Sigma$ subtended by a surface Σ when observed by a point $P \notin \Sigma$ is given by the formula (see e.g. [79]):

$$|\hat{P}_\Sigma| = \int_\Sigma \frac{\vec{s} \cdot \hat{n}}{s^3}\, d\sigma, \tag{3.76}$$

where, if Q denotes a generic point of Σ, $\vec{s} := \overrightarrow{PQ}$, $s = |\vec{s}|$, $\hat{n} = \hat{n}(Q)$ is the unit normal in Q to Σ and $d\sigma = d\sigma(Q)$ is the surface element on Σ. In our case, the most natural choice for Σ would be C; however, analytical computations are simpler by choosing the lower half sphere, i.e., $\Sigma = \Omega_- := \{x \in \mathbb{R}^3 : |x| = 1 \wedge x_3 \leq 0\}$.

Of course, we have $r(P) = 1$, while, by symmetry, it is not restrictive to assume that $\theta(P) \in [0, \pi/2)$ and $\varphi(P) = 0$ (the case $\theta(P) = \pi/2$ will be discussed separately). In the following, we shall set $\theta_P := \theta(P)$ and denote with (r, θ, φ) the spherical coordinates of the generic point $Q \in \Omega_-$. Then, the vectors $\vec{s}$ and $\hat{n}$ can be expressed in Cartesian components as $\vec{s} = (\sin\theta\cos\varphi - \sin\theta_P, \sin\theta\sin\varphi, \cos\theta - \cos\theta_P)$ and $\hat{n} = (\sin\theta\cos\varphi, \sin\theta\sin\varphi, \cos\theta)$. Inserting these representations into (3.76), with the identifications $\Sigma = \Omega_-$ and $\hat{P} = \hat{P}_{\Omega_-}$, we find

$$f(\theta_P) := |\hat{P}|(\theta_P) = \frac{1}{2\sqrt{2}} \int_{\frac{\pi}{2}}^{\pi} \sin\theta \left[\int_0^{2\pi} \frac{d\varphi}{\sqrt{1 - \sin\theta\cos\varphi\sin\theta_P - \cos\theta\cos\theta_P}} \right] d\theta. \tag{3.77}$$

It is easy to verify that $f(0) = 2\pi\left(1 - \frac{\sqrt{2}}{2}\right)$, a well-known result concerning right cones. We now want to show that $f(0)$ is the minimum amplitude of the solid angle $\hat{P}$. To this end, we shall compute f' and show that $f'(\theta_P) \geq 0 \ \forall \theta_P \in [0, \pi/2)$. Since it is possible to prove that the derivation operator $\frac{d}{d\theta_P}$ can be brought inside the integrals (as a consequence of Lebesgue's dominated convergence theorem and Lagrange's mean value theorem), we have

$$f'(\theta_P) = \frac{1}{4\sqrt{2}} \int_{\frac{\pi}{2}}^{\pi} \sin\theta \left[\int_0^{2\pi} \frac{\sin\theta\cos\varphi\cos\theta_P - \cos\theta\sin\theta_P}{\sqrt{(1 - \sin\theta\cos\varphi\sin\theta_P - \cos\theta\cos\theta_P)^3}} d\varphi \right] d\theta. \tag{3.78}$$

Then, it suffices to prove that the internal integral in $d\varphi$ is non-negative for each $\theta_P \in [0, \pi/2)$ and $\theta \in [\pi/2, \pi]$. To this end, we put $a := \sin\theta\cos\theta_P \geq 0$, $b := -\cos\theta\sin\theta_P \geq 0$, $c := 1 - \cos\theta\cos\theta_P \geq 1$ and $d := \sin\theta\sin\theta_P \geq 0$, where the inequalities follows from the ranges of θ_P and θ. With these notations, the integrand function can be written as

$$g(\varphi) := \frac{a\cos\varphi + b}{\sqrt{(c - d\cos\varphi)^3}}, \tag{3.79}$$

and we want to prove that $\int_0^{2\pi} g(\varphi)d\varphi \geq 0$.

If $a > 0$, we put $\varphi_1 := \arccos(b/a)$, $\varphi_2 := \arccos(-b/a)$, $\varphi_3 := \varphi_1 + \pi$ and $\varphi_4 := \varphi_2 + \pi$. Then, easy computations show that if $a = 0$, then $g(\varphi) \geq 0 \ \forall \varphi \in [0, 2\pi]$; instead, if $a > 0$, we have $g(\varphi) \geq 0 \ \forall \varphi \in [0, \varphi_2] \cup [\varphi_3, 2\pi]$. Moreover, for $a > 0$, the following relations hold:

1) $g(\varphi) \geq |g(\varphi + \pi)| \ \forall \varphi \in [0, \varphi_1] \Longrightarrow \int_0^{\varphi_1} g(\varphi)d\varphi - \int_{\pi}^{\varphi_3} |g(\varphi)|d\varphi \geq 0$;

2) $g(\varphi) \geq |g(\varphi - \pi)| \ \forall \varphi \in [\varphi_4, 2\pi] \Longrightarrow \int_{\varphi_4}^{2\pi} g(\varphi)d\varphi - \int_{\varphi_2}^{\pi} |g(\varphi)|d\varphi \geq 0$.

By summing the two last inequalities and remembering that $g(\varphi) \leq 0 \ \forall \varphi \in [\varphi_2, \varphi_3]$, we find that

$$\int_0^{\varphi_1} g(\varphi)d\varphi + \int_{\varphi_2}^{\varphi_3} g(\varphi)d\varphi + \int_{\varphi_4}^{2\pi} g(\varphi)d\varphi \geq 0. \tag{3.80}$$

On the other hand, we already know that $g(\varphi) \geq 0 \ \forall \varphi \in [\varphi_1, \varphi_2] \cup [\varphi_3, \varphi_4]$, and then

$$\int_{\varphi_1}^{\varphi_2} g(\varphi)d\varphi + \int_{\varphi_3}^{\varphi_4} g(\varphi)d\varphi \geq 0. \tag{3.81}$$

Inequalities (3.80) and (3.81) together allows concluding that $\int_0^{2\pi} g(\varphi)d\varphi \geq 0$, as claimed. Summing up, we have proved that $f'(\theta_P) \geq 0 \ \forall \theta_P \in [0, \pi/2)$: in particular, by putting $\theta_P = 0$ in (3.78), we get $f'(0) = 0$, as it needs to be by symmetry.

In the case $\theta_P = \pi/2$, the cone of basis C and vertex P is clearly degenerate. We shall not discuss how the solid angle $\hat{P}$ can be defined in this case: for our purposes, it suffices to observe that any meaningful (i.e., not merely conventional) definition should be obtained by continuity as a limit case for $\theta_P \to \pi/2$: in particular, it must hold $f(\pi/2) = \liminf_{\theta_P \to (\pi/2)^+} f(\theta_P)$. Since f is non-decreasing in $[0, \pi/2)$, we can conclude that $f(0) \leq f(\theta_P) \ \forall \theta_P \in [0, \pi/2]$.

Although unnecessary for our purposes, we finally observe that the previous proof can be easily refined in order to prove that $f'(\theta_P) > 0$ for $\theta_P \in (0, \pi/2)$: hence $\theta_P = 0$ is a proper minimum point for f. □

CHAPTER 4

On the use of the linear sampling method for quantitative inverse scattering

Acoustical or electromagnetic scattering is a physical phenomenon where an incident wave is scattered by an inhomogeneity and the total field at any point is represented by the sum of the incident and the scattered field. From a mathematical viewpoint, in the direct problem the physical parameters and the geometry of the inhomogeneity are given and the unknown is represented by the scattered field. In the inverse scattering problem, one aims at recovering the shape and physical properties of the object of interest from measurements of the scattered field. The direct scattering problem is in general well-posed in the sense of Hadamard and therefore its approximate solution can be determined by means of stable numerical methods. On the contrary, the inverse scattering problem is ill-posed in the sense of Hadamard (specifically, the operator mapping the unknown physical parameters characterizing the inhomogeneity onto the measured scattered field is compact) and its solution must be addressed by means of some regularizing approach [41].

Most inverse scattering methods belong to two different sets of algorithms: the family of qualitative approaches and the family of quantitative approaches. Qualitative methods [23] require the regularized solution of one-parameter family of linear integral equations of the first kind. More specifically, in these approaches the support of the scatterer is characterized by the set of parameter values for which the linear integral equation can be (exactly or approximately) solved. The advantages of qualitative methods are that they are rather fast and need very few a priori information to work. On the other hand, the output information is rather poor since they are essentially visualization techniques and do not provide quantitative reconstructions of the inhomogeneity. Quantitative inverse scattering methods [41, 12] are iterative schemes that start from some initialization map of the refractive index of the scatterer and reconstruct its point values after an optimized number of iterations. In principle they can provide all required information on the problem although by means of a notable computational effort. Further, they

can suffer local minima problems, since the number of unknowns is impressively larger than the data amount typically at disposal in scattering experiments or because often the initialization of the method is not sufficiently precise for a proper convergence to the solution.

The effectiveness of a quantitative method can be consistently increased by incorporating into the minimization process the a priori information on the scatterer that one has at disposal. Although the most traditional way is to use this information to initialize the method, an improvement in its performances can be achieved when such an information is integrated inside the minimization process, for example, by decreasing the complexity of the target [52], or by guiding the iterative process through a plug in of the information into the choice of the minimization technique.

Recent trends in inverse scattering are interested in the formulation of hybrid methods, where a priori information on the inhomogeneous background surrounding the inhomogeneity of interest and qualitative techniques are utilized in order to decrease the number of unknowns to be determined by means of some quantitative method [69, 19]. In fact, since the main goal of qualitative methods is to highlight the presence and the shape of an inhomogeneity inside a background, it is possible to perform the quantitative process only on the pixels individuated by the qualitative technique. Moreover, recent developments in qualitative inverse scattering proof that qualitative methods are even able to provide constant estimates [56, 57] on the refractive index by exploiting their capability in retrieving the so called transmission eigenvalues of the scatterer. And these estimates can be, for example, utilized as an initialization estimate of the refractive index for quantitative methods.

This chapter is dedicated to an analysis of the use of qualitative methods as a tool for reducing the complexity of a problem that has to be solved through quantitative techniques. More precisely, the first section is dedicated to the description of a hybrid method based on the implementation of a quantitative technique inspired by the so-called *inhomogeneous Lippmann-Schwinger equation*; then, in the second section, a method able to provide constant estimates on the refractive index of the scatterer from the knowledge of the smallest transmission eigenvalue will be proposed. In both sections, theoretical and computational tools will be analyzed and qualitative and quantitative techniques will be as well resumed.

4.1. A hybrid method for the focused reconstruction of buried objects

This section basically presents the arguments of [55]. More precisely, the aim of the section is to describe a rather general strategy for the formulation of hybrid techniques, based on the following three steps:

1. the information on the physical characteristics of the background are coded in the corresponding Green's function;

2. a segmentation between the background and the unknown is realized by applying a qualitative method, thus decreasing the number of degrees of freedom of the problem;

3. a quantitative method is applied only in the region highlighted by the qualitative method (i.e. previous step), in order to reconstruct the point values of the refractive index in the unknown region.

Although this scheme is of fully general applicability, in this section we present a specific application of the scheme: more precisely, the information on the background is obtained from other imaging modalities and the Green's function is numerically computed by means of a method of moments [59, 88] that solves the forward scattering problem. Then the linear sampling method [28] is applied in its near-field formulation for inhomogeneous backgrounds, in order to visualize the scatterer of interest and an active contour based procedure [32] is used for extracting the shape of its support. Finally, the inverse scattering problem is solved by applying the contrast source inversion method [104] to the Lippmann-Schwinger equation with inhomogeneous background.

The plan of the section is as follows: in Section 4.1.1, with the arguments of [41], we resume the proof of equivalence between differential and integral formulation for the scattering problem of a scatterer embedded in a homogeneous background. In Section 4.1.2 we set up the scattering problem of a scatterer buried in an inhomogeneous background and provide a rather general deduction of an integral formulation associated to the differential scattering problem. In Section 4.1.3 we recall the formulation of the linear sampling method in the near-field case and provide the formulation of the contrast source inversion method in the general case of the inhomogeneous Lippmann-Schwinger equation. Finally, in Section 4.1.4 some numerical examples are described, also including an application to medical imaging.

4.1.1. The homogeneous Lippmann-Schwinger equation

Let consider the scattering problem associated to a scatterer of refractive index n embedded in the vacuum

$$\Delta u + nu = 0 \qquad \mathbb{R}^2 \tag{4.1}$$

$$u = u^i + u^s \qquad \mathbb{R}^2 \tag{4.2}$$

$$\lim_{r\to\infty}(\frac{\partial u^s}{\partial r} - iku^s) = 0 \tag{4.3}$$

where we suppose that $n \in C^1(\mathbb{R}^2)$, that $m := 1 - n$ has compact support D and that $Re(n(x)) > 1$ and $Im(n(x)) \geq 0$ for each $x \in R^2$.

Definition 4.1.1. *For each $\varphi \in C_0^0(\mathbb{R}^2)$, we define as volume potential*

$$w(x) := \int_{\mathbb{R}^2} \varphi(y)\Phi(x,y)dy \qquad x \in \mathbb{R}^2 \tag{4.4}$$

and as fundamental solution to the Helmholtz equation

$$\Phi(x,y) := \frac{1}{4\pi}\frac{e^{ik|x-y|}}{|x-y|} \qquad x \neq y. \tag{4.5}$$

Following the arguments of [41], it is possible to state the following theorem.

Theorem 4.1.1. *The volume potential w exists as an improper integral for all $x \in \mathbb{R}^2$ and has the following properties:*

- *if $\varphi \in C_0^0(\mathbb{R}^2)$, then $w \in C^{1,\alpha}(R^2)$ and the orders of differentiation and integration can be interchanged;*
- *if $\varphi \in C_0^0(\mathbb{R}^2) \cap \mathbb{C}^{0,\alpha}(\mathbb{R}^2)$, then $w \in C^{2,\alpha}(\mathbb{R}^2)$ and $\Delta w + k^2 w = -\varphi$ in $\mathbb{R}^2$;*
- *for some positive constant C depending on the support of φ we have $\|w\|_{2,\alpha,\mathbb{R}^2} \leq C\|\varphi\|_{0,\alpha,\mathbb{R}^2}$ with $\|\cdot\|_{p,\alpha,\mathbb{R}^2}$ norm of $\mathbb{C}^{p,\alpha}(\mathbb{R}^2)$;*
- *if $\varphi \in C_0^0(\mathbb{R}^2) \cap C^{1,\alpha}(\mathbb{R}^2)$, then $w \in C^{3,\alpha}(\mathbb{R}^2)$.*

Moreover, given two bounded domains D and G, the volume potential

$$(V\varphi)(x) := \int_D \varphi(y)\Phi(x,y)dy \qquad x \in \mathbb{R}^2 \tag{4.6}$$

defines a bounded operator $V : L^2(D) \to H^2(G)$.

Before providing an integral formulation equivalent to (4.1)-(4.3) we recall some classic tools: if D is a bounded domain of class C^1 and ν denotes the unit normal vector to the boundary ∂D directed into the exterior of D, then we have the *Green's formulas*

$$\int_D [u\Delta v + \nabla u \cdot \nabla v]dx = \int_{\partial D} u\frac{\partial v}{\partial \nu}ds \quad \text{for } u \in C^1(\bar{D}), v \in C^2(\bar{D}) \tag{4.7}$$

$$\int_D [u\Delta v - v\Delta u]dx = \int_{\partial D} [u\frac{\partial v}{\partial \nu} - v\frac{\partial u}{\partial \nu}]ds \qquad \text{for } u, v \in C^2(\bar{D}). \tag{4.8}$$

Theorem 4.1.2. *If $u \in C^2(R^2)$ is a solution of (4.1)-(4.3), then u is a solution of the homogeneous Lippmann-Schwinger equation*

$$u(x) = u^i(x) - k^2 \int_D \Phi(x, y)m(y)u(y)dy \tag{4.9}$$

for each $x \in \mathbb{R}^2$. Conversely, if $u \in C^0(\mathbb{R}^2)$ is a solution of (4.9), then $u \in C^2(\mathbb{R}^2)$ and u is a solution of (4.1)-(4.3).

Proof. Let $u \in C^2(\mathbb{R}^2)$ solution to (4.1)-(4.3). Let $x \in \mathbb{R}^2$ be an arbitrary point and B an open ball with exterior unit normal ν containing the support of m and such that $x \in B$. Since $\Delta u + k^2 u = mk^2 u$ we have that, from Green's formulas,

$$u(x) = \int_{\partial B} [\Phi(x, y)\frac{\partial u}{\partial \nu}(y) - u(y)\frac{\partial \Phi(x, y)}{\partial \nu}]ds(y) - \int_B \Phi(x, y)m(y)u(y)dy. \tag{4.10}$$

Applying Green's formulas to u^i we have that

$$u^i(x) = \int_{\partial B} [\Phi(x, y)\frac{\partial u^i}{\partial \nu}(y) - u^i(y)\frac{\partial \Phi(x, y)}{\partial \nu}]ds(y). \tag{4.11}$$

Using again Green's formulas and exploiting the Sommerfeld radiation condition (4.3), we have that [41]

$$\int_{\partial B} [\Phi(x, y)\frac{\partial u^s}{\partial \nu}(y) - u^s(y)\frac{\partial \Phi(x, y)}{\partial \nu}]ds(y) = 0 \tag{4.12}$$

and then, by (4.2), that (4.9) is satisfied.

Let now suppose that $u \in C^1(\mathbb{R}^2)$ is a solution to (4.9) and let define u^s as

$$u^s(x) := -k^2 \int_D \Phi(x, y)m(y)u(y)dy \qquad x \in \mathbb{R}^2. \tag{4.13}$$

Since Φ satisfies (4.3) uniformly with respect to y on compact sets and m is compactly supported, it is possible to verify that u^s satisfies (4.3). Since $m \in C_0^1(\mathbb{R}^2)$, from (4.9) and Theorem 4.1.1 we have that $u^s \in C^2(\mathbb{R}^2)$ and $\Delta u^s + k^2 u^s = k^2 mu$. From $\Delta u^i + k^2 u^i = 0$ we have that

$$\Delta u + k^2 u = \Delta u^i + k^2 u^i + \Delta u^s + k^2 u^s = k^2 mu \tag{4.14}$$

which implies $\Delta u(x) + k^2 n(x)u(x) = 0$ for each $x \in \mathbb{R}^2$.

□

4.1.2. The inhomogeneous Lippmann-Schwinger equation

We consider a rather general two-dimensional and time-harmonic scattering problem whereby the background medium is inhomogeneous and described by a piecewise continuously differentiable refractive index [41, 42]

$$n_b(x) = \frac{1}{\varepsilon_0}\left[\varepsilon(x) + \mathrm{i}\frac{\sigma(x)}{\omega}\right]. \tag{4.15}$$

In (4.15), $\varepsilon_0 > 0$ is the electric permittivity of vacuum, $\varepsilon(x) \geq 1$ and $\sigma(x) \geq 0$ are the point values of the electric permittivity and conductivity, ω is the angular frequency, and $\mathrm{i} = \sqrt{-1}$. More precisely (see e.g. fig. 4.1), we assume that there exists a finite number of open and connected C^2-domains $\Lambda_i \subset \mathbb{R}^2$, with $i = 0, \ldots, N$, such that 1) $\Lambda_i \cap \Lambda_j = \emptyset$ for $i \neq j$; 2) $\mathbb{R}^2 = \cup_{i=0}^{N} \bar{\Lambda}_i$; 3) Λ_i is bounded for each $i \neq 0$; 4) $n_b|_{\Lambda_i} \in C^1(\bar{\Lambda}_i)$ for all $i = 0, \ldots, N$; 5) $n_b(x) = \tilde{n}_0 \in \mathbb{C}$ for $x \in \Lambda_0$, with $\mathrm{Im}\{\tilde{n}_0\} \geq 0$; 6) there exists a subset J_0 of the finite set $\{1, 2, \ldots, N\}$ such that $\tilde{\Lambda}_0 := \mathrm{int}\,\{x \in \mathbb{R}^2 : n_b(x) = \tilde{n}_0\} = \Lambda_0 \cup (\cup_{j \in J_0} \Lambda_j)$ (in particular, $J_0 = \emptyset$ if and only if $\tilde{\Lambda}_0 = \Lambda_0$). Finally, we assume that the magnetic permeability is constant in all $\mathbb{R}^2$. Note that the boundaries $\partial\Lambda_i$ are curves where a discontinuity of n_b might occur, but, in our framework, some of the domains Λ_i are chosen *a priori*, even inside a homogeneous region, just to host a scatterer that will be introduced later: this trick allows some notational simplifications. Finally, we define the open and possibly non-connected subset $\tilde{\Lambda}_0 := \mathrm{int}\,\{x \in \mathbb{R}^2 : n_b(x) = \tilde{n}_0\} \supset \Lambda_0$.

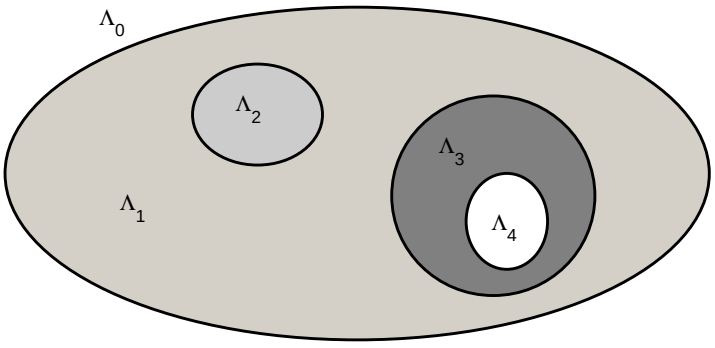

Figure 4.1: Scheme of the reference background for the scattering problem. In this case, $\tilde{\Lambda}_0 = \Lambda_0 \cup \Lambda_4$.

Next, we define the Green's function $G(x, y)$ of the background as the radiating solution of the equation [42]

$$\Delta_x G(x, y) + k^2 n_b(x)\, G(x, y) = -\delta(x - y) \quad \text{for} \quad x \in \mathbb{R}^2, \tag{4.16}$$

where $k = \omega/c$ is the wave number in vacuum, c being the speed of light in free space. The existence and uniqueness of $G(x, y)$ (at least for $y \in \tilde{\Lambda}_0$) can be proved as in [42]: in fact, if we denote the Green's function of the outmost medium by $\Phi(x, y) = \frac{\mathrm{i}}{4} H_0^{(1)}(\tilde{k}_0 \, |x - y|)$, where $H_0^{(1)}$ is the Hankel function of first kind of order zero, $\tilde{k}_0 := k\sqrt{\tilde{n}_0}$ and $\mathrm{Im}\{\sqrt{\tilde{n}_0}\} \geq 0$, we can write

$$G(x, y) = \Phi(x, y) + u_b^s(x, y), \tag{4.17}$$

where $u_b^s(x, y)$ is the perturbation to $\Phi(x, y)$ due to the inhomogeneous medium.

In our problem, the scatterer is assumed to take up the spatial region $D = \cup_{i=1}^{M} \Lambda_i$, with $1 \leq M \leq N$; accordingly, the whole propagation medium is described by a refractive index $n(x)$ such that, in general, $n(x) \neq n_b(x)$ for $x \in \Lambda_i$, with $i = 1, \ldots, M$. In any case, we still require that $n|_{\Lambda_i} \in C^1(\bar{\Lambda}_i)$ for all $i = 0, \ldots, N$. Moreover, for a unit point source placed at $x_0 \in \tilde{\Lambda}_0 \setminus \overline{(\tilde{\Lambda}_0 \cap D)}$, we denote by $u(x, x_0)$ the non-zero component of the total electric field, which vibrates perpendicularly to the scattering plane. Then, the differential form of the scattering problem we are interested in is [42]

$$\begin{cases} \Delta_x u(x, x_0) + k^2 n(x)\, u(x, x_0) = -\delta(x - x_0) \qquad \text{for} \quad x \in \mathbb{R}^2 & \text{(a)} \\ u(x, x_0) = u^i(x, x_0) + u^s(x, x_0) & \text{(b)} \\ \lim\limits_{r \to \infty} \left[\sqrt{r} \left(\dfrac{\partial u^s}{\partial r} - \mathrm{i}\, \mathrm{Re}\{\tilde{k}_0\} u^s \right) \right] = 0, & \text{(c)} \end{cases} \tag{4.18}$$

where $u^i(x, x_0) = G(x, x_0)$ is the incident field, $u^s(x, x_0)$ is the scattered field and (4.18)(c) is the Sommerfeld radiation condition, which holds uniformly in all directions $\hat{x} = x/|x|$. If $\mathrm{Im}\{\tilde{n}_0\} > 0$, such a condition can be relaxed [42] by only requiring the boundedness of $u^s(\cdot, x_0)$ in $\mathbb{R}^2$.

It is worth pointing out that eq. (4.18)(a) is to be understood as a set of $N + 1$ equations, one for each domain Λ_i, with $i = 0, \ldots, N$, linked by proper transmission conditions at the boundaries $\partial\Lambda_i$. These conditions are expressed by the continuity of the tangential components of both the total electric field E and the magnetic field H: from the time-harmonic Maxwell equations and the assumption that the magnetic permeability is constant in $\mathbb{R}^2$, it is easily seen that this amounts to the continuity of u and $\frac{\partial u}{\partial \nu}$, where ν is the normal at a point of $\partial\Lambda_i$. Since the same conditions hold for the incident field (which is the total field in absence of the scatterer), we can look for a solution $u^s(\cdot, x_0)$ to problem (4.18) such that $u^s(\cdot, x_0) \in C^1(\mathbb{R}^2)$ and $\Delta u^s(\cdot, x_0) \in C^0\left(\bar{\Lambda}_i\right)$ for all $i = 0, \ldots, N$. Again, the existence and uniqueness of such a solution can be proved by paralleling arguments contained in [41, 42].

The goal of the present section is to derive an integral equation for the scattered field $u^s(\cdot, x_0)$ from the differential formulation (4.18) of our scattering problem. The natural candidate for an integral formulation is the 'generalized' Lippmann-Schwinger equation

$$u^s(x, x_0) = -\tilde{k}_0^2 \int_{\mathbb{R}^2} G(x, y) m(y) u(y, x_0)\, dy, \tag{4.19}$$

where $m(x) := [n_b(x) - n(x)]/\tilde{n}_0$ (note that $\operatorname{supp} m$ coincides with the support $\bar{D}$ of the scatterer, and is therefore compact). In fact, an exact equivalence between differential and integral formulation is proved in [41] for the three-dimensional acoustic and electromagnetic cases under strong regularity assumptions on the refractive index: the background is assumed to be homogeneous (i.e., $G(x,y) = \Phi(x,y)$ and $n_b \equiv \tilde{n}_0 \in \mathbb{C}$), and n must be continuously differentiable on the whole space. In particular, under such assumptions, this proof can provide a rigorous justification of the following heuristic procedure: compute $\Delta_x u^s(x, x_0)$ by interchanging the Laplacian operator with the integral in (4.19), then substitute

$$\Delta_x \Phi(x,y) = -\tilde{k}_0^2 \Phi(x,y) - \delta(x-y) \tag{4.20}$$

into (4.19) to obtain

$$\Delta_x u^s(x,x_0) + \tilde{k}_0^2 u^s(x,x_0) = -[-\tilde{k}_0^2 m(x) u(x,x_0)]. \tag{4.21}$$

Eq. (4.21) suggests regarding the term in square brackets at its right-hand side as an equivalent, although unknown, source radiating the field $u^s(x,x_0)$ in the background, which is consistent with the physical interpretation of (4.19). In any case, by means of eq.s (4.20) and (4.21), it is easily verified that u^s, as given by (4.19), solves problem (4.18).

However, as correctly pointed out in [74], even a mere discontinuity of the physical parameters at the interface between the scatterer and the (homogeneous) background suffices to invalidate the previous procedure: as a consequence, even with a homogeneous background, the integral formulation becomes more complicated (owing to boundary terms on $\partial\Lambda_i$) and its equivalence with the differential formulation is more difficult to prove.

To our knowledge, equivalence results for the two formulations are not available when the background is inhomogeneous. In this section, we shall limit ourselves to deriving the integral equation (4.19) (for $x \in \tilde{\Lambda}_0$) from the differential problem (4.18): indeed, a thorough discussion of the equivalence between (4.19) and (4.18) would be very technical and beyond the framework of this work. However, it is likely that an exact equivalence actually holds, since, as recalled above, the scattered field u^s is in $C^1(\mathbb{R}^2)$: then, the boundary contributions on each $\partial\Lambda_i$ that would appear in (4.19) from Green's second theorem [41] applied in each domain Λ_i cancel out, as detailed in the following Lemma 4.1.3 and Theorem 4.1.4.

Finally, it is worth noting that, even in two dimensions, the previous argument fails [74] whenever the magnetic permeability is discontinuous across $\partial\Lambda_i$. This is analogous to what happens in the two or three-dimensional acoustic case [74], where the pressure field is continuous across the discontinuities of the fluid density, but not continuously differentiable.

Lemma 4.1.3. *Let Λ_i (with $i = 0, \dots, N$), $n_b(x)$, $G(x,y)$ be as above, let $B_R = \{x \in \mathbb{R}^2 : |x| < R\}$ be such that $B_R \supset \cup_{i=1}^N \bar{\Lambda}_i$, and define $\Lambda_{N+1} = B_R \setminus \cup_{i=1}^N \bar{\Lambda}_i$. Moreover, let $w \in C^1(\bar{B}_R)$ be such that $\Delta w \in C^0(\bar{\Lambda}_i)$ for all $i = 1, \dots, N+1$. Then, the following generalization of Green's*

formula holds:

$$w(x) = \int_{\partial B_R} \left[\frac{\partial w}{\partial \nu}(y) G(y,x) - w(y)\frac{\partial G(y,x)}{\partial \nu(y)}\right] ds(y) + \\ - \int_{B_R} \left[\Delta w(y) + k^2 n_b(y) w(y)\right] G(y,x)\, dy \qquad \forall x \in B_R \cap \tilde{\Lambda}_0. \tag{4.22}$$

Proof. Consider an arbitrary point $x \in \Lambda_R := B_R \cap \tilde{\Lambda}_0$: since Λ_R is open, there exist $\rho > 0$ and a ball $B(x,\rho) = \{y \in \mathbb{R}^2 : |y - x| < \rho\}$ such that $\bar{B}(x,\rho) \subset \Lambda_R$. Moreover, $G(\cdot, x)$ solves a particular case of the differential problem (4.18), with the identifications $x_0 = x$, $u(\cdot, x_0) = G(\cdot, x)$, $u^i(\cdot, x_0) = \Phi(\cdot, x)$ and $n = n_b$: accordingly, we have that [42] $G(\cdot, x) \in C^1\left(\bar{B}_R \setminus \{x\}\right)$, $\Delta G(\cdot; x) \in C^0\left(\bar{\Lambda}_R \setminus \{x\}\right)$ and $\Delta G(\cdot; x) \in C^0(\bar{\Lambda}_i)$ for all $i \in \{1, \ldots, N\} \setminus J_0$, where the index set J_0 has been defined in assumption no. 6) soon below eq. (4.15). Then, given the regularity properties assumed for w, we can apply the usual Green's second theorem [41, 65] in the domain $\Lambda_R \setminus \bar{B}(x,\rho)$, i.e.,

$$\int\limits_{\Lambda_R \setminus \bar{B}(x,\rho)} \left[G(y,x)\Delta w(y) - w(y)\Delta_y G(y,x)\right] dy = \tag{4.23}$$
$$= \int\limits_{\partial\Lambda_R \cup \partial B(x,\rho)} \left[G(y,x)\frac{\partial w(y)}{\partial \nu} - w(y)\frac{\partial G(y,x)}{\partial \nu(y)}\right] ds(y),$$

as well as in any other domain Λ_i, with $i \in \{1, \ldots, N\} \setminus J_0$, i.e.,

$$\int\limits_{\Lambda_i} \left[G(y,x)\Delta w(y) - w(y)\Delta_y G(y,x)\right] dy = \tag{4.24}$$
$$= \int\limits_{\partial\Lambda_i} \left[G(y,x)\frac{\partial w(y)}{\partial \nu} - w(y)\frac{\partial G(y,x)}{\partial \nu(y)}\right] ds(y).$$

In (4.23) and (4.24) it is understood that the unit normal is chosen as outward with respect to each domain. We now sum eq. (4.23) with all the eq.s (4.24) obtained for $i \in \{1, \ldots, N\} \setminus J_0$: we note that, except for ∂B_R and $\partial B(x,\rho)$, all the boundary integrals are taken twice, with opposite orientation of the unit normal. Since the integrand functions are continuous on the boundaries, these integrals cancel out. Moreover, by eq. (4.16), we can substitute $\Delta_y G(y,x) = -k^2 n_b(y) G(y,x)$ for $y \neq x$ into (4.23) and (4.24). As a result, we find

$$\int\limits_{B_R \setminus \bar{B}(x,\rho)} \left[\Delta w(y) + k^2 n_b(y) w(y)\right] G(y,x) dy = \tag{4.25}$$
$$= \int\limits_{\partial B_R \cup \partial B(x,\rho)} \left[G(y,x)\frac{\partial w(y)}{\partial \nu} - w(y)\frac{\partial G(y,x)}{\partial \nu(y)}\right] ds(y).$$

We now focus on the integral over $\partial B(x,\rho)$, say $I_{\partial B(x,\rho)}$, at the right-hand side of (4.25):

remembering eq. (4.17), we have

$$I_{\partial B(x,\rho)} = \int_{\partial B(x,\rho)} \left[\Phi(y,x)\frac{\partial w(y)}{\partial \nu} - w(y)\frac{\partial \Phi(y,x)}{\partial \nu(y)}\right] ds(y) + \\ + \int_{\partial B(x,\rho)} \left[u_b^s(y,x)\frac{\partial w(y)}{\partial \nu} - w(y)\frac{\partial u_b^s(y,x)}{\partial \nu(y)}\right] ds(y). \tag{4.26}$$

Now, the second integral in (4.26) vanishes as $\rho \to 0$, since the integrand is bounded and the measure of the integration domain tends to zero. As regards the first integral in (4.26), we recall [23] the following asymptotic behaviors

$$\Phi(y,x) = \frac{1}{2\pi}\ln\frac{1}{|x-y|} + O(1) \quad \text{as} \quad |x-y| \to 0 \tag{4.27}$$

$$\frac{\partial \Phi(y,x)}{\partial \nu(y)} = \frac{1}{2\pi}\frac{1}{|x-y|} + O(|x-y|\ln|x-y|) \quad \text{as} \quad |x-y| \to 0. \tag{4.28}$$

By using (4.27) and (4.28), the integral mean value theorem applied to the integral in (4.26) easily show that the latter tends to $-w(x)$ as $\rho \to 0$. Then, thesis (4.22) is obtained by taking $\rho \to 0$ in eq. (4.25): indeed, remembering eq. (4.17) and the regularity of $u_b^s(y,x)$, the singularity of $G(y,x)$ for $y \to x$ is only due to $\Phi(y,x)$, i.e., it is weak and then the integral on B_R converges. □

Theorem 4.1.4. *Let Λ_i (with $i = 0,\dots,N+1$), D, $n_b(x)$, $n(x)$, $m(x)$, $G(x,y)$ be as above and let $x_0 \in \tilde{\Lambda}_0 \setminus \overline{(\tilde{\Lambda}_0 \cap D)}$ be as above.. If $u^s(\cdot,x_0) \in C^1(\mathbb{R}^2)$, with $\Delta u^s(\cdot,x_0) \in C^0\left(\bar{\Lambda}_i\right)$ for all $i = 0,\dots,N$, is a solution of the differential problem (4.18), then $u^s(\cdot,x_0)$ solves the integral equation (4.19) for $x \in \tilde{\Lambda}_0$.*

Proof. Consider an arbitrary point $x \in \tilde{\Lambda}_0$. Let $B_R := \{x \in \mathbb{R}^2 : |x| < R\}$ be an open disk with exterior unit normal ν and radius R large enough, so that $B_R \supset \left[\cup_{i=1}^{N} \bar{i} \cup \{x\}\right]$. By hypothesis, $u^s(\cdot,x_0)$ is regular enough in the domain B_R to be represented by means of the generalized Green's formula (4.22) in $\Lambda_R := B_R \cap \tilde{\Lambda}_0$, i.e.,

$$u^s(x,x_0) = \int_{\partial B_R} \left\{\frac{\partial u^s(y,x_0)}{\partial \nu(y)}G(y,x) - u^s(y,x_0)\frac{\partial G(y,x)}{\partial \nu(y)}\right\} ds(y) + \\ - \int_{B_R} \left\{\Delta_y u^s(y,x_0) + k^2 n_b(y) u^s(y,x_0)\right\} G(y,x)dy, \quad x \in \Lambda_R. \tag{4.29}$$

First we prove that the integral on ∂B_R in (4.29) is zero. To this end, consider $B_r := \{x \in \mathbb{R}^2 : |x| < r\}$ such that $r > R$, and apply Green's second theorem [41] in the domain $B_r \setminus B_R$: by choosing the unit normal ν as outgoing from both B_R and B_r, and observing that both the fields $u^s(\cdot,x_0)$ and $G(\cdot,x)$ verify the same Helmholtz equation in $B_r \setminus B_R \subset \Lambda_0$ (where $n_b(x) = n(x) = \tilde{n}_0$), we find

$$\int_{\partial B_R} \left\{\frac{\partial u^s(y,x_0)}{\partial \nu(y)}G(y,x) - u^s(y,x_0)\frac{\partial G(y,x)}{\partial \nu(y)}\right\} ds(y) = \\ = \int_{\partial B_r} \left\{\frac{\partial u^s(y,x_0)}{\partial \nu(y)}G(y,x) - u^s(y,x_0)\frac{\partial G(y,x)}{\partial \nu(y)}\right\} ds(y) \tag{4.30}$$

We now recall [41] that any radiating solution v of the Helmholtz equation (with generic wave number $k > 0$) outside a disk in $\mathbb{R}^2$ has the following asymptotic behavior

$$v(x) = \frac{e^{\mathrm{i}kr}}{\sqrt{r}} \left\{ v_\infty(\hat{x}) + O\left(\frac{1}{r}\right) \right\}, \qquad r = |x| \to \infty, \tag{4.31}$$

where v_∞ is the far-field pattern of v. If v^1 and v^2 are two such solutions, from (4.31) we find [41]

$$v^1(x) \frac{\partial v^2(x)}{\partial r} = \mathrm{i}k \frac{e^{2\mathrm{i}kr}}{r}\, v^1_\infty(\hat{x})\, v^2_\infty(\hat{x}) + O\left(\frac{1}{r^2}\right), \qquad r \to \infty, \tag{4.32}$$

uniformly for all directions. By applying (4.32) to the radiating fields $u^s(\cdot, x_0)$ and $G(\cdot, x)$, we easily find that the integrand function at the right-hand side of (4.30) is $O\left(\frac{1}{r^2}\right)$ and then the integral itself vanishes as $r \to \infty$. This is even more true if the wave number $k > 0$ is replaced by $k\sqrt{\tilde{n}_0}$ with $\mathrm{Im}\left\{\sqrt{\tilde{n}_0}\right\} > 0$, since the attenuation of the fields and their derivatives is faster.

As regards the integral on B_R in (4.29), we observe that a simple manipulation of eq. (4.18)(a) yields

$$\Delta_x u(x, x_0) + k^2 n_b(x)\, u(x, x_0) = -\delta(x - x_0) + k^2 \tilde{n}_0 \frac{n_b(x) - n(x)}{\tilde{n}_0} u(x, x_0). \tag{4.33}$$

If we now remember eq.s (4.16) and (4.18)(b), as well as the identification $u^i(\cdot, x_0) = G(\cdot, x_0)$ and the definitions $\tilde{k}_0 := k\sqrt{\tilde{n}_0}$, $m(x) := [n_b(x) - n(x)]/\tilde{n}_0$, from (4.33) we have

$$\Delta_x u^s(x, x_0) + k^2 n_b(x)\, u^s(x, x_0) = \tilde{k}_0^2 m(x) u(x, x_0). \tag{4.34}$$

Note that at the right-hand side of (4.34) the singularity of $u(x, x_0)$ for $x = x_0$ is cancelled out by $m(x)$, since $\operatorname{supp} m = \bar{D}$ is compact and $x_0 \notin \operatorname{supp} m$ by hypothesis. Then, by substituting (4.34) into (4.29), we can write

$$u^s(x, x_0) = -\tilde{k}_0^2 \int_{\mathbb{R}^2} G(y, x) m(y) u(y, x_0)\, dy \qquad \forall x \in \tilde{\Lambda}_0, \tag{4.35}$$

which is immediately written in the form (4.19) by using the reciprocity property [42, 70] $G(y, x) = G(y, x)$. □

We call eq. (4.19) the 'inhomogeneous Lippmann-Schwinger equation', to emphasize that the reference background is (or may be) inhomogeneous. In the next section, we shall apply an inversion algorithm to this equation in order to compute the point values of m, i.e., of the refractive index of the scatterer under investigation.

4.1.3. A hybrid scheme

In general, iterative methods for the quantitative solution of inverse scattering problems can be applied to the homogeneous Lippmann-Schwinger equation. Such methods take as input

the scattering data collected by antennas placed outside the investigated area and inside a homogeneous zone, and provide, as output, the reconstruction of the refractive index everywhere in the inhomogeneous region. The main drawback of this computational approach is that, particularly when the scattering experiment is performed with a single and fixed frequency, the number of unknowns is typically much larger than the number of measured data, and therefore the reconstruction accuracy is often rather low (the accuracy could be improved by applying the procedure to multi-frequency data). However there are situations where just a certain part of the inhomogeneous region is unknown and of interest for practical applications, while information is available about the refractive index of the rest of the domain. In this case the quantitative inverse scattering method can be applied to the inhomogeneous Lippmann-Schwinger equation, provided one is able to compute the Green's function of the inhomogeneous (and known) background and to qualitatively distinguish between the target scatterer and the background. In the following of this section, we describe an implementation of this approach essentially based on the contrast source inversion method. Therefore, in order to realize the proposed hybrid approach, the ingredients we need are: a method for computing the Green's function of the background, a qualitative method to highlight the scatterer inside the background itself and a quantitative scheme for the inversion of the inhomogeneous Lippmann-Schwinger equation.

The Green's function computation

A handy way to compute the Green's function is given by the method of moments (MOM) [59, 88]. Since $G(\cdot, x_0)$ solves a particular case of problem (4.18) with the identifications $u(\cdot, x_0) = G(\cdot, x_0)$, $u^i(\cdot, x_0) = \Phi(\cdot, x_0)$ and $n(x) = n_b(x)$, it also satisfies the homogeneous Lippmann-Schwinger equation [41]

$$G(x, x_0) = \Phi(x, x_0) - k^2 \int_{\mathbb{R}^2} \Phi(x, y) m_b(y) G(y, x_0)\, dy \quad \text{for } x \in \mathbb{R}^2, \tag{4.36}$$

with $m_b(x) := n_0 - n_b(x)$ and $x_0 \in \tilde{\Lambda}_0$. Since $\operatorname{supp} m_b$ is compact, the integration domain in (4.36) is bounded: then, we can consider a finite partition of $\operatorname{supp} m$ by L cells, which can be taken so small that m_b and $G(\cdot, x_0)$ can be assumed to be constant inside each cell. Then, eq. (4.36) can be approximated as

$$G(x, x_0) \approx \Phi(x, x_0) - k^2 \sum_{j=1}^{L} m_b(y_j) G(y_j, x_0) \int_{cell_j} \Phi(x, y) dy, \tag{4.37}$$

where $y_j \in \mathbb{R}^2$ identifies the center of the j-th cell. Further, following [88], we approximate each square cell as a circular cell of the same area, so that the integral in eq. (4.37) can be

evaluated as

$$\int_{cell_j} \Phi(x,y)dy = \frac{\mathrm{i}}{4}\int_{cell_j} H_0^{(1)}(k_0|x-y|)dy \approx$$
$$\approx \begin{cases} \dfrac{\mathrm{i}\pi k_0 a_j}{2} J_1(k_0 a_j) H_0^{(1)}(k_0|x-y_j|) & x \notin cell_j \\ \dfrac{\mathrm{i}}{2}\left[\pi k_0 a_j H_1^{(1)}(k_0 a_j) + 2\mathrm{i}\right] & x \in cell_j, \end{cases} \tag{4.38}$$

where $a_j = \sqrt{\Delta_j/\pi}$, Δ_j is the area of the j-th cell, J_1 is the Bessel function of first order and $H_1^{(1)}$ is the Hankel function of first kind of order one. We point out that the method can be notably speeded up by utilizing the fast Fourier transform algorithm as it is described for example in [15, 109]: we shall adopt this version of the MOM method for our numerical simulations.

The linear sampling method

The linear sampling method (LSM) [28] is the earliest and most used qualitative method in inverse scattering: in the case of an object embedded in a homogeneous background, it provides a reconstruction of its support by only knowing the field measured around it. When the background is inhomogeneous and its Green's function is known, the LSM can be extended to the case of an inhomogeneity immersed in a medium with piecewise constant refractive index. The basic idea is to write and to approximately solve the modified far-field equation [30, 42]

$$\int_\Omega [u^s(x,x_0) - u_b^s(x,x_0)] g_z(x_0)\, dx_0 = G(x,z) \quad \text{for } x \in \Omega, \tag{4.39}$$

where $\Omega := \{x \in \mathbb{R}^2 : |x| = R_\Omega\} \subset \Lambda_0$ is the circle where emitting and receiving antennas are placed and $z \in \mathbb{R}^2$ is a sampling point inside the investigation domain enclosed by Ω. In (4.39), the Green's function $G(x,z)$ and the field $u_b^s(x,x_0)$ can be computed by exploiting the knowledge of the background, while $u^s(x,x_0)$ represents the measurements, i.e., the data of the inverse scattering problem.

In fact, it can be proved [30, 42] that there exists an approximate solution of (4.39) whose $L^2(\Omega)$-norm is bounded inside the scatterer, grows up as z approaches its boundary from inside and remains very large outside, thus behaving as an indicator function for the support $\bar{D}$ of the scatterer itself. This result inspires a simple algorithm that approximately solves the modified far-field equation by means of a regularization procedure. More precisely, the LSM requires the choice of a grid containing the scatterer; then, for each point z of the grid, a discretized version of the modified far-field equation is solved by using the Tikhonov regularization method [103] and the Euclidean norm of the regularized solution is plotted for each z. As a result, the boundary of the scatterer is highlighted by the points of the grid corresponding to the largest

increase of the Euclidean norm. We point out that this algorithm can be notably speeded up by applying a no-sampling formulation [6], which is the one adopted in the present work.

Finally, we remark that, for the purposes of our implementation, a univocal identification of the shape of the scatterer is performed by post-processing the LSM through an active contour technique [5, 32]: for reasons that will be clear in the next subsection, we choose the parameters of this edge detection algorithm in such a way that a slight overestimate of the scatterer is favoured.

The contrast source inversion method

In our hybrid scheme, the contrast source inversion (CSI) method [104, 105] is the technique we use for the quantitative inversion of the inhomogeneous Lippmann-Schwinger equation. More precisely, the CSI method computes the point values of the refractive index $n(x)$ inside an investigation domain T containing the scatterer support $\bar{D} = \operatorname{supp} m$. The idea at the basis of the CSI method is to split an inverse scattering problem described by an integral equation such as (4.19) into two different problems, one defined inside the scatterer and the other one on the curve Ω where antennas are placed. More formally, remembering (4.18)(b), equation (4.19) is equivalently recast in the form

$$u(x, x_0) = u^i(x, x_0) - k^2 \int_T G(x, y) m(y) u(y, x_0)\, dy \tag{4.40}$$

and then replaced by the system

$$\begin{cases} w(x, x_0) = m(x) u^i(x, x_0) - m(x) \left[\mathcal{G}^T w(\cdot, x_0)\right](x) & \text{for } x \in T \quad \text{(a)} \\ u^s(x, x_0) = -\left[\mathcal{G}^\Omega w(\cdot, x_0)\right](x) & \text{for } x \in \Omega, \quad \text{(b)} \end{cases} \tag{4.41}$$

where $w(x, x_0) := m(x) u(x, x_0)$, the operator $\mathcal{G}^T : L^2(T) \to L^2(T)$ is defined as

$$\left[\mathcal{G}^T f\right](x) = k^2 \int_T G(x, z) f(z)\, dz \qquad \forall x \in T, \tag{4.42}$$

and $\mathcal{G}^\Omega : L^2(T) \to L^2(\Omega)$ is defined as

$$\left[\mathcal{G}^\Omega f\right](x) = k^2 \int_T G(x, z) f(z)\, dz \qquad \forall x \in \Omega. \tag{4.43}$$

Note that eq. (4.41)(a) is obtained from eq. (4.40) by multiplying both members for m, while eq. (4.41)(b) is the restriction of eq. (4.19) for $x \in \Omega$: in particular, $u^s(x)$ for $x \in \Omega$ represents the data of the inverse scattering problem.

The CSI method consists in minimizing the functional

$$F(w, m) = \frac{\|u^s - \mathcal{G}^\Omega w\|_\Omega^2}{\|u^s\|_\Omega^2} + \frac{\|m u^i - w - m\mathcal{G}^T w\|_T^2}{\|m u^i\|_T^2}, \tag{4.44}$$

where we dropped the dependence on x, x_0, and $\|\cdot\|_\Omega$, $\|\cdot\|_T$ denote the L^2-norms on the spaces $L^2(\Omega)$, $L^2(T)$ respectively. The minimization of F is performed by applying gradient algorithms [82] and the updates are alternately computed for m and w. The information on the background is again encoded into the Green's function, i.e., into the operators $\mathcal{G}^T$ and $\mathcal{G}^\Omega$.

In the standard case of a homogeneous background, the implementation of the approach described above is well-established and does not require further discussion. Instead, in the inhomogeneous case two issues need to be addressed. First, we observe that eq. (4.41)(a) is written for $x \in T$; on the other hand, the integral equation (4.19) whence eq. (4.41)(a) should derive has been proved in Theorem 4.1.4 only for $x \in \tilde{\Lambda}_0$ and, in general, T is not contained in $\tilde{\Lambda}_0$. To overcome this drawback, we observe that the purpose of the CSI algorithm is to compute the values of $n(x)$ for $x \in T$, and these values do not depend on the reference background inside T. Then, we can think that the original background in T is replaced by a new one, which hosts the same homogeneous medium occupying $\tilde{\Lambda}_0$. In other words, this amounts to replacing the refractive index n_b with $\tilde{n}_b$, such that $\tilde{n}_b(x) = n_0$ for all $x \in T$ and $\tilde{n}_b(x) = n_b(x)$ for all $x \notin T$. Of course, the background Green's function $G(x, z)$ in eqs. (4.42) and (4.43) must be replaced accordingly, i.e., by $\tilde{G}(x, z)$. We point out that a good choice of the investigation domain T is the region highlighted by the LSM, as explained in subsection 4.1.3: indeed, such region is an overestimate of D, i.e., it contains D, but is also very small, thus minimizing the number of points where $n(x)$ is to be computed, i.e., the number of unknowns of the problem. As a result, also the number of measurements necessary for a successful implementation of the method is optimized.

This same trick, i.e., changing the background as above, is also useful to address the second issue, which is concerned with the computation of the Green's function $G(x, z)$. Indeed, eq.s (4.42) and (4.43) show that both x and z vary in T: then, in particular, also the singular case $x = z$ is of interest. Now, $G(x, z)$ satisfies eq. (4.36) (with the identification $z = x_0$), which implies that if $z \in \operatorname{supp} m_b$ and $x = z$, the integrand function at the right-hand side of (4.36) is affected by a double singularity for $y = z$: one due to $\Phi(z, y)$, the other one due to $G(y, z)$. This prevents us from applying the usual approximation scheme outlined in eq.s (4.37) and (4.38): accordingly, an *ad hoc* quadrature rule should be created to numerically compute the integral. Such problem is avoided by the previous choice of the new background, i.e., of $\tilde{n}_b$: indeed, the region T is now erased by the actual integration domain in (4.36), since $\tilde{m}_b := n_0 - \tilde{n}_b$ vanishes inside T and $z \in T$.

4.1.4. Numerical examples

This section is dedicated to a numerical validation of the hybrid inversion technique presented above. A first group of experiments is dedicated to assess the effectiveness of the inhomogeneous Lippmann-Schwinger approach with respect to the traditional homogeneous-one: in this sense,

a comparison between the operations of both (homogeneous and inhomogeneous-background) CSI techniques, when applied to simple numerical phantoms, will be presented. Then, in a second group of numerical experiments, the effectiveness of the whole hybrid method, as well as its worthwhileness for real applications, will be shown through some realistic simulations concerning breast cancer detection.

Homogeneous and inhomogeneous quantitative inversion: a numerical example

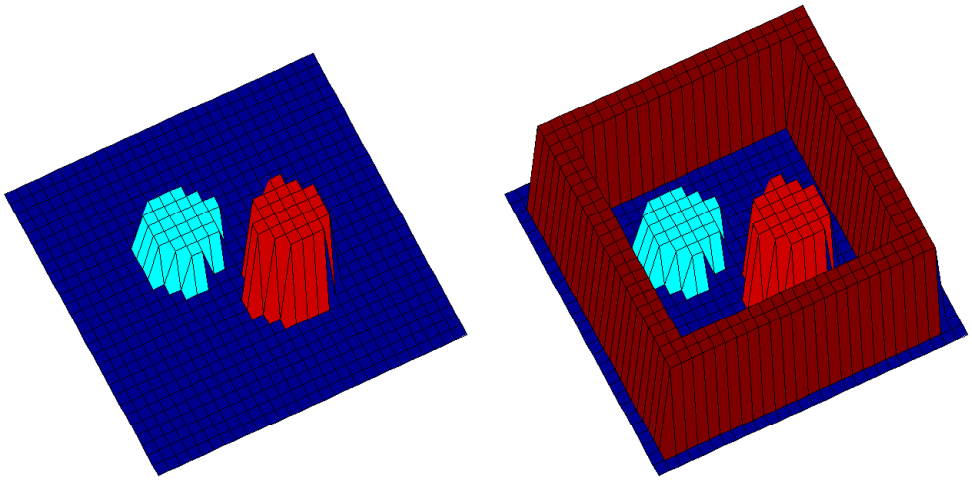

(a) (b)

Figure 4.2: Plot of the numerical phantoms utilized for the experiments. Value of the contrast functions showed in Figure 4.3 (a) and (c).

The first group of numerical examples is concerned with the reconstruction of the two numerical phantoms of Figure 4.2 (a) and (b). The aim is to show that, for those situations in which a classic (i.e. homogeneous-background) quantitative method fails, the effectiveness of the reconstruction can be recovered when some information is assumed as background. This is the case of Figure 4.2 (b): if CSI is able to reconstruct the presence of the scatterer in Figure 4.2 (a), it fails when the same scatterer is embedded in a square barrier in the way of Figure 4.2 (b). Nevertheless, if the presence of the square barrier is assumed as background and the inhomogeneous-background CSI is applied, then a proper reconstruction of the scatterer is restored. A more precise description of these results is provided in Figure 4.3 and in the remaining part of this subsection.

Figure 4.3 (a) and (c) represent the projection on the plane of the (non-absorbing) dielectric phantoms of Figure 4.2 (a) and (b) where the wave length λ is equal to 1 and the field is measured on 30 points on a circle of ray 3λ and for 30 incidences. Since the main aim of the experiment is to compare the operation of the two approaches (classic CSI and inhomogeneous

background CSI) in a significant situation, no noise has been added to the field data. Figure 4.3 (b) and (d) are, respectively, the homogeneous-background CSI[1] reconstructions of phantoms (a) and (c). Figure 4.3 (e) and (f) concerns with the inhomogeneous-background CSI: (f) is the reconstruction of (c) when (e) is assumed as background; in particular, the reconstruction is performed just on the pixels inside the green square in (e).

The hybrid approach validated against realistic numerical breast phantoms

With the following numerical examples we want to test the efficacy of the hybrid technique when applied to realistic scattering situations. The set is a $2D$ mammographic session where the index of refraction of the scatterer (i.e. breast) is provided by highly realistic numerical phantoms[2] obtained from the segmentation of MRI (Magnetic Resonance Imaging) images [71] to whom a circular tumor of diameter 0.5 cm has been artificially added (we refer to [72] for the computation of the value of index for tumoral tissues at fixed frequencies). All the experiments are performed at frequency $f = 3GHz$, measuring the field on 30 antennas placed on a circle of ray 6 cm surrounding the breast. The incidence directions are 30 and the field values are perturbed with a 3% of noise.

Figure 4.4 shows the values of the relative permittivity $\varepsilon_r(x)$ and of the conductivity $\sigma(x)$ of the tissues at frequency $f = 3GHz$. We remind that the index of refraction is given by $n(x) = \frac{1}{\varepsilon_0}[\varepsilon(x)+\mathrm{i}\frac{\sigma(x)}{\omega}]$, where ε_0 is the electric permittivity of the hosting medium. Although, for clarity, in all the figures presented in this subsection the refractive index is plotted considering ε_0 as the permittivity of the vacuum, the breast is surrounded by a matching layer [75] of refractive index equal to $18 + \mathrm{i}0.06$ which embeds also the curve where antennas are placed.

A whole and precise reconstruction of a scatterer such heterogeneous as breast is extremely difficult to be achieved: the main difficulty lies in the heterogeneity of the refractive index and in the wideness of the range of values that it can assume from point to point and from tissue to tissue. Moreover, in order to properly describe the variety of the tissues, a large number of unknowns has to be taken into account: in practical applications, their number can be disproportionate to the number of field data and the effective achievability of a truthful reconstruction can be out of range. Figure 4.5 provides an idea of the quality of the reconstruction that can be achieved by applying tout court a quantitative technique to the reconstruction of a scatterer of the shape of the one plotted in Figure 4.4: since, with a homogeneous background approach, one has to reconstruct everywhere in the investigated region, the reconstructed refractive index can not be as precise as the exact one (other examples of quantitative reconstruction of breast slices can be found for example in [52]). For these reasons, an inhomogeneous-background approach to the problem can be helpful in the sense that, since a part of the scatterer can be assumed as background (when a priori known), the reconstruction can be performed on a

[1] implemented in the error-reducing version of [105] initialized through backpropagation

[2] downloadable at uwcem.ece.wisc.edu/home.htm

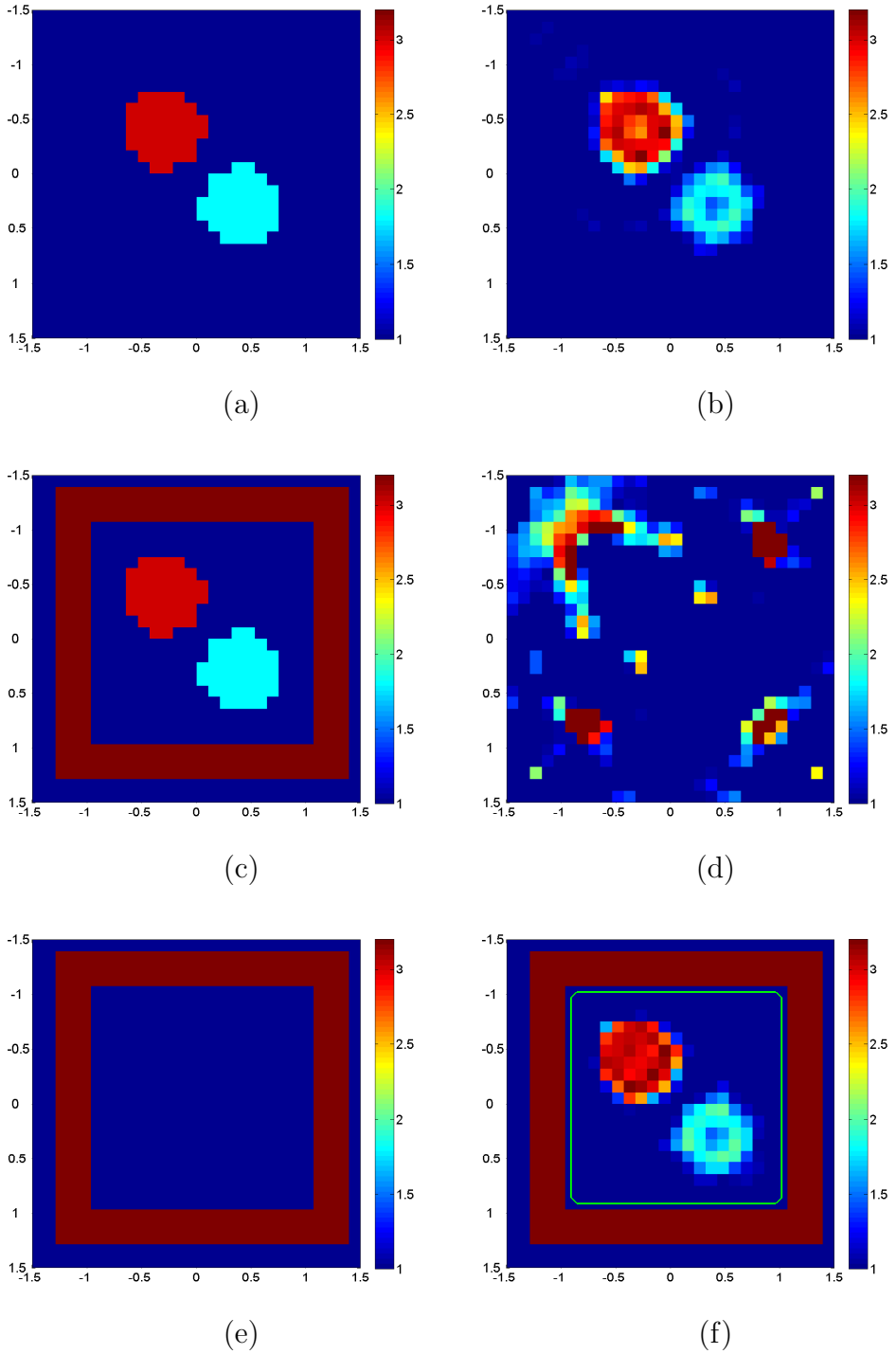

Figure 4.3: (a) and (c) are the exact values of the refractive indexes of the phantoms. (b) and (d) are the corresponding reconstructions achievable using the homogeneous CSI. (f) is the reconstruction of (c) obtained through the inhomogeneous CSI when (e) is assumed as background. All the CSI reconstructions are obtained after 500 iterations.

fewer number of pixels, reducing the number of unknowns and increasing the quality of the reconstruction.

In the first numerical example, whose results are collected in Figure 4.6, the idea is to reconstruct both glandular and tumoral tissues using, as background, the a priori information on skin layer, fat layer and matching fluid around the breast that can be provided, for example, by the segmentation of the most recent MRI image of the patient's breast. Figure 4.6 (a) and (b) show the value of permittivity and conductivity of the background utilized for the application of the nSLSM, the qualitative technique which allows the identification of the unknown region. (c) is the reconstruction provided by the nSLSM (i.e. plot of one over the squared norm of the solution to the far field equation); from (c), through the application of active-contours techniques, the support of the unknown region is extracted. (d) represents value of the permittivity of the background used for applying the inhomogeneous-background CSI (the corresponding conductivity is analogous): we remind that, in order to avoid the occurrence of the theoretical and computational problems described in Section 4.1.3, the value of the hosting medium has to be substituted inside the unknown region so that the integral of (4.36) vanishes inside the area under investigation. The inhomogeneous-background CSI reconstruction is presented in (e) for the relative permittivity and (f) for the conductivity.

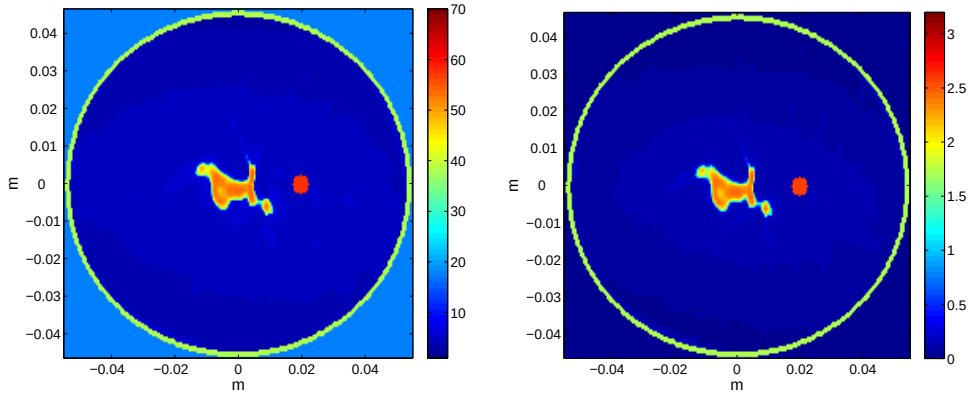

(a) (b)

Figure 4.4: Exact profile of the scatterer. (a) permittivity and (b) conductivity at 3 GHz of frequency.

In the second numerical example we utilize the inhomogeneous-background CSI as a tool able to verify the nature of an inhomogeneity detected by the nSLSM. In this case, the whole healthy breast slice (provided by the segmentation of the most recent MRI image of the patient's breast) is wholly assumed as background and the reconstruction is performed on the only pixels where the presence of the tumor has been highlighted. In Figure 4.7, (a), (b) and (c) concerns with the nSLSM: (a) and (b) show the relative permittivity and the conductivity of the considered background while (c) is the nSLSM output, useful for the reconstruction of the

support of the inclusion. (d) plots the relative permittivity of the background utilized for the inhomogeneous CSI and where the value of the matching fluid is artificially substituted in the area detected by the nSLSM (the corresponding conductivity is analogous, i.e., obtained from Figure 4.4 (b) where the value $\sigma = 0.001$ is substituted inside the unknown region). Finally, (e) and (f) are the inhomogeneous-background CSI reconstructions.

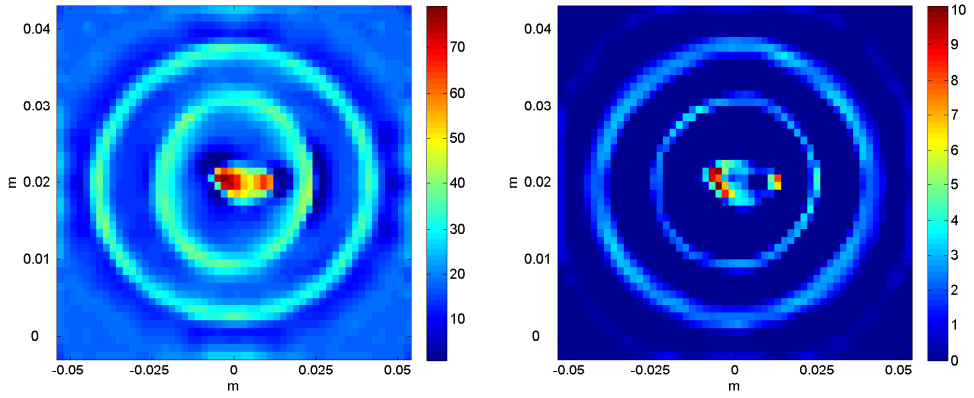

(a) (b)

Figure 4.5: Example of reconstruction provided by the classic (i.e. homogeneous-background) CSI method for 3 GHz of frequency, 30 measurements and 30 emissions, 500 iterations. Field data perturbed by 3% noise.

A third and a fourth example, (collected in Figure 4.8), describe the behavior of the method when one has at disposal data subjected to a bigger noise perturbation than in the previous examples. In Figure 4.8 (a), (c) and (d) one wants again to reconstruct the presence and the value of the refractive index for glandular and tumoral tissue inside the breast and for data perturbed by a 5% of noise: (a) is the output provided by the nSLSM which highlights the region of inhomogeneity (we remind that matching fluid, skin and fat layer are here assumed as known); (c) and (d) are the reconstructions of electric permittivity and conductivity provided by the application of the inhomogeneous-background CSI method. Figure 4.8 (b), (e) and (f) represent the results obtained when one want to detect and reconstruct the only tumor with field data perturbed by a 3% noise and background n_b perturbed by 5% of noise: in fact, the aim of this experiment is to take into account also an unperfect knowledge of the background. nSLSM output, permittivity and conductivity reconstructions are collected respectively in (b), (e) and (f).

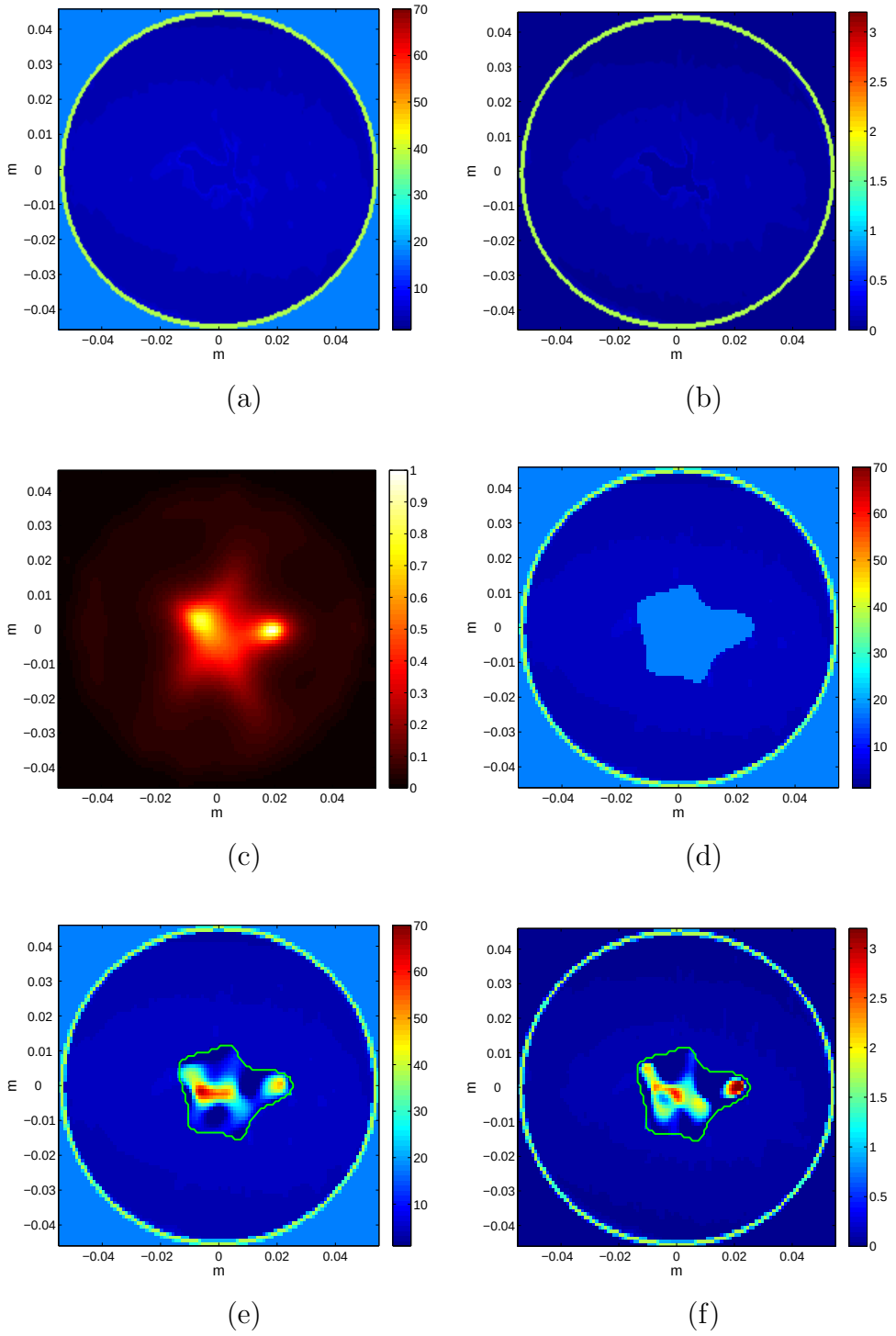

Figure 4.6: Reconstruction of glandular and tumoral tissue. (a) and (b) are the utilized nSLSM background; (c) is the nSLSM reconstruction; (d) shows the permittivity of the background utilized for the inhomogeneous-background CSI (the corresponding conductivity is analogous); (e) and (f) are, respectively, the reconstructed permittivity and conductivity after 500 iterations and where the green line delimits the region of reconstruction. Field data perturbed by 3% noise.

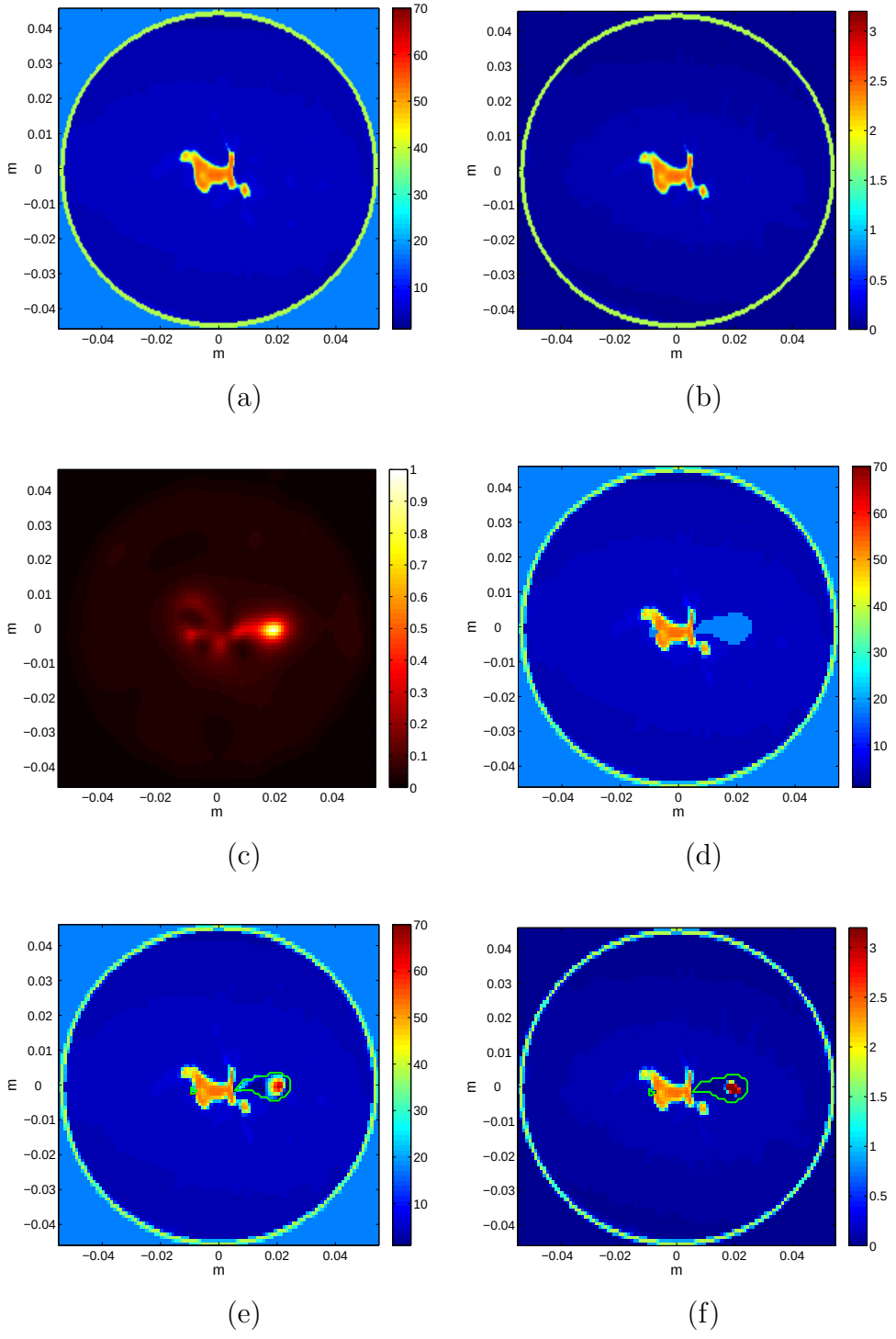

Figure 4.7: Reconstruction of the only tumoral tissue. (a) and (b) are the utilized nSLSM background; (c) is the nSLSM reconstruction; (d) shows the permittivity of the background utilized for the inhomogeneous-background CSI; (e) and (f) are, respectively, the reconstructed permittivity and conductivity after 500 iterations and where the green line delimits the region of reconstruction. Field data perturbed by 3% noise.

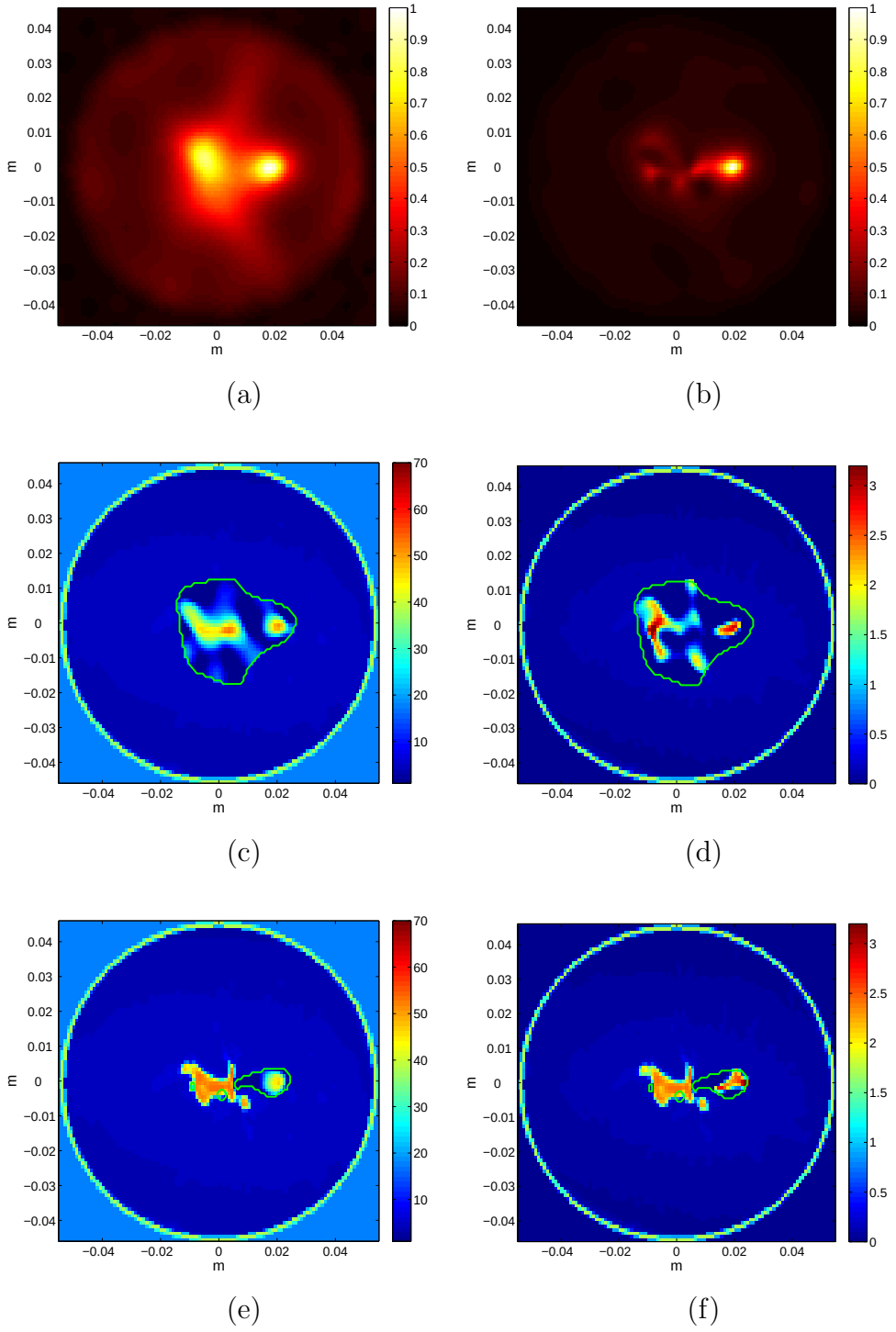

Figure 4.8: Results of two different experiments: (a), (c) and (d) are in the same perspective of Figure 4.6, i.e., one wants to reconstruct presence and refractive index of both glandular and tumoral tissue; for (b), (e) and (f), the aim is to retrieve information on the only tumoral tissue as done in Figure 4.7. (a), (c) and (d) are respectively nSLSM output, reconstructed relative permittivity and reconstructed conductivity (after 500 iterations) for field data perturbed by 5% of noise. (b), (e) and (f) are respectively nSLSM output, reconstructed relative permittivity and reconstructed conductivity (after 500 iterations) for data perturbed by 3% of noise and assuming a partial knowledge of the background, i.e., pixelwise perturbing n_b with a 5% of noise.

4.2. Computing estimates on material properties from transmission eigenvalues

This work is motivated by the inverse scattering problems, those problems where one is interested in reconstructing the shape and the material properties of an inclusion from electromagnetic farfields measurements. More precisely we are interested in complementing the so called sampling methods [23, 68], (those methods that enables one to reconstruct just the geometry of the scatterer), by providing estimates on the material properties. We shall use for that purpose the so-called transmission eigenvalues [41]. These special frequencies can be determined from the knowledge of the farfields for a range of frequencies. They also correspond to values of the wavenumbers for which the so called homogeneous interior transmission problem has a non trivial solution. Our work is in the same spirit of [43] but we shall employ a different and (in principle) a simpler method.

The proposed method is based on reformulating the interior transmission eigenvalue problem into a (standard, generalized) eigenvalue problem for the material coefficients. In the case of constant coefficients the value of the material parameter corresponds with the smallest eigenvalue. The obtained eigenvalue problem corresponds to a fourth order operator that we shall solve using an appropriate mixed second order formulation of the problem. To obtain the desired approximation of the refractive index, one needs to determine the first transmission eigenvalue from the farfield data. We shall review here the method proposed in [29, 25] based on a frequency sampling of the farfield solution. We then extend this method to the case of scatterers with multiply connected components so that one is able to detect the transmission eigenvalues associated with each connected components.

In these first investigations we restrict ourselves to a two dimensional setting of the problem that models electromagnetic scattering from infinite cylinders and treat both transverse electric (TE) and transverse magnetic (TM) polarizations. We present a number of numerical experiments that validate our methodology for homogeneous and non homogeneous inclusions and backgrounds. We also treat the case of a background with absorption and the case where the geometry is also unknown (but reconstructed using the linear sampling algorithm).

The outline of this second part of the chapter of the chapter is the following. Section 4.2.1 is dedicated to introducing the forward and the inverse scattering problem for TM polarizations. We introduce our method for constructing constant approximation of the refractive index in the Section 4.2.2. Section 4.2.3 corresponds with the extension of our results to the case of TE polarizations. The last two sections (4.2.4 and 4.2.5) are dedicated to numerical experiments that validate our approach and illustrate its effectiveness. We finally remark that the results here presented are taken from [56] and [57].

4.2.1. Forward and inverse scattering problem

We consider the scattering of a time harmonic electromagnetic plane wave by an inhomogeneous infinite cylinder with cross section D such that the electric field $E = (0, 0, u \exp^{-i\omega t})$ is polarized parallel to the axis of the cylinder (TM polarization). Supposing the index of refraction n dependent only on the two coordinates orthogonal to the cylinder axis and factorizing out the time harmonic component we obtain that the total field u satisfies [41]:

$$\Delta u(x) + k^2 n(x) u(x) = 0 \qquad \text{in } \mathbb{R}^2 \tag{4.45}$$

$$u(x) = u^i(x) + u^s(x), \qquad \text{with } u^i(x) = \exp^{ikx\cdot d}, \tag{4.46}$$

$$\lim_{r\to\infty} \sqrt{r}\left(\frac{\partial u^s(x)}{\partial r} - iku^s(x)\right) = 0 \text{ uniformly with respect to } \hat{x} := \frac{x}{|x|}, \tag{4.47}$$

where $x \in \mathbb{R}^2$, $k > 0$ is the wave number, $r = |x|$ and $d \in \Omega = \{\frac{x}{|x|} : x \in \mathbb{R}^2\}$.

The index of refraction n is assumed to be a piecewise continuously differentiable function with discontinuities across non intersecting $\mathcal{C}^2$ curves. Moreover we suppose that $Im(n) \geq 0$ and that, with $m := 1 - n$ and $\bar{D}$ being the support of m, $\bar{D}$ is compact with the complement of D connected and boundary ∂D smooth.

Problem (4.45)-(4.47) has a unique solution $u \in H^2_{loc}(\mathbb{R}^2)$ and the corresponding scattered field u^s has the asymptotic behavior [41]:

$$u^s(x) = \frac{\exp^{ikr}}{\sqrt{r}} u_\infty(\hat{x}, d) + O(r^{-3/2}) \tag{4.48}$$

as $r \to \infty$ uniformly with respect to $\hat{x} \in \Omega$.

The knowledge of the so-called *farfield pattern* $u_\infty(\hat{x}, d)$ for all observation directions $\hat{x} \in \Omega$, all incident directions $d \in \Omega$ and for a range of frequencies k (that will be specified later) forms the data of the *inverse problem* of determining D and n. In fact, although the shape of D will be determined at a fixed frequency k, for the reconstruction of n, the knowledge of $u_\infty(\hat{x}, d)$ for a range of k will be required. As it will be better specified in the following, even in this last case the method will operate without combining data of different frequencies; for this reason we suppressed the mention to k in the notation.

Let Φ be the radiating fundamental solution of the Helmholtz equation

$$\Phi(x, y) = \frac{i}{4} H_0^{(1)}(k|x - y|), \tag{4.49}$$

where $H_0^{(1)}$ is the Hankel function of the first kind of order 0 and consider

$$\Phi_\infty(\hat{x}, z) := \frac{\exp^{i\pi/4}}{\sqrt{8\pi k}} \exp^{-ik\hat{x}\cdot z} \tag{4.50}$$

the farfield pattern of $\Phi(\cdot, z)$. Central to the Linear Sampling Method is the *farfield equation*

$$(Fg_z)(\hat{x}) = \Phi_\infty(\hat{x}, z) \tag{4.51}$$

where the *farfield operator* $F : L^2(\Omega) \to L^2(\Omega)$ is defined by:

$$(Fg)(\hat{x}) = \int_\Omega u_\infty(\hat{x}, d) g(d) ds(d) \tag{4.52}$$

We recall that Fg is the farfield associated to the incident wave

$$v_g(x) := \int_\Omega \exp^{ikx\cdot d} g(d) ds(d) \tag{4.53}$$

called Herglotz wave function with density g. We recall hereafter the main theorem associated with the LSM (see [28] for instance). We shall assume in the sequel that $Re(n) - 1$ or $1 - Re(n)$ is positive definite on D.

Theorem 4.2.1. *Except possibly for a discrete set of values of k when $Im(n) = 0$, it holds:*

1. *if $z \in D$, for every $\varepsilon > 0$ there is a solution $g_z^\varepsilon \in L^2(\Omega)$ of the inequality*

$$\|Fg_z^\varepsilon - \Phi_\infty(\cdot, z)\|_{L^2(\Omega)} < \varepsilon \tag{4.54}$$

such that

$$\lim_{\varepsilon \to 0} \|v_{g_z^\varepsilon}\|_{L^2(D)} < \infty \tag{4.55}$$

and that

$$\lim_{z \to \partial D} \|v_{g_z^\varepsilon}\|_{L^2(D)} = \infty. \tag{4.56}$$

2. *if z is not in D, then for every $\varepsilon > 0$ and g_z^ε satisfying*

$$\|Fg_z^\varepsilon - \Phi_\infty(\cdot, z)\|_{L^2(\Omega)} < \varepsilon \tag{4.57}$$

we have that

$$\lim_{\varepsilon \to 0} \|v_{g_z^\varepsilon}\|_{L^2(D)} = \infty. \tag{4.58}$$

The linear sampling method consists in solving the regularized (F is compact between infinite dimensional spaces) farfield equation for each z in a grid containing D and visualizing the indicator function $z \mapsto \|g_z\|_{L^2(\Omega)}$. This method therefore solves the inverse scattering problem of determining the shape of an unknown object D from the knowledge of its farfield pattern u_∞ for all observation directions and all incident directions at a given frequency.n. However its fails to do so if this frequency coincides with so called *transmission eigenvalues* that will be defined in the sequel.

We recall that for $z \in \mathbb{R}^2$, the equation $Fg_z = \Phi_\infty(\cdot, z)$ has a solution $g_z \in L^2(\Omega)$ if and only if there exists $w \in H^2(D)$ and a Herglotz wave function v_{g_z} such that w and v_{g_z} are solution of

$$\Delta w + k^2 n w = 0, \qquad \Delta v_{g_z} + k^2 v_{g_z} = 0 \qquad \text{in } D, \tag{4.59}$$

$$w - v_{g_z} = \Phi(\cdot, z), \qquad \frac{\partial w}{\partial \nu} - \frac{\partial v_{g_z}}{\partial \nu} = \frac{\partial \Phi}{\partial \nu}(\cdot, z) \qquad \text{on } \partial D. \tag{4.60}$$

Equations (4.59)-(4.60) form the so called interior transmission problem. As it will be better clarified in the next section, transmission eigenvalues identify wave numbers for which the farfield operator may not be complete in $L^2(\Omega)$. In particular, when k is such that the homogeneous problem associated to equations (4.59)-(4.60) admits a non trivial solution (w, v) with v a Herglotz wave function, then farfield operator F is not complete in $L^2(\Omega)$ [41]. In [31] the set of transmission eigenvalues has been proved to be infinite and countable.

The case of inhomogeneous background. We conclude this section by noting that an adaptation of the linear sampling method to the problem of detecting an object embedded in an inhomogeneous background has been well established for example in [37] (for TM polarized plane waves and impenetrable objects) and in [42] (for near field measurements and penetrable objects). In the inhomogeneous cases, the kernel of the farfield operator has to be modified by subtracting its background analogous and the right hand side should be replaced by the farfield of the background Green's function. The index n_b of the inhomogeneous background is assumed to verify similar regularity assumptions as n and to be equal to 1 outside a ball.

Following [37] if $u^s_{b,\infty}$ denotes the farfield pattern of the background medium (i.e. without the inclusion D) and if $G_\infty(\cdot, z)$ is the farfield of the Green function corresponding to the inhomogeneous background and to a point source at z, then Theorem 4.2.1 holds with

$$(Fg)(\hat{x}) := \int_\Omega [u_\infty(\hat{x}, d) - u^s_{b,\infty}(\hat{x}, d)] g_z(d) ds(d) \tag{4.61}$$

and Φ_∞ replaced by G_∞. If $u_b(\cdot, d)$ denotes the total field associated with the background, i.e. solution to (4.45)-(4.47) with $n = n_b$, then the Herglotz wave is defined in the present case as

$$v_g(x) := \int_\Omega u_b(x, d) g(d) ds(d) \tag{4.62}$$

and forms the incident wave that generates, for the inclusion D, a farfield equals to Fg.

4.2.2. Derivation of a constant approximation of the refractive index

We consider the case of a non-absorbing (i.e. $Im(n) = 0$) inhomogeneous medium embedded in a (possibly inhomogeneous) background and we assume that LSM or other qualitative methods

[23, 68] have already been used to determine the support D of the target. The aim of this section is to determine an estimate of the index of refraction $n(x)$ under the assumption that the support D is known.

To achieve this goal we shall make use of the first transmission eigenvalue and consider the interior transmission eigenvalue problem as an eigenvalue problem where the eigenvalue is the index of refraction. This is why we first need to provide a clearer definition of transmission eigenvalues and comment on their identification using farfield data.

Transmission eigenvalues and their identification using farfield data

We start analyzing the case of a TM polarized scattering problem of an inhomogeneous medium in the vacuum. Using the notation and assumptions of the second section, we define the *interior transmission problem* [41, 44] as the problem of finding $w, v \in L^2(D)$, with $w - v \in H^2(D)$, such that

$$\Delta w + k^2 n w = 0 \qquad \text{in } D \tag{4.63}$$

$$\Delta v + k^2 v = 0 \qquad \text{in } D \tag{4.64}$$

$$w - v = f \qquad \text{on } \partial D \tag{4.65}$$

$$\frac{\partial w}{\partial \nu} - \frac{\partial v}{\partial \nu} = g \qquad \text{on } \partial D \tag{4.66}$$

for some boundary data $f \in H^{\frac{3}{2}}(\partial D)$ and $g \in H^{\frac{1}{2}}(\partial D)$.

We have that the farfield operator F is injective with dense range provided that k is not a *transmission eigenvalue*, i.e. a value of k for which the homogeneous (i.e. $f = 0$ and $g = 0$ in (4.65) and (4.66)) interior transmission problem has a non trivial solution. We also recall that for $z \in D$, the farfield equation has a nearby solution $g_z^\varepsilon \in L^2(\Omega)$ that satisfies (4.54)-(4.55) if there exists a couple (w_z, v_z) solution of (4.63)-(4.66) with $f = \Phi(\cdot, z)$ and $g = \frac{\partial}{\partial \nu}\Phi(\cdot, z)$.

Since the linear sampling method is expected to fail when k is a transmission eigenvalue and, in particular, for almost all $z \in D$ the norm of a regularized solution $g_{z,\alpha}$ satisfying

$$\lim_{\alpha \to 0} \|F g_{z,\alpha} - \Phi_\infty(\cdot, z)\|_{L^2(\Omega)} = 0 \tag{4.67}$$

is expected to be large for such values of k [26, 29], a possible method for finding transmission eigenvalues would be to solve (4.67) for few fixed $z \in D$ and for values of k in an interval: the transmission eigenvalues would correspond with large values of $k \mapsto \|g_z\|_{L^2(\Omega)}$.

The following theorem formalizes previous considerations (the formulation is an adaptation of the results in [26]).

Theorem 4.2.2. *Let $g_{z,\alpha}$ satisfy (4.67) and z be a point of $\mathbb{R}^2$; let $v_{g_{z,\alpha}}$ be the Herglotz wave function associated to $g_{z,\alpha}$ and let us assume that k is a transmission eigenvalue. Then for almost every $z \in D$, $\|v_{g_{z,\alpha}}\|_{L^2(D)}$ cannot be bounded as $\alpha \to 0$. Otherwise, if k is not a*

transmission eigenvalue, then there exists $g_{z,\alpha}$ satisfying (4.67) such that $\|v_{g_{z,\alpha}}\|_{L^2(D)}$ is bounded as $\alpha \to 0$ for each $z \in D$.

Let us denote by $P(D,k,n)$ the interior transmission problem (4.63)-(4.66) for a domain D of refractive index n and with boundary data $f = \Phi(\cdot,z)$ and $g = \frac{\partial}{\partial \nu}\Phi(\cdot,z)$.

We give in following a corollary of the previous theorem that indicates how, for multiply connected inclusions D, one can identify the transmission eigenvalues associated with each connected component. More precisely, assume that $D = \bigcup_{\hat{j}\in\{j_0,\dots,j_m\}} D_{\hat{j}}$ with $m \in \mathbb{N}$ and $D_{\hat{j}}$ connected for each $\hat{j} \in \{j_0,\dots,j_m\}$ and refer to $P(D_{\hat{j}},k,n_{\hat{j}})$ as the interior transmission problem associated to $D_{\hat{j}}$, with $n_{\hat{j}}$ restriction of n to $D_{\hat{j}}$. We remark that, obviously, the set of transmission eigenvalues for D is the union of transmission eigenvalues for $D_{\hat{j}}$ for $\hat{j} \in \{j_0,\dots,j_m\}$.

Let us consider the farfield equation associated to the whole D and let $g_{z,\alpha}$ satisfy (4.67).

Corollary 4.2.3. *Let $j_p, j_q \in \{j_0,\dots,j_m\}$ and let k^* be a transmission eigenvalue for $P(D_{j_p},k,n_{j_p})$ and not for $P(D_{j_q},k,n_{j_q})$. Then*

- *$\|v_{g_{z,\alpha}}\|_{L^2(D)}$ is unbounded for almost every $z \in D_{j_p}$.*
- *For each $z \in D_{j_q}$ there exists a $g_{z,\alpha}$ satisfying (4.67) such that $\|v_{g_{z,\alpha}}\|_{L^2(D)}$ is bounded.*

Proof. First, we point out that if (w,v) is a solution of $P(D,k,n)$, then $(w_{\bar{j}},v_{\bar{j}})$ (restriction of (w,v) to $D_{\bar{j}}$) would be a solution of $P(D_{\bar{j}},k,n_{\bar{j}})$ and that

$$\|v\|^2_{L^2(D)} = \sum_{\bar{j}\in\{j_0,\dots,j_m\}} \|v_{\bar{j}}\|^2_{L^2(D_{\bar{j}})}. \tag{4.68}$$

- Let k^* be a transmission eigenvalue for $P(D_{j_p},k,n_{j_p})$. Then, from Theorem 4.2.2, it follows that $\|v_{g_{z,\alpha},j_p}\|_{L^2(D_{j_p})}$ has to be unbounded for almost every $z \in D_{j_p}$. Then, by (4.68), $\|v_{g_{z,\alpha}}\|_{L^2(D)}$ is unbounded for almost every $z \in D_{j_p}$.
- If $z \in D_{j_q}$, $(0,-\Phi(\cdot,z))$ is a (bounded) solution of $P(D_{j_p},k,n_{j_p})$. Hence, (w,v) such that $w = 0$ on D, $v = 0$ on $D_{\bar{j}}$ for each $\bar{j} \neq j_p$ and $v = -\Phi(\cdot,z)$ on D_{j_p} is a bounded solution of $P(D,k^*,n)$. Denseness of the set of Herglotz wave functions implies the existence of a $g_{z,\alpha}$ such that $\|v_{g_{z,\alpha}} - v\|_{L^2(D)} \to 0$ for $\alpha \to 0$. This implies that $\|Fg_{z,\alpha} - \Phi(\cdot,z)\|_{L^2(\Omega)} \to 0$ for $\alpha \to 0$.

□

Identification of the refractive index

As explained before, solving the homogeneous interior transmission eigenvalue problem means, knowing the shape of D and the pointwise values of n, find k^* such that there exists a non

trivial solution u of the problem $P(D,k,n)$ (from now we will refer to $P(D,k,n)$ as to the homogeneous interior transmission problem).

Let us change the point of view: since transmission eigenvalues are detectable without knowing $n(x)$, it is possible to consider directly the problem $P(D,k^*,n)$ where D and k^* are known and n is unknown. Moreover, supposing n constant, $P(D,k^*,n)$ could be treated as a classical generalized eigenvalue problem.

Now, we are ready to explain the idea of the whole method. Given the inverse scattering problem of detecting an inhomogeneous medium of index n, one can first reconstruct the shape of the unknown object D using the LSM (or other similar qualitative methods). Then, fixing a z in D and plotting the norm of g (solution of (4.67)) for every k in an interval, transmission eigenvalues k^* of $P(D,k,n)$ can be detected. With their knowledge, it will be possible to solve the problem of finding n^* so that $P(D,k^*,n^*)$ has a non trivial solution; i.e. finding n^* for which k^* is a transmission eigenvalue of $P(D,k,n^*)$.

Proposition 4.2.4. *Assume that n is constant. Then, the homogeneous interior transmission problem $P(D,k,n)$ is equivalent to the problem of finding $u \in H_0^2(D)$ satisfying*

$$(\Delta + k^2)\Delta u = -k^2 n(\Delta + k^2)u \qquad \text{in } D. \tag{4.69}$$

Further, the eigenvalue problem: find $(u,n) \in H_0^2(D) \times \mathbb{R}$ satisfying (4.69), admits a countable number of eigenvalues $n \in \mathbb{R}$.

Proof. The equivalence between (4.64)-(4.66) (with n constant) and (4.69) can be easily proved by setting $u = w - v$ ([23, 78]).
Problem (4.69) is equivalent to $(\Delta + k^2)^2 u = \lambda(\Delta + k^2)u$ with $\lambda = k^2(1-n)$. The operator $(\Delta + k^2)^2 : H_0^2(D) \mapsto H_0^2(D)$ is bijective and self adjoint while operator $(\Delta + k^2) : H_0^2(D) \mapsto H_0^2(D)$ is compact, injective and self adjoint. Then, the existence of a countable number of real eigenvalues λ can be proved applying classical spectral theory for compact self adjoint operators. □

Remark 4.2.1. *The constant approximation n^* of n is chosen as the smallest eigenvalue of problem (4.69) associated to the smallest transmission eigenvalue k_0^*.*

The main difficulty related to numerical solutions of the eigenvalue problem (4.69) comes from the fourth order operator which requires the use of C^1 finite elements. We shall in the following provide mixed formulations of the problem that allows the use of C^0 finite elements. These formulations, inspired by classical mixed formulation for the biharmonic problem, are those used in the numerical simulations (done with standard P_1 Lagrange finite elements).

Proposition 4.2.5. *Assume that n is constant. Then if $u \in H_0^2(D) \cap H^3(D)$ is such that (4.69) is valid, then u and $\upsilon = (\Delta + k^2)u$ are solution of the variational problem: "Find $u \in H_0^1(D)$*

and $\mathrm{U} \in H^1(D)$ *such that*

$$\int_D (\mathrm{U}\mathrm{V} + \nabla u \nabla \mathrm{V} - k^2 u \mathrm{V} - \nabla \mathrm{U} \nabla v) dx = -k^2 n \int_D (k^2 uv - \nabla u \nabla v) dx \tag{4.70}$$

for all $v \in H_0^1(D)$, $\mathrm{V} \in H^1(D)$*".*
Conversely, if $u \in H_0^1(D) \cap H^3(D)$ *and* $\mathrm{U} \in H^2(D)$ *are solutions of (4.70), then* $u \in H_0^2(D)$ *and satisfies (4.69).*

Proof. Substituting $\mathrm{U} = (\Delta + k^2)u$, equation (4.69) becomes $\Delta \mathrm{U} = -k^2 n \mathrm{U}$. Multiplying both equations respectively against test functions $\mathrm{V} \in H^1(D)$ and $v \in H_0^1(D)$ and applying Green's identity we obtain

$$\int_D (\nabla u \nabla \mathrm{V} - k^2 u \mathrm{V}) dx = -\int_D \mathrm{U}\mathrm{V} dx \tag{4.71}$$

and

$$-\int_D \nabla \mathrm{U} \nabla v dx = -k^2 n \int_D (k^2 uv - \nabla u \nabla v) dx. \tag{4.72}$$

Summing the two equations we obtain (4.70).

Reciprocally, starting with (4.70) we can go back to equations (4.69) by assuming that $u \in H_0^1(D) \cap H^3(D)$ and $\mathrm{U} \in H^2(D)$. Using Green's identity we obtain that (4.71) is equivalent to

$$\int_D (\mathrm{U} - \Delta u - k^2 n u) \mathrm{V} dx = \int_{\partial D} \frac{\partial u}{\partial \nu} \mathrm{V}\, ds(x) \tag{4.73}$$

for all $\mathrm{V} \in H^1(D)$. Since $\mathcal{C}_c^\infty(D) \subset H^1(D)$ we get $\int_D (\mathrm{U} - \Delta u - k^2 n u) \mathrm{V} dx = 0$ for all $\mathrm{V} \in \mathcal{C}_c^\infty(D)$. Hence, $\mathrm{U} - \Delta u - k^2 n u = 0$ almost everywhere in D and consequently $\frac{\partial u}{\partial \nu} = 0$ almost everywhere on ∂D. The latter implies in particular that $u \in H_0^2(D)$. Similar arguments applies to (4.72) and prove that $\Delta \mathrm{U} = -k^2 n \mathrm{U}$ almost everywhere in D, which implies (4.69). □

The case of an inhomogeneous background

The approach described in the previous subsection can be extended to the case in which the medium is embedded in an inhomogeneous background. Let us consider the case where the inclusion D is embedded in a background with index n_b. Then the homogeneous interior transmission problem is formulated as follows:

$$\Delta w + k^2 n_D w = 0 \qquad \text{in } D, \tag{4.74}$$

$$\Delta v + k^2 n_b v = 0 \qquad \text{in } D, \tag{4.75}$$

$$w = v \qquad \text{on } \partial D, \tag{4.76}$$

$$\frac{\partial w}{\partial \nu} = \frac{\partial v}{\partial \nu} \qquad \text{on } \partial D. \tag{4.77}$$

where n_D denotes the index of D. Taking $u = w - v$ in (4.74)-(4.77) and applying the operator $\Delta + k^2 n_D$ to the difference (4.74)-(4.75) we obtain

$$(\Delta + k^2 n_D)\frac{1}{k^2(n_b - n_D)}(\Delta + k^2 n_b)u = 0 \qquad \text{in } D \tag{4.78}$$

$$u = 0, \qquad \frac{\partial u}{\partial \nu} = 0 \qquad \text{on } \partial D. \tag{4.79}$$

Substituting

$$\mathrm{U} := \frac{1}{k^2(n_b - n_D)}(\Delta + k^2 n_b)u \tag{4.80}$$

we obtain

$$\Delta \mathrm{U} = -k^2 n_D \mathrm{U} \qquad \text{in } D. \tag{4.81}$$

Multiplying (4.81) by a test function $v \in H_0^1(D)$ and (4.80) by $k^2(n_b - n_D)\mathrm{V}$ with $\mathrm{V} \in H^1(D)$, applying the Green's formula, taking into account the boundary conditions satisfied by u and adding the two equations, one ends up with the following variational formulation

$$\int_D (k^2 n_b(u\mathrm{V} - \mathrm{U}\mathrm{V}) - \nabla u \nabla \mathrm{V} - \nabla \mathrm{U} \nabla v)dx = \lambda \int_D (\mathrm{U}v + \mathrm{U}\mathrm{V})dx, \tag{4.82}$$

which is valid for all $v \in H_0^1(D)$ and $\mathrm{V} \in H^1(D)$ and with $\lambda := -k^2 n_D$. Using this procedure and similar arguments as in the proof of Proposition 4.2.5, one can prove the following.

Proposition 4.2.6. *If n_D is assumed to be constant and $\exists w, v \in L^2(D)$ and $w - v =: u \in H_0^2(D) \cap H^3(D)$ such that (4.74)-(4.77) is valid, then u and $\mathrm{U} = \frac{1}{k^2(n_b - n_D)}(\Delta + k^2 n_b)u$ are solution of the variational problem: "Find $u \in H_0^1(D)$ and $\mathrm{U} \in H^1(D)$ such that*

$$\int_D (k^2 n_b(u\mathrm{V} - \mathrm{U}\mathrm{V}) - \nabla u \nabla \mathrm{V} - \nabla \mathrm{U} \nabla v)dx = \lambda \int_D (\mathrm{U}v + \mathrm{U}\mathrm{V})dx \tag{4.83}$$

for all $v \in H_0^1(D)$, $\mathrm{V} \in H^1(D)$".
Conversely, if $u \in H_0^1(D) \cap H^3(D)$ and $\mathrm{U} \in H^2(D)$ are solutions of (4.83), then $u \in H_0^2(D)$ and satisfies (4.78).

Remark 4.2.2. *In the case of inhomogeneous background, (4.51) takes the form of*

$$[Fg_z](\cdot) = G_\infty(\cdot, z), \tag{4.84}$$

where G_∞ and F are defined as (4.61), taking into account the presence of the inhomogeneous background. As in the homogeneous case, $k \mapsto \|g_z\|_{L^2(\Omega)}$ is expected to have peaks for k being a transmission eigenvalue for a.e. $z \in D$. This procedure allows us to compute the transmission eigenvalues from farfield data.

A remark on the case of absorbing background

It is well known that, when a non-absorbing object of support D is embedded in a background such that $Im(n_b) > 0$, then there are no real transmission eigenvalues associated with (4.74)-(4.77) [41]. Since complex transmission eigenvalues are not detectable by the procedure previously indicated in (Remark 4.2.2), this means that our method providing estimates on the index of refraction is not applicable.

However, in this preliminary remark something is not sufficiently precise: the definition of the background index inside D has no physical meaning since the "physical index" of the medium inside D is n. For backgrounds with constant indexes or for layered backgrounds, a "natural extension" of the definition of the background index inside D can be defined. But this is mainly only for a mathematical or numerical convenience.

This simple consideration suggests that there can be some degrees of freedom in the definition of n_b inside D, which is the part used in the interior transmission problem (4.74)-(4.77). As far as the inverse problem of determining n is concerned, this is feasible since at this stage we assume that D is known. In particular if we choose n_b to be a real constant (different from n_D) in D, then we are back again to the case where the interior transmission problem has real eigenvalues and therefore one would be able to apply the procedure previously explained to get estimates on n_D. This procedure will be validated by some numerical experiment in the numerical sections.

Of course there is an extra price to pay: it is hidden in the step of determining the transmission eigenvalue from farfield data. Indeed when one complexifies the background index, this makes the computation of $u^s_{b,\infty}$ in (4.61) more costly.

We finally observe that this procedure can also be applied in the case without absorption if one would like to use the (simpler) formulation of the interior transmission problem with constant index.

4.2.3. The case of TE polarization

Our results for TM polarized waves can be extended to the case of transverse electric (TE) polarization, i.e. the case for which the magnetic component of the field (originated by the incidence of a time harmonic plane wave) vibrates parallel to the axis of the infinite cylinder that is assumed to have cross section D. The main steps of the inversion algorithm are the same as in the TM case and we shall hereafter only give a sketch of the main differences.

Let us first quickly introduce the direct scattering problem for a scatterer D of refractive index n in the case of TE incident plane waves. The total field $u \in H^1_{\text{loc}}(\mathbb{R}^2)$ satisfies

$$\nabla \cdot (\frac{1}{n(x)} \nabla u(x)) + k^2 u(x) = 0 \qquad \text{in } \mathbb{R}^2, \tag{4.85}$$

$$u(x) = u^i(x) + u^s(x) \quad \text{with} \quad u^i(x) = \exp^{ikx\cdot d}, \tag{4.86}$$

$$\lim_{r\to\infty} \sqrt{r}(\frac{\partial u^s(x)}{\partial r} - iku^s(x)) = 0. \tag{4.87}$$

The associated farfield pattern as well as the farfield operator can be deduced as in the TM case. Theorem 4.2.1 is also still valid in the present case under the same assumption on the refractive index.

Transmission eigenvalues

In this case, the homogeneous interior transmission problem is defined as follows [25]: find $\tilde{w}, v \in L^2(D)$ such that $\tilde{w} - v \in H^1(D)$, $\nabla \cdot (\frac{1}{n}\nabla\tilde{w} - \nabla v) \in L^2(D)$ and

$$\nabla \cdot (\frac{1}{n}\nabla\tilde{w}) + k^2\tilde{w} = 0 \qquad \text{in } D, \tag{4.88}$$

$$\Delta v + k^2 v = 0 \qquad \text{in } D, \tag{4.89}$$

$$\tilde{w} = v \qquad \text{on } \partial D, \tag{4.90}$$

$$\frac{1}{n}\frac{\partial\tilde{w}}{\partial\nu} = \frac{\partial v}{\partial\nu} \qquad \text{on } \partial D. \tag{4.91}$$

Since the linear sampling method works independently from wave polarization, results obtained in the case of transverse magnetic waves as well as Theorem 4.2.2 and Corollary 4.2.3 could be extended to the case of transverse electric polarization. Hence, again, transmission eigenvalues are detectable from the knowledge of farfield patterns and the resolution of the eigenvalue problem $P(D, k_0^*, n)$ can provide us with a constant approximation n^* of n.

Mixed formulations of the refractive index eigenvalues problems

We shall explain here how problem (4.88)-(4.91) can be formulated as an eigenvalue problem for a constant n, assuming that k and D are known.

Proposition 4.2.7. *Considering n constant, problem (4.88)-(4.91) is equivalent to the problem of finding* $u := \frac{1}{n}\tilde{w} - v \in H^2(D)$ *such that*

$$(\Delta + k^2)\Delta u = -k^2 n(\Delta + k^2)u \qquad \text{in } D \tag{4.92}$$

$$\Delta u = 0, \qquad \frac{\partial u}{\partial\nu} = 0 \qquad \text{on } \partial D. \tag{4.93}$$

Proof. Substituting $w = \frac{1}{n}\tilde{w}$ and using (4.88) and (4.89) it is easy to obtain

$$\Delta w + k^2 n w = 0 \qquad \text{in } D, \tag{4.94}$$

$$\Delta v + k^2 v = 0 \qquad \text{in } D, \tag{4.95}$$

$$\Delta w = -k^2\tilde{w} = -k^2 v = \Delta v \qquad \text{on } \partial D \tag{4.96}$$

$$\frac{\partial w}{\partial\nu} = \frac{\partial v}{\partial\nu} \qquad \text{on } \partial D. \tag{4.97}$$

The equivalence between (4.94)-(4.97) and (4.92)-(4.93) can be shown as is the TM case. □

Proposition 4.2.8. *Assuming n constant then: if $u \in H^3(D)$ is such that (4.92)-(4.93) is valid, then u and $\mathrm{U} := \Delta u$ are solution of the problem: "Find $u \in H^1(D)$ and $\mathrm{U} \in H_0^1(D)$ such that*

$$\int_D (\mathrm{U}v + \nabla u \nabla \mathrm{V} + k^2 \mathrm{U}\mathrm{V} - \nabla \mathrm{U} \nabla \mathrm{V}) dx = -k^2 n \int_D (k^2 u \mathrm{V} - \nabla u \nabla \mathrm{V}) dx. \tag{4.98}$$

for all $v \in H^1(D)$, $\mathrm{V} \in H_0^1(D)$".

Conversely, if $u \in H^3(D)$ and $\mathrm{U} \in H_0^1(D) \cap H^2(D)$ are solutions of (4.98), then (4.92)-(4.93) is satisfied by u.

Proof. Substituting $\mathrm{U} = \Delta u$, equation (4.92) becomes $(\Delta + k^2)\mathrm{U} = -k^2 n(\Delta + k^2)u$. Multiplying both equations respectively against test functions $v \in H^1(D)$ and $\mathrm{V} \in H_0^1(D)$ and applying Green's identity we obtain

$$\int_D \mathrm{U} v dx = -\int_D \nabla u \nabla v dx \tag{4.99}$$

and

$$\int_D (-\nabla \mathrm{U} \nabla \mathrm{V} + k^2 \mathrm{U}\mathrm{V}) dx = -k^2 n \int_D (k^2 u \mathrm{V} - \nabla u \nabla \mathrm{V}) dx. \tag{4.100}$$

Summing the two equations we obtain (4.98). The reverse implication is a classical exercise similar to the one done at the end of the proof of Proposition 4.2.5.

□

The case of an inhomogeneous background

The case of a scatterer embedded in an inhomogeneous background illuminated by TE polarized plane waves is more complex. Nevertheless, following the approach of [25], it is possible to write the homogeneous interior transmission problem as a generalized eigenvalue problem with $\lambda = -k^2 n_D$ as eigenvalues.

Let us again consider an inclusion D with index n_D embedded in a background with index n_b; the homogeneous interior transmission problem is formulated as follows:

$$\nabla \cdot (\frac{1}{n_D} \nabla w) + k^2 w = 0 \qquad \text{in } D, \tag{4.101}$$

$$\nabla \cdot (\frac{1}{n_b} \nabla v) + k^2 v = 0 \qquad \text{in } D, \tag{4.102}$$

$$w = v \qquad \text{on } \partial D, \tag{4.103}$$

$$\frac{1}{n_D} \frac{\partial}{\partial \nu} w = \frac{1}{n_b} \frac{\partial}{\partial \nu} v \qquad \text{on } \partial D. \tag{4.104}$$

Taking the gradient of (4.101) and (4.102) and substituting $\mathbf{w} = \frac{1}{n_D} \nabla w$ and $\mathbf{v} = \frac{1}{n_b} \nabla v$ in

(4.101)-(4.104) we obtain

$$\nabla(\nabla \cdot \mathbf{w}) + k^2 n_D \mathbf{w} = 0 \qquad \text{in } D, \tag{4.105}$$

$$\nabla(\nabla \cdot \mathbf{v}) + k^2 n_b \mathbf{v} = 0 \qquad \text{in } D, \tag{4.106}$$

with boundary conditions

$$\nu \cdot \mathbf{w} = \nu \cdot \mathbf{w} \qquad \text{and } \nabla \cdot \mathbf{w} = \nabla \cdot \mathbf{v} \qquad \text{on } \partial D. \tag{4.107}$$

Setting $\mathbf{u} = \mathbf{w} - \mathbf{v}$ and taking the difference between (4.105) and (4.106) we obtain

$$\frac{1}{k^2(n_b - n_D)}(\nabla\nabla \cdot + k^2 n_b)\mathbf{u} = \mathbf{w}. \tag{4.108}$$

Then, applying $(\nabla\nabla \cdot + k^2 n_D)$ to both sides,

$$(\nabla\nabla \cdot + k^2 n_D)\frac{1}{k^2(n_b - n_D)}(\nabla\nabla \cdot + k^2 n_b)\mathbf{u} = 0 \qquad \text{in } D. \tag{4.109}$$

Substituting $\mathbf{U} = \frac{1}{k^2(n_b - n_D)}(\nabla\nabla \cdot + k^2 n_b)\mathbf{u}$ we obtain $(\nabla\nabla \cdot + k^2 n_D)\mathbf{U} = 0$ in D, which gives rise to the system

$$(\nabla\nabla \cdot + k^2 n_b)\mathbf{u} - k^2 n_b \mathbf{U} = -k^2 n_D \mathbf{U} \qquad \text{in } D, \tag{4.110}$$

$$\nabla\nabla \cdot \mathbf{U} = -k^2 n_D \mathbf{U} \qquad \text{in } D, \tag{4.111}$$

$$\nu \cdot \mathbf{u} = 0 \qquad \text{and} \qquad \nabla \cdot \mathbf{u} = 0 \qquad \text{on } \partial D. \tag{4.112}$$

The latter eigenvalue problem for eigenvalues $\lambda = -k^2 n_D$ can be formulated in a variational form as in the inhomogeneous TM case by respectively replacing the variational spaces $H^1(D)$ and $H_0^1(D)$ with

$$H_{\text{div}}(D) := \{\mathbf{V} \in L^2(D)^2 \; ; \; \nabla \cdot \mathbf{V} \in L^2(D)\} \ni \mathbf{U},$$

and

$$\{\mathbf{v} \in H_{\text{div}}(D) \; ; \; \nu \cdot \mathbf{u} = 0 \text{ on } \partial D\} \ni \mathbf{u}.$$

The numerical implementation of the resulting variational formulation requires the use of H_{div} elements. We did not validate our procedure in the present case.

4.2.4. Numerical experiments: the case where the shape is known

Before presenting some numerical results concerning the reconstruction of the shape and the constant approximation of the refractive index of unknown objects, let us show how - solving $P(D, k_0^*, n)$ as a generalized eigenvalue problem - we obtain a good approximation of n when both D and its first transmission eigenvalue are known.

We focus on the case of a circular geometry and we shall investigate two configurations: in the first one, the refractive index is constant (Figure 4.9 (a)) and in the second one the index of refraction has two different values in two concentric circles (Figure 4.9 (b)).

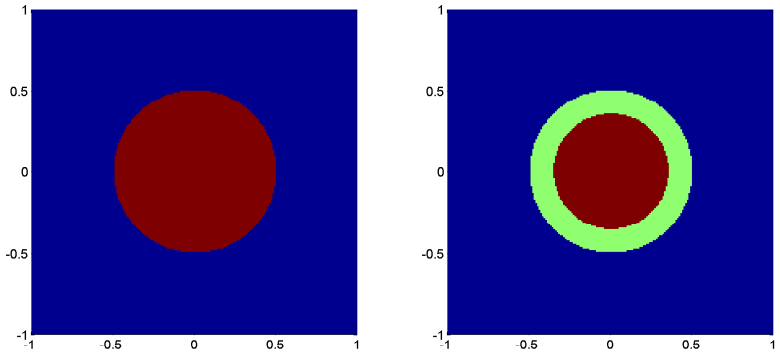

(a) (b)

Figure 4.9: Configuration of the refractive index in a circular domain D: homogeneous case (a), piecewise constant case (b).

In both cases the first transmission eigenvalue is analytically computable using the following result (that can be obtained using separation of variables).

Proposition 4.2.9. *For a circle of radius R and refractive index n, if $k^*_{0,\mathrm{TM}}$ and $k^*_{0,\mathrm{TE}}$ denote the first transmission eigenvalues respectively in the case of transverse magnetic and transverse electric polarized waves, then*

$$k^*_{0,\mathrm{TM}} = \min\{k | \exists p \in \mathbb{N} \ s.t. \ \det(A^{\mathrm{TM}}_{p,k}) = 0\},$$
$$k^*_{0,\mathrm{TE}} = \min\{k | \exists p \in \mathbb{N} \ s.t. \ \det(A^{\mathrm{TE}}_{p,k}) = 0\},$$

with

$$A^{\mathrm{TM}}_{p,k} := \begin{pmatrix} J_p(kR) & J_p(k\sqrt{n}R) \\ kJ_{p-1}(kR) - \frac{p}{R}J_p(kR) & k\sqrt{n}J_{p-1}(k\sqrt{n}R) - \frac{p}{R}J_p(k\sqrt{n}R) \end{pmatrix},$$
$$A^{\mathrm{TE}}_{p,k} := \begin{pmatrix} J_p(kR) & J_p(k\sqrt{n}R) \\ kJ_{p-1}(kR) - \frac{p}{R}J_p(kR) & \frac{1}{\sqrt{n}}(k\sqrt{n}J_{p-1}(k\sqrt{n}R) - \frac{p}{R}J_p(k\sqrt{n}R)) \end{pmatrix}.$$

Proposition 4.2.10. *For a circle made of two concentric layers of external radius R_e and internal radius R_i, if n_e and n_i respectively denote the refractive index of the exterior and interior layers and if $k^*_{0,\mathrm{TM}}$ and $k^*_{0,\mathrm{TE}}$ are the first transmission eigenvalues respectively in the case of transverse magnetic and transverse electric polarized waves, then*

$$k^*_{0,\mathrm{TM}} = \min\{k | \exists p \in \mathbb{N} \ s.t. \ \det(B^{\mathrm{TM}}_{p,k}) = 0\},$$
$$k^*_{0,\mathrm{TE}} = \min\{k | \exists p \in \mathbb{N} \ s.t. \ \det(B^{\mathrm{TE}}_{p,k}) = 0\},$$

with

$$B_{p,k}^{\mathrm{TM}} := \begin{pmatrix} J_p(kR_e) & -J_p(k\sqrt{n_e}R_e) & -H_p^{(1)}(k\sqrt{n_e}R_e) & 0 \\ J_p'(kR_e) & -J_p'(k\sqrt{n_e}R_e) & -H_p^{(1)'}(k\sqrt{n_e}R_e) & 0 \\ 0 & J_p(k\sqrt{n_e}R_i) & H_p^{(1)}(k\sqrt{n_e}R_i) & -J_p(k\sqrt{n_i}R_i) \\ 0 & J_p'(k\sqrt{n_e}R_i) & H_p^{(1)'}(k\sqrt{n_e}R_i) & -J_p'(k\sqrt{n_i}R_i) \end{pmatrix},$$

$$B_{p,k}^{\mathrm{TE}} := \begin{pmatrix} J_p(kR_e) & -J_p(k\sqrt{n_e}R_e) & -H_p^{(1)}(k\sqrt{n_e}R_e) & 0 \\ J_p'(kR_e) & -\frac{1}{n_e}J_p'(k\sqrt{n_e}R_e) & -\frac{1}{n_e}H_p^{(1)'}(k\sqrt{n_e}R_e) & 0 \\ 0 & J_p(k\sqrt{n_e}R_i) & H_p^{(1)}(k\sqrt{n_e}R_i) & -J_p(k\sqrt{n_i}R_i) \\ 0 & \frac{1}{n_e}J_p'(k\sqrt{n_e}R_i) & \frac{1}{n_e}H_p^{(1)'}(k\sqrt{n_e}R_i) & -\frac{1}{n_i}J_p'(k\sqrt{n_i}R_i) \end{pmatrix}.$$

Remark 4.2.3. *Studying or plotting the behavior of* $\det(A_{p,k}^{\mathrm{TM}})$, $\det(A_{p,k}^{\mathrm{TE}})$, $\det(B_{p,k}^{\mathrm{TM}})$, $\det(B_{p,k}^{\mathrm{TE}})$ *for* $k \in \mathbb{R}$*, one can observe that few* $p \in \mathbb{N}$ *(the firsts) are enough for determining* k_0^**.*

Problem $P(D, k_0^*, n)$ is solved with P_1-finite elements based on the variational formulations (4.70) and (4.98). The discretization step is $\sim \frac{1}{10}$ of the wavelength inside the medium. The matrices are assembled using FreeFem++[3] and the associate eigenvalue problem is solved in Matlab with the preset function *eigs*, in modality *'sm'* (i.e. look for smaller magnitude eigenvalues). Since the eigenvalue problem formulation correspond with a generalized eigenvalue problem for non self-adjoint matrices and with degenerate mass matrices, there is no guarantee for convergence of the algorithm. Moreover, the mixed formulation is equivalent to the original one only under regularity assumptions on the solution. This is why parasite values are observed in the numerical computations of the eigenvalues. These parasite values correspond to solutions u that do not satisfy the boundary condition $\partial u/\partial \nu = 0$ on ∂D. From the practical point of view we observed that these bad values can simply be cut off by respecting the lower bound $n^* = \min\{-\lambda/k_0^{*2} > 1\}$ [29, 25].

Figure 4.10 shows results achievable when D is a circle of radius 0.5 and has a constant refractive index. The value of n is well recovered, with a better precision occurring for small n. As it is clear from Figure 4.10, with the increasing of the value of n, k_0^* decreases, clustering around $k = 1$. Since the computation of transmission eigenvalues is precise up to two digits, the previous consideration suggests that the difference in precision between reconstructions for small and large values of n is due to a not enough precise approximation of k_0^* for large n.

[3] downloadable at http://www.freefem.org/ff++/

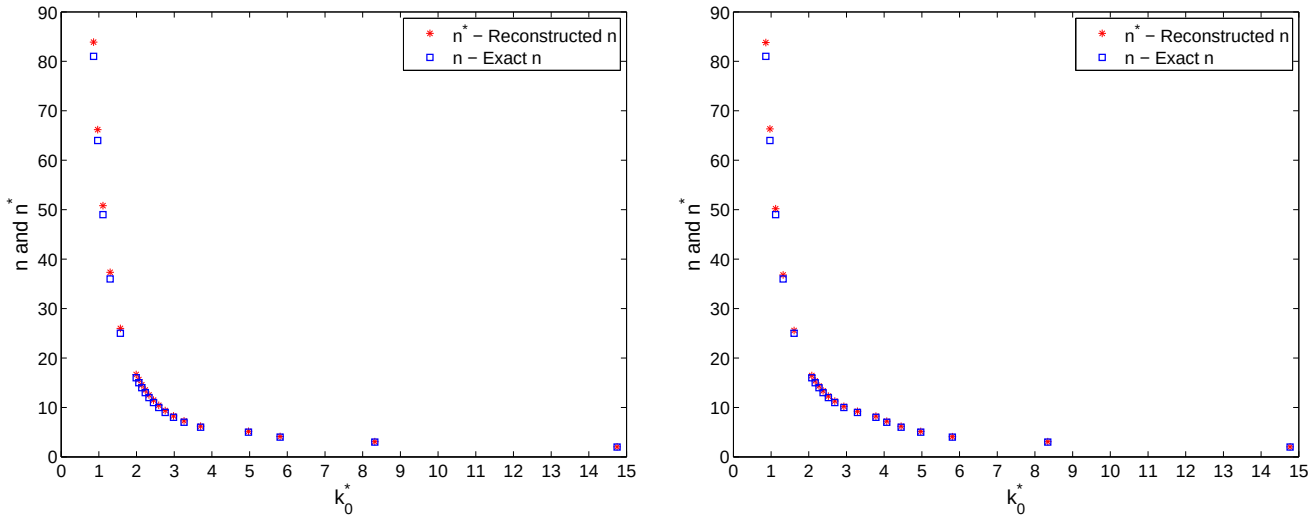

Figure 4.10: Reconstructed index for a homogeneous circle of radius 0.5. TM case (left) and TE case (right).

Figures 4.11 and 4.12 are associated with the two layered case where the areas of the two layers are equal ($R_e = 0.5$ and $R_i = \frac{1}{2\sqrt{2}}$). The values of n_e and n_i are varied by maintaining the difference $n_e - n_i$ equals to 6, (for example $(n_e, n_i) = (8, 2), (9, 3), ...$) for Figure 4.11. As in previous figures, we plot the value of the reconstructed value n^* of n (y-axis) against the first transmission eigenvalue (x-axis); blue lines corresponding to the value of n_i and n_e. They are over plotted in order to clarify wether or not n^* fall in $[n_i, n_e]$. In Figure 4.12 the role of n_e and n_i are reversed to emphasize how a different structure (and not only different values of n or different layer areas) could affect the reconstruction.

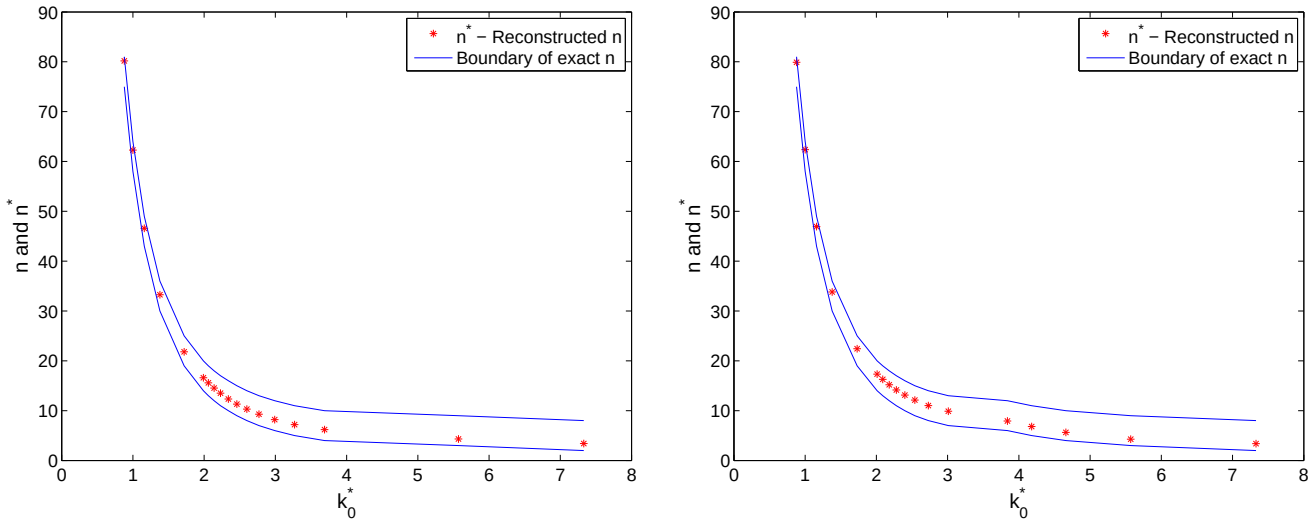

Figure 4.11: Reconstruction of the index in the case of a two layered circle ($R_e = 0.5$ and $R_i = \frac{1}{2\sqrt{2}}$). The exact refractive index is such that $n_e - n_i = 6$. The reconstructed value is shown by * and the solid line indicate the exact values of n_e and n_i. TM case (left) and TE case (right).

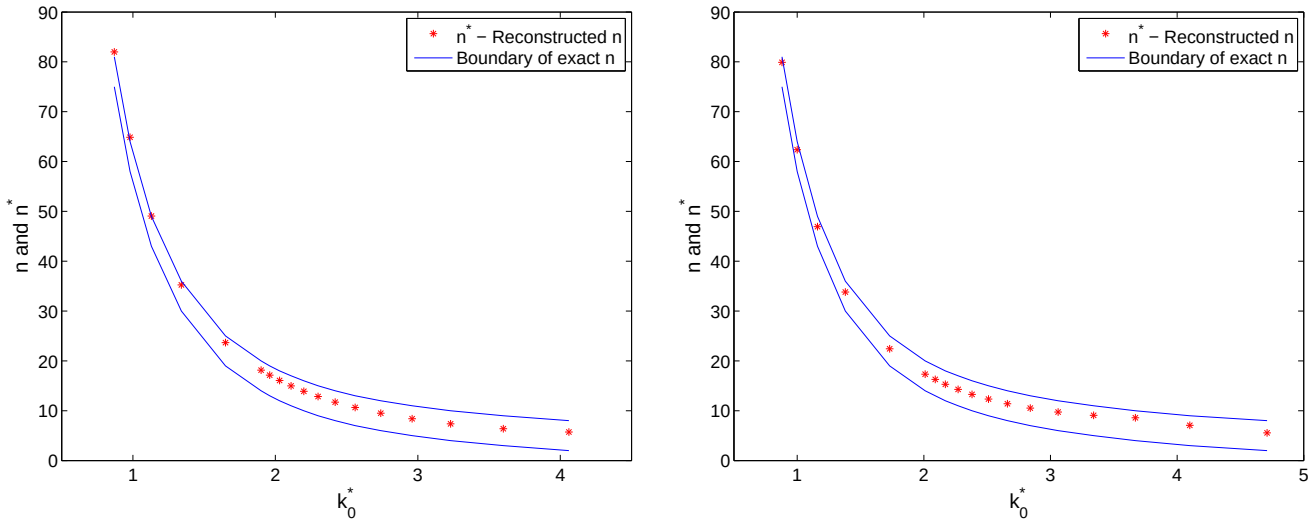

Figure 4.12: Same settings as in Figure 4.11 but with $n_i - n_e = 6$. TM case (left) and TE case (right).

In the previous examples one observes that it is not simple to relate the value of the reconstructed constant index n^* with non-constant refractive indexes. This is confirmed by next examples where we have not been able to observe a relation more accurate than

$$\min_{x\in D} n(x) \leq n^* \leq \max_{x\in D} n(x). \tag{4.113}$$

Understanding how transmission eigenvalues distribute depending on shape and dimension of the scatterer, on its index of refraction and on polarization of the wave, is, at present, still an open problem. The next few experiments are an overview of this complex relation between n^* and different configurations of the material inside D which is still a circle of radius 0.5.

With Figures 4.13 - 4.18, (respectively for TM and TE polarization), we want to investigate how different structures of n would lead to different transmission eigenvalues (and consequently to different n^*) even if $\min_D n$ and $\max_D n$ are not modified. In both cases we consider a circular scatterer of radius 0.5 containing a concentric circular layer of varying radius. For fixed values of the refractive index ($n_i = 6$, $n_e = 12$), ($n_i = 3$, $n_e = 15$) and ($n_i = 20$, $n_e = 26$), we show how k_0^* and n^* behave with respect to the radius of the internal circle R_i. Moreover, in each figure, the value of the obtained constant estimate of the refractive index is compared with the value of the weighted average of the refractive index (squared plotted).

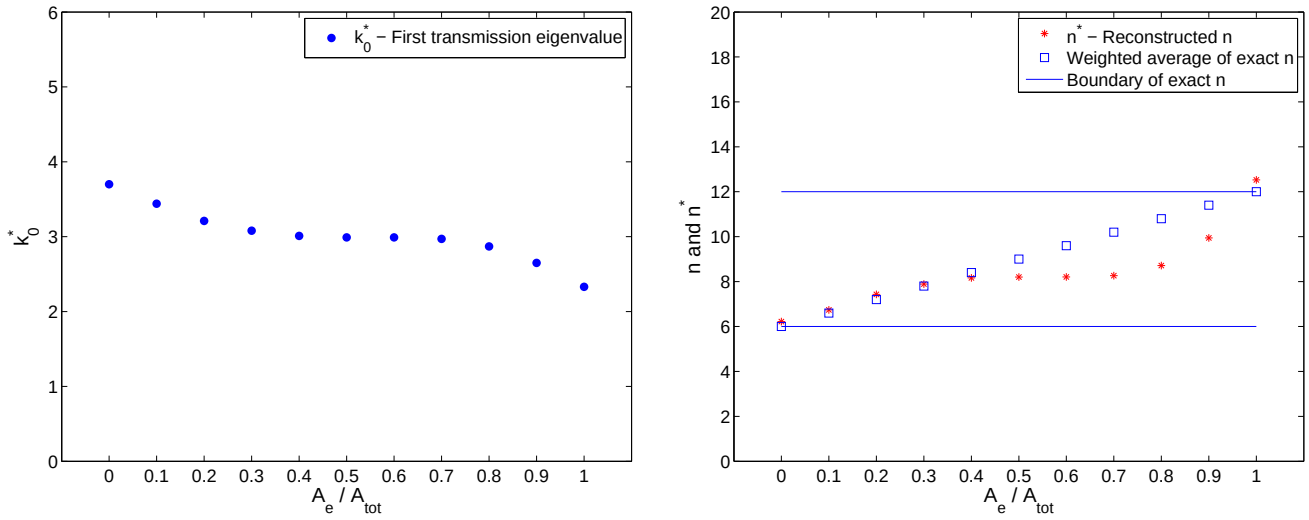

Figure 4.13: Results for TM polarized incident waves in the case of a two layered circle with $R_e = 0.5$ and a varying R_i. The exact index values are $n_i = 6$ and $n_e = 12$. The x-axis represents the values of A_e/A_{tot}, ratio of external layer area to the total circle area. Left: first transmission eigenvalue. Right: reconstructed n^*.

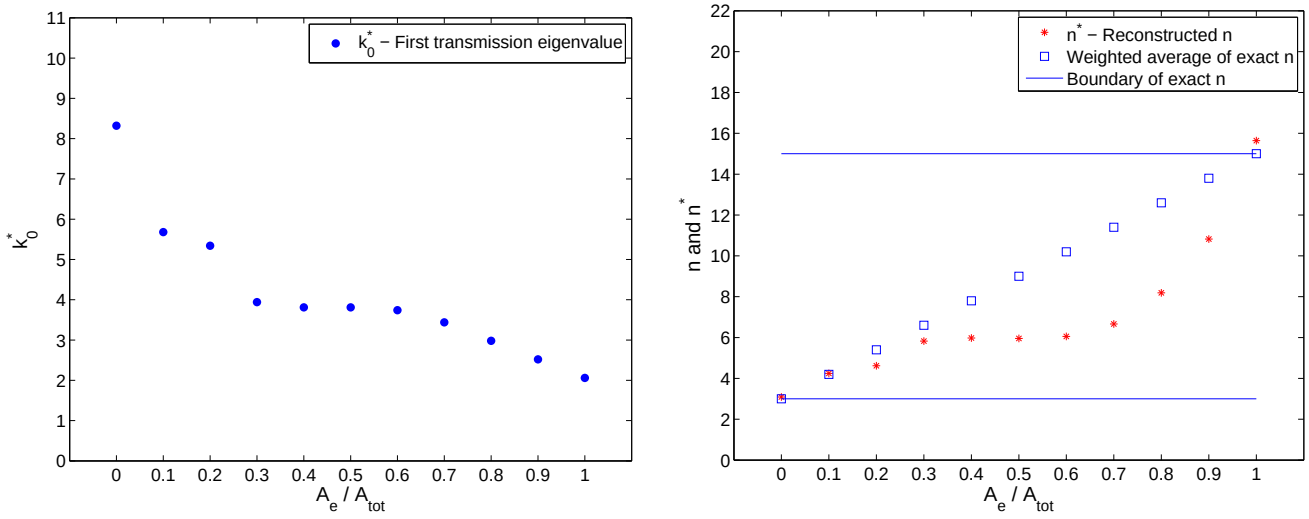

Figure 4.14: Results for TM polarized incident waves in the case of a two layered circle with $R_e = 0.5$ and a varying R_i. The exact index values are $n_i = 3$ and $n_e = 15$. The x-axis represents the values of A_e/A_{tot}, ratio of external layer area to the total circle area. Left: first transmission eigenvalue. Right: reconstructed n^*.

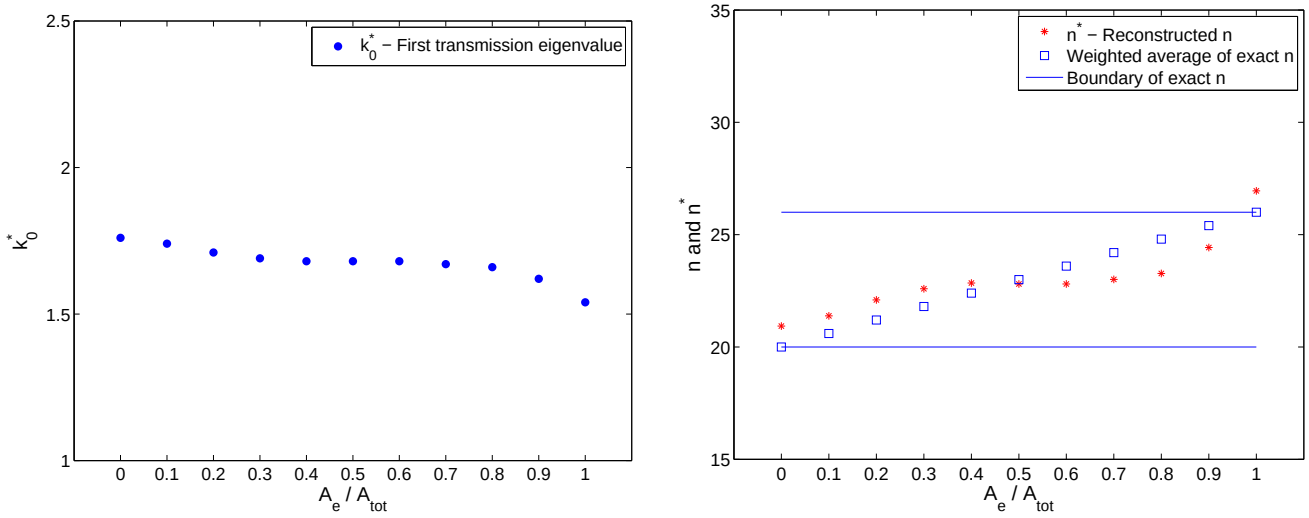

Figure 4.15: Results for TM polarized incident waves in the case of a two layered circle with $R_e = 0.5$ and a varying R_i. The exact index values are $n_i = 20$ and $n_e = 26$. The x-axis represents the values of A_e/A_{tot}, ratio of external layer area to the total circle area. Left: first transmission eigenvalue. Right: reconstructed n^*.

As expected, since the first transmission eigenvalue decreases with respect to the index of refraction [31], it should be increasing with respect to R_i (since $n_e > n_i$) and therefore decreasing with respect to the area of the external layer A_e. However, the dependence is completely nonlinear. The values of n^* have reversed monotonicity property with respect to the first transmission eigenvalue and therefore increases with A_e. The behavior of n^* is also nonlinear as demonstrated by the comparison with the weighted average of the exact n.

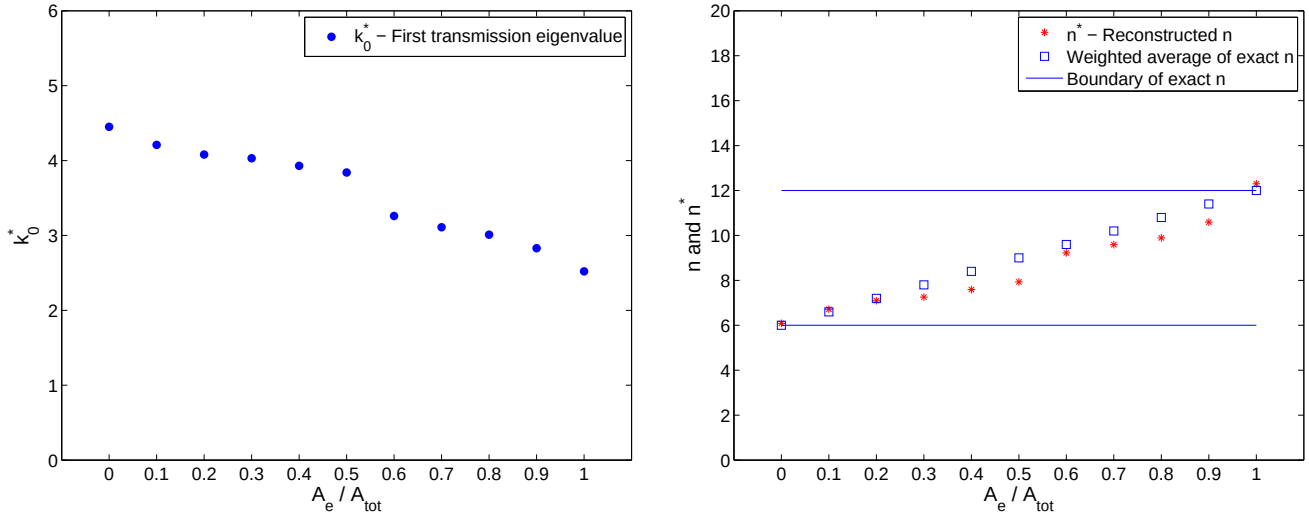

Figure 4.16: Results for TE polarized incident waves in the case of a two layered circle with $R_e = 0.5$ and a varying R_i. The exact index values are $n_i = 6$ and $n_e = 12$. The x-axis represents the values of A_e/A_{tot}, ratio of external layer area to the total circle area. Left: first transmission eigenvalue. Right: reconstructed n^*.

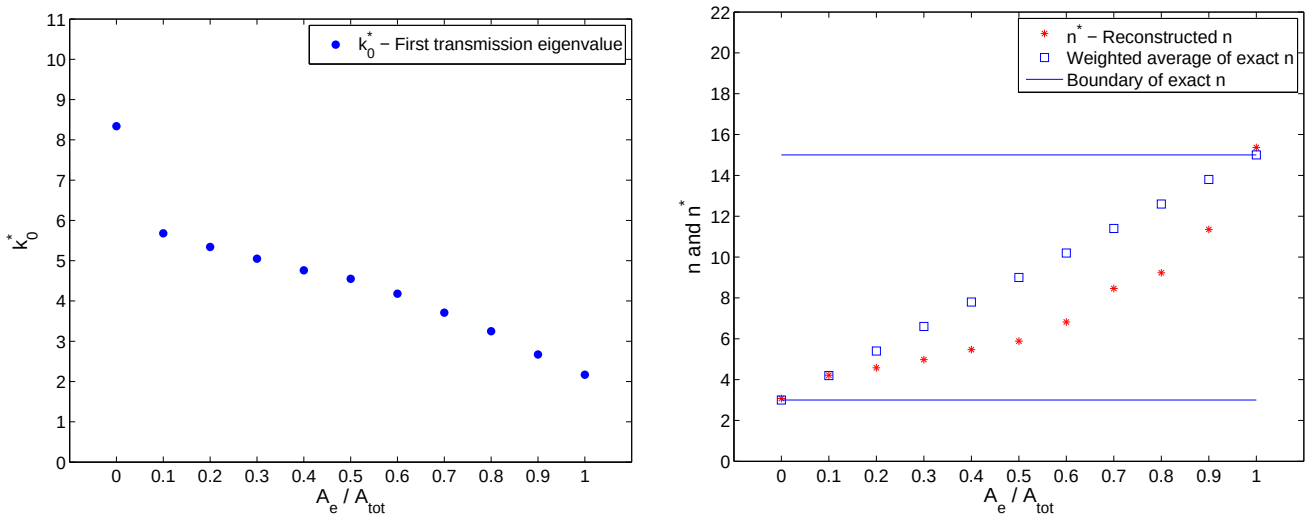

Figure 4.17: Results for TE polarized incident waves in the case of a two layered circle with $R_e = 0.5$ and a varying R_i. The exact index values are $n_i = 3$ and $n_e = 15$. The x-axis represents the values of A_e/A_{tot}, ratio of external layer area to the total circle area. Left: first transmission eigenvalue. Right: reconstructed n^*.

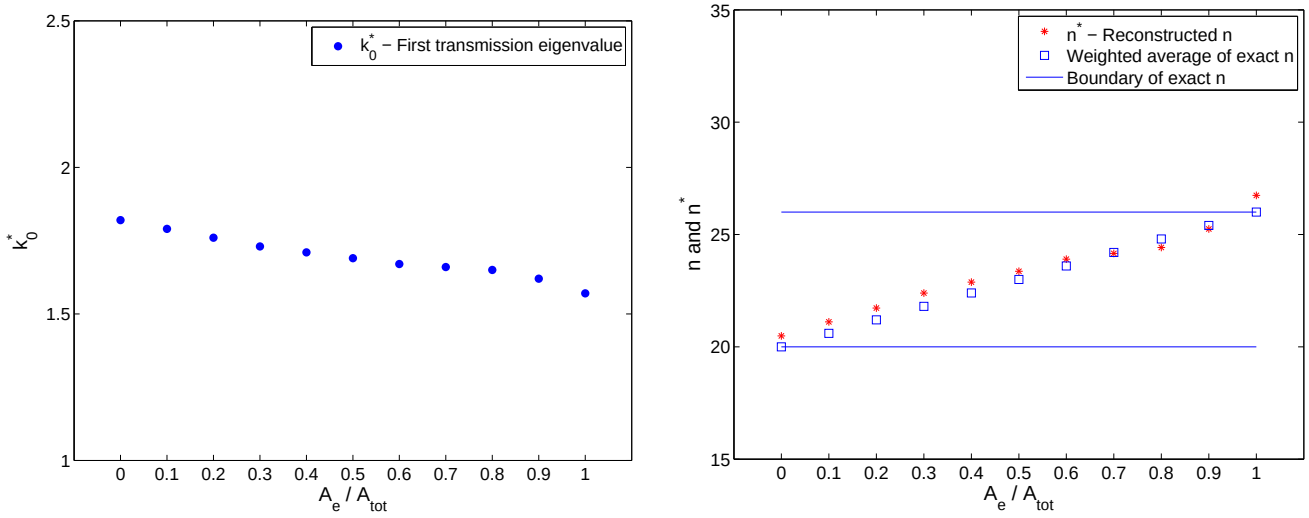

Figure 4.18: Results for TE polarized incident waves in the case of a two layered circle with $R_e = 0.5$ and a varying R_i. The exact index values are $n_i = 20$ and $n_e = 26$. The x-axis represents the values of A_e/A_{tot}, ratio of external layer area to the total circle area. Left: first transmission eigenvalue. Right: reconstructed n^*.

Finally, Figure 4.19 shows how transmission eigenvalues and associated estimates on the refractive index behave when the background is different from the vacuum. The scatterer is here a homogeneous sphere of fixed refractive index $n = 12$ while the background index n_b varies. Figure 4.19 (a) and (b) respectively show smallest transmission eigenvalues and computed estimates for values of n_b between 2 and 81.

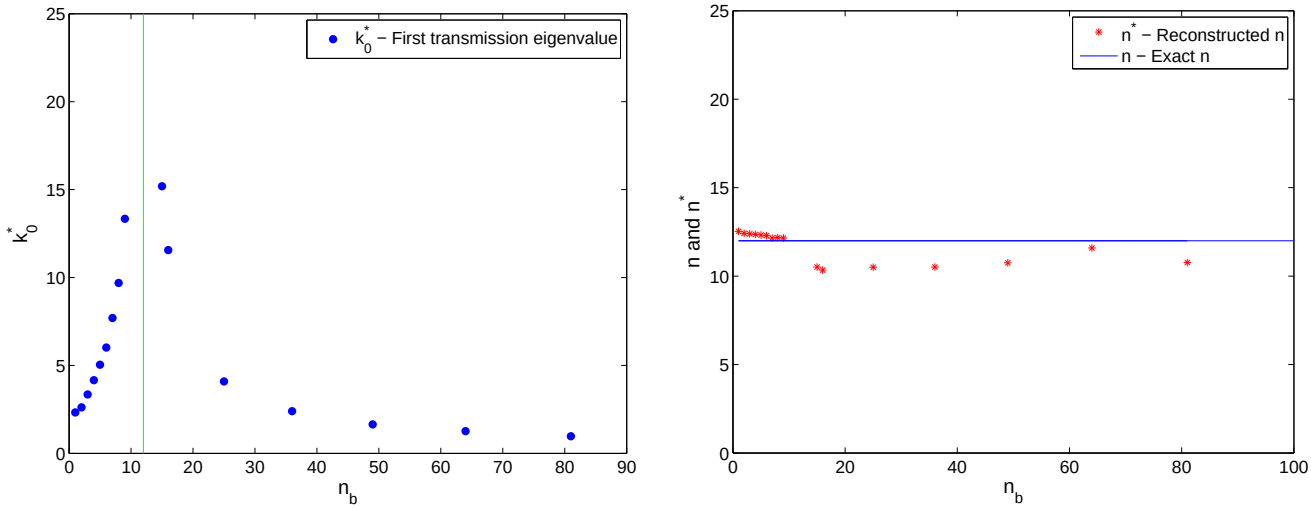

Figure 4.19: Results in the case of a circle of ray 0.5 and constant index of refraction $n = 12$ embedded in a background of constantly varying value n_b. Left: plot of first transmission eigenvalues for TM polarized incident waves. Right: plot of the reconstructed value n^* of n for TM polarized incident waves.

4.2.5. Numerical results for cases where the geometry is not known a priori

In this last section we present some numerical experiments and results that are related to a more realistic inverse scattering experiment: i.e. a situation where both the geometry D of the scatterer and its refractive index n are unknown and the only data at our disposal are the farfields associated with many incident directions. Since in the previous section it has been shown that the method performance for TM polarized waves and for TE polarized waves is similar, we show only simulations for TM waves. The inversion algorithm is the following:

- Apply the LSM algorithm (as described in Section 2) to find an approximation $\tilde{D}$ of the shape of D.
- Determine the smallest transmission eigenvalue k_0^* (for each connected component of D) using the method described in Section 3.
- Solve the eigenvalue problem $P(\tilde{D}, k_0^*, n)$ to obtain a constant approximation n^* of the exact index n inside D.

Following this scheme, for each example, we shall present both the LSM reconstruction and the graph of $k \mapsto \|g_z\|_{L^2(\Omega)}$ for several $z \in \tilde{D}$. Simulations are done using 20 emitting antennas, 20 measuring antennas and by corrupting the data with 5% multiplicative random noise.

Figures are collected in panels (Figures 4.20 - 4.26) and the values of the corresponding constant approximation of n are indicated in Tables 4.1 - 4.7.

The case of circular geometries

In this case comparisons can be made with the exact calculations made in previous section for transmission eigenvalues.

The first example corresponds with the two layered configuration of D (shown in Figure 4.9-right) with an external radius 0.5 and an internal radius 0.354, embedded in the vacuum where we considered four configurations for the indexes of refraction $n = n_e$ for the exterior layer and $n = n_i$ for the interior layer. Figure 4.20-(a1-a2) shows the LSM reconstruction for $n_e = 22$ and $n_i = 19$; for four different configurations of the index of refraction $(n_e = 8, n_i = 8)$, $(n_e = 11, n_i = 5)$, $(n_e = 22, n_i = 19)$ and $(n_e = 67, n_i = 61)$, we present $k \mapsto \|g_z\|_{L^2(\Omega)}$ that allows us to determine the first transmission eigenvalue. The corresponding values of n^* are collected in Table 4.1.

Figures 4.21, 4.22 and corresponding Tables 4.2, 4.3, describe the results achievable when the two layered inclusion of previous experiment is now embedded in an inhomogeneous background. The inhomogeneous background consists into a circular domain of radius 0.75 and with refractive index n_b embedded in the vacuum.

Figure 4.21 and Table 4.2 show how the method perform for objects embedded in a non-absorbing background. As expected, we observe that the transmission eigenvalues are different from those corresponding to the homogeneous background but the estimates n^* are roughly the same.

Figure 4.22 and Table 4.3 correspond with the case of an absorbing background. We develop here the idea explained in Section 4.2.2 and show that, when an artificial non-absorbing background of index $\tilde{n}_b$ is used inside the reconstructed domain, real transmission eigenvalues can be computed, allowing to find roughly the same values of n^* as in the non absorbing case. We remark that in this configuration the accuracy of $\tilde{D}$ (approximation of the shape of D) has a stronger influence on the accuracy of n^* since it affects the computation of the incident field for the background. The latter is used in computing $\|g_z\|_{L^2(\Omega)}$ and therefore affect the precision of the first transmission eigenvalue.

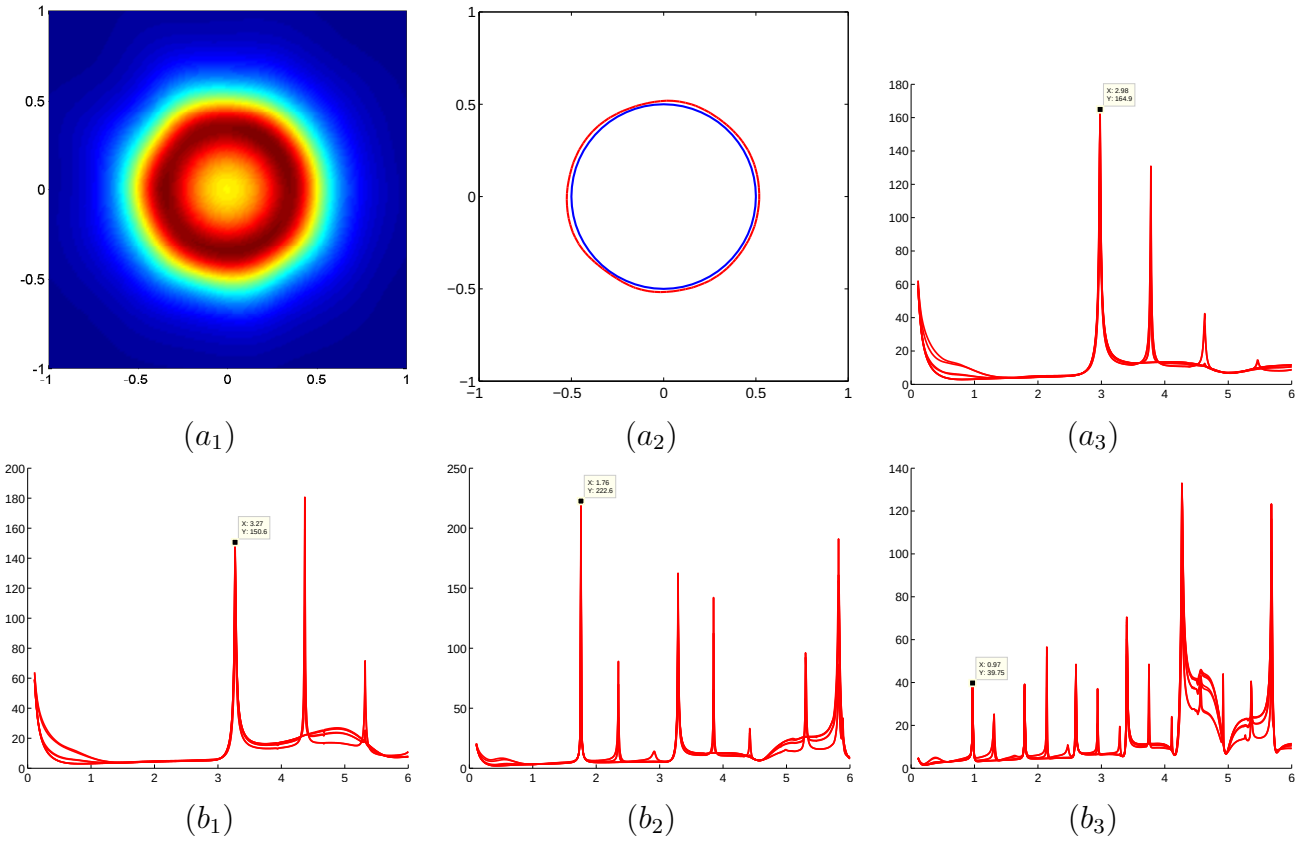

Figure 4.20: Two layered circular inclusion embedded in the vacuum (Figure 4.9-right). (a_1) LSM reconstruction at $k = 4.2$, $n_e = 22$ and $n_i = 19$. (a_2) reconstructed shape (red) versus exact shape (blue). (a_3), (b_1), (b_2), (b_3) plots of $k \mapsto \|g_z\|_{L^2(\Omega)}$ for several choices of z, respectively for $(n_e, n_i) = (8,8), (11,5), (22,19), (67,61)$.

n_e	n_i	k_0^*	n^* - exact shape	n^* - reconstructed shape
8	8	2.98	8.07	7.61
11	5	3.27	7.05	6.69
22	19	1.76	20.28	18.86
67	61	0.97	64.11	59.42

Table 4.1: Transmission eigenvalues and reconstructed index associated with Figure 4.20.

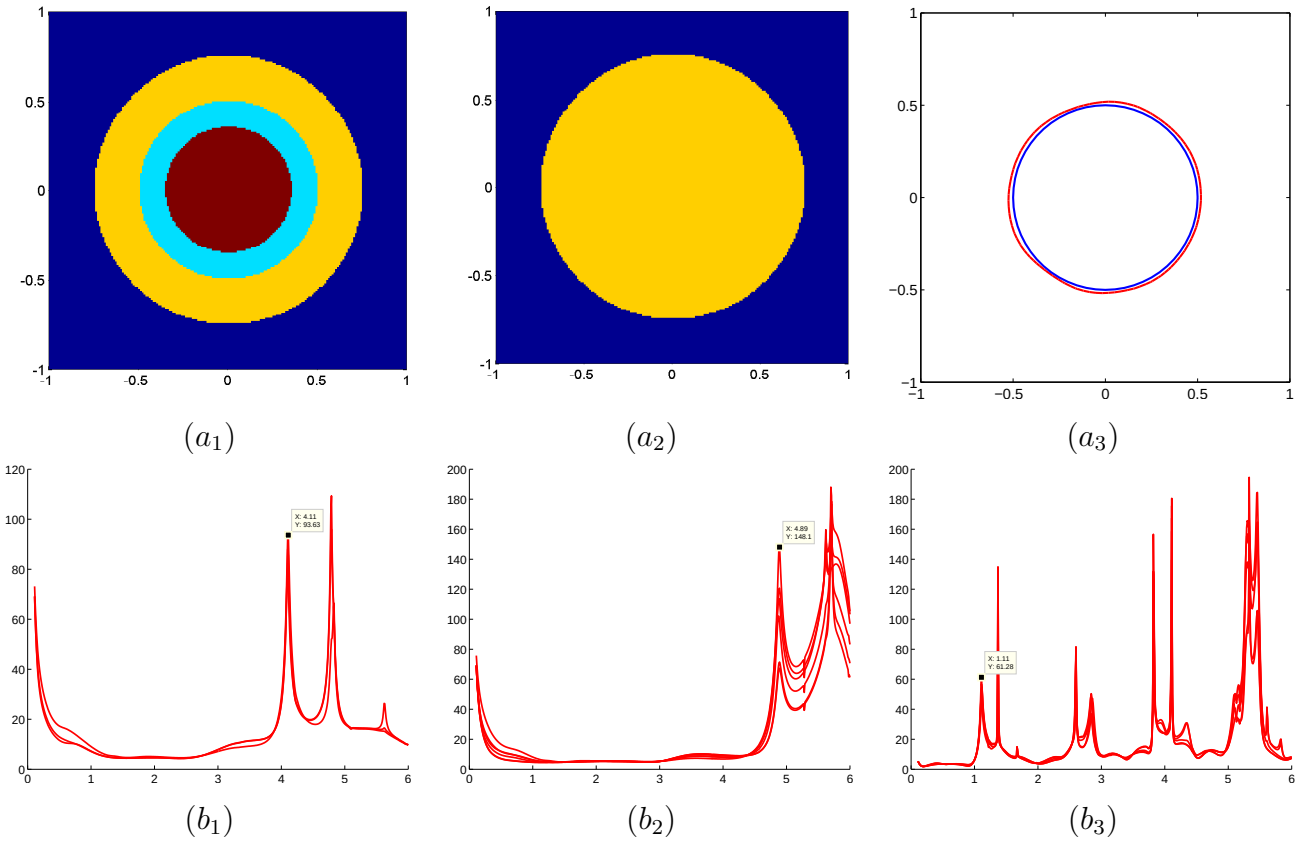

Figure 4.21: Two layered circular inclusion (a_1) embedded in an inhomogeneous background (a_2). (a_3): reconstructed shape (red) versus exact shape (blue). (b_1), (b_2), (b_3): plots of $k \mapsto \|g_z\|_{L^2(\Omega)}$ for several choices of z, respectively for $(n_e, n_i, n_b) = (8,8,2), (11,5,2), (67,61,10)$.

n_e	n_i	n_b	k_0^*	n^* - exact shape	n^* - reconstructed shape
8	8	2	4.11	8.09	7.70
11	5	2	4.89	6.92	5.04
67	61	10	1.11	64.35	61.44

Table 4.2: Transmission eigenvalues and reconstructed index associated with Figure 4.21.

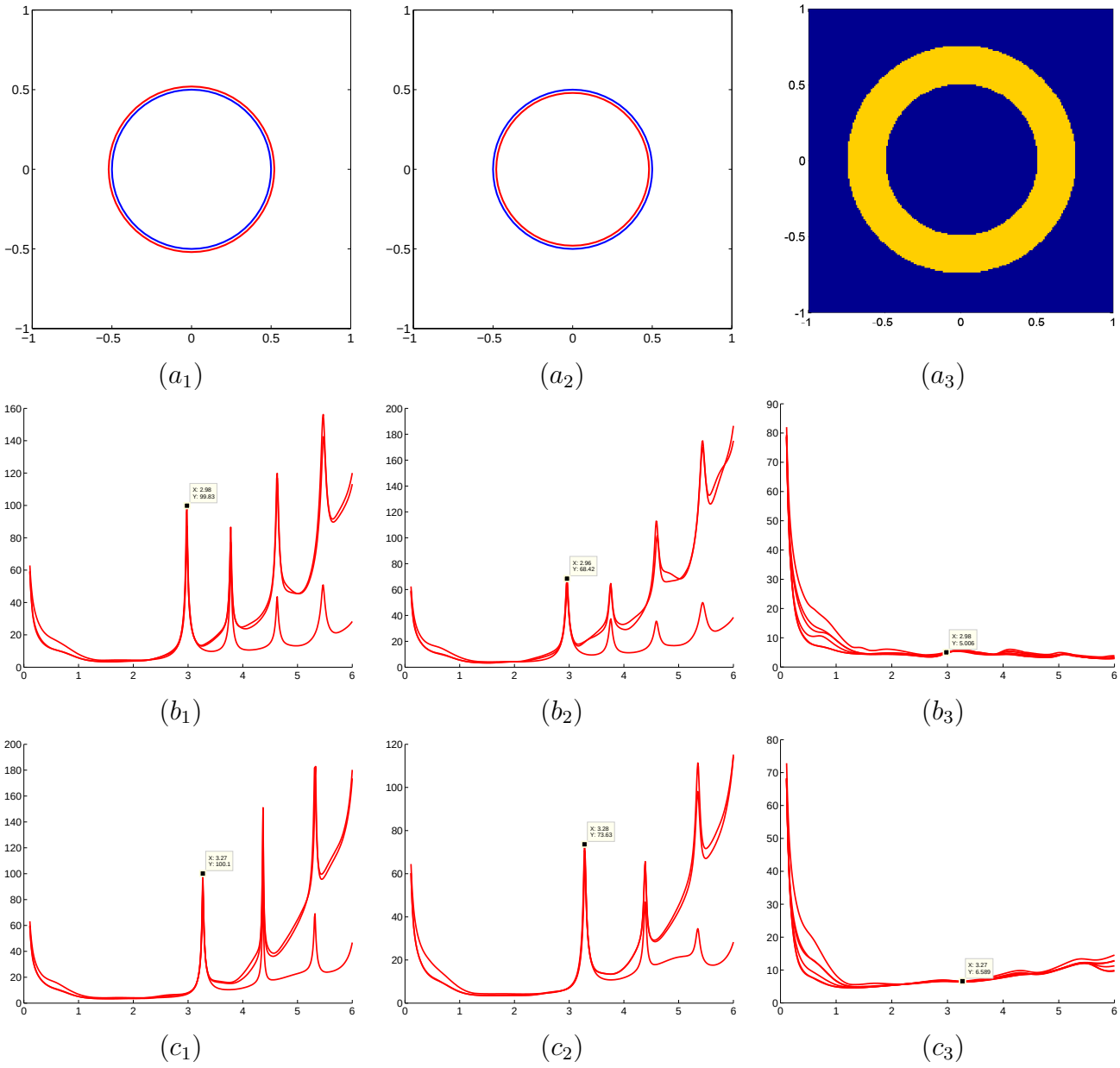

Figure 4.22: Two layered circular inclusion $(n_e, n_i) = (8, 8)$, embedded in an inhomogeneous absorbing background with $n_b = 2 + \imath$. (a_1), (a_2): reconstructed shape (red) versus exact shape (blue). (a_3): considered artificial background with $\tilde{n}_b = 1$ inside D. (b_1), (b_2), (b_3): plots of $k \mapsto \|g_z\|_{L^2(\Omega)}$ for several choices of z, respectively for the exact shape and artificial background, reconstructed shape (overestimated (a_1)) and artificial background, exact shape and true background. (c_1), (c_2), (c_3): same as (b_1), (b_2), (b_3) but for the case $(n_e, n_i) = (11, 5)$ and underestimated reconstructed shape (a_2).

n_e	n_i	n_b	$\tilde{n}_b$	$(k_0^*, \ n^*)$ - exact shape	$(k_0^*, \ n^*)$ - reconst. shape
8	8	$2+\imath$	1	(2.98, 8.07)	(2.96, 7.69)
11	5	$2+\imath$	1	(3.27, 7.05)	(3.28, 7.43)

Table 4.3: Transmission eigenvalues and reconstructed index associated with Figure 4.22.

Cases of non circular geometries

In Figure 4.23 and Figure 4.24 the case of scatterers that are not circular is investigated. In both figures a two layered inclusion is considered. The exact profile of D, the LSM reconstruction for $n_e = 22$, $n_i = 19$ and transmission eigenvalues for $(n_e, n_i) = (8,8), (11,5), (22,19)$ are respectively shown for a layered ellipse and for an ellipse embedded into a rectangle. Tables 4.4 and 4.5 present the values of n^* achievable using the values of k_0^* and the extracted profile $\tilde{D}$. One can draw roughly similar conclusions as in the case of circular geometries.

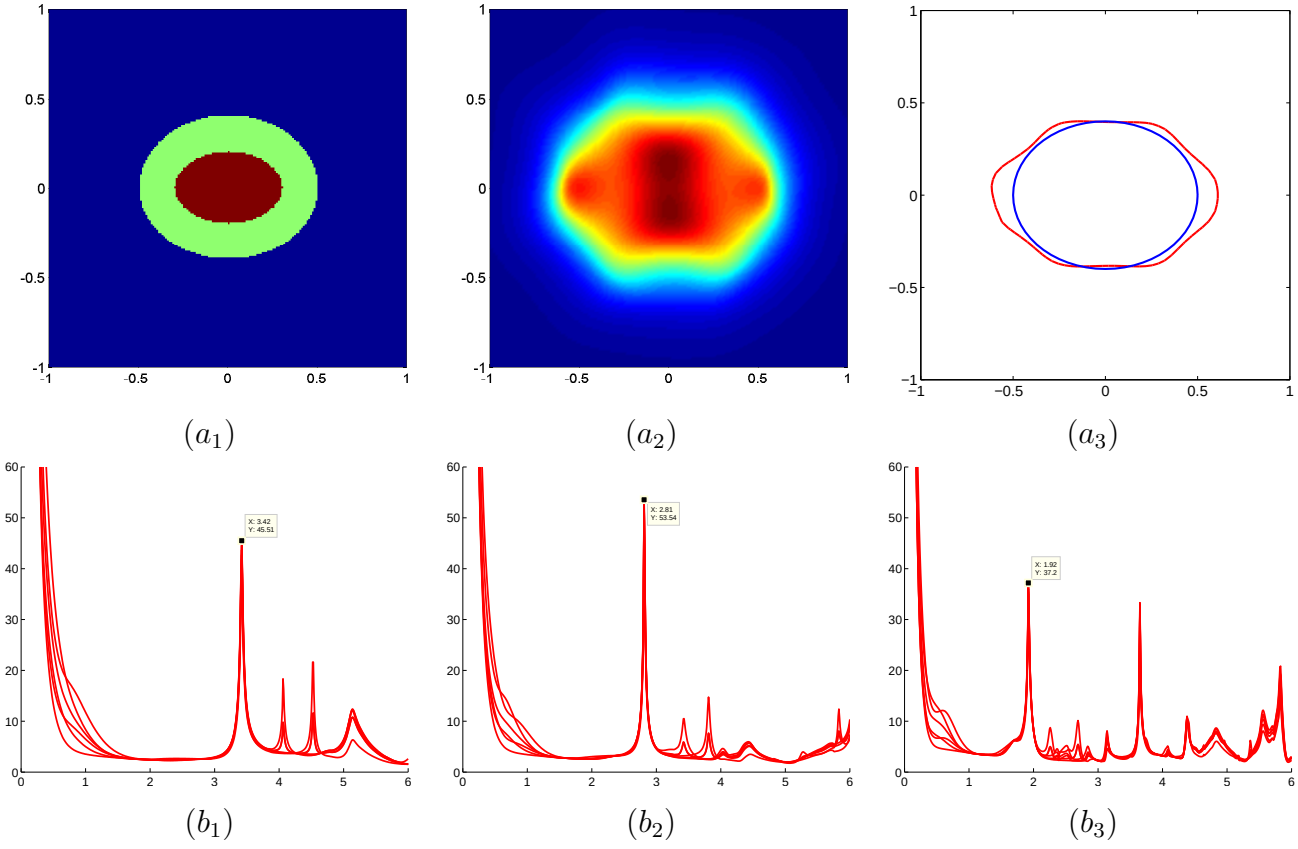

Figure 4.23: Two layered ellipsoidal inclusion (a_1) embedded in the vacuum. (a_2): LSM reconstruction for $k = 4.16$, $n_e = 22$ and $n_i = 19$. (a_3): reconstructed shape (red) versus exact shape (blue). (b_1), (b_2), (b_3): plots of $k \mapsto \|g_z\|_{L^2(\Omega)}$ for several choices of z, respectively for $(n_e, n_i) = (8,8), (11,5), (22,19)$.

n_e	n_i	k_0^*	n^* - exact shape	n^* - reconstructed shape
8	8	3.42	8.08	7.74
11	5	2.81	11.10	10.50
22	19	1.92	22.16	20.73

Table 4.4: Transmission eigenvalues and reconstructed index associated with Figure 4.23.

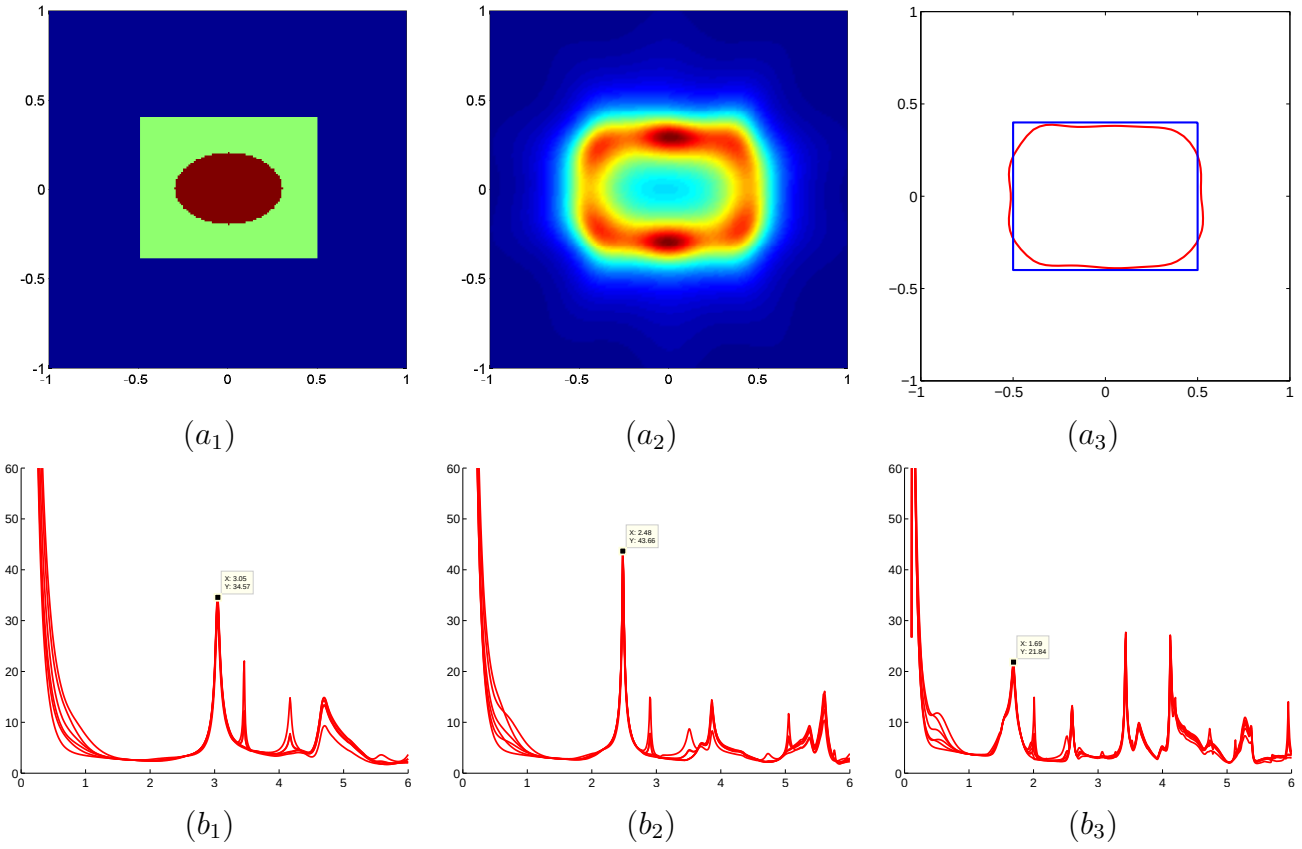

Figure 4.24: Rectangular inclusion containing an ellipsoidal layer (a_1) embedded in the vacuum. (a_2): LSM reconstruction for $k = 5.64$, $n_e = 22$ and $n_i = 19$. (a_3): reconstructed shape (red) versus exact shape (blue). (b_1), (b_2), (b_3): plots of $k \mapsto \|g_z\|_{L^2(\Omega)}$ for several choices of z, respectively for $(n_e, n_i) = (8, 8), (11, 5), (22, 19)$.

n_e	n_i	k_0^*	n^* - exact shape	n^* - reconstructed shape
8	8	3.05	8.94	9.37
11	5	2.48	12.62	13.27
22	19	1.69	25.53	26.90

Table 4.5: Transmission eigenvalues and reconstructed index associated with Figure 4.24.

Cases of multiply connected inclusions

Finally, inspired by Corollary 4.2.3, we present a simulation for a scatterer consisting in two distinct objects of different refractive indexes. Figures 4.25 and 4.26 jointly with Tables 4.6 and 4.7 prove that a reconstruction of both indexes of refraction is effectively achievable by considering $k \mapsto \|g_z\|_{L^2(\Omega)}$ first for several z in one connected component and second for several z in the other connected component. As one cas observe in part (b_1) of Figure 4.26, small peaks are present in $k \mapsto \|g_z\|_{L^2(\Omega)}$ preceding the first transmission eigenvalue. A closer look

reveals that those peaks correspond with the transmission eigenvalues of the other connected component (see part (b_3)). We think that this is due to the fact that the two connected components are close to each others. For instance, such perturbation is not observed in the case of Figure 4.25 where the distance between the two connected components is larger.

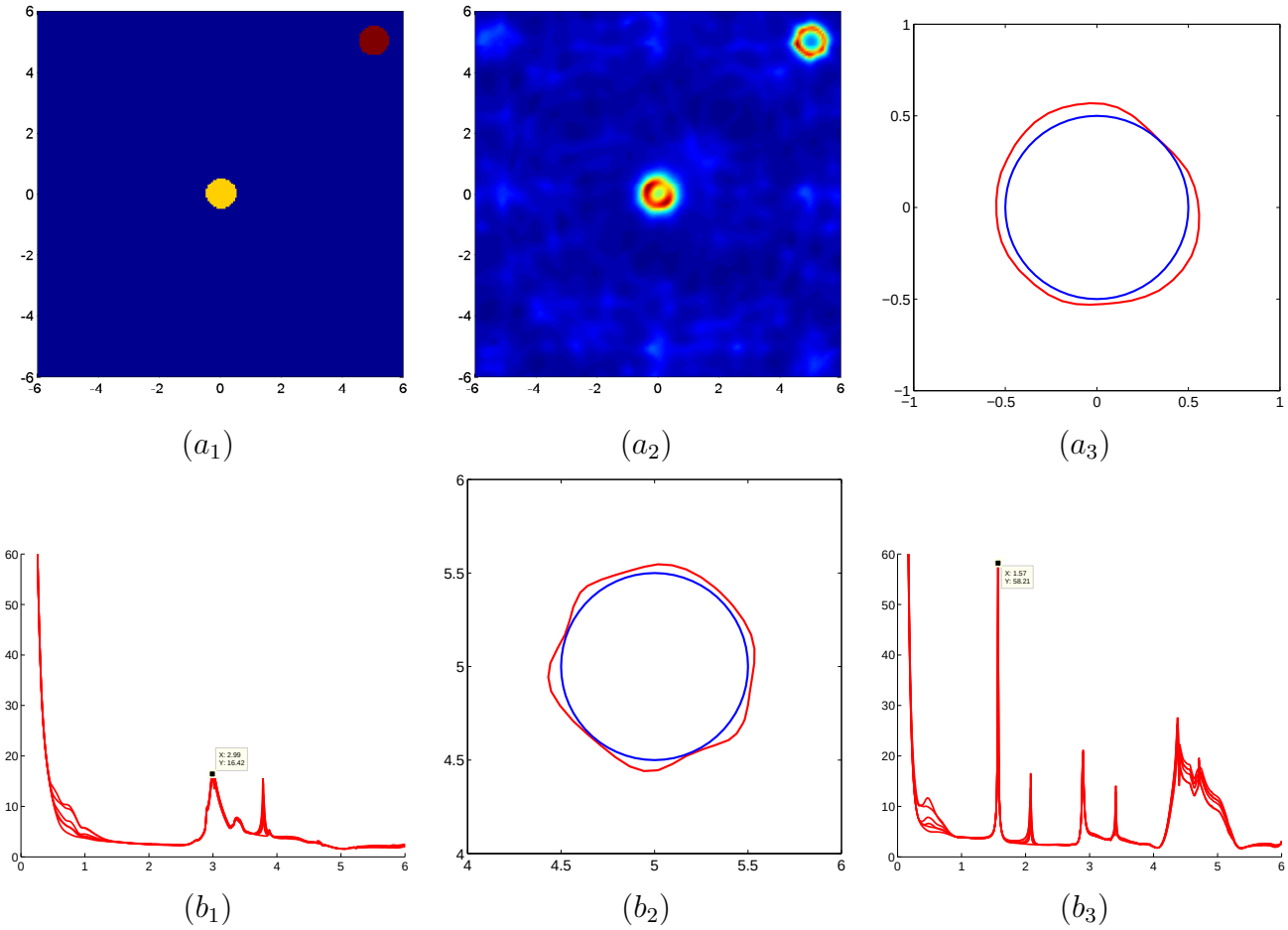

Figure 4.25: Two homogeneous circular inclusions (a_1): a circle c_1 centered at $(0,0)$ of refractive index $n = 8$ and a circle c_2 centered at $(5,5)$ of refractive index $n = 25$. (a_2): LSM reconstruction for $k = 4.2$. (a_3) and (b_2): reconstructed shape (red) versus exact shape (blue) respectively for c_1 and c_2. (b_1) and (b_3): plots of $k \mapsto \|g_z\|_{L^2(\Omega)}$ for several choices of z, respectively for c_1 and c_2.

circle	n	k_0^*	n^* - exact shape	n^* - reconstructed shape
c_1	8	2.99	8.03	7.17
c_2	25	1.57	25.17	24.60

Table 4.6: Transmission eigenvalues and reconstructed index associated with Figure 4.25.

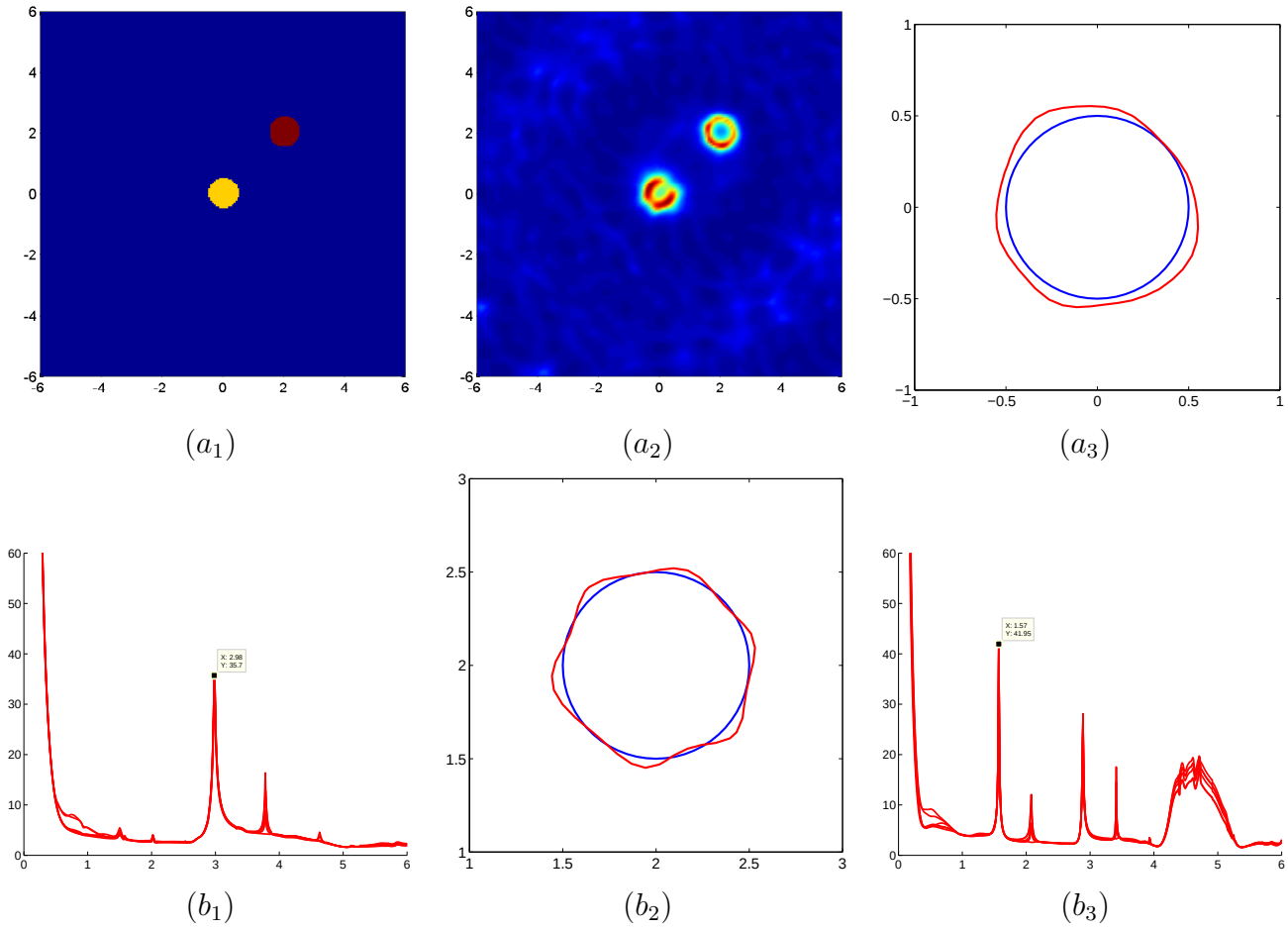

Figure 4.26: Two homogeneous circular inclusions (a_1): a circle c_1 centered at $(0,0)$ of refractive index $n = 8$ and a circle c_2 centered at $(2,2)$ of refractive index $n = 25$. (a_2): LSM reconstruction for $k = 4.2$. (a_3) and (b_2): reconstructed shape (red) versus exact shape (blue) respectively for c_1 and c_2. (b_1) and (b_3): plots of $k \mapsto \|g_z\|_{L^2(\Omega)}$ for several choices of z, respectively for c_1 and c_2.

circle	n	k_0^*	n^* - exact shape	n^* - reconstructed shape
c_1	8	2.98	8.07	7.17
c_2	25	1.57	25.17	24.60

Table 4.7: Transmission eigenvalues and reconstructed index associated with Figure 4.26.

4.2.6. The evidence of the existence of complex transmission eigenvalues

The arguments introduced in Section 4.2.2 suggest a way for providing an easy proof to the existence of complex transmission eigenvalues for a particular group of scattering settings. Until few years ago, it was unclear if complex transmission eigenvalues exist and only recently their effective existence has been proved for several scattering situations in [24]. The literature among complex transmission eigenvalues is still short, and most of the more recent publications investigate under which scattering conditions they may exist or not exists as well as the existence of regions where complex transmission eigenvalues can not occur (see for example [43, 27, 47, 61, 62, 67]).

Let $n(x)$ be absorbing and equal to $n(x) = a(x) + \mathrm{i}b(x)$, where $\mathrm{i} = \sqrt{-1}$ and a, b are real valued functions, and let consider the interior transmission problem

$$\Delta w + k^2 n w = 0 \qquad \text{in } D \tag{4.114}$$

$$\Delta v + k^2 n_b v = 0 \qquad \text{in } D \tag{4.115}$$

$$w - v = 0 \qquad \text{on } \partial D \tag{4.116}$$

$$\frac{\partial w}{\partial \nu} - \frac{\partial v}{\partial \nu} = 0 \qquad \text{on } \partial D \tag{4.117}$$

where the background refractive index n_b is complex inside D. In particular, if we assume that $n_b(x) = (1 + i\frac{b(x)}{a(x)})$ one has that $n = a \cdot n_b$ and that $\frac{n}{n_b} = a$. Then, substituting $\tilde{k} = k\sqrt{n_b}$ one obtains

$$\Delta w + \tilde{k}^2 a w = 0 \qquad \text{in } D \tag{4.118}$$

$$\Delta v + \tilde{k}^2 v = 0 \qquad \text{in } D \tag{4.119}$$

$$w - v = 0 \qquad \text{on } \partial D \tag{4.120}$$

$$\frac{\partial w}{\partial \nu} - \frac{\partial v}{\partial \nu} = 0 \qquad \text{on } \partial D \tag{4.121}$$

which admits an infinite countable number of real transmission eigenvalues $\tilde{k}^*$. This implies that (4.114)-(4.117) admits, at least, a countable number of complex transmission eigenvalues $k^* = \frac{\tilde{k}^*}{\sqrt{n_b}}$.

Hence, in principles, techniques providing transmission eigenvalues (and corresponding estimates on the material properties) from far field data can be adapted to the case of absorbing scatterers (or, at least, to those scatterers of the previously defined particular shape): in fact, by choosing a background such that and given the complex wave number $\tilde{k}$, the interior transmission problem can be rewritten in the form of (4.118)-(4.121) allowing the detection of transmission eigenvalues. Unfortunately, in practice, such a suitable n_b can not be a priori known (since n is unknown): hence, the effective applicability of the technique to this particular situation has to be discarded.

4.2.7. Conclusions

In this work, we have presented a method able to provide estimates on the index of refraction of a scatterer by the knowledge of the first transmission eigenvalue. Such an estimate has been shown to coincide with the value of the refractive index in the case of homogeneous scatterers and to fall between the minimum and the maximum of the index when one deals with scatterers of non-constant refractive index. Moreover, the method has been extended to the case of scatterers embedded in an absorbing background and to the case of multi-connected scatterers, enabling to achieve a different estimate for each connected component.

In a practical framework, this method is thought to complement the class of qualitative methods since its operation requires as input an approximation of the shape of the scatterer; moreover, in order to find the first transmission eigenvalue, it utilizes the same mathematical tools of the linear sampling method, the most well known qualitative method.

From a more general point of view, the results here presented numerically shows the concrete feasibility of retrieving realistic information on the scatterer from the spectrum of the interior transmission problem.

For future developments, it would be interesting to better understand the relation between the smallest transmission eigenvalue k_0^* and the whole sequence of eigenvalues associated to $P(D, k_0^*, n)$. A further open problem of more general relevance would be to study the possible relations between all the other transmission eigenvalues and the refractive index.

CHAPTER 5

Ant colony optimization in cryosurgery planning

In Chapter 2, Section 2, the problem of the cryosurgery planning has been presented and a review on the state of the art among the existing planning algorithms has been provided.

This chapter is dedicated to show that the resolution of a cryosurgery planning problem can be performed through the application of a particular genetic algorithm. More specifically, this chapter will present the application of the statistical based approach called ant colony optimization method (ACO) [96] to the planning of a cryosurgery session.

Section 5.1 will introduce the ACO algorithm, while in Section 5.2 ACO is tested against a $2D$ section of a prostate phantom in the planning of different experimental aspects. Finally, Section 5.3 will face the problem of reducing the computational cost of ACO in order to speed up the method by integrating it with a geometrical based a priori optimization, when one wants to find the best position of the probes.

5.1. The ant colony optimization procedure

Ant colony optimization (ACO) is a statistical based optimization method developed in the nineties with the aim of providing, in a limited amount of time, a reliable although not optimal solution to some NP-hard combinatorial optimization problems. More recently, ACO has been generalized to continuous domains [96]. In view of its generality and wide range of applicability, ACO has been successfully applied to a wide range of problems (e.g. [19], [49]).

ACO takes inspiration from the way in which ants find and carry food to their nest. While an ant is going back to the nest after having taken some food, it releases a pheromone trace: this trace serves as a trail for next ants, which are able to reach food detecting pheromone. Since the pheromone decays in time, its density is higher if the path to food is shorter and more crowded; on the other hand, more pheromone attracts more ants, making longer paths to be forgotten until, at the end, all ants follow the same trail.

Ants' behavior is paraphrased in ACO identifying the cost function $\mathcal{F}$ with the length of the path to food, and the pheromone traces with a probability density which is updated at each iteration depending on the value of the cost function for a set of states. In practice, at each iteration, the cost function is evaluated on a set of P admissible states, and the states are ordered according to increasing values of the cost function. Then ACO defines a probability distribution which is more dense in correspondence of the cheaper states (i.e. the states with smallest values for $\mathcal{F}$) and, on its basis, Q new states are extracted; a comparison procedure identifies the new best P states which form the next set of states.

In more details, the starting point of the algorithm is a set of P states,

$$\begin{aligned} B := \{\mathbf{U}_k = (u_{1,k}, ..., u_{N,k}), \quad & \text{such that} \\ & \mathbf{U}_k \in S \subset I\!R^N,\ k = 1, \ldots, P\} \end{aligned} \tag{5.1}$$

that are ordered in terms of growing cost, namely, $\mathcal{F}(\theta_{\mathbf{U}_1}) \leq \cdots \leq \mathcal{F}(\theta_{\mathbf{U}_P})$.

Next, for any $j = 1, \ldots, N$ e $i = 1, \ldots, P$, one computes the parameters

$$m_{i,j} = u_{j,i}, \qquad s_{i,j} = \frac{\xi}{P-1} \sum_{p=1}^{P} |u_{j,p} - u_{j,i}|$$

and defines the Probability Density Function (PDF)

$$\mathcal{G}_j(t) = \sum_{i=1}^{P} w_i \mathcal{N}_{[m_{i,j}, s_{i,j}]}(t)$$

where $\mathcal{N}_{[\mu,\sigma]}(t)$ is a Gaussian function with mean value μ and standard deviation σ and

$$w_i = \mathcal{N}_{[1,qP]}(i) \tag{5.2}$$

with $i = 1, \ldots, P$ and ξ, q real positive parameters to be fixed.

It follows that $\mathcal{G}_j$ is a superposition of normal PDFs, each one of mean $u_{j,i}$ and of variance $s_{i,j}$ proportional to the average distance between $u_{j,i}$ and the corresponding degrees of freedom of the other P configurations.

By sampling Q times S with $\mathcal{G}_j$, the procedure generates Q new states $\mathbf{U}_{P+1}, ..., \mathbf{U}_{P+Q}$ enlarging the set B to the set of states $\tilde{B} := \{\mathbf{U}_1, ..., \mathbf{U}_{P+Q}\}$. If $\mathbf{U}_{k_1}, ..., \mathbf{U}_{k_Q}$ are the Q states of $\tilde{B}$ of greatest cost, the updated B is defined as

$$B = \tilde{B} \setminus \{\mathbf{U}_{k_1}, ..., \mathbf{U}_{k_Q}\}.$$

This procedure converges to an optimal solution of the problem by exploiting the fact that the presence of weights w_i in the definition of $\mathcal{G}_j$ gives emphasis to solutions of lower costs since $w_1 > \cdots > w_P$. This fact, associated to the influence that a proper choice of parameters ξ and q has on the shape of the Gaussian functions, determines the way in which the method tunes the impact of the worse and best solutions.

The algorithm ends when the difference between any two states of B is less than a predefined quantity or when the maximum allowable number of iterations is reached. The initial set B of trial states is chosen by sampling a uniform probability distribution.

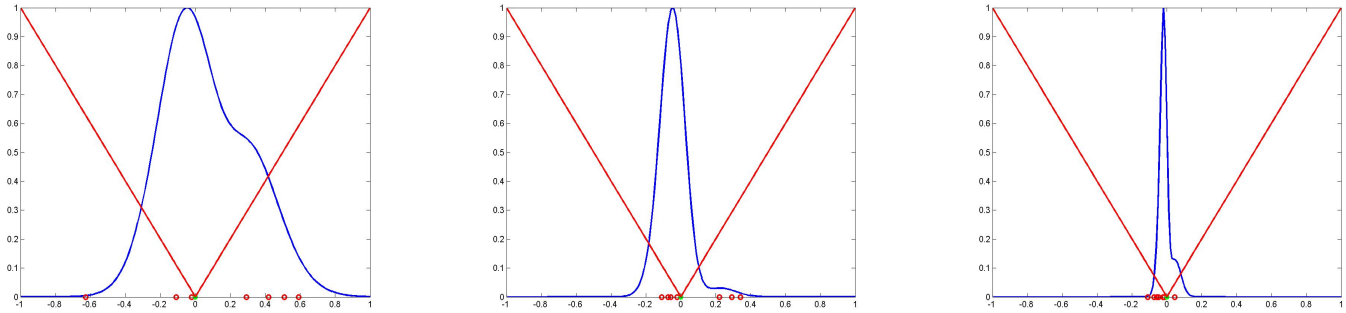

(a) (b) (c)

Figure 5.1: The operation of ACO in case of the minimization of the function $|x|$ (red line). The blue line represents the probability density function at the current iteration while red circles are the P configurations. The green star is the target value (i.e. minimum of $|x|$). (a), (b) and (c) are shots of the evolution of the method respectively during one of the initial, intermediate and final steps of the procedure.

5.2. ACO and prostate cryosurgery

In this section we describe a new systematic procedure to deal with cryosurgery planning based on the application of the ant colony optimization (ACO) method. The strength of this approach lies in the generality of its formulation since ACO is independent of the physical

interpretation and from the number of the parameters subjected to optimization. In other words, through ACO, one is able to set different kinds of free planning parameters without changing the optimization technique.

As a first application, here we consider the problem of determining the best location for cryprobes and cryoheaters. The algorithm is based on an iterative procedure consisting in the solution of several (direct) Stefan problems at each step. Every step begins with the assumption that the placement of cryoprobes and cryoheaters is given while cryoprobes, cryoheaters, tumor and background tissue are at the temperature of 37 ^{o}C. Next the direct Stefan problem is solved as the temperature of the cryoprobes is lowered down to -145 ^{o}C, until the tumor is almost completely frozen. The resulting temperature field is processed to evaluate the defect weighting function [73] providing a quantitative estimate of the mismatch between the frozen tissue at sufficiently low temperature and the tissue to be destroyed. ACO utilizes this cost functional and yields the new positions of cryoprobes and cryoheaters in order that the next step can begin. The procedure stops when the further correction of the position of cryoprobes and cryoheaters becomes negligible.

Section 5.2.1 provides a description of the numerical algorithm we implemented in order to solve the direct Stefan problem in biological tissues whose mathematical model has been given in Chapter 2. Section 5.2.2 contains some numerical examples including an application of our method to a more sophisticated planning than the only optimization of the location of the cryoprobes. Finally, our conclusions are offered in Section 5.2.3[1].

5.2.1. Numerical solution of the direct Stefan problem

The problem of finding the temperature distribution determined by a group of cold and hot cryoprobes of given positions and temperature laws is solved by an Euler-Galerkin approach, i.e. a method combining a finite difference approximation of the time-derivative and a finite element approach solving the space dependent part of the differential problem (2.58)-(2.59).

The approximation scheme is iterative in time. If T_M is the duration of the cryosurgery experiment and $\Delta t = T_M/n$ is the time step, at each iteration $\tau = 0, 1, ..., n$ we set

$$\frac{\partial}{\partial t}\theta_{\tau+1} \approx \frac{1}{\Delta t}(\theta_{\tau+1} - \theta_\tau). \tag{5.3}$$

The functions a, k, and b are defined at every step of the iterative process in terms of the value of the temperature distribution at the previous step. A further comparison with (5.3) shows that equation (2.58) can be approximated by

$$\frac{a(\theta_\tau)}{\Delta t}(\theta_{\tau+1} - \theta_\tau) = \nabla \cdot (k(\theta_\tau)\nabla(\theta_{\tau+1})) + \chi(\theta_\tau)b(\theta_{\tau+1}) \tag{5.4}$$

[1]The results showed in Section 5.2 are contained in [54]

where θ_τ is given and $\theta_{\tau+1}$ is the unknown. Integration of (5.4) against test functions $\varphi \in H_0^1(V)$ and use of the Green's identity lead to the variational formulation

$$\int_V a(\theta_\tau)\,\frac{\theta_{\tau+1}-\theta_\tau}{\Delta t}\,\varphi\,dv = \\ = \int_V [-k(\theta_\tau)\,\nabla\varphi\cdot\nabla\theta_{\tau+1} + \, b(\theta_{\tau+1})\,\varphi]\,dv. \tag{5.5}$$

The finite element approximation of (5.4) is based on (5.5), where boundary conditions (2.59) are imposed through penalization [2].

Given an operation time T_M, the Euler-Galerkin approach provides an approximation of the temperature distribution during the evolution from $t = 0$ to $t = T_M$. The effectiveness of the cryosurgery simulation can be quantitatively assessed by introducing a simple cost function that counts one all defective pixels (i.e. all pixels in the tumoral region whose temperature is higher than a reference temperature and all the pixels in the healthy tissue whose temperature is smaller than this reference temperature) and zero all correctly treated pixels (i.e. all pixels in the tumoral region whose temperature is smaller than a reference temperature and all the pixels in the healthy tissue whose temperature is higher than this reference temperature). More formally, a specific configuration of the cryosurgery design is represented by a state variable $\mathbf{U}$, which is a list of N operating parameters (e.g. number and position of cryoprobes, temperature variation, etc.) whose admissible values are contained in $S \subset IR^N$. The cost function is the *defect weighting function* $\mathcal{F} : S \to IN$ such that

$$\mathcal{F}(\theta_{\mathbf{U}}) = \int_V \mu(\theta_{\mathbf{U}}(\mathbf{x}))d\mathbf{x} \tag{5.6}$$

where $\theta_{\mathbf{U}}$ is the temperature distribution associated to $\mathbf{U}$ and

$$\mu(\theta(\mathbf{x})) := \begin{cases} 0 & \text{if } \theta(\mathbf{x}) < \bar{\theta} \text{ and } \mathbf{x} \text{ is diseased} \\ 1 & \text{if } \theta(\mathbf{x}) < \bar{\theta} \text{ and } \mathbf{x} \text{ is healthy} \\ 1 & \text{if } \theta(\mathbf{x}) \geq \bar{\theta} \text{ and } \mathbf{x} \text{ is diseased} \\ 0 & \text{if } \theta(\mathbf{x}) \geq \bar{\theta} \text{ and } \mathbf{x} \text{ is healthy.} \end{cases} \tag{5.7}$$

The most appropriate choice of the constant reference temperature $\bar{\theta}$ is discussed in [73], where the defect weighting function was first introduced. In our applications we have used $\bar{\theta} = -22^o$C as suggested in that paper. The cost function (5.6) plays a central role in the optimization procedure for the cryosurgery planning.

5.2.2. Numerical Examples

In this section the optimization method is tested against the same $2D$ prostate phantom used in [73] (see Figure 5.2).

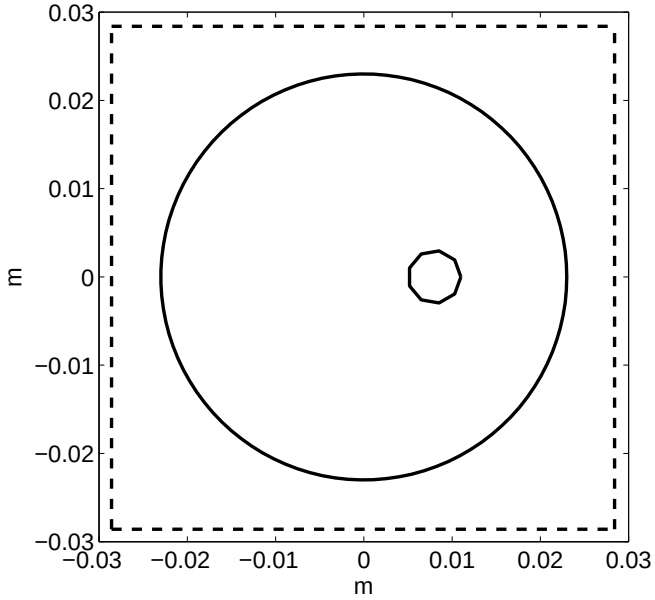

Figure 5.2: Prostate phantom used for numerical tests. Dashed lines delimit the area under investigation; the smallest circle inside the biggest one identifies the urethra contour. The same phantom has been used in [73].

The optimization process is performed minimizing (5.6) on a square containing the phantom and discretized by a grid of 1 mm x 1 mm pixels. Given a configuration of cryoprobes, the distribution of temperature is computed through the open source software FreeFem++[2]. The initial temperature is set to 37 ^{o}C everywhere and cryoprobes are supposed to reach -145 ^{o}C in 30 seconds by a linear decrease law; the temperature at the boundary of the urethra is set at 37 ^{o}C (see [86]) and external Dirichlet conditions are given on a square of side 0.1 m embedding the investigation domain. Phase change region V_2 is identified as the set of pixels of temperature between $\theta_m = -6$ ^{o}C and $\theta_M = 0$ ^{o}C while the threshold value $\bar{\theta}$ is -22 ^{o}C (see [73]); cryoprobes as well as cryoheaters have a circular cross-section with diameter of 1 mm. The other values are chosen according to Table 5.1.

In the first numerical example we look for both the optimal positions of a set of cryoprobes and the optimal duration of the cryosurgery experiment, (i.e. no cryoheaters are considered). Results are shown in Figures 5.3 - 5.4 and in Table 5.2 where the behavior of the method is tested for different numbers of cryoprobes and for different values of ACO's parameters P and Q (P is chosen as multiple of the number of probes $+1$ whereas $Q = [\frac{P}{2}] + 1$ where $[\cdot]$ denotes the floor function). The value of $\mathcal{F}(\mathbf{U}_{opt})$, with $\mathbf{U}_{opt}$ optimal configurations, generally decreases as P and Q increase, although some exception to this trend can occur due to the complete randomness of the initialization of the method.

It is interesting to note that the level curve distribution in Figure 5.3 (c) implies a gradient

[2]downloadable at http://www.freefem.org/ff++/

of temperature from -45^oC to $+37^o$C (on the urethra boundary) over a very small distance (around 2 mm). This abrupt behavior is difficult to realize in a real experiment. However, this drawback is not due to the optimization method but to the simplistic model adopted, particularly in the definition of the boundary conditions. The aim of our work is to assess the reliability of a novel computational approach in the case of a model widely adopted in the scientific literature. We also point out that one of the strengths of this approach is that the generalization to more realistic models is straightforward.

Finally, Figure 5.5 gives an idea of how probes group during the optimization process, converging to the final configuration in the case of 15 cryoprobes.

Parameters	Units of measurements	Values
k_1	W / (^{o} C$\cdot$ m)	1.76
k_3	W / (^{o} C$\cdot$ m)	0.50
$\rho_1 c_1$	MJ / (^{o} C $\cdot$ m^3)	1.67
$\rho_3 c_3$	MJ/(^{o} C$\cdot$ m^3)	3.35
$\rho_b w_b c_b$	kW/ (^{o} C $\cdot$ m^3)	40
q_m	kW / m ^{3}	33.8
θ_b	^{o} C	37
L	MJ/m ^{3}	300

Table 5.1: Model parameters used in the numerical procedure.

In the second experiment we consider the presence of cryoheaters as well as cryoprobes. Figure 5.6 shows the optimal solution of an experiment in which 14 cryoprobes and 3 cryoheaters have to be placed and an optimal duration has to be set: cryoprobes are constrained to fall inside the prostate, while cryoheaters are placed outside the prostate, at the same side of the urethra. Again, ACO converges to a configuration which guaranties the death of most the tumoral tissue, keeping healthy tissues over temperature $\bar{\theta}$ (the ratio between defected and total pixels is equal to 3.2% and the duration of the experiment is set by ACO to 571 seconds).

A last example shows the efficacy of our optimization method when it is applied to a more complex operation planning characterized by two distinct stages. In the first one, we want to setup the probes position; in the second one, we want to control the temperature of each cryoprobe in order that the cold front keeps on freezing the tumoral cells without invading the healthy tissue. The introduction of such a second stage is motivated by the fact that, in order to kill a tumoral cell, one has to keep its temperature low enough for an appropriate amount of time. Moreover, recent studies claimed that the killing power of cold is increased when cells are subjected to several cycles of thaw and freeze [51] and the duration of these cycles is generally decided by medical doctors based on physiological considerations. These facts can consistently increase the duration of the operation beyond the time established by

N^o cryoprobes	P	Q	Duration (sec)	Defected/Total (%)
8	27	14	1289	8.9
9	20	11	874	7.7
9	30	16	737	7.3
10	11	6	609	9.7
10	22	12	546	6.1
11	12	7	573	9.8
11	24	13	587	5.5
11	36	19	552	3.5
12	13	7	618	4.0
12	26	14	587	3.7
12 (Fig. 5.3)	39	20	586	1.9
13	14	8	493	5.2
13	28	15	524	2.9
14	15	8	456	5.7
14	30	16	494	3.0
15	32	17	347	2.1
15 (Fig. 5.4)	48	25	298	1.8
16	34	18	427	2.5

Table 5.2: Results for geometry of Figure 5.2 in the case of $q = 0.05$ and $\xi = 0.5$. Columns respectively collect the values of: number of cryoprobes, P, Q (parameters of ACO), optimal duration for the experiment and ratio between still defected area (i.e. $\mathcal{F}(\mathbf{U}_{opt})$) and investigated area.

the first stage and hence a manner to control the ice propagation during the extended time becomes an essential planning tool.

Therefore, in more details, let us suppose that an optimal configuration of cryoprobes has been fixed in the first stage together with an optimal duration T_1. Let us further suppose that - for physiological reasons - tumoral tissues are required to maintain their temperature under the killing value $\bar{\theta}$ for a time $T_2 > T_1$. In the second stage our optimization approach is generalized to optimally determine the best temperature that each cryoprobe has to maintain in order to kill tumoral tissues and keep healthy tissues safe.

The results of this two-stage strategy are shown in Figure 5.7 and Table 5.3. Specifically, Panels (a) and (b) in Figure 5.7 represent the optimal positions for the 15 cryoprobes determined in stage 1 and the corresponding isotherms together with the cost function representation at $T_1 = 298$ seconds. Then, Panels (c) and (d) give the result of the second step when the cryoprobes are kept fixed and their temperatures are reported in Table 5.3. Finally, Panels (e) and (f) of Figure 5.7 show what would happen if the second stage were neglected and the

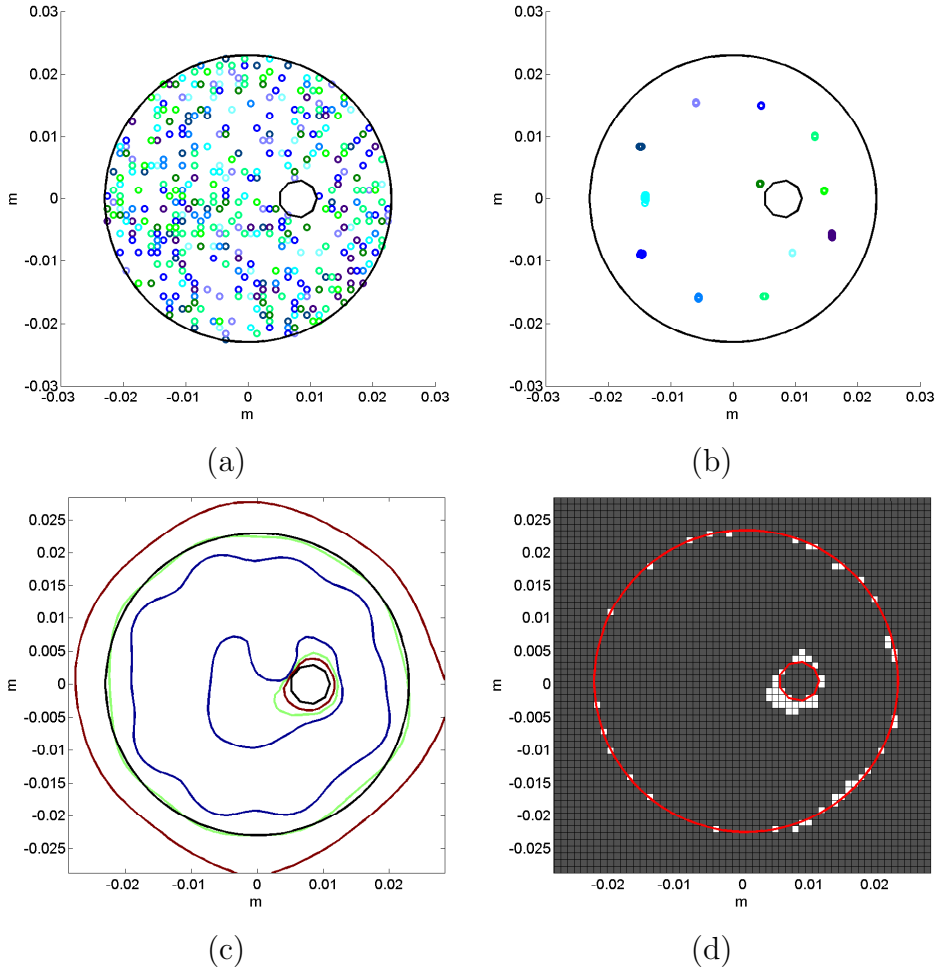

Figure 5.3: Case of 12 cryoprobes. (a) Initial position of $P = 39$ configurations (where each circle represents a cryoprobe and where cryoprobes of different colors belong to different configurations). (b) Final position of the P configurations collapsed into one after ACO. (c) Temperature distribution for the optimal solution (i.e. the one characterized by the minimum value of the cost function): 0^o C-isotherm is red, -22^o C-isotherm is green, -45^o C-isotherm is blue. (d) Plot of the defected (i.e. x s.t. $\mu(\theta(\mathbf{x})) = 1$) pixels (white).

cryoprobes were maintained at -145 ^{o}C up to time $T_2 = 15$ minutes.

In summary, the performances of the ACO method applied in finding the best position of the cryoprobes are nicely consistent with the state of the art in cryosurgery planning and, for example, with the force-field analogy method (see [73]). Further, its applicability to more general cryosurgical situations is confirmed by the good results obtained in the two-stage example showed in Figure 5.7 and Table 5.3. The computational time is of the same magnitude of most of the other optimization methods utilized in cryosurgery, although this is still far from performance requirements needed by real-time operations. Particularly for the $3D$ case (but just for the determination of the cryoprobes' position), on-line designing is currently guaranteed only by geometry-based methods as bubble packing. In this perspective, the opportunity of integrating ACO with a geometry-based method providing some a priori uniform distribution

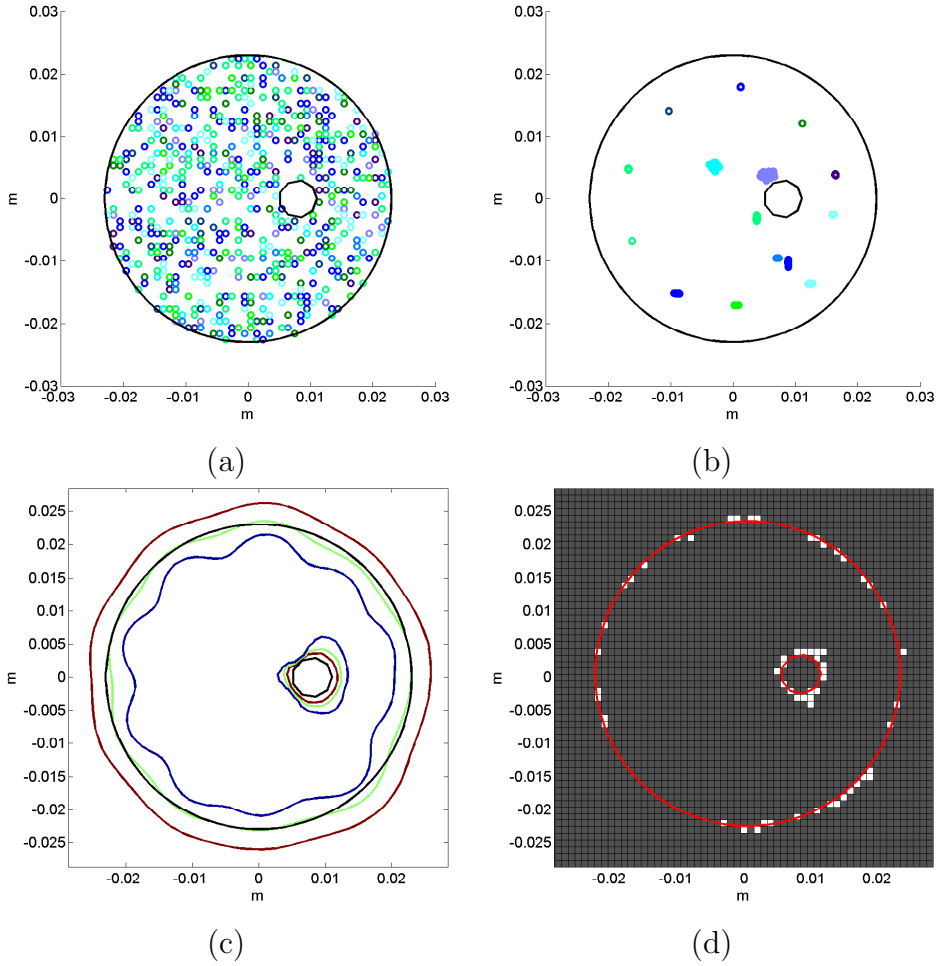

Figure 5.4: Case of 15 cryoprobes. (a) Initial position of $P = 48$ configurations (where each circle represents a cryoprobe and where cryoprobes of different colors belong to different configurations). (b) Final position of the P configurations after ACO. (c) Temperature distribution for the optimal solution (i.e. the one characterized by the minimum value of the cost function): 0^o C-isotherm is red, -22^o C-isotherm is green, -45^o C-isotherm is blue. (d) Plot of the defected (i.e. x s.t. $\mu(\theta(\mathbf{x})) = 1$) pixels (white).

of the cryoprobes should be considered.

5.2.3. Conclusions

In Section 5.2 we have introduced a novel optimization method for cryosurgery planning. The algorithm utilizes ACO to choose the optimal parameter configurations, where the computation of the cost function to minimize is based on the numerical solution of several direct Stefan problems. With respect to gradient-based methods, this approach can be implemented in a more straightforward way; with respect to heuristic methods, it guaranties a better flexibility and generalization power. Indeed the ACO-based method may be easily adapted to deal with a variety of parameters entering the numerical simulation of a cryosurgery experiment. Also, the

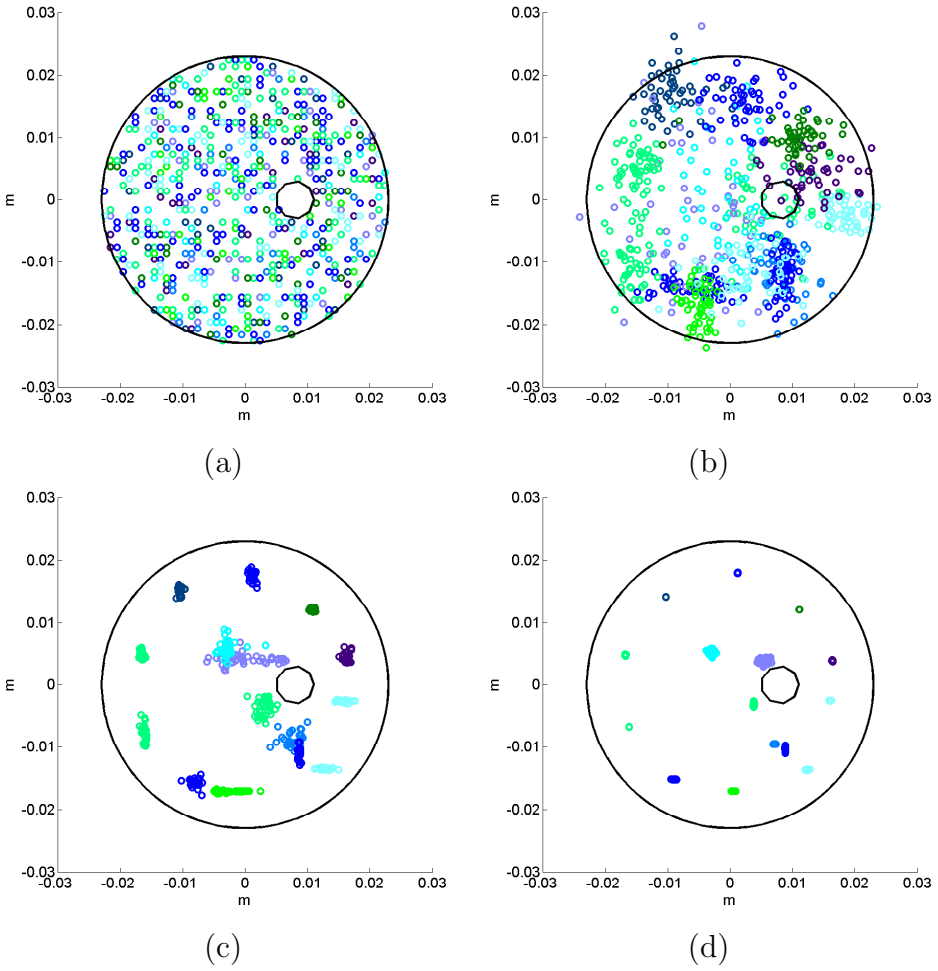

Figure 5.5: Evolution of ACO iterations in the case of 15 cryoprobes. (a) is the initial condition. (b) and (c) are the situations of the P configurations respectively after a quarter and three quarter of iterations. (d) is the final situation of the P configurations.

parameters to be optimized may be divided into families to be processed in subsequent steps. Finally, if continuous functions are involved in the description of a state, they may be replaced by piecewise constant functions thus reducing the optimization problem to a finite number of degrees of freedom.

There are no a priori restrictions on the choice of the independent initial states, although common practice can suggest choices that may reduce the number of iterations. Every iteration requires the solution of several direct independent Stefan problems, but a notable saving of time may be achieved by parallelized computation that can be very naturally realized.

To simplify computations, in this work we have been concerned with a $2D$ domain, but the approach in terms of ACO can be straightforwardly generalized to a 3-dimensional framework. Similarly, more realistic models for the direct Stefan problems can be considered where, e.g., the thermal conductivity of the solid phase depends on the temperature. Freeze-thaw processes of different cooling rates can also be considered for optimization. Also the definition of the

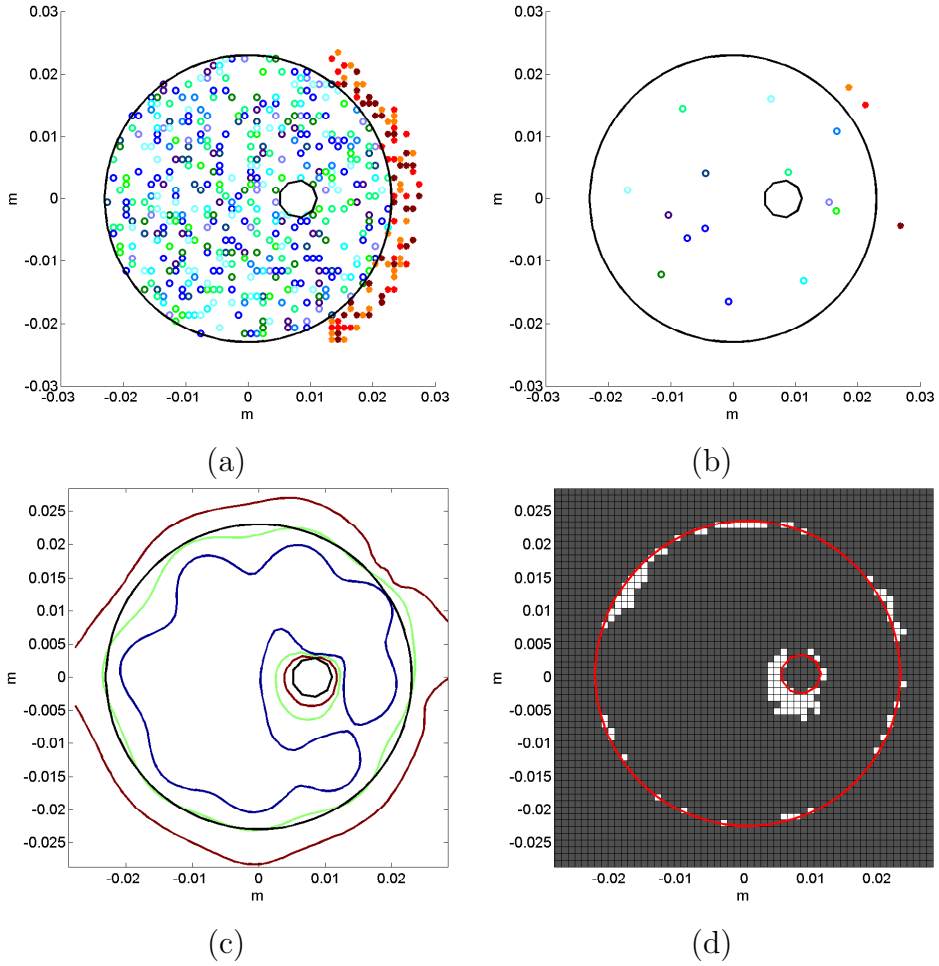

Figure 5.6: Case of 14 cryoprobes and 3 cryoheaters (where empty and filled circles represent the position of cryoprobes and cryoheaters and where probes of different colors belong to different configurations); $q = 0.015$, $\xi = 0.4$, $P = 36$, $Q = 19$. (a) Initial position of the P configurations. (b) Final position of the P configurations after ACO. (c) Temperature distribution for the optimal solution (i.e. the one characterized by the minimum value of the cost function): 0^o C-isotherm is red, -22^o C-isotherm is green, -45^o C-isotherm is blue. (d) Plot of the defected (i.e. x s.t. $\mu(\theta(\mathbf{x})) = 1$) pixels (white).

cost function can be modified to obtain a more accurate description of defective pixels.

A	1	2	3	4	5	6	7	8
B	-128	-114	-118	-134	-123	-128	-122	-112
C	-145	-145	-145	-145	-145	-145	-145	-145

A	9	10	11	12	13	14	15
B	-110	-138	-122	-128	-137	-113	-117
C	-145	-145	-145	-145	-145	-145	-145

Table 5.3: Temperature optimization in a two-stage planning (second stage): the cryoprobes' configuration is in Figure 5.7 (c). Lines A indicate the cryoprobes position (see Figure 5.7); lines B contain the cryoprobes temperature when a second optimization stage (concerning the temperature) is applied; lines C contain the cryoprobes temperature at the end of the first optimization stage (concerning positions).

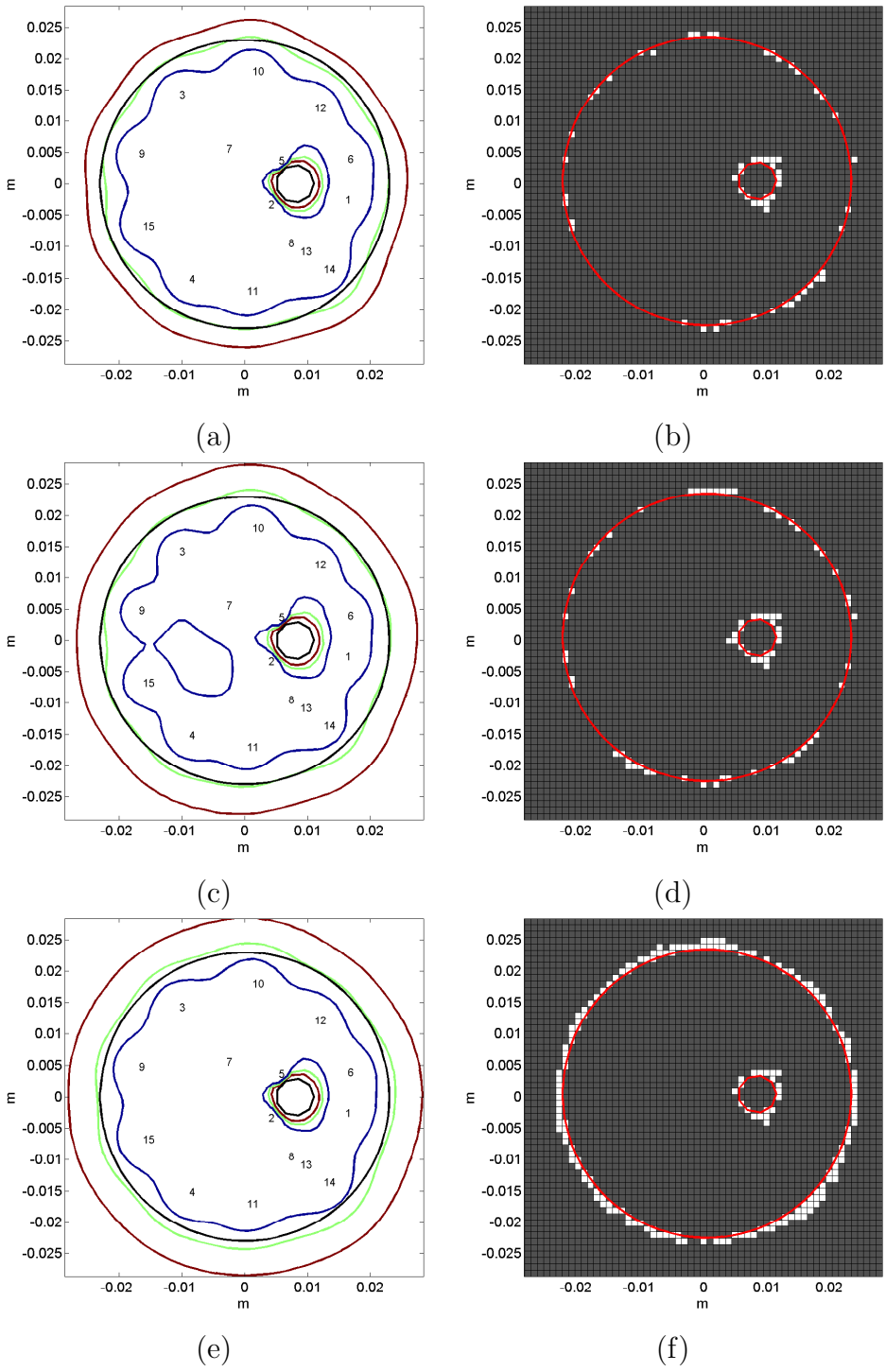

Figure 5.7: Two stage planning: case of 15 cryoprobes, $P = 48$, $Q = 25$, $q = 0.015$, $\xi = 0.5$. (a) and (b) contain the first stage results (see Figure 5.4). (c) Temperature distribution after 15 minutes with cryoprobes' temperature optimization: 0^o C-isotherm is red, -22^o C-isotherm is green, -45^o C-isotherm is blue. (d) Plot of the defected (i.e. x s.t. $\mu(\theta(\mathbf{x})) = 1$) pixels (white) with cryoprobes' temperature optimization. (e) Temperature distribution after 15 minutes without cryoprobes' temperature optimization: 0^o C-isotherm is red, -22^o C-isotherm is green, -45^o C-isotherm is blue. (f) Plot of the defected pixels (white) without cryoprobes' temperature optimization.

5.3. On the importance of computational lightness in cryosurgery planning

If one realistically wants to place side by side a planning tool to cryosurgery operation, it is necessary to face the problem of the computational cost that the planning technique requires as well as of its cost in terms of time employed for converging to an optimal configuration. The structure of the planning problem is such that the information on suitable configurations of the free parameters is encoded inside a direct thermic problem made by non-standard heat equations (i.e. Pennes equation, see Chapter 2, Section 2) implying a phase change of non-trivial modelization. The straightforward inversion of this problem is not possible so, often, inversion procedures are iterative and requiring, at each iteration, the solution of the direct problem in order to evaluate the goodness the last step. The numerical resolution of the direct thermic problem requires a considerable amount of time and, hence, the cost of a full computation of the most appropriate configuration of the free experimental parameters (i.e. of a complete planning) can become very large when the thermic problem is solved at each iteration. Since the idea is that every cryosurgery operation has to be preceded by a corresponding planning, the duration of a cryosurgery planning has to be on the order of minutes.

One way to solve the problem of reducing the duration of the planning procedure is to initialize the inversion technique (or, even, base the entire procedure) through geometrical considerations avoiding the computation of the temperature distribution at each step. The definition of the positions of the cryoprobes is one of the most important aspects inside a planning procedure and it generally requires a large amount of time; for this reason, we will first face this particular problem although remarking that proper initializations may accelerate the optimization of all the parameters.

Let, hence, consider the case in which one has to set the position of the probes depending on the value of the temperature they reach and on the shape of the tumoral region: the planning procedure may simply follow few principles. A freezing probe has to be both far enough from the tumoral boundary to keep non-tumoral tissues healthy and close enough to freeze the whole tumoral area; moreover, two different probes are needed to be as close to each other as little is the target area and, viceversa, as far as big is the tumor. These simple considerations suggest that a possibility to initialize such a planning procedure is to pick the positions of the probes in a way that they can homogeneously cover the whole tumoral region. In other words to choose their positions in a way that the distance occurring between tumoral boundaries and probes, and between a probe and its closest correspondent, is approximatively the same for each probe.

Following these simple principles, one can obtain a satisfactory initial configuration for the position of the probes. Bubble-packing [99] basically works following these criteria and, although the first idea was to utilize it as initialization tool for force-field [100], its only oper-

ation seems to be already enough precise and not requiring further optimization steps. As it will be better explained in Section 5.3.1, also ACO lends itself to an utilization based on the previously mentioned geometrical considerations.

5.3.1. A geometrical initialization technique for cryosurgery planning

The aim of this section is to describe a strategy able to provide a good a priori distribution of the positions of the cryoprobes inside the target tumoral region without making use of the numerical resolution of the direct thermic problem. The structure of the method will be based again on ACO.

Let suppose that one wants to place N cryoprobes. Based on the principle that a homogeneous distribution of probes inside a region can approximately provide its complete freezing, the aim of the here presented strategy is to divide the target area into N regions of the same size and to choose the position of the probes such that each probe belongs to a different region, being placed approximatively at its center. More precisely, at each iteration, ACO will extract a set of Q (or $P+Q$ if it is the first step) configurations (i.e. positions of the probes); then all the pixels of the tumoral region will be divided into N families, where the j^{th} family includes all the pixels for which the closest probe is the j^{th}-one; then the pixels of each family are summed and a cost function is defined in order to make the technique converging to a solution for which all the regions have similar values of area.

Hence, if $(u_{1,k}, ..., u_{N,k})$ are the positions of the probes of a particular state $\mathbf{U}_k$ and z stands for a generic pixel of the investigation domain, then it is possible to label all the pixels and define the families of pixels

$$\Psi_j = \{z \in \mathfrak{P} | j = \min_{i=1,...,N} \|z - u_i\|\} \tag{5.8}$$

with $\|\cdot\|$ opportune norm and with $\mathfrak{P}$ set of the pixels belonging only to the target region (i.e. to the region to be freezed) and not to its outer part. Then, in order to assign a cost to each state, one has to choose a function that evaluates the difference between the values of the areas of Ψ_j for each $j = 1, ..., N$ and such that the cost is zero when all the Ψ_j, with $j = 1, ..., N$, include the same number of pixels. One possible choice is the following

$$\mathcal{F}(\mathbf{U}_k) = \max_{i=1,...,N}(\sharp\Psi_i) - \min_{i=1,...,N}(\sharp\Psi_i), \tag{5.9}$$

where $\sharp\Psi_j$ indicates the number of elements of Ψ_j. Finally, when ACO has converged to a configuration $\bar{\mathbf{U}}$ which identifies (in the sense of equation 5.8) N regions with almost equal areas, the optimal configuration for the positions of the probes can be, then, taken as $\mathbf{U}^g = (u_1^g, ..., u_N^g)$, where u_j^g is the barycenter of Ψ_j.

Hence, the initialization process can be summarized as follows:

- Apply ACO by choosing as cost function (5.9) and with $\mathbf{U}_k$ state of positions of probes.
- Given the optimal configuration $\bar{\mathbf{U}}_k$ with the corresponding Ψ_j, $j = 1, ..., N$, compute $\mathbf{U}^g$.

Once the optimal preliminary configuration $\mathbf{U}^g$ is obtained, one can start the optimization process described in Section 5.2 taking into account $\mathbf{U}^g$ as initialization. More specifically, the optimization process does not need to start anymore with a uniform probability distribution $\mathcal{G}_.$. In fact, for each $j = 1, ..., N$, it will be possible to choose $\mathcal{G}_j$ as a Gaussian function centered in u_j^g and with an opportunely defined variance. An initial utilization of a uniform probability density function will be required only for those parameters which have not been covered by the initialization.

Although detailed only for freezing probes, the previous initialization technique can be easily adapted to initialize also cryoheaters. Moreover, its generalization to the three dimensional case is rather trivial: in fact, in the case of three dimensions, the norm at equation 5.8 can be substituted by a function of the distance between the pixel z and the straight line (or the segment) representing the probe and *a priori* restrictions on admissible values (insertion depth, angle of tilt or positions) can be implemented as usual (see Section 5.2.1).

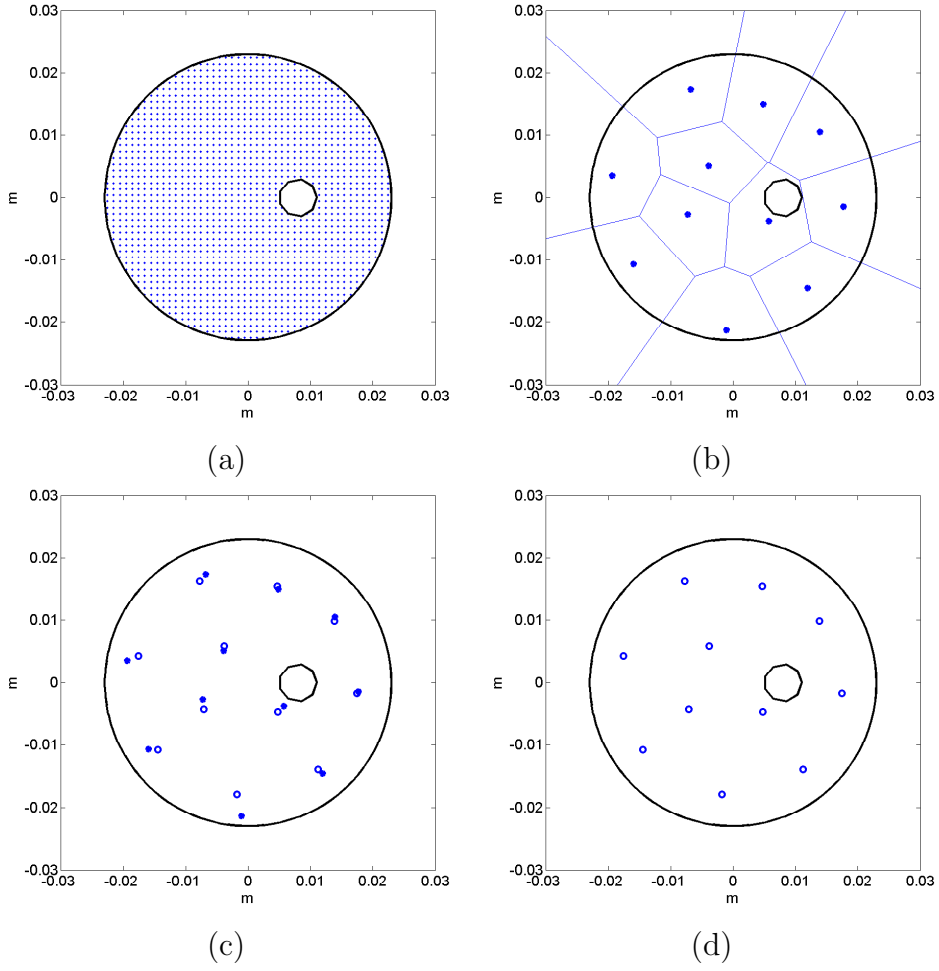

Figure 5.8: Example of the initial distribution provided by the technique described in Section 5.3.1 in the case of 11 freezing probes and with $P = 36$, $Q = 19$, $q = 0.05$, $\xi = 0.5$. (a) shows the pixels (blue points) belonging to the target area, i.e. belonging to $\mathfrak{P}$; (b) represents the converged configuration $\bar{\mathbf{U}}$ (blue stars) with its corresponding regions Ψ_j with j=1,...,11 (delimitated by segments); in (c) $\bar{\mathbf{U}}$ (stars) is plotted together with $\mathbf{U}^g$ (empty circles); (d) shows the final configuration $\mathbf{U}^g$.

Bibliography

[1] R. Abraham and J. E. Marsden. *Foundations of Mechanics*. The Addison-Wesley Publishing Company, Inc., Reading, Massachusetts, second edition, 1987.

[2] G. Allaire. *Numerical Analysis and Optimization*. Oxford University Press, Oxford, 2007.

[3] R. Aramini. *On Some Open Problems in the Implementation of the Linear Sampling Method*. PhD thesis in mathematics, Università degli Studi di Trento, Dipartimento di Matematica, 2007.

[4] R. Aramini, M. Brignone, G. Caviglia, A. Massa, and M. Piana. The linear sampling method in a lossy background: an energy perspective. *Inverse Problems in Science and Engineering*, 19:963–984, 2011.

[5] R. Aramini, M. Brignone, J. Coyle, and M. Piana. Postprocessing of the linear sampling method by means of deformable models. *SIAM J. Sci. Comput.*, 30(5):2613–2634, 2008.

[6] R. Aramini, M. Brignone, and M. Piana. The linear sampling method without sampling. *Inverse Problems*, 22:2237–2254, 2006.

[7] R. Aramini, G. Caviglia, and G. Giorgi. The role of point sources and their power fluxes in the linear sampling method. *SIAM J. Appl. Math.*, 71:1044–1069, 2011.

[8] R. Aramini, G. Caviglia, A. Massa, and M. Piana. The linear sampling method and energy conservation. *Inverse Problems*, 26:055004, 2010.

[9] T. Arens. Why linear sampling works. *Inverse Problems*, 20:163–173, 2004.

[10] T. Arens and A. Lechleiter. The linear sampling method revisited. *J. Integral Equations Appl.*, 21(2):179–202, 2009.

[11] R. Baissalov, G. A. Sandison, B. J. Donnelly, J. K. Saliken, J. G. McKinnon, K. Muldrew, and J. C. Rewcastle. A semi-empirical treatment planning model for optimization of multiprobe cryosurgery. *Physics in Medicine and Biology*, 45:1085–1098, 2000.

[12] A. B. Bakushinsky and M. Yu. Kokurin. *Iterative Methods for Approximate Solution of Inverse Problems*. Springer, Dordrecht, 2004.

[13] C. A. Balanis. *Advanced Engineering Electromagnetics*. John Wiley & Sons, Inc., New York, 1989.

[14] C. Bonacina, G. Comini, A. Fasano, and M. Primicerio. Numerical solution of phase change problems. *Int. J. Heat Mass Transfer*, 16(10):1825–1832, 1973.

[15] G. Bozza. *Numerical methods for inverse and ill-posed problems in electromagnetics*. PhD thesis in electronic and computer engineering and telecommunications, Università degli Studi di Genova, 2009.

[16] G. Bozza, M. Brignone, and M. Pastorino. Application of the no-sampling linear sampling method to breast cancer detection. *IEEE Trans. Biomed. Eng.*, 57(10):2525–2534, 2010.

[17] M. Brignone, R. Aramini, G. Bozza, and M. Piana. No sampling linear sampling for 3d inverse scattering problems. In E. De Bernardis, R. Spigler, and V. Valente, editors, *Applied and Industrial Mathematics in Italy III. Selected Contributions from the 9th SIMAI Conference, Rome, Italy, 15-19 September 2008*, volume 82 of *Series on Advances in Mathematics for Applied Sciences*, pages 146–155. World Scientific Publishing Co. Pte. Ltd., Singapore, 2010.

[18] M. Brignone, G. Bozza, R. Aramini, M. Pastorino, and M. Piana. A fully no-sampling formulation of the linear sampling method for three-dimensional inverse electromagnetic scattering problems. *Inverse Problems*, 25:015014, 2009.

[19] M. Brignone, G. Bozza, A. Randazzo, M. Piana, and M. Pastorino. A hybrid approach to 3d microwave imaging by using linear sampling and aco. *IEEE Trans. Ant. Prop.*, 56(10):3224–3232, 2008.

[20] F. Cakoni. Recent developments in the qualitative approach to inverse electromagnetic scattering theory. *J. Comput. Appl. Math.*, 204:242–255, 2007.

[21] F. Cakoni and D. Colton. On the mathematical basis of the linear sampling method. *Georg. Math. J.*, 10(3):411–425, 2003.

[22] F. Cakoni and D. Colton. Open problems in the qualitative approach to inverse electromagnetic scattering theory. *Europ. J. Appl. Math.*, 16:411–425, 2005.

[23] F. Cakoni and D. Colton. *Qualitative Methods in Inverse Scattering Theory*. Springer, Berlin, 2006.

[24] F. Cakoni, D. Colton, and D. Gintides. The interior transmission eigenvalue problem. *SIAM Journal on Mathematical Analysis*, 42:2912–2921, 2010.

[25] F. Cakoni, D. Colton, and H. Haddar. The computation of lower bounds for the norm of the index of refraction in an anisotropic media. *Journal of Integral Equations and Applications*, 2:203–227, 2009.

[26] F. Cakoni, D. Colton, and H. Haddar. On the determination of dirichlet and transmission eigenvalues from far field data. *Comptes Rendu Mathematique*, 7, 2010.

[27] F. Cakoni, D. Colton, and H. Haddar. The interior transmission eigenvalue problem for absorbing media. *preprint*, 2012.

[28] F. Cakoni, D. Colton, and P. Monk. *The Linear Sampling Method in Electromagnetic Scattering*. CBMS-NSF SIAM Publications, Philadelphia, 2006.

[29] F. Cakoni, D. Colton, and P. Monk. On the use of transmission eigenvalues to estimate the index of refraction from far field data. *Inverse Problems*, 23:507–522, 2007.

[30] F. Cakoni, M. Fares, and H. Haddar. Analysis of two linear sampling methods applied to electromagnetic imaging of buried objects. *Inverse Problems*, 22:845–867, 2006.

[31] F. Cakoni, D. Gintides, and H. Haddar. The existence of an infinite set of transmission eigenvalues. *SIAM Journal on Mathematical Analysis*, 42:237–255, 2010.

[32] T. F. Chan and L. A. Vese. Active contour without edges. *IEEE Trans. in Im. Proc.*, 10:266–277, 2001.

[33] K. J. Chua and S. K. Chou. On the study of the freeze-thaw thermal process of a biological tissue. *Appl. Thermal Engin.*, 29:3696–3709, 2009.

[34] J. K. Cohen. Cryosurgery of the prostate: techniques and indications. *Rev. Urol.*, 6, 2004.

[35] F. Collino, M'B. Fares, and H. Haddar. On the validation of the linear sampling method in electromagnetic inverse scattering problems. Rapport de recherche n. 4665, Institut National de Recherche en Informatique et en Automatique (INRIA), Rocquencourt, December 2002.

[36] D. Colton and H. Haddar. An application of the reciprocity gap functional to inverse scattering theory. *Inverse Problems*, 21:383–398, 2005.

[37] D. Colton, H. Haddar, and M. Piana. The linear sampling method in inverse electromagnetic scattering theory. *Inverse Problems*, 19:S105–S137, 2003.

[38] D. Colton and A. Kirsch. A simple method for solving inverse scattering problems in the resonance region. *Inverse Problems*, 12:383–383, 1996.

[39] D. Colton and R. Kress. *Integral Equation Methods in Scattering Theory.* John Wiley & Sons, Inc., New York, 1983.

[40] D. Colton and R. Kress. *Inverse Acoustic and Electromagnetic Scattering Theory.* Springer, Berlin, first edition, 1992.

[41] D. Colton and R. Kress. *Inverse Acoustic and Electromagnetic Scattering Theory.* Springer, Berlin, second edition, 1998.

[42] D. Colton and P. Monk. A linear sampling method for the detection of leukemia using microwaves. *SIAM J. Appl. Math.*, 58(3):926–941, 1998.

[43] D. Colton, P. Monk, and J. Sun. Analytical and computational methods for transmission eigenvalues. *Inverse Problems*, 26:1–16, 2010.

[44] D. Colton, L. Päivärinta, and J. Sylvester. The interior transmission problem. *Inverse Problems and Imaging*, 1:13–28, 2007.

[45] D. Colton and M. Piana. The simple method for solving the electromagnetic inverse scattering problem: the case of te polarized waves. *Inverse Problems*, 14:597–614, 1998.

[46] D. Colton, M. Piana, and R. Potthast. A simple method using morozov's discrepancy principle for solving inverse scattering problems. *Inverse Problems*, 13:1477–1493, 1997.

[47] F. Delbary, M. Brignone, G. Bozza, R. Aramini, and M. Piana. A visualization method for breast cancer detection by using microwaves. *SIAM J. Appl. Math.*, 70(7):2509–2533, 2010.

[48] A. J. Devaney. Diffraction tomography. In W. M. Boerner et al., editor, *Inverse Methods in Electromagnetic Imaging,* Part 2, pages 1107–1135. D. Reidel Publishing, Boston, 1985.

[49] M. Dorigo and L. M. Gambardella. Ant colony system: a cooperative learning approach to the travelins salesman problem. *Trans. Evol. Comp.*, 1, 1997.

[50] H. W. Engl, M. Hanke, and A. Neubauer. *Regularization of Inverse Problems.* Kluwer Academic Publishers, Dordrecht, 1996.

[51] A. A. Gage and J. Baust. Mechanisms of tissue injury in cryosurgery. *Cryobiology*, 37, 1998.

[52] C. Gilmore, A. Abubakar, W. Hu, T. M. Habashy, and P. M. van den Berg. Microwave biomedical data inversion using the finite-difference contrast source inversion method. *IEEE Transactions on antennas and propagation*, 57:1528–1538, 2009.

[53] G. Giorgi. Metodi qualitativi in tomografia a microonde: applicazioni alla diagnosi del tumore al seno. M.sc. thesis, Universit degli Studi di Genova, Genova, 2008.

[54] G. Giorgi, L. Avalle, M. Brignone, M. Piana, and G. Caviglia. An optimization approach to multiprobe cryosurgery planning. *Comput. Meth. in Biomech. and Biomed. Engin.*

[55] G. Giorgi, M. Brignone, R. Aramini, and M. Piana. The inhomogeneous lippmann-schwinger equation and its application to inverse scattering problems. *preprint.*

[56] G. Giorgi and H. Haddar. Computing estimates on material properties from transmission eigenvalues. *preprint.*

[57] G. Giorgi and H. Haddar. Computing estimates on material properties from transmission eigenvalues. Rapport de recherche n. 7729, Institut National de Recherche en Informatique et en Automatique (INRIA), Rocquencourt, 2011.

[58] M. Hanke. Why linear sampling really seems to work. *Inverse Problems and Imaging*, 2(3):373–395, 2008.

[59] R. F. Harrington. *Field computation by Moments Methods.* IEEE PRESS, Piscataway, 1993.

[60] F. S. Hillier and G. J. Lieberman. *Introduction to Operations Research.* McGraw - Hill, 2001.

[61] M. Hitrik, K. Krupchyk, P. Ola, and L. Paivarinta. Transmission eigenvalues for operators with constant coefficients. *SIAM J. Math. Analysis*, 42:2965–2986, 2010.

[62] M. Hitrik, K. Krupchyk, P. Ola, and L. Paivarinta. The interior transmission problem and bounds on transmission eigenvalues. *Math. Research Letters*, 18:279–293, 2011.

[63] J. J. Faran Jr. Sound scattering by solid cylinders and spheres. *Journal of the Acoustical Society of America*, 2:405–418, 1951.

[64] F. G. Keanini and B. Rubinsky. Optimization of multiprobe cryosurgery. *Trans. ASME*, 114:796–801, 1992.

[65] O. D. Kellogg. *Foundations of Potential Theory.* Springer Verlag, Berlin, 1967.

[66] A. Kirsch. Characterization of the shape of a scattering obstacle using the spectral data of the far-field operator. *Inverse Problems*, 14:1489–1512, 1998.

[67] A. Kirsch. On the existence of transmission eigenvalues. *Inverse Problems and Imaging*, pages 155–172, 2009.

[68] A. Kirsch and N. Grinberg. *The Factorization Method for Inverse Problems*. Oxford University Press Inc., New York, 2008.

[69] R. Kress and P. Serranho. A hybrid method for two-dimensional crack reconstruction. *Inverse Problems*, 21:773–784, 2005.

[70] L. D. Landau and E. M. Lifshitz. *Electrodynamics of continuous media*, volume 8 of *Course of Theoretical Physics*. Pergamon Press, Oxford, second edition, 1984.

[71] M. Lazebnik, L. McCartney, D. Popovic, C. B. Watkins, M. J. Lindstrom, J. Harter, S. Sewall, A. Maglioccio, J. H. Booske, M. Okoniewski, and S. C. Hagness. A large-scale study of the ultrawideband microwave dielectric properties of normal breast tissue obtained from reduction surgeries. *Physics in Medicine and Biology*, 52, 2007.

[72] M. Lazebnik, M. Okoniewski, J. H. Booske, and S. C. Hagness. Highly accurate debye models for normal and malignant breast tissue dielectric properties at microwave frequencies. *IEEE Microwave and Wireless Components Letters*, 17(12):822–824, 2007.

[73] D. C. Lung, T. F. Stahovic, and Y. Rabin. Computerized planning for multiprobe cryosurgery using a force-field analogy. *Comp. Meth. in Biomech. and Biomed. Eng.*, 7, 2004.

[74] P. A. Martin. Acoustic scattering by inhomogeneous obstacles. *SIAM J. Appl. Math.*, 64(1):297–308, 2003.

[75] P. M. Meaney, S. A. Pendergrass, M. W. Fanning, D. Li, and K. D. Paulsen. Importance of using a reduced contrast coupling medium in 2d microwave breast imaging. *J. of Electromagn. Waves and Appl.*, 17(2):333–355, 2003.

[76] P. Monk. *Finite Element Methods for Maxwell's Equations*. Oxford University Press, New York, 2003.

[77] G. M. Onik and D. Atkinson. Cryosurgery of liver cancer. *Seminars in Surgical Oncology*, 9:309–317, 1993.

[78] L. Paivarinta and J. Sylvester. Transmission eigenvalues. *SIAM Journal on Mathematical Analysis*, 40:738–753, 2008.

[79] W. K. H. Panofsky and M. Phillips. *Classical Electricity and Magnetism*. Dover Publications, Inc., New York, second edition, 2005.

[80] H. H. Pennes. Analysis of tissue and artherial blood temperature in the resting human foream. *J. Appl. Phys.*, 1:93–122, 1948.

[81] M. Piana. On uniqueness for anisotropic inhomogeneous inverse scattering problems. *Inverse Problems*, 14:1565–1579, 1998.

[82] E. Polak. *Optimization.* Springer, New York, 1997.

[83] R. Potthast. A fast new method to solve inverse scattering problems. *Inverse Problems*, 12:731–742, 1996.

[84] Y. Rabin, D. C. Lung, and T. F. Stahovic. Computerized planning of cryosurgery using cryoprobes and cryoheaters. *Technology in Cancer Research and Treatment*, 3, 2004.

[85] Y. Rabin and A. Schitzer. Numerical solution of the multidimensional freezing problem during cryosurgery. *Trans. ASME*, 120:32–37, 1998.

[86] Y. Rabin and T. F. Stahovic. Cryoheater as a means of cryosurgery control. *Phys. Med. Biol.*, 48:619–632, 2003.

[87] W. T. Reid. Anatomy of the ordinary differential equation. *The American Mathematical Monthly*, 82(10):971–984, 1975.

[88] J. H. Richmond. Scattering by a dielectric cylinder of arbitrary cross section shape. *IEEE Trans. Ant. Prop.*, 13:334–341, 1965.

[89] M. R. Rossi, D. Tanaka, K. Shimada, and Y. Rabin. An efficient numerical technique for bioheat simulations and its application to computerized cryosurgery planning. *Comp. Meth. Progr. Biom.*, 85:41–50, 2007.

[90] M. R. Rossi, D. Tanaka, K. Shimada, and Y. Rabin. Computerized planning of cryosurgery using bubble-packing: an experimenthal validation with a phantom material. *Int. J. of Heat and Mass Transfer*, 51:5671–5678, 2008.

[91] M. R. Rossi, D. Tanaka, K. Shimada, and Y. Rabin. Computerized planning of prostate cryosurgery using variable cryoprobe insertion depth. *Cryobiology*, 60:71–79, 2010.

[92] L. I. Rubinstein. *The Stefan Problem.* American Mathematical Society, Providence, 1971.

[93] M. Scala, G. Margarino, G. Amoretti, G. Mereu, and G. Mereto. Usefulness of cryosurgery in preneoplastic and neoplastic pathology of the head and the neck region. *Minerva Chir.*, 42:369–377, 1987.

[94] A. Schitzer. Cryosurgery analysis and experimentation of cryoprobes in phase changing media. *J. Heat Transf.*, 133:011005–011017, 2011.

[95] J. D. Shea, P. Kosmas, S. C. Hagness, and B. D. Van Veen. Three-dimensional microwave imaging of realistic numerical breast phantoms via a multiple-frequency inverse scattering technique. *Medical Physics*, 37(8):4210–4226, 2010.

[96] K. Socha and M. Dorigo. Ant colony optimization for continuous domains. *Eur. J. Oper. Res.*, 50:1180–1189, 2003.

[97] J. Sun. Estimation of transmission eigenvalues and the index of refraction from cauchy data. *Inverse Problems*, 27:1–11, 2011.

[98] A. Tacchino, J. Coyle, and M. Piana. Numerical validation of the linear sampling method. *Inverse Problems*, 18:511–527, 2002.

[99] D. Tanaka, K. Shimada, , M. R. Rossi, and Y. Rabin. Cryosurgery planning using bubble packing in 3d. *Comp. Meth. in Biomech. and Biomed. Eng.*, 11:113–121, 2007.

[100] D. Tanaka, K. Shimada, and Y. Rabin. Two-phase computerized planning of cryosurgery using bubble-packing and force-field analogy. *ASME Journal of Biomechanical Engineering*, 128:49–58, 2006.

[101] B. Tang, R. G. Wan, K. B. Muldrew, and B. J. Donnelly. A finite element model for cryosurgery with coupled phase change and thermal stress aspects. *Finite Elements in Analysis and Design*, 44:288–297, 2008.

[102] D. Theodorescu. Cancer cryotherapy: evolution and biology. *Rev. Urol.*, 6:S9–S19, 2004.

[103] A. N. Tikhonov, A. V. Goncharski, V. V. Stepanov, and A. G. Yagola. *Numerical Methods for the Solution of Ill-posed Problems*. Kluwer Academic Publishers, Dordrecht, 1995.

[104] P. M. van den Berg and R. E. Kleinmann. A contrast source inversion method. *Inverse Problems*, 13:1607–1620, 1997.

[105] P. M. van den Berg, A. L. van Broekhoven, and A. Abubakar. Extended contrast source inversion. *Inverse Problems*, 15:1325–144, 1999.

[106] W. Walter. *Differential and Integral Equations*. Springler, Berlin, 1970.

[107] J. Zhang, G. A. Sandison, J. Y. Murthy, and L. X. Xu. Numerical simulations for heat transfer in prostate cancer cryosurgery. *J. Biomech. Engin.*, 127:279–294, 2005.

[108] G. Zhao, H. Zhang, X. Guo, D. Luo, and D. Gao. Effect of blood flow and metabolism on multidimensional heat transfer during cryosurgery. *Med. Engin. and Phys.*, 29:205–215, 2007.

[109] Q. Z. Zhong, H. L. Qing, C. Xiao, E. Ward, G. Ybarra, and W. T. Joines. Microwave breast imaging: 3-d forward scattering simulation. *IEEE Trans. Biomed. Eng.*, 50(10):1180–1189, 2003.

[110] R. Zoughi. *Microwave Non-Destructive Testing and Evaluation*. Kluwer Academic Publishers, Norwell, 2000.

Acknowledgements

After three intense years I have many people to thank:

- My advisors Michele Piana and Houssem Haddar, since they allowed me joining their respective research groups where it has been a pleasure to spend these years. But also for their help in many situations and for having introduced me to topics that made my working days really pleasant.

- The Genova's scattering group: Riccardo Aramini, Massimo Brignone and Giacomo (Franco) Caviglia. It has really been a pleasure to work with you, guys! You made easy a lot of difficult situations by always providing support and friendship.

- All the rest of the MIDA group, current and past members (and the list is long): Federico Benvenuto, Giovanni Bozza, Cristina Campi, Jingnan Guo, Anna Maria Massone, Annalisa Pascarella, Sampsa Pursiainen, Alberto Sorrentino and Gabriele Torre. Group of friends. A special thank to Silvia Allavena for the number of times she helped me to menage bureaucratic deadlines but mainly for the pleasure to share the Ph.D. experience from the beginning to the end.

- The wonderful people I met at Ecole Polytechnique during all the months spent there. They made me feeling, at the CMAP, a bit more as at home: Davide Barilari, Yosra Boukari, Elie Bretin, Nicolas Chaulet, Qiang Chen, Anne Cossonniere, Wallis Filippi, Armin Lechleiter, Simon Marmorat, Georgios Michailidis, Giovanni Migliorati, nh Lim Nguyen.

- All the undergraduate and graduate students, postdocs, etc, at Università di Genova. Mates of lunches, dinners, evenings but in particular coffee breaks: Paola Bisio, Andrea Carbonaro, Michela Chessa, Stefano Gagliardo, Neeraj Kumar, Valeriano Lanza, Gianvittorio Luria, Lucia Mantovani, Renza Morino, Fabio Pasquali, Micol Spinelli, Matteo Varbaro and many others.

- I wish to remind and to thank also the few persons met during summer schools and conferences that shared with me tourist trips and good moments: Jerome Goddard, Hector

Chang and Andrea Ballerini (Delaware 2009), Gabriele Arnulfo, Raluca Andrei, Chiara Olivieri and Saverio Salzo (Lipari 2009), Fabian Dunker and Frank Werner (College Station 2011), Stefano Marranò and Thibaut Lienart (Vancouver 2011), Sara Simona Dessì, Ortal Mizrahy and Estefania Rosendo (Corvallis 2011), Yannick Fisher (Mexico City 2011) and all I am forgetting.

- All the members of *Casa Baldis* except the mean householders and two or three past elements that we do not forget.

A final and more general thank to my family and to all the friends who supported me during these three years: an appreciated support or friendship does not need to be necessarily related to Mathematics.